THESIS FOR THE DEGREE OF LICENTIATE OF ENGINEERING

Modeling mesoscopic unconventional superconductors

PATRIC HOLMVALL

Department of Microtechnology and Nanoscience (MC2)
Applied Quantum Physics Laboratory
CHALMERS UNIVERSITY OF TECHNOLOGY

Göteborg, Sweden 2017

Modeling mesoscopic unconventional superconductors
PATRIC HOLMVALL

Thesis for the degree of Licentiate of Engineering
ISSN 1652-0769
Technical Report MC2-375

Applied Quantum Physics Laboratory
Department of Microtechnology and Nanoscience (MC2)
Chalmers University of Technology
SE-412 96 Göteborg
Sweden
Telephone: +46 (0)31-772 1000

Author email: holmvall@chalmers.se

Cover: Mesoscopic pieces in the puzzle of unconventional superconductivity. This thesis answers the questions of how these pieces fit together, and what picture they portray when brought together.

Printed by Chalmers Reproservice
Göteborg, Sweden 2017

Modeling mesoscopic unconventional superconductors
Thesis for the degree of Licentiate of Engineering

PATRIC HOLMVALL

Department of Microtechnology and Nanoscience (MC2)
Applied Quantum Physics Laboratory
Chalmers University of Technology

Abstract

High-temperature superconducting materials are often experimentally realized as thin films that can be patterned into devices operating in the mesoscopic regime. On this length scale, various finite-size and surface effects heavily influence the nature of the superconducting state, and can induce new ground states with spontaneously broken symmetries. Motivated by the wide technological application of such mesoscopic devices and the many open questions regarding the new emergent ground states, this thesis sets out to study mesoscopic grains. In particular, a recently discovered phase which spontaneously breaks translational and time-reversal symmetries will be studied, referred here to as the "loop-current phase". The aim is to study how this phase responds to magnetic and geometric perturbations.

The quasiclassical theory of superconductivity is used to simulate mesoscopic thin-film grains in equilibrium, with a strong emphasis on d-wave superconductors, e.g. the cuprates. The properties of the loop-current phase are cataloged, with an explanation of how and why it occurs. Various phase diagrams are produced, and the magnetic-field dependent thermodynamics is studied.

In conclusion, the loop-current phase occurs at pairbreaking interfaces that host quasiparticle midgap states. The phase is associated with a spontaneous superfluid momentum which drives circulating current loops that break continuous translational symmetry, providing an energetically favorable Doppler shift of the midgap states. The phase is found to be robust against external fields in the whole Meissner state, but not against very high fields in the mixed state. The phase is lost when there is a competing effect which significantly broadens the spectrum, e.g. a strong external vector potential. The phase transition is associated with a large jump in the heat capacity, serving as a hallmark for the phase to be observed experimentally. It is predicted that the phase leads to a broadening of the spectrum which is consistent with experimental findings.

Keywords: Unconventional superconductivity, quasiclassical theory, Andreev bound states, phase transitions, spontaneous symmetry breaking, translational symmetry, time-reversal symmetry, mesoscopic thin-films

Acknowledgements

First and foremost, I would like to thank Tomas Löfwander and Mikael Fogelström for giving me the chance to work as a PhD candidate in their group, and for all the supervision. I feel fortunate to have supervisors who are always available.

I am forever indebted to Mikael Håkansson for all the time he spent helping me during his busy times of thesis and paper writing, and most importantly, for developing and handing over such an amazing computational framework. It is rare to see a physicist develop such an advanced and beautiful code. This code has shaped my PhD project.

At the time of this writing, I have been a member of the group of Applied Quantum Physics at MC2, Chalmers, for exactly three years. During these years I have been fortunate to meet a number of people whose company I have enjoyed very much. I thank my colleagues for all the help and for all the great times. From interesting physics discussions to swedish Fika, it has all been a pleasure. Getting beaten in ping-pong by Yevgeniy Korniyenko and in squash by Kevin Marc Seja also counts as a pleasure. I am grateful to Maciej Misiorny and Raffaella Negretti for helping me develop my skills with illustration, writing and publication. I acknowledge Jens Schulenborg for developing the template for this thesis.

During these years, I have also benefited greatly from discussing superconductivity with many of the people that I met. In particular, I would like to mention Anton Vorontsov, Per Delsing, Dag Winkler, Alexei Kalaboukhov and Vitaly Shumeiko. I thank Oleksii Shevtsov, Daniel Persson and Niclas Wennerdal for helping me with quasiclassical theory. I also thank the latter and Mr. Gibson for sharing our thirties life crisis, filled with intense skateboarding sessions and rock 'n' roll concerts.

Special thanks to all the great teachers and mentors I have had throughout the years. Andreas Martin Heinz has been defining in my development as a scientist. The same goes to everyone else in the Subatomic physics department at Chalmers, and especially Håkan T. Johansson, for all the fun discussions and computer-related help.

I extend my deepest gratitude to my family and to all my friends, especially Niclas Johansson, Dundar, Elof, Emil and Peter. Thank you for sticking around and for always being there for me even in my absence.

Last but not least, I thank Laura for all her love and support - *"Siempre excelente, nunca perfecto, todo bien"*.

List of publications

This thesis is based on the following appended papers:

[I] P. Holmvall, A. B. Vorontsov, M. Fogelstrom, and T. Lofwander, "Spontaneously broken translational symmetry at edges of high-temperature superconductors: thermodynamics in magnetic field", ArXiv e-prints (2017), arXiv:1711.07946 [cond-mat.supr-con].

[II] P. Holmvall, T. Löfwander, and M. Fogelström, "Spontaneous generation of fractional vortex-antivortex pairs at single edges of high-Tc superconductors", ArXiv e-prints (2017), arXiv:1706.06165 [cond-mat.supr-con], accepted for publication in J. of Physics: Conf. Ser., the proceedings of the 28th International Conference on Low Temperature Physics.

These publications are always referred to as paper I and paper II.

List of figures

List of tables

Nomenclature

Abbreviations

ABS	Andreev bound states
AFM	Atomic force microscopy
BCS	Bardeen-Cooper-Schrieffer
DOS	Density of states
FS	Fermi surface
FFLO	Fulde-Ferrell-Larkin-Ovchinnikov phase
GS	Ground state
HTS	High-temperature superconductors
LDOS	Local density of states
MED	Magnetic energy density
MGS	Midgap states
MS	Metastable state
N	Normal state
NMR	Nuclear magnetic resonance
OP	Order parameter
S	Superconducting state
SC	Superconductor
STM	Scanning tunneling microscope
SQUID	Superconducting quantum interference device
YBCO	Yttrium barium copper oxide
ZBCP	Zero-bias conductance peak

Symbols

Δ	Superconducting order parameter
η	Pairing-symmetry basis-function of the order parameter
$\delta\Omega$	Free-energy difference between normal and superconducting states
γ	Coherence function, Riccati amplitude
f	Quasiclassical pair propagator
g	Quasiclassical quasiparticle propagator
N	DOS
N_F	Normal-state DOS at the Fermi surface
λ	Superconducting coupling constant
λ_L	London penetration depth
λ_0	Zero-temperature London penetration depth
Λ_L	London parameter
ξ_0	Zero-temperature coherence length
κ	Ginzburg-Landau parameter
κ_0	Zero-temperature Ginzburg-Landau parameter
Φ_0	Magnetic flux quantum
e	Elementary charge ($e = -\|e\|$)
c	Speed of light
k_B	Boltzmann constant
h	Planck constant
$\hbar$	Reduced Planck constant
$E_{\boldsymbol{k}}$	Excitation energy
$\xi_{\boldsymbol{k}}$	Single-particle energy measured relative to the Fermi energy in the normal state

μ	Energy shift of the chemical potential between the normal and superconducting states
ϵ_F	Fermi energy
ϵ_n	Matsubara energy
$\boldsymbol{j}$	Current density
$\boldsymbol{j}_s$	Supercurrent density
$\boldsymbol{j}_{qp}$	Quasiparticle current density
$\boldsymbol{H}$	Magnetic field
Φ_{ext}	External flux applied to the system
$\boldsymbol{B}$	Magnetic flux density
$\boldsymbol{B}_{\mathsf{ext}}$	External magnetic flux density applied to the system
$\boldsymbol{B}_{\mathsf{ind}}$	Magnetic flux density induced by currents in the system
$\boldsymbol{A}$	Magnetic vector potential
$\boldsymbol{A}_{\mathsf{ext}}$	Magnetic vector potential associated with an external flux
$\boldsymbol{A}_{\mathsf{ind}}$	Magnetic vector potential induced by currents in the system
$\boldsymbol{p}_s$	Superfluid momentum
$\boldsymbol{p}_F$	Fermi momentum
$\boldsymbol{v}_F$	Normal-state Fermi velocity on the Fermi surface
T_c	Superconducting transition temperature
j_d	Depairing current
θ_{p_F}	Angle relative at Fermi momentum direction

Operators and matrices

$\hat{A}$	Object in Nambu $\otimes$ spin-space
$\tilde{A}$	Particle-hole conjugation
G^R	Retarded Green function
G^M	Matsubara Green function

Contents

1 Introduction

To inspire curiosity, my father once asked me in my physics freshman year *"How come there is still considerable active basic research on materials and, in particular, metals?"*. What he was referring to is that although the first alloys were made almost 6000 years ago, and the first metal tools another 4000 years before that, new materials are still found on an almost daily basis, with many interesting phenomena that are not yet fully understood. This thesis studies how the phenomenon of superconductivity behaves in such materials when realized on the mesoscopic scale, the intermediate scale between the microscopic and the macroscopic, and how on this scale, spontaneous magnetic fields and currents can arise. The traditional microscopic theories used to study superconductivity tend to become intractable at this length scale, however, and the main challenge therefore lies in making realistic models and simulations of such systems. This challenge is overcome by using the quasiclassical theory of superconductivity, implemented in a computational framework that utilizes high-performance computing. The aim of this chapter is to give a background to this research and to explain the main concepts mentioned above. The chapter starts by using the frameworks of solid state and condensed matter physics to describe how electrical resistance arises in conducting materials, and how it completely vanishes in the superconducting state. This is followed by an introduction of the most relevant properties of superconductivity. The chapter is written on a very general level intended for a broader audience. The same concepts are then described on a much more detailed and technical level in the rest of the thesis. The chapter ends with a statement of the research topic and an outline of the thesis.

1.1 Background

The main objective of solid state physics is to describe the electronic and thermal properties of solids, mainly metals, through the distribution and interactions of the constituent atoms. At zero temperature, the equilibrium distribution of the atoms is a perfectly periodic lattice, referred to as a *crystal lattice*. In conductors, electrons are delocalized from the lattice points into conduction electrons that are free to move around in the lattice, rendering the lattice points into positively charged ions, called *cations*. Different excitation mechanisms, such as increased temperature and external perturbations, lead to deviations and vibrations of the cations about their equilibrium points. If these deviations propagate, they can be quantized into *collective excitations* known as *phonons*. Understanding the electronic and thermal properties of solids boils down to understanding the behavior of the conduction electrons in their interaction with the lattice, the phonons, with each other, and with various perturbations.

Condensed matter physics is a generalization of solid state physics to study also other phases of matter, e.g. liquids and Bose-Einstein condensates, and constitutes one of the most active disciplines of physics. Unlike nuclear and particle physics where the fundamental interactions between the elementary particles are unknown[1], the electromagnetic interaction which lies at the heart of most condensed matter physics phenomena is well-known even on a quantum level, and therefore also the governing equations describing the dynamics. What then prevents us from solving these equations once and for all, to learn everything there is to know about these condensed matter systems? The difficulty comes from the great number of particles involved, typically on the order of Avogadro's number ($\sim 10^{23}$). This sheer number of particles gives rise to a plethora of new phases and phenomena, further exemplifying how great complexity can arise in nature due to ordering at higher levels. By analogy, consider how only electrons and nucleons when brought together form atoms, which in turn form molecules, then DNA, proteins, and eventually, a consciousness reading and reflecting on this text.

Although the interactions are well-known and relatively simple, trying to solve the equations of motion for $\sim 10^{23}$ particles is far beyond any contemporary, and perhaps even future, computational capability. Instead of trying to achieve this hopeless goal, the main aim of condensed matter physics is to formulate simplified models which shed as much of the complexity as possible, without losing the ability to describe the essential physics. A great number of such simplified models and theories have been developed, but we are still nowhere close to being able to describe all the observed phenomena. Therefore, to answer the opening question of this chapter, it is the complexity of trying to model and understand all the

[1]For example, we currently do not know a closed form of the attractive interaction between nucleons (protons and neutrons) that binds matter together, and many nuclear physicists question if we ever will.

emergent phenomena that gives rise to most of the basic research in condensed matter physics and materials science. Furthermore, the development of new technologies provides new tools to study and fabricate novel materials. As we learn more about how these novel materials can be used, new technologies arise, forming a cycle. An example is nanotechnology, which has enabled single-atom precision in the manipulation of matter, and paved the way for peculiar realizations of materials. Examples of such realizations are completely two-dimensional materials, one-dimensional nanowires, and intriguing proximity structures, together constituting the basic building blocks for devices in quantum electronics.

Materials realized in such a microscopic nano-scale regime show unique phenomena not present on the larger macroscopic scale. The aim of this thesis is to study how the phenomenon of *superconductivity* behaves on the nano scale. Superconductivity is a phase that exists in some materials below a certain critical temperature T_c. Below this temperature[2], the materials undergo a phase transition into a state where a gap opens up in the energy spectrum, resulting in perfect diamagnetism and a complete loss of the electrical (DC) resistance. Thus, in contrast to the solid-liquid transition where the crystal structure of a material changes, the superconducting phase transition is associated with a change in the spectral and electromagnetic properties of a material. Before describing these properties further and introducing the research topic of this thesis, a brief explanation will be given of what leads to electrical resistance in metal conductors above the superconducting transition temperature, in the so-called *normal state*.

[2]Examples of superconductors are elemental aluminum with $T_c \approx 1.2$ K, alloys like NbTi with $T_c \approx 10$ K, and more complex compounds like the ceramic "cuprate" $YBa_2Cu_3O_7$ (YBCO) with $T_c \approx 90$ K. At pressures of 150 GPa, H_2S becomes superconducting at $T_c \approx 203$ K.

1.2 Electrical resistance and the normal state

Although there is typically an astonishing number of interacting particles involved in condensed matter phenomena, much of the basics can be well described with an independent single-particle picture. The following marks the starting point of Landau-Fermi liquid theory [1–3] to describe the conduction electrons in such a picture. Apart from being used for this description, the theory is considered beyond the scope of this thesis. For a more thorough review of the theories of condensed matter physics, see the for example the standard text books of Refs. [4–6], or the more modern works of Refs. [7, 8]. For a more advanced treatment, see for example Refs. [9–11].

Consider a good metal conductor in thermal equilibrium at temperature $T = 0$ K. The Pauli exclusion principle causes the non-excited electrons to populate different energy levels, filling up the so-called *Fermi sphere*, with the highest occupied state at the *Fermi energy*, ϵ_F. In the absence of interactions, the unperturbed electrons behave like a free-electron gas, and can be treated as independent particles with single-particle energy levels. Imagine that interactions, for example with other electrons or with the crystal lattice, are turned on sufficiently slowly, such that the adiabatic theorem of Born and Fock applies [12]. The system then remains in its eigenstate[3], but with energy levels shifted with a one-to-one correspondence, where the new energy levels can be seen as a new modified ground state. The system still obeys fermion statistics, and if the states are assumed to have similar momenta, then the dispersion relation forces the new fermions to have a new *renormalized* mass m^*, which can be orders of magnitude different than the electron mass. These new fermions are called *quasiparticles*, or *quasi-electrons*. Holes[4] are similarly renormalized into *quasi-holes*. Thus, the independent particle model is modified into an independent quasiparticle model in the presence of interactions, the latter which *dresses* electrons and holes with a surrounding distortion cloud which renormalizes the dynamical properties (e.g. the effective mass and magnetic moment), but leaves the conserved quantum numbers (e.g. charge and spin) unchanged. As long as the one-to-one correspondence of the energy levels holds in the presence of interactions, these quasiparticles constitute what is commonly called a *Fermi liquid*. The excitations of the Fermi liquid are superpositions of quasiparticle states, rather than normal single-particle states.

[3]Formally, a state is an eigenstate if $\hbar/\epsilon < \tau$, where $\hbar$ is the Planck constant, ϵ the energy and τ the lifetime of the state.

[4]In an environment of electrons (for example in the conduction band), the absence of an electron can be treated as a quasiparticle, referred to as a hole. The holes have opposite charge as the electrons, and move through the displacement of electrons. A common misconception is that a hole is synonymous with a positron, the antiparticle of the electron. The positron is an elementary particle that can exist in the absence of electrons, while the hole is a quasiparticle that cannot.

Landau showed that the Fermi-liquid model holds even when the direct[5] electron-electron interaction is relatively strong, since the electron-electron cross section is reduced due to screening by the crystal lattice, and more importantly, because the scattering rate is tremendously suppressed by the Pauli exclusion principle. The Pauli principle, together with energy and momentum conservation, asserts that only electrons of energy $\epsilon = k_B T$ lying in a thin shell $\delta_\epsilon \equiv |\epsilon - \epsilon_F| \ll \epsilon_F$ around the Fermi surface can interact in scattering processes, yielding a small phase space which goes to zero exactly at the Fermi surface. Here, k_B is the Boltzmann constant and T the temperature. The renormalized properties are essentially constant within this shell. Naively, the quasiparticles should have a finite lifetime, as these excitations can decay to the independent-electron ground state. Fermi's golden rule states, however, that the lifetime of the free quasi-electrons should be inversely proportional to the vanishing phase space, and hence be extremely long.

Electrical resistance is caused by scattering of the conduction electrons. The Pauli principle together with the screening therefore causes the electron-electron interaction to have a negligible influence on the electrical resistance. This is especially true at finite temperatures and in good conductors. Instead, resistance mainly arises due to scattering against the lattice, and due to the deviation of the cations from their equilibrium points. At higher temperatures, for example, the dominant contribution is due to phonons. What happens to the resistance in clean conductors at lower temperatures, and especially as the temperatures approaches absolute zero, was initially the matter of some debate [13]. Dewar expected the resistance to smoothly go to zero with temperature due to a suppressed scattering amplitude. Lord Kelvin, Clay and (initially) Kamerlingh Onnes believed that the electron mobility would fall to zero with temperature, yielding a minimum in the resistance at some finite temperature, then infinite resistance at absolute zero. Matthiessen predicted that *defects* (e.g. impurities, grain boundaries and other lattice imperfections) would cause the resistance to level off to a finite value. Such defects create scattering centers, giving rise to a temperature-independent addition to the resistance, which is the dominant contribution at lower temperatures. In the absence of such defects, the lattice would be perfectly periodic, and there would be perfect conductivity [9]. Indeed, Matthiessen was right, since it is virtually impossible to get rid of all defects in samples of any considerable size. Thus, even exceptionally clean[6] conductors have finite resistances at zero temperatures due to trace amount of defects.

Therefore, it came as an astounding surprise to most when Kamerlingh Onnes in 1911 cooled down mercury below 4.2 K and saw absolutely zero resistance [14]. He could measure a *persistent current* which seemed to flow indefinitely in the absence of voltages and external fields, without any sign of degradation. The

[5] "Direct" refers to lowest order electron-electron interactions through the exchange of photons.
[6] A material is said to be dirty (impure) or clean (pure) at high respectively low concentrations of defects.

phenomenon was eventually termed superconductivity. Rather than being just perfect conductors, it was shown in 1933 that these materials also exhibit perfect *diamagnetism*, i.e. they perfectly expel external magnetic fields in their bulk interior. This effect is known as the Meissner effect, or the Meissner-Ochsenfeld effect, after its discoverers [15]. A great number of elements were later found to exhibit these properties, and today, 53 of the pure elements in the periodic table are known to be superconducting under various conditions [16]. As it turns out, many of these elements are less ideal conductors such as mercury, rather than good conductors. Copper, for example, does not become superconducting at lower temperatures. How come then that some conductors can overcome the scattering caused by defects and various interactions while others cannot? An important difference to note between copper and mercury is a low respectively high phonon contribution to the electrical resistance. The rising suspicion [17] that superconductivity is somehow related to the electron-phonon interaction was confirmed by experimental measurement of the *isotope effect*[7] [18, 19]. Thus, it is the very same interaction which gives rise to high resistances in poor conductors at finite temperatures that is responsible for the total absence of resistance at low temperatures! Before explaining this absurd phenomenon of superconductivity, it seems fitting to reverberate the final words of Ashcroft and Mermin's seminal work on solid state physics [4],

> *"In no other subject are the two fundamental branches of solid state physics - the dynamics of electrons and the vibrations of the lattice of ions - so intimately fused, with such spectacular consequences".*

[7] The isotope effect states that the superconducting transition temperature scales as $T_c \propto M^{-1/2}$, where M is the mass of the isotopes of the crystal lattice. This assumes that the interaction potential and the normal-state density of states at the Fermi surface both remain the same between the isotopes of comparison.

1.3 Superconductivity

Although superconductivity was discovered more than one hundred years ago, it is still a topic of intense scientific research of both a fundamental and an applied nature. Much like condensed matter physics in general, this owes to a continuous discovery of new materials, and an overabundance of phenomena and phases within the superconducting state which cannot be fully described in terms of the currently available theoretical models. This was however not always the conviction. By the end of the 1970s, it was believed that superconductivity was completely understood. The microscopic theory of Bardeen, Cooper and Schrieffer (BCS) [20, 21], could together with its extensions account for most experimental observations, forming a very concise and beautiful picture of superconductivity, today known as classic superconductivity or *conventional superconductivity*.

1.3.1 Conventional superconductivity

Conventional superconductors are either elements or alloys, typically with $T_c < 30$ K, and where the superconductivity is induced by the electron-phonon interaction. The latter gives rise to an attractive interaction between electrons[8] which overcomes their repulsive Coulomb interaction. Studying the effects of such a net attractive electron-electron interaction on a free-electron gas is commonly referred to as the *Cooper problem*, after Leon Cooper [22], who studied such a situation following Bardeen's suggestion. Cooper showed that in the presence of an arbitrarily weak net attractive interaction between electrons close to the Fermi surface, the Fermi liquid becomes unstable[9] to the formation of a new ground state. Similarly to the case of Bose-Einstein condensation of a superfluid, this ground state is occupied by a *condensate* of collective excitations. In a superconductor, these collective excitations consist of pairs of electrons with opposite spins and momenta, known as *Cooper pairs*. The pairs are composite bosons[10], but care needs to be taken in the interpretation, however, as Cooper pairs do not follow Bose-Einstein statistics. While they all occupy the same ground state and lie exactly at the chemical potential (which reduces to the Fermi energy in chemical equilibrium), they are not allowed to occupy the same momentum state, since the constituent electrons still follow Fermi-Dirac statistics and obey the Pauli exclusion principle. This is the crucial difference with respect to a Bose-Einstein condensate of

[8] From here on, quasiparticles are often just called particles.

[9] Superconductivity leads to a breakdown of the independent quasiparticle model and Fermi-liquid behavior. Superconductivity is but one example of a *non Fermi-liquid*, just like strange metals, Luttinger liquids, superfluid helium-3, and quite generally other phases close to quantum critical points.

[10] According to the Ehrenfest-Oppenheimer-Bethe rule [23, 24], any composite particle containing an even (odd) number of fermions is a boson (fermion). Fore example, the helium-3 atom is a fermion (3 nucleons and 2 electrons), while helium-4 atoms (4 nucleons, 2 electrons) and Cooper pairs (2 electrons) are composite bosons.

superfluid helium-4. In order to avoid misinterpretations, some deem it best to think along the line that there are no Cooper pairs, just electrons with coherent quantities like spins and momenta. Nevertheless, the paired electrons constitute a bound state with a certain binding energy. Since these electrons were originally situated around the Fermi surface, a gap of size $|\Delta|$ opens up in the excitation spectrum between the Fermi energy and the first excited states. At $T = 0$ K, the gap is typically $|\Delta| \approx 1.76 k_B T_c$, such that the energy difference between the two energy bands in the semiconductor representation is $2|\Delta| \approx 0.1$–1 meV. There are no available states to scatter to within this gap, and at low energies, the Cooper pairs can flow through the lattice without any resistance, very much like a superfluid. To scatter, to break a pair or to add a quasiparticle, an energy of $2|\Delta|$ has to be supplied. Furthermore, the typical size (the radius of gyration) of a Cooper pair is on the order of the *superconducting coherence length*, defined as

$$\xi(T) = \frac{\hbar v_F}{|\Delta(T)|}, \tag{1.1}$$

where $\hbar$ is the reduced Planck constant and v_F the Fermi velocity in the normal state. This length scale describes the typical scale of variations of superconductivity, and is much larger than the average distance between electrons. The pairs are thus highly overlapping, implying strong correlations. Apart from the Pauli principle, however, there is no explicit interaction of a dynamical nature between the pairs. The excitations above the gap primarily correspond to broken pairs rather than pairs with higher momenta, since the density of states falls off rather rapidly with momentum. Far above (below) the Fermi energy, the excitations are primarily electron-like (hole-like) quasiparticles. Close to the Fermi energy and the gap, they are coherent particle-hole mixtures (i.e. a superposition between particle-like and hole-like states). These elementary quasiparticle excitations are commonly known as *Bogoliubons*, with well-defined spins and momenta. The particle and hole nature of the quasiparticles can be inverted through scattering processes known as *Andreev reflection*.

1.3.2 Andreev reflection

The superconducting gap gives rise to interesting tunneling properties. Consider for example an interface between a normal metal and an insulator, where an electron in the normal metal with an energy within the insulating gap impinges on the interface. It cannot enter the insulator since there are no available states, and consequently, will be normal reflected. The process conserves energy, charge and spin, but not momentum. Consider now an interface between a normal metal and a superconductor. Again, there will be no available quasiparticle states for an electron impinging on the interface from the normal metal with an energy within the superconducting gap. Instead of being normal reflected, however, the electron

can be retro-reflected as a hole of opposite spin, depositing a charge of $2e$ in the superconducting condensate, i.e. injecting a Cooper pair into the superconductor. This process is called Andreev reflection and conserves momentum, energy and spin [25, 26]. The retro-reflected hole is phase coherent with the incident electron, since it has a well-defined relative phase. The phase coherence propagates into the normal metal on a length scale of the superconducting coherence length. Thus, superconductivity leaks into the normal metal in what is known as the *proximity effect* [27, 28]. Similarly, holes can be retro-reflected as electrons, injecting charges $-2e$ into the condensate. If there are multiple Andreev reflections occurring forming a closed loop with a total phase shift of $n2\pi$ where $n \in \mathbb{Z}$, bound states called *Andreev bound states* (ABS) are formed with energies within the superconducting gap. Additionally, these states can also exist on surfaces of superconductors. Andreev reflection is equivalent to particle-hole conversion in scattering processes inside a superconductor.

1.3.3 Order parameter and symmetry breaking

The main features of the superconducting state (e.g. persistent currents and Cooper pairs) can be better understood as direct consequences of symmetry breaking, and therefore explained in terms of Landau's theory of phase transitions [29]. According to Landau, a phase transition is associated with the development of an order parameter which lowers or breaks the symmetry, and that is non-zero in the phase and zero otherwise. As it turns out, the whole condensate can be described by the same pair wave function Ψ, which can be chosen as the order parameter[11] $\Delta = \Psi$, which generally is complex

$$\Delta = |\Delta| e^{i\chi}. \tag{1.2}$$

Here, the amplitude corresponds to the temperature-dependent gap $|\Delta|$, and the phase χ is spatially non-uniform and the same for all the condensate pairs. Hence, the latter spontaneously breaks U(1) gauge symmetry[12]. Furthermore, the ground state has a macroscopic population since the number of particles participating in the condensation is typically on the order of Avogadro's number. Note that particle number and phase are cannonically conjugate variables, fulfilling Heisenberg's uncertainty relation. By fixing the phase, there is an uncertainty in the number of particles. This uncertainty is however small compared to the total number of particles. This allows a quite precise specification of the particle number and the phase simultaneously. Thus, the superconducting state is a macroscopic quantum

[11] Note that later on, the order parameter will instead be chosen to be a mean-field expectation value of a product of field operators.

[12] The symmetry is broken both spontaneously and continuously, which means the Cooper pair is by definition a massless Nambu-Goldstone boson [30, 31]. Similarly, the phonon is also a Nambu-Goldstone boson, since the existence of a lattice breaks the continuous symmetry.

phenomenon, which exhibits a *phase rigidity*. The condensate acts and moves as whole, and to disrupt the phase of this state requires a disruption of a macroscopic number of particles. Furthermore, it is the spatial variations of the phase of the order parameter which give rise to fluctuations in particle number, and consequently, which drive supercurrents.

1.3.4 Unconventional superconductivity

The picture of a perfectly understood superconductivity started to fracture in 1979 with the discovery of several materials which could not be explained with the BCS theory [32, 33]. The picture completely shattered in 1986 when Bednorz and Müller observed superconductivity in the compound $La_{2-x}Ba_xCuO_4$ with $T_c \approx 35$ K [34]. Since then, a great number of materials have been found which exhibits superconductivity, either directly or in proximity to a superconductor, that does not fit in the BCS model. These materials range from complex compounds like $Tl_2Ba_2Ca_2Cu_3O_{10}$, to relatively simple ones like FeSe, with transition temperatures reaching $T_c \approx 200$ K. Hence, these materials are commonly called *high-temperature superconductors* (abbreviated HTS, HTSC or high T_c), and generally refer to materials with transition temperatures higher than 30 K[13].

Although many aspects of the superconductivity in HTS are similar to those in the conventional superconductors (e.g. quasiparticle pairs and persistent currents brought about by a net attractive electron-electron interaction), there are also many important differences. For example, conventional superconductivity arise in normal state metals which follow Landau-Fermi liquid theory with well-defined propagating degrees of freedom (phonons). Hence, the pairing interaction responsible for superconductivity (the electron-phonon interaction) is well-known and fully described by the BCS theory. HTS on the other hand, arise in Mott insulators, where the propagating degrees of freedom are unknown, as is then the pairing mechanism. Therefore, there is currently no theory which can describe HTS from first principles. To find such a theory, the normal state of the Mott insulators first has to be fully understood. Furthermore, while conventional superconductors are formally defined to break only U(1) gauge symmetry, *unconventional superconductors* (i.e. HTS) break additional symmetries. The additional broken symmetries give rise to a much richer landscape of physics. For example, electrons of opposite spins and momenta are paired with a singlet s-wave pairing symmetry in conventional superconductivity, while the electrons can be paired with equal spin in unconventional superconductors. Both triplet and higher order singlet pairing symmetries are possible in the latter, as well as multi-component order parameters having mixtures of different symmetries.

As an example of unconventional superconductors, and of particular interest for

[13]The predicted maximum transition temperature for conventional superconductors is ~ 30 K, although MgB_2 was shown to have a transition temperature of 39 K [35].

this work, are the family of superconductors discovered by Bednorz and Müller. These are commonly called *cuprates* due to the existence of copper-dioxide (CuO_2) planes. Superconductivity is mainly constricted to these CuO_2 planes, with a suppression of propagation between planes. The order parameter of the cuprates breaks the fourfold rotation symmetry of the crystal lattice, and was shown around 1990 to have an anisotropic singlet d-wave pairing symmetry [36, 37].

1.3.5 d-wave superconductors, midgap states and further symmetry breaking

The cuprates mainly have a tetragonal crystal structure with a pairing symmetry which is often written in Cartesian and polar form as [38]

$$\eta_{d_{x^2-y^2}} = \hat{p}_x^2 - \hat{p}_y^2 = \sqrt{2}\cos(2\theta_p), \tag{1.3}$$

respectively, where θ_p is the angle relative to the crystal a-axis. For strong suppression between the superconducting CuO_2 planes, a cylindrical symmetry is often assumed with line nodes at which the order parameter is suppressed. The anisotropy gives rise to a *gapless* density of states which extends all the way to the Fermi energy, where it goes to zero linearly [37]. These properties modify certain behavior of the superconducting state. For example, thermodynamic quantities like the heat capacity show a power law behavior at lower temperatures, as opposed to an exponential one for the fully gapped superconductors. Thus, the density of states is closely related to both transport properties and thermodynamic properties, and is typically determined by measuring either the tunneling conductance or extracted from the heat capacity in calorimetric measurements [39]. These measurements can therefore be used to infer the pairing symmetry of a superconductor. In such measurements, it is very difficult however to discriminate a d-wave symmetry from an anisotropic s-wave symmetry. To clearly discriminate these two, another property of the d-wave order parameter can be exploited which the anisotropic s-wave lacks, namely the existence of lobes of different signs. Such lobes enable scattering processes that induce a sign change and a suppression of the order parameter. As an example, consider a [110] interface, i.e. an interface that is 45° misaligned with respect to the crystal ab-axes, with specular reflection. An incoming and an outgoing scattering trajectory couples a positive and a negative lobe, inducing a sign change in the order parameter. Since the order parameter is single valued, it is suppressed exactly at the interface, recovering on a length scale of the superconducting coherence length. The suppression implies that superconducting pairs are broken, and such a [110] interface is therefore referred to as a *pairbreaking* interface. Such pair breaking might also occur at defects and impurities [40]. The broken pairs generate a huge density of *midgap states* (MGS), exactly in the middle of the gap at the Fermi energy [41]. Hence, these states are examples of Andreev bound states. The MGS thus

provides a strong fingerprint of the order parameter symmetry, and give rise to many different effects, like zero-bias conductance peaks in tunneling and transport measurements, paramagnetic currents and spontaneous symmetry breaking [41–43]. To understand the latter, consider the internal energy which scales with the product of the occupation, the density of states and the energy. In equilibrium, for example, a high density of MGS exactly at the Fermi energy will overlap with a finite occupation of the smeared Fermi-Dirac distribution, and hence, lead to a substantial internal energy. In shifting these states symmetrically around the Fermi energy, roughly half of the states will be occupied at a lower energy than before, leading to a considerable lowering of the free energy. Any mechanism that can provide such a shift is energetically favorable, and therefore opens up the possibility of further, spontaneous, symmetry breaking [44, 45]. The goal of the thesis is to study an example of such a mechanism, referred here to as the "loop-current phase", in which a superfluid momentum appears spontaneously and drive circulating currents that break translational and time-reversal symmetries [46–48]. In particular, superconducting *grains* will be studied, defined as superconductors with a size comparable to the superconducting coherence length. This length scale generally falls between the microscopic and macroscopic regime, and is known as the *mesoscopic regime*. The field of mesoscopic physics was mainly introduced in the early 1980s, and is an active sub-discipline of condensed matter physics.

1.3.6 Mesoscopic superconductivity and the quasiclassical approximation

Superconducting materials are often experimentally realized as thin films that can be patterned into devices, with the aim to exploit the properties of superconductivity. These devices are for example used as extremely sensitive sensors and as components in various electronics circuits. They commonly operate in the mesoscopic regime, combining phenomena that vary on different length scales. A system is defined as mesoscopic if its size $\mathcal{L}$ in at least one of its dimensions fulfills [49]

$$a_0 \ll \lambda_F \lesssim l_0 < \mathcal{L} < l_\phi \lesssim l_{\text{in}} \tag{1.4}$$

where a_0 is the Bohr radius, λ_F the Fermi wave length of the electron, l_0 the elastic mean free path, l_ϕ the quantum coherence length (not to be confused with the superconducting coherence length) and l_{in} is the energy relaxation length. In short, it means that the sample is large with respect to the atomic lattice separation, but still small enough for quantum coherence effects to play an important role. Put in another way, the microscopic scale is too short for the mesoscopic effects to have a chance to fully develop, while they might instead be too local or averaged out by bulk effects on the macroscopic scale. In analogy, observing a painting with a microscope or from outer space does not make too much sense

- to recognize the full beauty of the picture, the proper scale of observation is relevant.

The superconducting coherence length is the length scale over which the order parameter, and hence superconductivity, usually changes. It is much larger than the atomic scale, which means that the superconductor can be treated as homogeneous even though there is a discrete lattice. Therefore, the full microscopic theories which takes the atomic scale into account will often contain more information than necessary. To make comparisons with experiment, the atomic degree of freedom is typically discarded once calculations are done. Furthermore, these theories often scale poorly with increasing system size. To save time and effort, it is convenient to work within a theoretical framework that never incorporates the atomic degree of freedom in the first place. This is the main concept of the *quasiclassical theory of superconductivity*, in which the short-wavelength (hence high energy) contributions are averaged out, or baked into parameters whose values are taken from experiments. This is formally done by integrating the wave function over energy close to the Fermi surface and discarding the high-energy corrections. This step is known as the *quasiclassical approximation*. Hence, only low-lying excitations close to the Fermi surface are considered, and the rapid oscillations of the wave function on the atomic scale are replaced by the envelope varying on the coherence length scale. In other words, the quasiclassical theory of superconductivity is in some sense a natural language to describe many superconducting phenomena. Close to interfaces, however, superconductivity can vary on shorter length scales, and the quasiclassical approximation breaks down. To remedy this, the theory is supplied with boundary conditions derived from microscopic theories.

The basic understanding is however far from complete when it comes to how superconductivity behaves on the mesoscopic length-scale, where the superconducting state and its properties often are influenced by various finite-size and surface effects. These effects give rise to new interesting phenomena which are not present in bulk samples. Understanding these properties, and how they can be exploited to make new devices, are topics of modern research. The goal of this thesis is to study some of these properties in hopes of adding to the current knowledge.

1.4 Research topic and scope of the thesis

The main motivation for this thesis has been hinted at throughout this introduction. The goal is to study meso-scaled superconducting grains, in the hopes of adding to the current understanding of the properties that arise in such systems. This work considers clean grains in the weak-coupling limit, that are in vacuum and equilibrium, with spin-degeneracy, a cylindrically symmetric Fermi surface, and mainly with d-wave pairing symmetry. Of particular interest are midgap states and Andreev bound states caused by pairbreaking [110] interfaces in such grains, and the spontaneous symmetry breaking which might occur through energetically favorable shifts of these states to finite energies. Several mechanisms inducing such shifts have been proposed previously in the literature, some of which involve spontaneous time-reversal symmetry breaking through spontaneous currents [46, 50–54]. Even though there are many experiments in support of such currents, for example tunneling experiments [55–61], experimental verification of the associated magnetic fields remains controversial [62, 63]. A possible explanation was offered through the recently discovered "loop-current phase" [46–48], in which the spontaneous currents and magnetic fields enter as a necklace of loop currents tied to pairbreaking interfaces, where neighboring loops circulate clockwise and anti-clockwise. The size of these circulating currents are on the order of 5–$6\xi_0$, and the associated flux is microscopic, making them notoriously difficult to detect experimentally. It is the purpose of paper I to study how this phase responds to an external magnetic field. In summary, the phase is found to be robust in the whole Meissner state and for weak fields in the mixed state. Furthermore, the response leads to several signatures that might be observable in experiments. Previously, a similar phase was found in thin films, here referred to as the "Vorontsov phase", caused by a close proximity of pairbreaking interfaces [53, 64–67]. In paper II, it is shown that the loop-current phase occurs without such finite-size effects. This is done by considering grains with a single pairbreaking [110] interface. In Ref. [46], as well as in paper I and paper II, it is argued why the loop-current phase is believed to be competitive against other suggested mechanisms. Furthermore, the thesis and its appended papers discuss the experimental significance of the phase, mainly in the form of it as a source of broadening of zero-bias conductance peaks.

Along the way, general properties of superconductivity will be explained, and several basic results for both bulk systems and mesoscopic grains will be presented. The thesis contains a collection of derivations of various quantities related to electrodynamics, thermodynamics, quasiclassical theory, and BCS theory.

1.5 Outline of the thesis

The idea of this introduction has been to give a complete overview of the aspects of superconductivity that are relevant to this thesis and its research. The rest of the thesis goes into deeper detail of the methods used to do this research, such that the appended papers and the research results hopefully can be understood. The thesis contains eight chapters and seven appendices, which are organized as follows.

Chapter 2 introduces the quasiclassical theory of superconductivity, which is the main theoretical framework used in this thesis. Chapter 3 explains how this theory is implemented. The multiple possible solutions for the order parameter are discussed, together with ideas and suggestions for speeding up calculations. Chapter 4 introduces some fundamental electrodynamics properties of superconductors, and the main electrodynamical quantities of the results. In particular, homogeneous superconductors and superconductors with physical holes are considered. Along the same line, Ch. 5 introduces fundamental thermodynamic properties and the main thermodynamic quantities. These properties are used to study phases and phase transitions in the results. Chapter 6 presents a few basic results for mesoscopic superconducting grains, in particular related to midgap states, vortex phenomena and flux quantization in solenoids. Chapter 7 is devoted to cataloging various properties of the loop-current phase. The most basic properties are stated together with an explanation of how and why the phase arises. This is followed by a study of various geometric effects, external-field response, and a discussion of experimental verification. Chapter 8 summarizes and concludes the thesis, together with an outlook of open questions and potential future research.

The appendices mainly contain a collection of calculations that were too lengthy for the main thesis. Appendix A explains the choice of units, and compares the most common systems of units. A table of normalization units is presented, which are used as a scale for the results, and to make equations dimensionless. A summary of dimensionless equations is provided in App. B. In condensed matter physics, it is common to switch between different representations, for example, App. C shows how to go from a summation over momenta to integration over energies. Appendix D derives the BCS gap equation, the transition temperature T_c and various properties related to the gap. Appendix E introduces the Shelankov projectors and uses these to derive the Riccati equations. The latter are first order differential equations which in general are more convenient to handle than the standard Eilenberger equation. Appendix F is devoted to spin-triplet superconductivity and showing how various expressions are modified, in particular for unitary p-wave superconductivity. Finally, App. G derives a few useful symmetry relations for quasiclassical Green functions in thermal equilibrium.

2 The quasiclassical theory of superconductivity

The theory of Bardeen, Cooper and Schrieffer (BCS) is often hailed as one of the greatest theoretical achievements in condensed matter physics [20, 21]. It was the first theory to give a proper account of the microscopic origin of superconductivity, and could together with its extensions explain conventional superconductivity. Unconventional superconductivity, on the other hand, is often defined as superconductors that do not conform to the BCS theory or its extensions. Although these superconductors are significantly different from the conventional superconductors and has an unknown pairing mechanism, the BCS theory can still be used to give surprisingly accurate predictions of their properties. The reason is that the BCS theory contains the most important ingredient for superconductivity, i. e. a net attractive interaction between electrons leading to a bound state. The precise nature of the attractive interaction is not crucial to describe some of these properties, and the great success of the BCS theory in its application to even unconventional superconductors stems from the fact that the typical energies involved in superconductivity, e.g. the gap and the binding energy, are small in comparison to other relevant energy scales. This enables a separation of scales and the application of a quasiclassical approximation. The aim of this chapter is to briefly sketch how to use this approximation to go from BCS theory to the quasiclassical theory of superconductivity and the Eilenberger equation. This equation, together with the superconducting gap equation, forms the basis for the theoretical framework used in this thesis. In short, the steps are based on expressing the BCS theory in the powerful language of many-body Green functions. In particular, mean-field Green functions for quasiparticle and pair propagators are introduced. These propagators are known as the Gor'kov Green functions, and their equation of motion as the Gor'kov equation. Applying the quasiclassical approximation to the Gor'kov equation, along with certain tricks, yields the Eilenberger equation. For a full derivation of the Gor'kov and Eilenberger equations, see for example the book by Kopnin [68], or Refs. [69, 70]. For a more thorough treatment of BCS theory, see for example Schrieffer [71], de Gennes [72] and Tinkham [73].

2.1 BCS theory

In its original formulation, the BCS theory and its Hamiltonian is written in terms of fermionic creation ($c^\dagger$) and annihilation (c) operators acting on single-particle states of spins α, β, momenta $\boldsymbol{k}, \boldsymbol{l}$, and single-particle energies $\xi_{\boldsymbol{k}}$

$$\mathcal{H}_{\mathrm{BCS}} = \sum_{\boldsymbol{k}\alpha} \xi_{\boldsymbol{k}} c^\dagger_{\boldsymbol{k}\alpha} c_{\boldsymbol{k}\alpha} + \frac{1}{2} \sum_{\boldsymbol{k}\boldsymbol{l}\alpha\beta} c^\dagger_{\boldsymbol{k}\alpha} c^\dagger_{-\boldsymbol{k}\beta} V_{\boldsymbol{k}\boldsymbol{l}\alpha\beta} c_{-\boldsymbol{l}\beta} c_{\boldsymbol{l}\alpha}. \tag{2.1}$$

Here, V is the spin-dependent attractive interaction and $\xi_{\boldsymbol{k}} = \epsilon_{\boldsymbol{k}} - \mu$ is relative to the Fermi surface (FS), where μ is the chemical potential and $\epsilon_{\boldsymbol{k}}$ is the single-particle dispersion. For a spin-singlet systems with a spin-independent pairing, α and β describe opposite spins, and each sum over spin simply produces a factor of 2. The BCS ground state of Cooper pairs is written as a product of pairwise creation operators acting on the vacuum state $|0\rangle$

$$|\Psi_{\mathrm{BCS}}\rangle = \prod_{\boldsymbol{k}} \left(|u_{\boldsymbol{k}}| + |v_{\boldsymbol{k}}| \, e^{i\chi} c^\dagger_{\boldsymbol{k}\alpha} c^\dagger_{-\boldsymbol{k}\beta} \right) |0\rangle \,, \tag{2.2}$$

where χ is the coherent superfluid phase, and where $u^2_{\boldsymbol{k}}$ and $v^2_{\boldsymbol{k}}$ are the probabilities of a state being empty or occupied, respectively, such that $\left| u^2_{\boldsymbol{k}} + v^2_{\boldsymbol{k}} \right| = 1$. Equation (2.2) thus describes pairwise occupation of states with opposite momenta. It is convenient to introduce a mean-field approximation, in which products of four operators are replaced with a product of two operators times a mean-field average. The approximation is to introduce

$$c_{\boldsymbol{k}\alpha} c_{-\boldsymbol{k}\beta} = \langle c_{\boldsymbol{k}\alpha} c_{-\boldsymbol{k}\beta} \rangle + \delta_{\boldsymbol{k}\alpha\beta}, \tag{2.3}$$

$$\delta_{\boldsymbol{k}\alpha\beta} \equiv \left(c_{\boldsymbol{k}\alpha} c_{-\boldsymbol{k}\beta} - \langle c_{\boldsymbol{k}\alpha} c_{-\boldsymbol{k}\beta} \rangle \right), \tag{2.4}$$

expanding in δ and only keeping first-order terms. As mentioned in the introduction, the vast number of particles involved in the superconducting condensate ensures that fluctuations about the expectation values are small compared to the total number of particles (see for example Chs. 3.3–3.5 of Tinkham [73]). The superconducting order parameter is defined as the mean-field average

$$\Delta_{\boldsymbol{k}\alpha\beta} = -\sum_{\boldsymbol{l}} V_{\boldsymbol{k}\boldsymbol{l}\alpha\beta} \langle c_{\boldsymbol{l}\alpha} c_{-\boldsymbol{l}\beta} \rangle \,. \tag{2.5}$$

With the corresponding equations to Eqs. (2.3)–(2.5) for creation operators, and dropping a constant term containing only mean field averages that only modifies the chemical potential, the mean-field Hamiltonian can be written as

$$\mathcal{H}_{\mathrm{M}} = \sum_{\boldsymbol{k}\alpha} \xi_{\boldsymbol{k}} c^\dagger_{\boldsymbol{k}\alpha} c_{\boldsymbol{k}\alpha} - \frac{1}{2} \sum_{\boldsymbol{k}\alpha\beta} \left(\Delta_{\boldsymbol{k}\alpha\beta} c^\dagger_{\boldsymbol{k}\alpha} c^\dagger_{-\boldsymbol{k}\beta} + \Delta^\dagger_{\boldsymbol{k}\alpha\beta} c_{-\boldsymbol{k}\alpha} c_{\boldsymbol{k}\beta} \right). \tag{2.6}$$

This Hamiltonian can be diagonalized and solved exactly through the canonical Bogoliubov-Valatin transformations [74, 75], yielding the excitation spectrum

$$E_{\boldsymbol{k}} = \sqrt{\xi_{\boldsymbol{k}}^2 + \Delta_{\boldsymbol{k}}^2}, \tag{2.7}$$

which illustrates that Δ is indeed an energy gap. This gap has to be solved self-consistently through the superconducting gap equation. The gap equation is derived together with an expression for the superconducting transition temperature T_c in App D, using a variational method. The BCS gap equation at temperature T is

$$1 = V_0 N_F \int_0^{2\pi} \frac{d\theta_{p'_F} |\eta(\theta_{p'_F})|^2}{2\pi} \int_0^{\hbar\omega_c} d\xi \frac{\tanh\left(\frac{k_B T}{2}\sqrt{\xi^2 + \Delta^2 |\eta(\theta_{p'_F})|^2}\right)}{\sqrt{\xi^2 + \Delta^2 |\eta(\theta_{p'_F})|^2}}. \tag{2.8}$$

This equation is valid in the weak-coupling limit $N_F V_0 \leq 0.3$, which holds for all elemental superconductors except Pb and Hg [76, 77]. Here, N_F is the normal-state density of states (DOS) at the FS, and V_0 is the pair interaction which is attractive below the energy cutoff $\hbar\omega_c$. Typically[1], $\epsilon_F \gg \hbar\omega_c \gg k_B T_c \sim \Delta(T = 0) \sim \hbar v_F/\xi_0$, where ϵ_F is the Fermi energy, v_F the Fermi velocity at the FS, and $\xi_0 \equiv \hbar v_F/2\pi k_B T_c$ is the superconducting coherence length at zero temperature. For a phonon-mediated coupling, ω_c is taken to be the Debye frequency ω_D. Furthermore, η is the orthogonal basis function describing the momentum pairing symmetry, at angle $\theta_{p'_F}$ between the scattering direction and the Fermi momentum direction $\hat{p}_F$. Examples of typical s-wave and d-wave pairing symmetries are

$$\eta_s(\theta_{p_F}) = 1, \tag{2.9}$$

$$\eta_{d_{x^2-y^2}}(\theta_{p_F}) = \sqrt{2}\cos(2\theta_{p_F}). \tag{2.10}$$

The BCS gap equation of Eq. (2.8) is valid in bulk systems where $\boldsymbol{k}$ is a good quantum number, i.e. systems that have a plane wave dispersion and no spatial dependence. To consider spatial dependence, the standard creation and annihilation operators in momentum space have to be replaced by field operators in spatial space. This is for example done in the Bogoliubov de-Gennes (BdG) theory. This theory also deals with some of the other major short-comings of the standard BCS theory as expressed in Eqs. (2.1) and (2.2), namely that these equations treat standard single-particle states, while quasiparticle excitations are no longer single-particle states but rather coherent particle-hole mixtures known as Bogoliubons. Particles and holes therefore have to be treated on an equal footing, which is not provided by Eq. (2.1). Bogoliubov solved this by introducing field operators for the quasiparticle excitations in particle-hole space. This space is also

[1]For conventional superconductors, typically $\epsilon_F/k_B \sim 10000$ K, $\hbar\omega_c/k_B \sim 300$ K $\pm$ 100 K and $\Delta/k_B \ll 30$ K [78].

known as Nambu-Gor'kov space, or simply as Nambu space [30]. Applying the quasiclassical approximation to the BdG theory yields Andreev theory and the Andreev equations, but both of these theories are beyond the scope of this thesis. Instead, an alternative route is taken, through many-body Green functions and the Gor'kov equation.

2.2 Green function approach: The Gor'kov equation

The goal of the following is to introduce propagators (correlators) both for quasiparticles and for superconducting pairs, denoted by the Green functions G and F, respectively. These Green functions are related to various observables and give information about the dynamics of the system. The Green functions are solved from their equations of motion, which will be introduced as well.

In the Heisenberg picture, the fermionic Heisenberg field operators are

$$\psi_\alpha^\dagger(\boldsymbol{x},\tau) = e^{(\mathcal{H}-\mu\mathcal{N})\tau}\Psi_\alpha^\dagger(\boldsymbol{x})e^{-(\mathcal{H}-\mu\mathcal{N})\tau}, \tag{2.11}$$
$$\psi_\alpha(\boldsymbol{x},\tau) = e^{(\mathcal{H}-\mu\mathcal{N})\tau}\Psi_\alpha(\boldsymbol{x})e^{-(\mathcal{H}-\mu\mathcal{N})\tau}, \tag{2.12}$$

where $\mathcal{H}$ is the Hamiltonian, $\mathcal{N}$ the particle-number operator, and where $\Psi_\alpha^\dagger(\boldsymbol{x})$ and $\Psi_\alpha(\boldsymbol{x})$ are the Schrödinger particle-field operators creating and annihilating a particle with spin α at position $\boldsymbol{x}$. Here, τ is the imaginary time $\tau = it$. In this thesis, only time-independent systems will be considered, and τ will consequently denote the time difference $\tau = \tau_1 - \tau_2 = i(t_1 - t_2)$ in the following. The BCS Hamiltonian can be rewritten in terms of the Heisenberg field operators as

$$\tilde{\mathcal{H}}_{\mathrm{BCS}} = \mathcal{H}_0 + \mathcal{H}_1 + \mathcal{H}', \tag{2.13}$$
$$\mathcal{H}_0 = \sum_\alpha \int d\boldsymbol{x}\psi_\alpha^\dagger(\boldsymbol{x},\tau)\left(-\frac{\boldsymbol{p}^2}{2m} - \mu\right)\psi_\alpha(\boldsymbol{x},\tau), \tag{2.14}$$
$$\mathcal{H}_1 = \frac{1}{2}\sum_{\alpha\beta}\int d\boldsymbol{x}d\boldsymbol{x}'\psi_\beta^\dagger(\boldsymbol{x}',\tau)\psi_\alpha^\dagger(\boldsymbol{x},\tau)\lambda\psi_\alpha(\boldsymbol{x},\tau)\psi_\beta(\boldsymbol{x}',\tau), \tag{2.15}$$

where $\mathcal{H}_0$ is the non-interacting Hamiltonian, $\mathcal{H}_1$ the pairing Hamiltonian, $\lambda < 0$ the coupling constant from the pairing interaction, and $\mathcal{H}'$ describes any additional interactions. In the presence of a vector potential $\boldsymbol{A}$, the momentum operator $\boldsymbol{p}$ is

$$\boldsymbol{p} = -i\hbar\boldsymbol{\nabla} - \frac{e}{c}\boldsymbol{A}(\boldsymbol{x}). \tag{2.16}$$

The mean-field averages[2] of the Heisenberg operators over the ground state are defined as the Green functions

$$G_{\alpha\beta}(\boldsymbol{x},\boldsymbol{x}',\tau) = \left\langle T_\tau\psi_\alpha(\boldsymbol{x},\tau)\psi_\beta^\dagger(0,\boldsymbol{x}')\right\rangle, \tag{2.17}$$
$$G_{\alpha\beta}^\dagger(\boldsymbol{x},\boldsymbol{x}',\tau) = \left\langle T_\tau\psi_\alpha^\dagger(\boldsymbol{x},\tau)\psi_\beta(0,\boldsymbol{x}')\right\rangle, \tag{2.18}$$

where T is the time-ordering operator

$$T_\tau\psi_\alpha(\boldsymbol{x},\tau)\psi_\beta^\dagger(0,\boldsymbol{x}') = \begin{cases}\psi_\alpha(\boldsymbol{x},\tau)\psi_\beta^\dagger(0,\boldsymbol{x}'), & \tau > 0,\\ -\psi_\beta^\dagger(0,\boldsymbol{x}')\psi_\alpha(\boldsymbol{x},\tau), & \tau < 0.\end{cases} \tag{2.19}$$

[2]Here, the average is over the grand canonical distribution $\langle\ldots\rangle = \mathrm{tr}\left[\exp\left((\Omega-\mathcal{H})/k_BT\right)\ldots\right]$, where $\Omega(T,\mathcal{V},\mu)$ is the thermodynamic potential and $\mathcal{V}$ is the volume.

Here, G and $G^\dagger$ are quasiparticle propagators. Given an electron-like quasiparticle of spin β at position $\boldsymbol{x}'$, the propagator $G_{\alpha\beta}(\boldsymbol{x}, \boldsymbol{x}', \tau)$ expresses the probability amplitude for the particle to be found at $\boldsymbol{x}$ with spin α after the time interval τ, by averaging over all possible paths from $\boldsymbol{x}'$ to $\boldsymbol{x}$. Conversely, $G^\dagger_{\alpha\beta}(\boldsymbol{x}, \boldsymbol{x}', \tau)$ describes the opposite movement for a hole-like quasiparticle. To describe superconducting pairs, the anomalous Green functions F and $F^\dagger$ are introduced as

$$F_{\alpha\beta}(\boldsymbol{x}, \boldsymbol{x}', \tau) = \langle T_\tau \psi_\alpha(\boldsymbol{x}, \tau)\psi_\beta(0, \boldsymbol{x}')\rangle\,, \tag{2.20}$$

$$F^\dagger_{\alpha\beta}(\boldsymbol{x}, \boldsymbol{x}', \tau) = \left\langle T_\tau \psi^\dagger_\alpha(\boldsymbol{x}, \tau)\psi^\dagger_\beta(0, \boldsymbol{x}')\right\rangle. \tag{2.21}$$

These are pair propagators describing the annihilation and creation of Cooper pairs, respectively. Similar to G and $G^\dagger$, they are also related via particle-hole conjugation. Furthermore, the anomalous Green functions are vanishing in the normal state and non-vanishing in the superconducting state, and are consequently used to define the superconducting order parameter

$$\Delta_{\alpha\beta}(\boldsymbol{x}) = -\lambda F_{\alpha\beta}(\boldsymbol{x}, \boldsymbol{x}' = \boldsymbol{x}, \tau = 0). \tag{2.22}$$

This is a self-consistency equation since F depends in turn on Δ, as will be seen in the following equations. The arguments $(\boldsymbol{x}, \boldsymbol{x}', \tau)$ are temporarily dropped for brevity. Gor'kov used the Heisenberg equations of motion to obtain the following generalized Dyson equations for the BCS theory

$$\left(\hbar\frac{\partial}{\partial\tau} + \frac{\boldsymbol{p}^2}{2m} - \mu\right) G_{\alpha\beta} + \Delta_{\alpha\gamma} F^\dagger_{\gamma\beta} = \hbar\delta_{\alpha\beta}\delta^{(3)}(\boldsymbol{x} - \boldsymbol{x}')\delta(\tau), \tag{2.23}$$

$$-\left(\hbar\frac{\partial}{\partial\tau} - \frac{\boldsymbol{p}^2}{2m} + \mu\right) G^\dagger_{\alpha\beta} + \Delta^*_{\alpha\gamma} F_{\gamma\beta} = \hbar\delta_{\alpha\beta}\delta^{(3)}(\boldsymbol{x} - \boldsymbol{x}')\delta(\tau), \tag{2.24}$$

$$\left(-\hbar\frac{\partial}{\partial\tau} - \frac{\boldsymbol{p}^2}{2m} + \mu\right) F_{\alpha\beta} + \Delta_{\alpha\gamma} G^\dagger_{\gamma\beta} = 0, \tag{2.25}$$

$$\left(\hbar\frac{\partial}{\partial\tau} - \frac{\boldsymbol{p}^2}{2m} + \mu\right) F^\dagger_{\alpha\beta} + \Delta^*_{\alpha\gamma} G_{\gamma\beta} = 0, \tag{2.26}$$

where the derivative in $\boldsymbol{p}$ acts on unprimed coordinates. These equations are known as the Gor'kov equations [79], and can be expressed more compactly in 4×4 Nambu $\otimes$ spin-space (denoted with the "hat" symbol), by introducing

$$\hat{G} = \begin{pmatrix} G_{\alpha\beta} & F_{\alpha\beta} \\ -F^\dagger_{\alpha\beta} & G^\dagger_{\alpha\beta} \end{pmatrix}, \tag{2.27}$$

$$\hat{\Delta} = \begin{pmatrix} 0 & \Delta_{\alpha\beta} \\ -\Delta^*_{\alpha\beta} & 0 \end{pmatrix}. \tag{2.28}$$

Introduce also the Pauli matrices in spin space

$$\sigma_0 = \begin{pmatrix} 1 & 0 \\ 0 & 1 \end{pmatrix}, \qquad \text{(unit matrix)} \tag{2.29}$$

$$\sigma_x = \sigma_1 = \begin{pmatrix} 0 & 1 \\ 1 & 0 \end{pmatrix}, \tag{2.30}$$

$$\sigma_y = \sigma_2 = \begin{pmatrix} 0 & -i \\ i & 0 \end{pmatrix}, \tag{2.31}$$

$$\sigma_z = \sigma_3 = \begin{pmatrix} 1 & 0 \\ 0 & -1 \end{pmatrix}, \tag{2.32}$$

with their corresponding matrices in Nambu-spin space, denoted $\hat{\tau}_i$ for $i \in [0, 3]$ (not to be confused with the imaginary time τ), and with $\hat{\tau}_0 = \hat{1}$ being the unit matrix. The matrix Gor'kov equation can then be written as

$$\left[\hat{\tau}_3 \hbar \frac{\partial}{\partial \tau} + \left(\frac{\boldsymbol{p}^2}{2m} - \mu\right)\hat{1} - \hat{\Delta}\right] \otimes \hat{G} = \hat{1}, \tag{2.33}$$

where $\otimes$ is a time-convolution product [80]. In Nambu-spin space, it is a matrix product and an integral over common time and energy variables. In a mixed representation, it can be written

$$(A \otimes B)(x, p) = \exp\left(\frac{i\hbar}{2}\frac{\partial^A}{\partial x}\frac{\partial^B}{\partial p} - \frac{i\hbar}{2}\frac{\partial^A}{\partial p}\frac{\partial^B}{\partial x}\right) A(x, p)B(x, p). \tag{2.34}$$

For the time-independent systems considered in this thesis, $\otimes$ reduces to simple matrix multiplication. The corresponding equations to Eqs. (2.23)–(2.26) for $\boldsymbol{p}$ acting on primed coordinates produce the equation

$$\hat{G} \otimes \left[\hat{\tau}_3 \hbar \frac{\partial}{\partial \tau} + \left(\frac{\boldsymbol{p}^2}{2m} - \mu\right)\hat{1} - \hat{\Delta}\right] = \hat{1}. \tag{2.35}$$

Finally, Fourier transforming to energy and momentum space in the center-of-mass coordinate $\boldsymbol{R}$, the Gor'kov equations become

$$\left[\left(z + \frac{e}{c}\boldsymbol{v}_F \cdot \boldsymbol{A}\right)\hat{\tau}_3 + \xi_{\boldsymbol{p}}\hat{1} - \hat{\Delta}\right] \otimes \hat{G}(\boldsymbol{p}, \boldsymbol{R}) = \hat{1}, \tag{2.36}$$

$$\hat{G} \otimes \left[\left(z + \frac{e}{c}\boldsymbol{v}_F \cdot \boldsymbol{A}\right)\hat{\tau}_3 + \xi_{\boldsymbol{p}}\hat{1} - \hat{\Delta}\right](\boldsymbol{p}, \boldsymbol{R}) = \hat{1}, \tag{2.37}$$

where z is the complex energy and $\xi_{\boldsymbol{p}} = \boldsymbol{v}_F(\boldsymbol{p}_F) \cdot (\boldsymbol{p} - \boldsymbol{p}_F) - \mu$ the single-particle energies at momentum $\boldsymbol{p}$. Here $\boldsymbol{v}_F(\boldsymbol{p}) = \boldsymbol{\nabla}_{\boldsymbol{p}}\xi_{\boldsymbol{p}}$ and $\boldsymbol{p}_F$ are the Fermi velocity and momentum at the FS, respectively. It is worth mentioning that the Green functions introduced above are the imaginary-time Matsubara (M) Green functions valid in equilibrium, defined in the finite time interval $-\hbar/k_BT < \tau < \hbar/k_BT$.

Fourier transforming from time to energy, the corresponding Green functions are only defined over a set of discrete and imaginary energies $z = i\epsilon_n$, known as the Matsubara energies (or frequencies in natural units)

$$\epsilon_n \equiv \pi k_B T(2n+1), \tag{2.38}$$

with $n \in \mathbb{Z}$ [81]. There are also real-time retarded (R) and advanced (A) Green functions, defined for energies $z = \epsilon \pm i0^{\pm}$ with $+$ for R and $-$ for A, where ϵ is a real energy and $0^{\pm}$ is an infinitesimal shift. Furthermore, in non-equilibrium, the Gor'kov equations are extended into 8×8 Keldysh $\otimes$ Nambu $\otimes$ spin-space, with energies on the real axis $z = \epsilon$ and corresponding non-equilibrium Keldysh (K) Green functions. The different Green functions are related through various symmetry properties. Non-equilibrium is beyond the scope of this thesis, however, and only the Matsubara and retarded propagators will be used in the end.

The Gor'kov equation provides a powerful microscopic theoretical framework to study superconductivity. By solving this equation, the Green functions can be used to obtain various observables of interest. As briefly mentioned in the introduction and in this chapter, however, superconductivity is often tied to low-lying excitations close to the Fermi surface, and described on the mesoscopic length scale of the superconducting coherence length, which is much larger than the atomic length scale. The goal of this thesis is to do numerical simulations of larger mesoscopic systems, where the microscopic theories with the full atomic resolution often are unfeasible with current computational capabilities. Furthermore, in comparing the solutions of the Gor'kov equation with experiment, it is often the case that the atomic degree of freedom is discarded at the end anyway. It is therefore convenient to work within a theoretical framework that operates on the mesoscopic length scale, such as the quasiclassical theory of superconductivity.

2.3 The quasiclassical approximation and the Eilenberger equation

The quasiclassical theory of superconductivity is is based on applying a quasiclassical approximation to the Gor'kov equations. This theory was developed by Eilenberger [82] and independently by Larkin and Ovchinnikov [83]. The formulation of Eilenberger is used in this thesis, and a brief overview will be given in this section. Again, for full details, see for example Refs. [68–70], as well as the references cited below.

Most superconducting phenomena are described by low-lying excitations close to the Fermi surface, since the superconducting energy gap Δ is typically much smaller than the Fermi energy ϵ_F. Consequently, the length scale which superconductivity typically varies over is the superconducting coherence length $\xi_0 \equiv \hbar v_F/2\pi k_B T_c$ which is much larger than the Fermi wavelength and the atomic scale. The quasiclassical approximation is thus based on separating the atomic and mesoscopic degrees of freedom, by expanding to leading order in the small parameters, e.g. $\hbar/p_F\xi_0$, Δ/ϵ_F, $k_B T_c/\epsilon_F$, see for example Refs. [69, 84–86]. This is formally done by separating the Gor'kov Green functions into high and low energy parts and discarding the high-energy part,

$$\hat{G} = \hat{G}_{\text{low}} + \hat{G}_{\text{high}} = \delta(\xi_{\boldsymbol{p}})\hat{g} + \hat{G}_{\text{high}} \approx \delta(\xi_{\boldsymbol{p}})\hat{g}. \tag{2.39}$$

Integrating this equation and imposing a cutoff ϵ_c yields the quasiclassical Green function $\hat{g}$

$$\hat{g}(\boldsymbol{p}_F, \boldsymbol{R}; z) = \frac{1}{a}\int_{-\epsilon_c}^{\epsilon_c} d\xi_{\boldsymbol{p}} \hat{G}(\boldsymbol{p}, \boldsymbol{R}; z), \tag{2.40}$$

where $k_B T_c \ll \epsilon_c \ll \epsilon_F$ and $|\xi_{\boldsymbol{p}}| \ll \epsilon_c$, i.e. considering a thin shell around the Fermi surface. Here, a is the spectral weight, which will drop out of the theory. As previously, $\boldsymbol{R}$ is the quasiparticle center-of-mass coordinate, and $\boldsymbol{v}_F(\boldsymbol{p}) = \boldsymbol{\nabla}_{\boldsymbol{p}}\xi_{\boldsymbol{p}}$. Thus, the rapid oscillations of the Green function on the atomic scale are integrated out and replaced with the envelope, which varies on the coherence length scale. The quasiclassical approximation generally holds very well in conventional superconductors, where the small parameters are on the order of 10^{-3}, while they in the unconventional superconductors typically are 10^{-2}–10^{-1} [68]. The approximation breaks down for example when superconductivity varies on a much shorter length scale than ξ_0, e.g. at interfaces, see Refs. [87–91] and references therein. To remedy this, boundary conditions are typically derived from microscopic theories and used as an input, see for example Ref. [80].

A quasiclassical equation of motion is not obtained by simply integrating the Gor'kov equation as above, due to an explicit dependence on $\xi_{\boldsymbol{p}}$ which is not bounded. To get rid of this difficulty, the "left-right-trick" is employed, where the left and right Gor'kov Eqs. (2.36) and (2.37) are gradient expanded to first order in $\xi_{\boldsymbol{p}}$ using Eq. (2.34), and then subtracted from each other. The resulting

equation is $\xi_{\boldsymbol{p}}$-integrated the same way as in Eq. (2.40), yielding the Eilenberger equation [82]

$$i\hbar \boldsymbol{v}_F \cdot \boldsymbol{\nabla}_R \hat{g}(\boldsymbol{p}_F, \boldsymbol{R}; z) + \left[\left(z + \frac{e}{c} \boldsymbol{v}_F \cdot \boldsymbol{A}(\boldsymbol{R}) \right) \hat{\tau}_3 - \hat{\Delta}(\boldsymbol{R}), \hat{g}(\boldsymbol{p}_F, \boldsymbol{R}; z) \right]_{\otimes} = 0, \quad (2.41)$$

where $[A, B]_{\otimes} = A \otimes B - B \otimes A$ with $\otimes$ defined as in Eq. (2.34) [80]. The Eilenberger equation is a transport-like equation which describes quasiparticles moving along classical trajectories defined by the Fermi velocity direction $\hat{\boldsymbol{v}}_F$. In performing the left-right-trick, the non-homogeneous Gor'kov equation was transformed into a homogeneous equation, resulting in the loss of the normalization information. Eilenberger showed that this information could be reintroduced through the following normalization condition [70, 82, 83]

$$\hat{g}^2 = -\pi^2 \hat{1}, \quad (2.42)$$

where the arguments $(\boldsymbol{p}_F, \boldsymbol{R}; z)$ have been dropped for a more compact notation. Care needs to be taken when solving the Eilenberger equation, as it is unstable in certain integration directions and contains additional unphysical solutions. A solution to these issues is given by the Riccati formalism, explained in Sec. 2.5.

The Nambu $\times$ spin-space Green function $\hat{g}$ can be written in terms of spin-space Green functions as

$$\hat{g} = \begin{pmatrix} g & f \\ \tilde{f} & \tilde{g} \end{pmatrix}, \quad (2.43)$$

where the tilde operator denotes particle-hole conjugation

$$\tilde{\alpha}(\boldsymbol{p}_F, \boldsymbol{R}; z, t) = \alpha^*(-\boldsymbol{p}_F, \boldsymbol{R}; -z^*, t), \quad (2.44)$$

Allowing for both spin-singlet (s) and spin-triplet (t) pairing, the spin-dependence can be written explicitly as

$$\begin{aligned} g &= (g_0 + \boldsymbol{g} \cdot \boldsymbol{\sigma})\, \sigma_0, & (2.45)\\ \tilde{g} &= \sigma_2 (\tilde{g}_0 - \tilde{\boldsymbol{g}} \cdot \boldsymbol{\sigma})\, \sigma_2, & (2.46)\\ f &= (f_s + \boldsymbol{f}_t \cdot \boldsymbol{\sigma})\, i\sigma_2, & (2.47)\\ \tilde{f} &= i\sigma_2 \left(\tilde{f}_s - \tilde{\boldsymbol{f}}_t \cdot \boldsymbol{\sigma} \right). & (2.48) \end{aligned}$$

Similarly, the order parameter is

$$\begin{aligned} \hat{\Delta} &= \begin{pmatrix} 0 & \Delta \\ \tilde{\Delta} & 0 \end{pmatrix}, & (2.49)\\ \Delta &= (\Delta_s + \boldsymbol{\Delta}_t \cdot \boldsymbol{\sigma})\, i\sigma_2, & (2.50)\\ \tilde{\Delta} &= i\sigma_2 \left(\tilde{\Delta}_s - \tilde{\boldsymbol{\Delta}}_t \cdot \boldsymbol{\sigma} \right). & (2.51) \end{aligned}$$

The order parameter is solved self-consistently through the superconducting gap equation, introduced in the following section.

2.4 Observables

Observables are obtained from the Green functions. Depending on which observables are of interest, it is convenient to use different Green functions. In this thesis, the Matsubara Green functions are used to calculate the superconducting gap, the current density and the free energy. The retarded Green functions are used to obtain the spectral observables, e.g. the density of states and the spectral current. The gap equation and the density of states are introduced in this section, while the currents are introduced in Ch. 4, and the free energy is introduced in Ch. 5.

2.4.1 The superconducting gap equation

The mean-field order parameter was defined in terms of the anomalous Gor'kov Green functions in Eq. (2.22). Following the notation of Ref. [86] and reintroducing spin-indices $\alpha\beta\gamma\rho$, the gap equation is expressed in terms of the quasiclassical pair-propagator f as

$$\Delta_{\alpha\beta}(\boldsymbol{p}_F, \boldsymbol{R}) = N_F k_B T \int d^2\boldsymbol{p}'_F \lambda_{\alpha\beta,\gamma\rho}(\boldsymbol{p}'_F, \boldsymbol{p}_F) \sum_{|\epsilon_n|\leq\Omega_c} f_{\gamma\rho}(\boldsymbol{p}'_F, \boldsymbol{R}; \epsilon_n) \tag{2.52}$$

where N_F is the normal state DOS at the FS per spin, the integral is over the Fermi momentum direction on the FS, ϵ_n the Matsubara energy, Ω_c a cutoff energy, and $\lambda_{\alpha\beta,\gamma\rho}(\boldsymbol{p}'_F, \boldsymbol{p}_F)$ is the interaction

$$\begin{aligned}\lambda_{\alpha\beta,\gamma\rho}(\boldsymbol{p}'_F, \boldsymbol{p}_F) &= (i\sigma_2)_{\alpha\beta}\lambda^{(g)}(\boldsymbol{p}'_F, \boldsymbol{p}_F)(i\sigma_2)_{\gamma\rho} \\ &\quad + (i\sigma_2\boldsymbol{\sigma})_{\alpha\beta} \cdot \overset{\leftrightarrow}{\lambda}{}^{(u)}(\boldsymbol{p}'_F, \boldsymbol{p}_F) \cdot (i\boldsymbol{\sigma}\sigma_2)_{\gamma\rho}.\end{aligned} \tag{2.53}$$

Here, g and u denotes even and odd-parity orthogonal basis functions η and $\boldsymbol{\eta}$, i.e. spin-singlet and spin-triplet, respectively. Allowing for a mixture of different singlet and triplet pairing channels, the interaction terms are are

$$\lambda^{(g)}(\boldsymbol{p}'_F, \boldsymbol{p}_F) = \sum_{\Gamma_g,\nu} \lambda_\Gamma \eta_{\Gamma_\nu}(\boldsymbol{p}_F)\eta^*_{\Gamma_\nu}(\boldsymbol{p}'_F), \tag{2.54}$$

$$\overset{\leftrightarrow}{\lambda}{}^{(u)}(\boldsymbol{p}'_F, \boldsymbol{p}_F) = \sum_{\Gamma_u,\nu} \lambda_\Gamma \boldsymbol{\eta}_{\Gamma_\nu}(\boldsymbol{p}_F) \otimes \boldsymbol{\eta}^\dagger_{\Gamma_\nu}(\boldsymbol{p}'_F), \tag{2.55}$$

where λ_Γ is the corresponding coupling constant, ν is an index denoting the pairing symmetry, and Γ_ν denotes an irreducible representations of the point group, the latter which is D_{4h} in this thesis. Examples of basis functions were given in Eqs. (2.9)–(2.10) and in Ref. [86]. Similarly, the order parameter is decomposed into singlet and triplet parts

$$\Delta(\boldsymbol{p}_F, \boldsymbol{R}) = \sum_\nu \Delta_\nu(\boldsymbol{R})\eta_{\Gamma_\nu}(\boldsymbol{p}_F), \tag{2.56}$$

$$\boldsymbol{\Delta}(\boldsymbol{p}_F, \boldsymbol{R}) = \sum_\nu \Delta_\nu(\boldsymbol{R})\boldsymbol{\eta}_{\Gamma_\nu}(\boldsymbol{p}_F), \tag{2.57}$$

respectively. From now on, consider a $2D$ superconductor in the xy-plane with a cylindrically symmetric FS such that $\int d^2\boldsymbol{p}_F = \int d\theta_{\boldsymbol{p}_F}/2\pi$, where $\theta_{\boldsymbol{p}_F} \in [0, 2\pi]$ is the angle of the Fermi momentum $\boldsymbol{p}_F$ relative to the crystal a-axis. Assume an order parameter with only a single pairing channel, i.e. that is either totally symmetric or anti-symmetric. For the anti-symmetric spin-triplet pairing, consider the case when the spin direction in $\boldsymbol{\Delta}_t$ (and consequently $\boldsymbol{\eta}$) is $\boldsymbol{d} = \hat{\boldsymbol{z}}$. Considering normalized basis functions such that $\eta_a \eta_b^* = \delta_{ab}$, the gap Eq. (2.52) can be multiplied by $i\sigma_2\eta^*$ to obtain the singlet and triplet gap equations

$$\Delta_s(\boldsymbol{R}) = V_s k_B T \int \frac{d\theta_{\boldsymbol{p}_F}}{2\pi} \eta^*_{\Gamma_s}(\boldsymbol{p}_F) \sum_{|\epsilon_n|\leq\Omega_c} f_s(\boldsymbol{p}_F, \boldsymbol{R}; \epsilon_n), \tag{2.58}$$

$$\Delta_t(\boldsymbol{R}) = V_t k_B T \int \frac{d\theta_{\boldsymbol{p}_F}}{2\pi} \eta^*_{\Gamma_t}(\boldsymbol{p}_F) \sum_{|\epsilon_n|\leq\Omega_c} f_t(\boldsymbol{p}_F, \boldsymbol{R}; \epsilon_n), \tag{2.59}$$

where the pairing interactions $-V_s$ and $-V_t$ are eliminated in favor of the transition temperature (see for example Ref. [92])

$$V_i^{-1} \equiv (-N_F\lambda_i)^{-1} = \ln\frac{T}{T_c} + \sum_{n\geq 0}\frac{2}{2n+1}. \tag{2.60}$$

Using the Matsubara symmetry in App. G, the equations are converted into a sum over only positive Matsubara energies

$$\Delta_s(\boldsymbol{R}) = V_s k_B T \int \frac{d\theta_{\boldsymbol{p}_F}}{2\pi} \eta^*_{\Gamma_s}(\boldsymbol{p}_F) \sum_{\epsilon_n>0}^{\Omega_c} \left(f_s(\boldsymbol{p}_F, \boldsymbol{R}; \epsilon_n) + \tilde{f}^*_s(\boldsymbol{p}_F, \boldsymbol{R}; \epsilon_n) \right), \tag{2.61}$$

$$\Delta_t(\boldsymbol{R}) = V_t k_B T \int \frac{d\theta_{\boldsymbol{p}_F}}{2\pi} \eta^*_{\Gamma_t}(\boldsymbol{p}_F) \sum_{\epsilon_n>0}^{\Omega_c} \left(f_t(\boldsymbol{p}_F, \boldsymbol{R}; \epsilon_n) - \tilde{f}^*_t(\boldsymbol{p}_F, \boldsymbol{R}; \epsilon_n) \right). \tag{2.62}$$

Similar expressions can be obtained for order parameters with multiple pairing channels, as well as for mixed singlet-triplet pairing.

2.4.2 The local density of states

The local density of states N is calculated from the imaginary part of the retarded Green function through the expression

$$\begin{aligned} N(\boldsymbol{R}; \epsilon) &= -N_F \frac{1}{2\pi} \int \frac{d\theta_{\boldsymbol{p}_F}}{2\pi} \operatorname{Im}\left[\operatorname{Tr}\left\{ \hat{\tau}_3 \hat{g}^R(\boldsymbol{p}_F, \boldsymbol{R}; \epsilon) \right\} \right] \\ &= -N_F \frac{2}{\pi} \int \frac{d\theta_{\boldsymbol{p}_F}}{2\pi} \operatorname{Im}\left[g_0^R(\boldsymbol{p}_F, \boldsymbol{R}; \epsilon) \right]. \end{aligned} \tag{2.63}$$

2.5 The Riccati formalism

The Riccati parametrization is an efficient and numerically stable method of solving the Eilenberger equation [80, 93–98], in which the quasiclassical Green function are rewritten in terms of the coherence functions $\gamma(\boldsymbol{p}_F, \boldsymbol{R}; z)$ and $\tilde{\gamma}(\boldsymbol{p}_F, \boldsymbol{R}; z)$. These objects correspond to the probability amplitude for electron-hole conversion and hole-electron conversion, respectively. Appendix E derives the coherence functions and a way of expressing the Green function in terms of them as

$$\hat{g} = -i\pi\hat{\mathcal{N}} \begin{pmatrix} \sigma_0 + \gamma\tilde{\gamma} & 2\gamma \\ -2\tilde{\gamma} & -\sigma_0 - \tilde{\gamma}\gamma \end{pmatrix}, \tag{2.64}$$

where

$$\hat{\mathcal{N}} = \begin{pmatrix} (\sigma_0 - \gamma\tilde{\gamma})^{-1} & 0 \\ 0 & (\sigma_0 - \tilde{\gamma}\gamma)^{-1} \end{pmatrix}. \tag{2.65}$$

The coherence functions, or Riccati amplitudes, are written as

$$\gamma(\boldsymbol{p}_F, \boldsymbol{R}; z) = (\gamma_s(\boldsymbol{p}_F, \boldsymbol{R}; z) + \boldsymbol{\gamma}_t(\boldsymbol{p}_F, \boldsymbol{R}; z) \cdot \boldsymbol{\sigma})\, i\sigma_2, \tag{2.66}$$

$$\tilde{\gamma}(\boldsymbol{p}_F, \boldsymbol{R}; z) = i\sigma_2 \left(\tilde{\gamma}_s(\boldsymbol{p}_F, \boldsymbol{R}; z) - \tilde{\boldsymbol{\gamma}}_t(\boldsymbol{p}_F, \boldsymbol{R}; z) \cdot \boldsymbol{\sigma}\right). \tag{2.67}$$

This parametrization automatically encodes the normalization condition into the definition of $\hat{g}$, removes the spurious solutions, and recasts the Eilenberger equation into a set of coupled Riccati-type ordinary differential equations

$$\left[i\hbar\boldsymbol{v}_F \cdot \boldsymbol{\nabla}_R + 2\left(z + \frac{e}{c}\boldsymbol{v}_F \cdot \boldsymbol{A}\right)\right]\gamma = \gamma\tilde{\Delta}\gamma - \Delta, \tag{2.68}$$

$$\left[i\hbar\boldsymbol{v}_F \cdot \boldsymbol{\nabla}_R - 2\left(z + \frac{e}{c}\boldsymbol{v}_F \cdot \boldsymbol{A}\right)\right]\tilde{\gamma} = \tilde{\gamma}\Delta\tilde{\gamma} - \tilde{\Delta}. \tag{2.69}$$

These equations are solved through integration along straight (ballistic) quasiparticle trajectories $\boldsymbol{s}(x)$ parametrized by the Fermi velocity according to $\boldsymbol{s}(x) = \boldsymbol{s}_0 + x\hat{\boldsymbol{v}}_F$, with opposite directions being stable for γ and $\tilde{\gamma}$, see for example Ref. [86]. Quantum coherence exists on the length-scale of the superconducting coherence length along these trajectories, but not between neighboring trajectories. Appendix E.4 solves these equations analytically. The following chapter gives a brief explanation of how these equations are implemented and solved numerically for non-bulk systems.

3 Implementation

Most of the results presented in this thesis were obtained with a simulation tool developed by Mikael Håkansson [99]. The tool is an application programming interface (API) written in C++/CUDA, that combines a wide range of useful components. Examples of components are a robust method for solving the Eilenberger equations numerically, tools for setting up complex 2D-geometries, treatment of boundary conditions, general multi-component order parameters, data post-processing and visualization. Through proper usage of object-orientation, each component is modular, making it easy to extend or replace. A main goal of the current PhD project is to both use the tool in its present state to study mesoscopic superconductors, but also to continue developing it. In particular, the purpose of the latter is to make extensions that allows the study of a wider variety of physics and systems than what is currently possible. So far, most of the time in this PhD project has been spent on understanding, analyzing and benchmarking the simulation tool. This has been a daunting task, as the tool lacks documentation and the original author is no longer involved in the project. The core of the API includes over a hundred files with some twenty thousand lines of code, and the full code base close to a thousand files.

The tool itself is not described here, as this was done in the thesis of the original author [99]. Instead, this chapter briefly describes the numerical method of solving the Eilenberger equations and the gap equation self-consistently. The discretization scheme is explained, followed by a discussion on convergence, methods of speeding up the calculations, and the multiple possible solutions for the order parameter. Finally, the Ozaki technique is described, which is an alternative approach to the Matsubara technique of treating integrals containing the Fermi-Dirac distribution.

3.1 Discretization

The quasiclassical Green functions $\check{g}^{R,A,K,M}$ contain the dynamics of the superconducting state, and most observables of interest can be obtained from them. The goal is therefore to solve the Eilenberger equation with respect to these Green functions. To eliminate spurious solutions and ensure numerical stability, the Green functions are expressed in terms of particle-hole coherence functions γ and $\tilde{\gamma}$ (also known as Riccati amplitudes). The resulting Riccati equations are less complex, provide well-defined and stable integration directions, and automatically incorporate the normalization condition of the Green functions. To solve the Riccati equations, the self-energies (and thus the superconducting order parameter) need to be known. The issue is that these in turn depend both on the Green functions and on themselves. There is thus a cyclic dependence, as illustrated in Fig. 3.1 (a). The problem is solved self-consistently, as described in Sec. 3.2. Here follows a description on how the problem is discretized and implemented.

At each spatial coordinate, the order parameter depends on the coherence functions propagating along every possible trajectory defined by the angle θ between the trajectory and the Fermi velocity on the Fermi surface [as illustrated in Fig. 3.1 (b)], summed over each discrete Matsubara energy. When the trajectories reach the edges of the system, appropriate boundary conditions are applied to match incoming and outgoing scattering trajectories, as shown in Fig. 3.1 (c). These boundary conditions are generally derived from microscopic theory. The order parameter and the coherence functions are defined on a discrete square lattice with lattice spacing h, as illustrated in Fig. 3.2 (a). Some of the observables, like the current, are defined between the lattice points of the order parameter (on the "links"). For every energy and discretized angle, the coherence functions are calculated along straight trajectories starting at the system edges in a lattice which is rotated with respect to the order parameter lattice, as shown in Fig. 3.2 (b). As

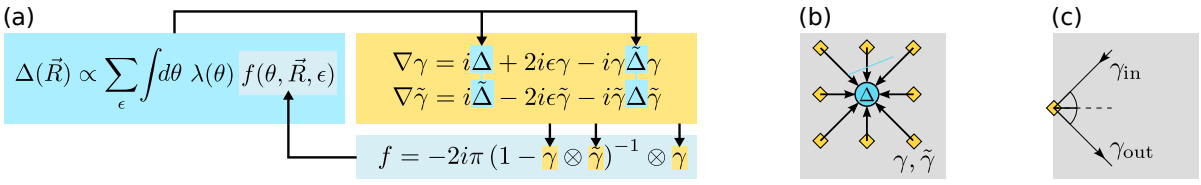

Figure 3.1: *(a) Illustration of the dependence between the order parameter Δ, the anomalous Green function f, and the coherence functions $\gamma, \tilde{\gamma}$. (b) The Riccati equations imply that the coherence functions are solved along ballistic trajectories defined by the angle with respect to the Fermi velocity, denoted θ. The gap equation implies that the order parameter depends on an integral over all such angles. (c) As the trajectories reach the edges of the system, appropriate boundary conditions are necessary to relate incoming and outgoing scattering trajectories. The figure shows the case of a clean superconducting grain in vacuum, with perfectly specular reflection.*

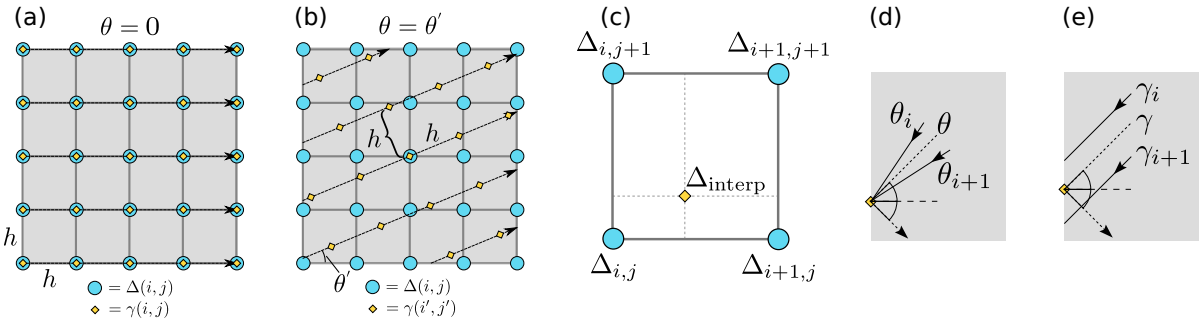

Figure 3.2: *(a) The order parameter and the coherence functions are discretized on square lattices with lattice spacing h. (b) For every energy and discretized angle, the coherence functions are calculated along ballistic trajectories from edge to edge in the system. Due to the varying angles, the lattices generally do not overlap. (c) The order parameter is bilinearly interpolated to account for the lattice mismatch. For general geometries, (d) the angles and (e) the positions of the trajectories at the edges generally do not match those of the outgoing scattering trajectories (the start trajectories of other angles). The angles and positions need to be interpolated as well. Some graphical elements were adapted from Ref. [99].*

shown in Figs. 3.2 (c)–(e), the two lattices will generally not overlap due to these rotations, which means that the order parameter has to be interpolated bilinearly to the coherence function lattice, as will the trajectory positions and angles due to a mismatch with "outgoing" scattering trajectories (i.e. starting trajectories for other angles). These interpolations are the most substantial sources of numerical errors. Higher resolution and clever interpolation tricks reduce these errors. Other sources of error include the finite cutoff in the energy sum, and the discretization of the angular integral in the gap equation. Furthermore, for complicated systems like spin-triplet systems with full spin dependence, there might not always exist solutions of a simple analytic form to the Riccati equations. An alternative approach is to solve the equations numerically, for example with the fourth-order Runge-Kutta algorithm [86], which might lead to further numerical errors. For the relatively simple systems studied in this thesis, however, the Riccati equations have exact analytic solutions.

Finally, here are some typical figures of merit for the simulations in this thesis:

lattice size: $N_x \times N_y \sim 800 \times 800$,

lattice spacing: $h \sim 0.1\xi_0$,

number of discrete angles: $N_\theta \sim 100$, (for LDOS calculations $N_\theta \sim 1600$),

number of Matsubara energies: $N_e \sim 1000$ (which corresponds to 20 Ozaki energies as described in Sec. 3.5).

3.1.1 Example: calculating the magnetic flux

Here follows an example of how the magnetic flux and the total magnetic flux density are calculated in the discretized lattice.

Consider a two-dimensional grain with area $\mathcal{A}$ and lattice spacings $\Delta x = \Delta y = h$. Let N_i and N_j be the number of lattice points along x and y, respectively, and N_{tot} be the total number of lattice points in the grain. The surface integral is discretized as

$$\mathcal{A} = \int dS \approx \sum_{i=0,j=0}^{N_i,N_j} \Delta x \Delta y = \sum_{k=0}^{N_{\text{tot}}-1} h^2, \tag{3.1}$$

such that the area is

$$\mathcal{A} = N_{\text{tot}} h^2. \tag{3.2}$$

From the definition of magnetic flux, it is found that

$$\Phi = \int B dS \approx \sum_{i=0}^{N_{\text{tot}}-1} B_i h^2. \tag{3.3}$$

The magnetic flux density in the grain is found to be

$$B = \frac{\Phi}{\mathcal{A}} \approx \frac{1}{\mathcal{A}} \sum_{i=0}^{N_{\text{tot}}-1} B_i h^2 = \frac{1}{N_{\text{tot}}} \sum_{i=0}^{N_{\text{tot}}-1} B_i, \tag{3.4}$$

yielding the total magnetic flux

$$\Phi \approx h^2 \sum_{i=0}^{N_{\text{tot}}-1} B_i. \tag{3.5}$$

3.2 Self-consistency algorithm

A simplified algorithm for solving the self-consistency equations is shown in Alg. 1. Note that the Riccati transport equations are first-order ordinary differential equations with a "memory" along each trajectory, meaning that the initial guess in step 7 propagates. The propagation length is typically quite short however, and after a few self-consistency iterations, the information about the guess is completely lost [100]. Note that setting $a = 1$ in step 12 (as done in this work) generally leads to a faster convergence, but might also lead to instability, as the algorithm then lies exactly on the convergence radius. The typical convergence criterion used in this thesis is that the total relative error fulfills

$$h(\Delta_i, \Delta_{i-1}) = \sum_{x,y}^{N_x,N_y} \frac{\|\Delta_{\text{i}}(x,y) - \Delta_{\text{i-1}}(x,y)\|}{\|\Delta_{\text{i-1}}(x,y)\|} \leq \delta_\epsilon = \begin{cases} 10^{-16}, & \Delta \in \mathbb{R}, \\ 10^{-8}\text{–}10^{-7}, & \Delta \in \mathbb{C}. \end{cases} \tag{3.6}$$

The reason for the lower criterion for $\Delta \in \mathbb{C}$ is that in this case, convergence usually "halts" at some point, probably due to ambiguity of the phase, that amplitude shifts back and forth between real and imaginary parts, or due to numerical/interpolation errors at the edges of the system. Ways of improving convergence are discussed in Sec. 3.4. The multiple possible solutions of Δ will be discussed in the following section.

Algorithm 1 Self-consistency algorithm (greatly simplified)

1: Set: $\Delta_0(\boldsymbol{R}) \leftarrow \Delta_{\text{guess}}(\boldsymbol{R})$.
2: Set: $g \leftarrow 0$.
3: Set: $\delta_\Delta \leftarrow c > \delta_\epsilon$, where $c \in \mathbb{R}$, and δ_ϵ is the convergence criterion.
4: **while** $\delta_\Delta > \delta_\epsilon$ **do**
5: **for** $|\epsilon_n| \leq \Omega_c$ **do**
6: **for** $\theta = 0, \ldots, 2\pi$ **do**
7: Initialize: $\gamma, \tilde{\gamma}$ at the boundary [typically: $(\gamma, \tilde{\gamma}) = (\gamma_{\text{bulk}}, \tilde{\gamma}_{\text{bulk}})$].
8: Solve the Riccati equations along ballistic trajectories.
9: **end for**
10: **end for**
11: Set: $f \leftarrow -2i\pi(1 - \gamma \otimes \tilde{\gamma})^1 \otimes \gamma$, where f is the anomalous Green function.
12: Set: $\Delta_i \leftarrow a\Delta_{i-1} + (1-a)g(\Delta_{i-1})$, where g is the RHS of the gap equation and $a \in [0, 1]$ is a real constant.
13: Set: $\delta_\Delta \leftarrow h(\Delta_i, \Delta_{i-1})$, where h is some residual or relative error.
14: Set: $i \leftarrow i + 1$.
15: **end while**
16: Calculate any desired observables.

3.3 On multiple solutions of the order parameter

For many systems, the order parameter has several possible solutions corresponding to local minima in the free energy landscape. The sought solution is the global minimum (the ground state). In principle, the converged solution should not depend on the initial guess, but given that the free energy landscape is often very flat and that there are several minima, the converged solution might be a local minimum. Solving the self-consistency equations numerically as described in the previous sections, there is no way of truly knowing which solution is the global minimum. The local minima might still be physically relevant for several reasons, however. To make the best out of the situation, the following should be considered:

1. "perturbing" the system during the simulation,
2. performing several simulations with different start guesses, comparing the free energy,
3. choosing a high convergence criterion.

Perturbing the system during simulation, for example by temperature or magnetic field annealing, might enable the system to shift between minima, while different start guesses might lie closer to different minima. Choosing a high convergence criterion is advantageous because the self-consistency algorithm sometimes finds its way out of local minima on its own. The choice of convergence criterion is however often influenced by the availability of time for the given simulation, and where (if ever) the convergence "stagnates". For general complex order parameters for example, convergence slows down exponentially after some iteration. It is therefore desirable to speed up the convergence as much as possible. Methods of doing so will be discussed in the following section.

3.4 Speeding up convergence

Increasing the convergence speed of the self-consistency iterations is important for finding the minima in the solution to the order parameter. Studying more complicated systems might even be infeasible if the convergence is too slow. What influences the convergence speed is of course how many iterations are required to reach a given precision, and how long time each iteration takes. Steps 1–3 below affect the number of iterations, while step 4 affects the iteration speed:

1. making "smart" initial guesses,
2. perturbing the system during the simulation,
3. using an "accelerator" to base the solution of each iteration on the previous ones,
4. optimizing and speeding up the algorithm itself.

Guesses are smart if they reflect the correct answer, and if they contain the right "seed" for it, such that the guess already lies relatively close to the minimum. For example an order parameter with a 2π phase winding might be a good initial guess for a system with an external flux quantum passing through an Abrikosov vortex or a solenoid. The right amount of complexity is also important; for a bulk system, a purely real order parameter can easily converge to machine precision in relatively few steps, while a complex order parameter with phase gradients is crucial for ever finding the loop-current phase. Another start guess that might be good is to start with a highly converged solution to a similar problem. Perturbing the system with annealing or random fluctuations might provide the seed for the correct answer, or reduce the amount of necessary iterations.

To heavily reduce the amount of iterations, an "acceleration" method can be used, as described in the following. The problem of solving the order parameter can be stated as a fixed-point iteration problem

$$F[\Delta_i, \Delta_{i-1}] = g[\Delta_{i-1}] - \Delta_i, \tag{3.7}$$

where g is the RHS of the gap equation, and the goal is to minimize F. Written on this form, it is straightforward to apply "accelerator algorithms" that attempt to estimate where the solution is converging towards, like the Newton-Raphson method for example. In this thesis work, the naive but useful "gradient accelerator" is employed, which bases the solution of the ith iteration on the slope of the solutions in the previous iterations

$$\Delta_{i+1} = g\left[\Delta_i\right] + \left(g\left[\Delta_{i-1}\right] - g\left[\Delta_{i-2}\right]\right) \times \min\left\{c, \frac{1}{4}\left|\frac{h(\Delta_{i-1}, \Delta_{i-2})}{h(\Delta_i, \Delta_{i-1})} - 1\right|^{-1}\right\}, \tag{3.8}$$

where h is the relative error from Eq. (3.6), and c is some upper bound for the accelerator step. A more advanced acceleration and immensely powerful one is the "Anderson acceleration" [101, 102] (also known as "Anderson mixing"), which has been used with great success in many branches of natural science. In superconductivity, it has for example been used to solve the self-consistency equations both in full microscopic theories [103] and in quasiclassical theory [104]. Anderson acceleration is essentially described in Algorithm 2 from Ref. [102].

Algorithm 2 Anderson acceleration (simplified)

1: Given: Δ_0 and $m \geq 1$
2: **for** $i = 1, 2, \ldots$ **do**
3: Set: $m_i = \min\{m, i\}$
4: Set: $F_i(f_{i-m_i}, \ldots, f_i)$, where $f_j = g(\Delta_j) - \Delta_j$
5: Determine $\alpha^{(i)} = (\alpha_0^{(i)}, \ldots, \alpha_{m_i}^i)^T$ that solves

$$\min_{\alpha=(\alpha_0,\ldots,\alpha_{m_i})^T} \|F_i\alpha\|_2 \quad \text{such that} \quad \sum_{j=0}^{m_i} \alpha_i = 1. \tag{3.9}$$

6: Set: $\Delta_{i+1} = (1-\beta_i)\sum_{j=0}^{m_i} \alpha_j^{(i)} \Delta_{i-m_i+j} + \beta_i \sum_{j=0}^{m_i} \alpha_j^{(i)} g(\Delta_{i-m_i+j})$ where $\beta_i > 0$ is a relaxation parameter (typically $\beta_i = 1$).
7: **end for**

Apart from optimizing the code, solving the self-consistency equation can be sped up by for example:

1. using the Metropolis-Hastings algorithm (not implemented),
2. using an adaptive discretization size (implemented),
3. using Richardson extrapolation (not implemented),
4. using the Ozaki technique instead of the Matsubara technique (implemented).

Systems with a flat free energy landscape, like the systems studied in this thesis, can often be quickly traversed by random walks. It is therefore proposed that the Metropolis-Hastings algorithm can be used to speed up the convergence of the self-consistency equations. The idea is to make some kind of random modification of the order parameter. The modification is accepted if it leads to a lower free energy, and accepted with a certain probability if it leads to a higher free energy (this is called the Metropolis step). The latter allows the algorithm to get out

of local minima in search of the global minimum. The question then is which kind of random modification to use. A method which is often highly successful is the bisection method, where the sample space (the order parameter lattice in this case), is divided into one or more regions. In each region, the value of the region midpoint $\Delta_{N/2}$ is shifted randomly, and the rest of the points are interpolated between this value and the values at the edges. This is followed by the Metropolis step. Then, each point between $\Delta_{N/2}$ and the edges are shifted randomly in the same way, followed by another Metropolis step. This continues until a random shift has been suggested to each point in the region. The bisection method and the Metropolis algorithm goes very well together with an adaptive step size [105].

An adaptive discretization size is based on starting with a low discretization, which allows the system to converge fast to a rough estimation of the correct solution. By then gradually increasing the number of discrete grid points, the precision gets finer and the approximation better. Care needs to be taken, however, as a too low convergence might lock the algorithm on a path towards a less favorable minimum, or in the worst case, instability.

The Richardson extrapolation technique is a "sequence accelerator" to improve the convergence of a sum. This can for example be used to reduce the number of energies required in the energy sum in the gap equation. Probably the most effective way of reducing the number of energies though is by using the Ozaki technique, which will be described in the following section.

3.5 Ozaki technique versus Matsubara technique

Calculation of the grand partition function, and in particular the Green function associated with the Fermi-Dirac function, are cornerstone problems not only in condensed matter physics, but in quantum field theory and many-body physics in general. The so-called Matsubara technique [81] was developed as a method for solving these problems. In superconductivity theory, the method is commonly used to treat the energy integrals that occur for example in the gap equation, as well as the expression for the free energy and the current density.

In short, the Matsubara technique is based on analytic continuation to imaginary time, $\tau \equiv it$. Since the resulting Matsubara Green function (g^M) is periodic in τ, its Fourier transform is only defined over a set of discrete (imaginary) energies $z = i\epsilon_n$, where $\epsilon_n \equiv \pi k_B T(2n+1)$ are called the Matsubara energies (or frequencies, in natural units). This makes it possible to replace the energy integral with a sum, where the latter requires far less terms to converge to the same precision as the former. Recently, a more efficient method was proposed by Ozaki [106], based on expressing the Fermi-Dirac function in a continued fraction representation. This method will from now on be referred to as the Ozaki technique, and was implemented with great performance gain in this thesis. Below is a description of the Ozaki technique directly following Ref. [106], and a benchmark against the Matsubara technique.

In the Matsubara technique, the Fermi-Dirac function $f(x)$ is expressed as

$$f(x) \equiv \frac{1}{1+\exp(x)} = \frac{1}{2} - \sum_{n=1}^{\infty} \frac{2x}{x^2 + \pi^2(2n-1)^2}, \tag{3.10}$$

where $x = \beta(z-\mu)$ is generally a complex number, $\beta \equiv 1/k_B T$, μ is the chemical potential and z a complex energy. Equation (3.10) has the residues $x = -1$ and poles distributed uniformly on the imaginary axis $x = \pm i\pi(2n-1)$. In contrast, the Ozaki technique provides an expression where the poles are distributed non-uniformly. As a result, there is an exponentially improved convergence compared to the Matsubara technique [see Fig. 3.3 (a) on p. 43]. The Ozaki technique is based on deriving the Fermi-Dirac function from a hypergeometric function as the continued fraction (see Ref. [106] for a proof)

$$f(x) \equiv \frac{1}{1+\exp(x)} = \frac{1}{2} - \cfrac{x/4}{1 + \cfrac{(x/2)^2}{3 + \cfrac{(x/2)^2}{5 + \cfrac{(x/2)^2}{\vdots \cfrac{}{(2M-1) + \cdots}}}}}. \tag{3.11}$$

Equation. (3.11) is exact in the limit $M \to \infty$. It is found that if the fraction is cut off at $M = 2N$, where N is a positive integer, then the expression can be

written into partial functions via the Padé approximation

$$f(x) \approx \frac{1}{2} + \sum_{p=1}^{N} \frac{R_p}{x - iz_p} + \sum_{p=1}^{N} \frac{R_p}{x + iz_p}, \tag{3.12}$$

where $R_p \in \mathbb{R}$ and $z_p \in \mathbb{R}$ are residues and poles, respectively, to be calculated. Equation (3.12) is exact as $N \to \infty$. There are analytic solutions to z_p and R_p, but these take on complicated expressions for larger N which are not elucidating. Instead, an alternative method for finding z_p and R_p is presented, in the form of an eigenvalue problem.

Generally, a continued fraction can be expressed as the $(1,1)$ element $(C^{-1})_{11}$ of the inverse of a tridiagonal matrix, as

$$(C^{-1})_{11} = \cfrac{1}{c_{11} + \cfrac{c_{12}c_{21}}{c_{22} + \cfrac{c_{23}c_{32}}{c_{33} + \cfrac{c_{34}c_{43}}{\ddots \\ \overline{c_{MM}}}}}}, \tag{3.13}$$

where the tridiagonal matrix C is

$$C = \begin{pmatrix} c_{11} & c_{12} & & & & 0 \\ c_{21} & c_{22} & c_{23} & & & \\ & c_{32} & c_{33} & c_{34} & & \\ & & \ddots & \ddots & \ddots & \\ 0 & & & & c_{M(M-1)} & c_{MM} \end{pmatrix}. \tag{3.14}$$

Comparing Eq. (3.11) with Eqs. (3.13) and (3.14), it is found that

$$c_{pp} = 2p - 1, \tag{3.15}$$

$$c_{p(p+1)} = c_{(p+1)p} = i\frac{x}{2}, \tag{3.16}$$

where $p \in [1, 2, \cdots, M]$ for c_{pp} and $p \in [1, 2, \cdots, (M-1)]$ for $c_{p(p+1)}$ and $c_{(p+1)p}$. Thus, the Fermi-Dirac function can be expressed as

$$f(x) \approx \frac{1}{2} - \frac{x}{4} \left\{ (ixB - A)^{-1} \right\}_{11}, \tag{3.17}$$

where A and B are the $(M \times M)$-matrices

$$A = \begin{pmatrix} -1 & 0 & & & 0 \\ 0 & -3 & 0 & & \\ & 0 & -5 & 0 & \\ & & \ddots & \ddots & \\ 0 & & & & -(2M-1) \end{pmatrix}, \tag{3.18}$$

and

$$B = \begin{pmatrix} 0 & \frac{1}{2} & & 0 \\ \frac{1}{2} & 0 & \frac{1}{2} & \\ & \ddots & \ddots & \ddots \\ 0 & & \frac{1}{2} & 0 \end{pmatrix}. \tag{3.19}$$

Equation (3.17) is exact as $M \to \infty$. Finding the singular points of Eq. (3.11) is equivalent to solving the generalized eigenvalue problem

$$Ab = ixBb, \tag{3.20}$$

where b is an eigenvector and x the eigenvalue. It can be proven that x is an imaginary number, such that $y = ix$ and z_p are real numbers. The eigenvalue problem to solve becomes

$$Ab = yBb, \tag{3.21}$$

$$\frac{x}{4}\left\{(yB - A)^{-1}\right\}_{11} = \frac{x}{4}\sum_{p=1}^{N}\left(\frac{R'_p}{y - z_p} - \frac{R'_p}{y + z_p}\right). \tag{3.22}$$

The poles and residues are found from the eigenvalues according to

$$z_p = \frac{1}{y_p}, \tag{3.23}$$

$$R'_p = \frac{1}{4}A_{p(p+1)}A_{(p+1)p}z_p^2. \tag{3.24}$$

The following routine can then be followed to replace any Matsubara sum with an Ozaki sum

1. Calculate the Matsubara cutoff $N_M = N_M(T) = \text{int}\left(\frac{\epsilon_c/k_BT_c}{2\pi T/T_c} - \frac{1}{2}\right)$, for some energy cutoff ϵ_c.

2. Obtain the Ozaki cutoff N_O as the pole number where the maximum Ozaki pole is $z_{N_O} \geq \epsilon_{N_M}$ [i.e. compare the solid and the dashed line in Fig. 3.3 (a)]. For example, $\epsilon_c = 30k_BT_c$ and $T = 0.1$ would give $N_M = 3 \times 10^5$ and $N_O = 343$. Note that in contrast to the Matsubara poles, the Ozaki poles are cutoff dependent (i.e. changing N_O changes the values of z_p and R'_p).

3. Given N_O, calculate z_p and R'_p according to the above equations.

4. Replace any Matsubara sum with the Ozaki sum $\sum_{n=1}^{N} F(\epsilon_n) \longrightarrow \sum_{p=1}^{N} R'_pF(z_p)$, where F is the summand.

Note that the Matsubara symmetry for negative energies derived in App. G also applies to the Ozaki technique, due to symmetric distribution of poles around $z = 0$.

Finally, Fig. 3.3 shows a benchmark of the Ozaki technique versus the Matsubara technique. See the caption for an explanation of the figure.

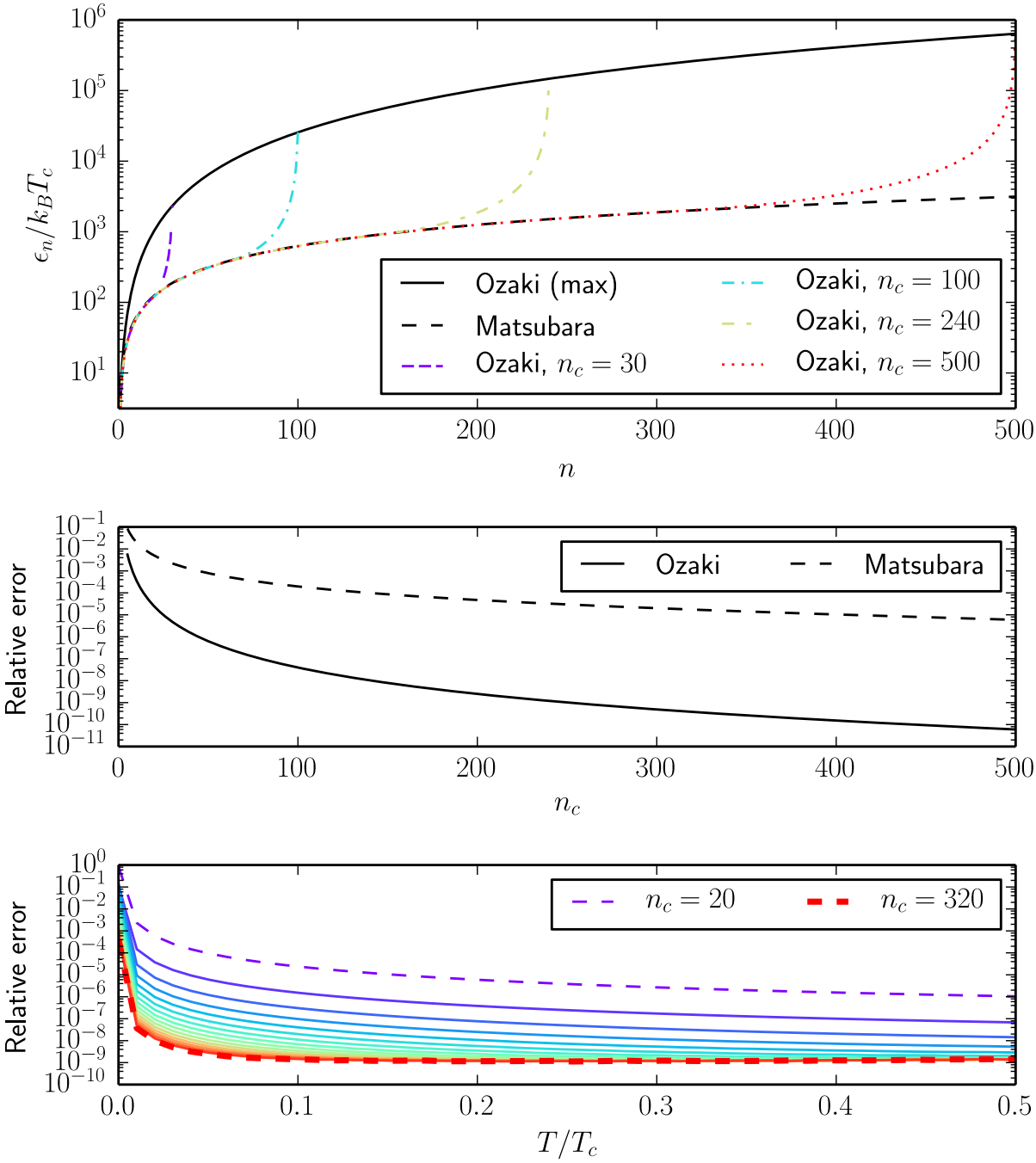

Figure 3.3: *Benchmark between the Ozaki and Matsubara techniques. Note that all ordinates are in log-scale. (a) The pole value (ϵ_n for Matsubara and z_p for Ozaki) as a function of the pole number n (dashed and dotted lines). The solid line shows the value of the maximum Ozaki pole at $n = n_c$. The Ozaki pole values increase exponentially, while the Matsubara pole values increase linearly. (b) Relative error of the s-wave bulk gap at $T = 0.1T_c$ versus the number of terms in the Ozaki sum (solid line) and Matsubara sum (dashed line). (c) Relative error (with respect to $n_c = 1000$) of the s-wave bulk gap versus temperature, for different number of terms in the Ozaki sum. Here, $\Delta n_c = 20$.*

4 Electrodynamics

The goal of this chapter is to introduce the main electrodynamical quantities of the appended papers, as well as some fundamental properties of superconductors. The chapter is divided into four sections.

The first section shows how the quantum-mechanical momentum operator is modified in the presence of an external magnetic field. The superfluid momentum is introduced, and gauge theory is briefly discussed. A gauge invariant expression is then derived for the probability density and the current density. This expression is used to derive the magnetic flux quantum in superconductors.

The second section goes through the magnetic classification and fundamental phase diagrams of superconductivity. It is shown how Doppler shifts caused by phase gradients in the order parameter, as well as by superfluid momenta, give rise to a current density. The latter is the total current density, including both supercurrents and quasiparticle currents.

The third section shows that a spin-degenerate superconductor couples to an external magnetic field through a Doppler shift to the energies in the Eilenberger equation. Appropriate magnetic vector potentials are derived for the case of uniform superconductors as well as superconductors with holes.

The fourth section derives the magnetic vector potentials that are induced by the currents in the superconductor.

The chapter is mainly written in Gaussian CGS units (unless otherwise specified) and uses the following sign convention for the elementary charge

$$e = -|e|. \tag{4.1}$$

For more information about units and conversions between SI and CGS units, see App. A.

4.1 Basic electrodynamics in quantum mechanics

This section emphasizes the necessity to distinguish between canonical and kinematical momenta in quantum mechanics. These momenta are subsequently used to derive an expression for the probability current. Finally, this expression is used to show that magnetic flux is quantized in superconductors, and to derive the corresponding flux quantum. Many of the calculations follow Sakurai [107].

4.1.1 Canonical, kinematical and superfluid momenta

Consider an electromagnetic field acting on a charge carrier with mass m and charge q. To treat such problems, the momentum operator $\boldsymbol{p} \equiv -i\hbar\boldsymbol{\nabla}$ has to be substituted for

$$\boldsymbol{p} \to \boldsymbol{p} - \frac{q}{c}\boldsymbol{A}, \tag{4.2}$$

where $\boldsymbol{A}(\boldsymbol{x})$ is the vector potential related to the magnetic flux density $\boldsymbol{B}$. It will soon be seen why this substitution is appropriate. The corresponding Hamiltonian is written

$$\begin{aligned} H &= q\phi + \frac{1}{2m}\left(\boldsymbol{p} - \frac{q}{c}\boldsymbol{A}\right)^2 \\ &= q\phi + \frac{1}{2m}\left(\boldsymbol{p}^2 - \frac{q}{c}\left(\boldsymbol{p}\cdot\boldsymbol{A} + \boldsymbol{A}\cdot\boldsymbol{p}\right) + \frac{q^2}{c^2}\boldsymbol{A}^2\right), \end{aligned} \tag{4.3}$$

where $\boldsymbol{x}$ the position operator, and $\phi(\boldsymbol{x})$ is the scalar potential related to the electric field $\boldsymbol{E}$. In the Heisenberg picture, the time derivative of the position operator is found to be

$$\begin{aligned} \frac{d\boldsymbol{x}}{dt} &\equiv \frac{[\boldsymbol{x}, H]}{i\hbar} \\ &= [\boldsymbol{x}, \phi] + \frac{1}{2im\hbar}\Bigg([\boldsymbol{x}, \boldsymbol{p}^2] - \\ &\qquad \frac{q}{c}\left([\boldsymbol{x}, \boldsymbol{p}\cdot\boldsymbol{A}] + [\boldsymbol{x}, \boldsymbol{A}\cdot\boldsymbol{p}] + \frac{q^2}{c^2}[\boldsymbol{x}, \boldsymbol{A}^2]\right)\Bigg), \end{aligned} \tag{4.4}$$

where the commutators are

$$[\boldsymbol{x}, \boldsymbol{p}] = i\hbar, \tag{4.5}$$

$$[\boldsymbol{x}, \boldsymbol{p}^2] = 2i\hbar\boldsymbol{p}, \tag{4.6}$$

$$[\boldsymbol{x}, \boldsymbol{p}\cdot\boldsymbol{A}] + [\boldsymbol{x}, \boldsymbol{A}\cdot\boldsymbol{A}] = 2i\hbar\boldsymbol{A}, \tag{4.7}$$

$$[\boldsymbol{x}, \phi] = 0, \tag{4.8}$$

$$[\boldsymbol{x}, \boldsymbol{A}] = [\boldsymbol{x}, \boldsymbol{A}^2] = 0. \tag{4.9}$$

Inserting the commutators in Eqs. (4.5)–(4.9) into Eq. (4.4), it is found that

$$\frac{d\boldsymbol{x}}{dt} = \frac{1}{m}\left(\boldsymbol{p} - \frac{q}{c}\boldsymbol{A}\right). \tag{4.10}$$

Hence, the generator of translations $\boldsymbol{p}$ is *not* the same as the momentum $md\boldsymbol{x}/dt$, and it is seen why the substitution in Eq. (4.2) was appropriate. The following definitions are used to distinguish the two different momenta

kinematical momentum: $\Pi \equiv m\frac{d\boldsymbol{x}}{dt} = m\boldsymbol{v} = \boldsymbol{p} - \frac{q}{c}\boldsymbol{A}$ (mechanical momentum),

canonical momentum: $\boldsymbol{p} = m\boldsymbol{v} + \frac{q}{c}\boldsymbol{A}$ (generator of translations).

The name canonical momentum stems from the fact that $\boldsymbol{p}$ fulfills the canonical commutation relations, while Π does not. The name kinematical momentum (or sometimes physical momentum) is chosen because Π represents the momentum that would be measured in an experiment. Note that in the presence of an external magnetic field, neither of these two momenta are necessarily conserved.

An important point is that the kinematical momentum is *gauge invariant*, while the canonical momentum is not. This means that the expectation value of the kinematical momentum, and hence the Hamiltonian in Eq. (4.3), are invariant under the following *gauge transformations* (just like Maxwell's equations)

$$\phi \;\rightarrow\; \phi - \frac{1}{c}\frac{\partial \Lambda}{\partial t}, \tag{4.11}$$

$$\boldsymbol{A} \;\rightarrow\; \boldsymbol{A} + \boldsymbol{\nabla}\Lambda, \tag{4.12}$$

where Λ can depend on both time and position. A particular choice of Λ thus corresponds to a particular *gauge*. It is convenient to choose a gauge which simplifies the problem at hand. According to Noether's theorem, global gauge invariance is related to charge conservation. The theory of superconductivity breaks U(1) gauge symmetry, through the existence of a complex-valued order parameter with a non-uniform phase χ. Consequently, $\boldsymbol{A}$ is the vector potential due to external magnetic fields as well as currents induced by gradients in this phase, and the arbitrary function Λ is appropriately chosen to be the phase χ of the superconducting order parameter. For example, a change in the phase $\chi/2$ of the singe-quasiparticle wave function by an arbitrary function $\lambda/2$ generates a change λ in the phase of the superconducting order parameter. The latter term can be compensated ("gauged away") by gauge transforming the vector potential

$$\boldsymbol{A} \rightarrow \boldsymbol{A} - \frac{\hbar c}{2e}\boldsymbol{\nabla}\chi. \tag{4.13}$$

Thus, Eq. (4.13) represents the gauge invariant vector potential in the superconducting state. The *superfluid momentum*, i.e. the Cooper pair momentum per quasiparticle, can be written

$$\boldsymbol{p}_s = \frac{\hbar}{2}\boldsymbol{\nabla}\chi - \frac{e}{c}\boldsymbol{A}, \tag{4.14}$$

which can be written as a dimensionless equation

$$\frac{1}{2\pi}\frac{\boldsymbol{p}_s}{p_0} = \frac{1}{2}\left(\xi_0\boldsymbol{\nabla}\right)\chi + \pi\frac{\boldsymbol{A}}{\Phi_0/\xi_0}, \tag{4.15}$$

$$p_0 \equiv \frac{k_B T_c}{v_F}, \tag{4.16}$$

where p_0 is a momentum ($[p_0] = \mathrm{kg{\cdot}m/s}$), $\xi_0 \equiv \hbar v_F/2\pi k_B T_c$ is the zero-temperature superconducting coherence length, and $\Phi_0 \equiv hc/2|e|$ is the magnetic flux quantum to be derived in Sec. 4.1.3 (hence the sign change in going from $e \to -|e|$ in introducing Φ_0). The gauge invariant probability current will now be derived.

4.1.2 Probability current

Probability density can be seen as a heterogeneous fluid, which in some sense can be treated equivalently to a superfluid. The probability current (also known as probability flux) is the flow of the probability density per unit time. This current fulfills the same continuity equations as the electric current in electrodynamics. Therefore, the equations derived in this section holds both for the probability current and for a supercurrent, and the fluid mentioned here can either be the probability density or a superfluid. Consider a fluid that can be described by a plane wave, with wave function ψ and phase χ

$$\psi = |\psi|\, e^{i\boldsymbol{k}\cdot\boldsymbol{r}} = |\psi|\, e^{i\chi}, \tag{4.17}$$

where the density is

$$n \equiv |\psi|^2 = \psi^*\psi. \tag{4.18}$$

For a superfluid, $n = n_p = \frac{1}{2}n_s$ is the density of Cooper pairs. Acting on this wave function with the momentum operator $\boldsymbol{p} \equiv -i\hbar\boldsymbol{\nabla}$

$$\boldsymbol{p}\psi = -i\hbar\boldsymbol{\nabla}\,|\psi|\, e^{i\boldsymbol{k}\cdot\boldsymbol{r}} = \hbar\boldsymbol{k}\psi = \hbar\left(\boldsymbol{\nabla}\chi\right)\psi. \tag{4.19}$$

The current density can be written in terms of the canonical momentum (defined in Sec. 4.1.1)

$$\boldsymbol{j} = q\boldsymbol{v}n = qn\Pi = \frac{q}{m}\left(\boldsymbol{p} - \frac{q}{c}\boldsymbol{A}\right)\psi^*\psi, \tag{4.20}$$

where for a supercurrent $q = 2e < 0$ and $m = 2m_e^*$. Noting the following relations,

$$\boldsymbol{\nabla}\psi = i\boldsymbol{\chi}\psi, \tag{4.21}$$

$$\boldsymbol{\nabla}\psi^* = -i\boldsymbol{\chi}\psi^*, \tag{4.22}$$

$$\begin{aligned}\psi^*\boldsymbol{\nabla}\psi - \psi\boldsymbol{\nabla}\psi^* &= \psi^*\left(i\boldsymbol{\nabla}\chi\right)\psi - \psi\left(-i\boldsymbol{\nabla}\chi\right)\psi^* \\ &= 2i\left(\boldsymbol{\nabla}\chi\right)|\psi|^2,\end{aligned} \tag{4.23}$$

it is possible to rewrite the current density on the familiar form

$$\boldsymbol{j} = i\frac{\hbar q}{2m}\left(\psi^*\boldsymbol{\nabla}\psi - \psi\boldsymbol{\nabla}\psi^*\right) - \frac{q^2}{mc}\boldsymbol{A}\psi^*\psi. \tag{4.24}$$

Alternatively, by using Eq. (4.23), it can also be written

$$\boldsymbol{j} = -\frac{\hbar q n}{m}\boldsymbol{\nabla}\chi - \frac{q^2 n}{mc}\boldsymbol{A}. \tag{4.25}$$

Introducing the London parameter Λ_L

$$\Lambda_L \equiv \frac{mc}{nq^2}, \tag{4.26}$$

which for a superfluid is $\Lambda_L = m_e^* c/2ne^2$, the current density can finally be written

$$\Lambda_L \boldsymbol{j} = -\left(\frac{\hbar c}{q}\boldsymbol{\nabla}\chi + \boldsymbol{A}\right). \tag{4.27}$$

This equation will now be used to derive the quantum of magnetic flux.

4.1.3 Flux quantization

It will now be shown that the magnetic flux Φ passing through a superconductor is quantized. The resulting magnetic flux quantum, denoted Φ_0, will also be derived. Consider a region that is either normal conducting (like the core of an Abrikosov vortex) or a hole (like in a loop), with area S_1 and penetrated by a flux Φ, as illustrated in Fig. 4.1. Let C be a contour encircling S_1 that lies far enough away such that any screening currents are vanishing (i.e. the distance between C and the boundary of S_1 should be large compared to the superconducting penetration depth λ_L). Integrating the probability current in Eq. (4.27) along the contour C

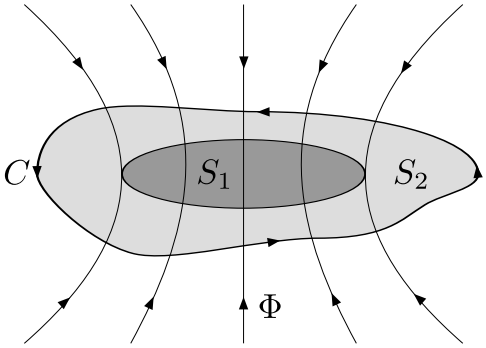

Figure 4.1: *Magnetic flux Φ penetrating a region that is either normal conducting or a hole, with area S_1. The contour C encircles this area.*

$$-\Lambda_L \oint_C \boldsymbol{j}_s \cdot d\boldsymbol{l} = \frac{\hbar c}{q}\oint_C (\boldsymbol{\nabla}\chi)\cdot d\boldsymbol{l} + \oint_C \boldsymbol{A}\cdot d\boldsymbol{l}, \tag{4.28}$$

where $d\boldsymbol{l}$ is an infinitesimal vector segment along C. Since the contour C was chosen such that any screening currents vanish, the Meissner effect ensures that the left-hand side also vanishes

$$-\Lambda_L \oint_C \boldsymbol{j}_s \cdot d\boldsymbol{l} = 0. \qquad \text{(Meissner effect)} \tag{4.29}$$

Furthermore, the superconducting order parameter must be a single-valued function at each point in space. This means that along any closed trajectory, the phase of the order parameter must return to the same value modulo 2π, and the second integral turns out to be

$$\frac{\hbar c}{q}\oint_C (\boldsymbol{\nabla}\chi)\cdot d\boldsymbol{l} = \frac{\hbar c}{q}(\chi_2 - \chi_1) = \frac{\hbar c}{q}2\pi k = \frac{hc}{q}k, \tag{4.30}$$

where k is an integer. Finally, applying Stokes' theorem and Maxwell's equations to the last integral yields

$$\oint_C \boldsymbol{A}\cdot d\boldsymbol{l} = \int_{S_2}(\boldsymbol{\nabla}\times\boldsymbol{A})\cdot d\boldsymbol{S} = \int_{S_2}\boldsymbol{B}\cdot d\boldsymbol{S} \equiv \Phi. \tag{4.31}$$

Strictly speaking, the flux Φ here is the total flux that passes through S_2 and not just S_1. It vanishes exponentially into the superconductor, though, making them approximately the same. Combining Eqs. (4.28)–(4.31),

$$\Phi = -k\frac{hc}{q} = k\frac{hc}{|q|}. \tag{4.32}$$

Thus, the flux is quantized, and the quantum of magnetic flux is defined for a superconductor as

$$\Phi_0 \equiv \frac{hc}{2|e|}, \qquad \text{(CGS)} \tag{4.33}$$

which is half the quantum of flux for a normal conductor ($q = e < 0$). In SI units, the flux quantum is instead $h/2|e|$. Historically, the quantization with $2e$ rather than e, as first suggested by Onsager, was an important indication that superconductivity involved pairs of electrons. Equation (4.32) shows that it is possible for the flux to be multiply quantized ($k > 1$), but for an Abrikosov vortex, this is an unstable state. The vortex will try to split into the more energetically favorable state with several vortices that each have $k = 1$. If the geometry is frustrated, or the region is a hole which cannot split, then it is possible to stabilize states with $k > 1$. These cases will be studied in the results Ch. 6 and Ch. 7.

4.2 The spectral current and the current density

In this section, the quasiclassical current density and spectral charge current will be introduced. In short, to obtain these quantities, one starts with the typical current density in quantum mechanics, for example Eq. (4.24), and goes through second quantization to replace ψ with the fermionic field operators. By taking the expectation value, the resulting current density can be expressed in terms of the mean-field Green functions. This is then followed by the quasiclassical approximation. The full derivation of these observables can be found in the first chapters of Ref. [68].

In homogeneous superconductors, the supercurrents are distributed over the continuum states. Any superfluid momenta or phase gradients give rise to Doppler shifts $\delta\epsilon$ of these continuum states (as well as of any midgap states)

$$\delta\epsilon = \boldsymbol{v}_F \cdot \boldsymbol{p}_s, \tag{4.34}$$

where $\boldsymbol{p}_s$ is the superfluid momentum from Eq. (4.14). To obtain the total current density, the contributions of the shifts are added up to form the *spectral current*

$$\boldsymbol{j}(\boldsymbol{p}_F, \boldsymbol{R}; \epsilon) = e\boldsymbol{v}_F N_F \left(\mathcal{N}_+(\boldsymbol{p}_F, \boldsymbol{R}; \epsilon) - \mathcal{N}_-(\boldsymbol{p}_F, \boldsymbol{R}; \epsilon)\right), \tag{4.35}$$

where $\boldsymbol{v}_F$ is the Fermi velocity on the Fermi surface at Fermi momentum $\boldsymbol{p}_F$, $\boldsymbol{R}$ is the center-of-mass coordinate, and $\mathcal{N}_\pm$ are the dimensionless DOS of comoving $(+)$ and countermoving $(-)$ excitations along the trajectory $\hat{\boldsymbol{p}}_F$

$$\mathcal{N}_\pm(\boldsymbol{p}_F, \boldsymbol{R}; \epsilon) = N(\pm\boldsymbol{p}_F, \boldsymbol{R}; \epsilon)/N_F. \tag{4.36}$$

Here, N_F is the normal-state DOS at the Fermi surface (per spin),

$$N_F \equiv \int_{\mathrm{FS}} \frac{d^2 p_F}{(2\pi\hbar)^3 \left|\boldsymbol{v}_F(\boldsymbol{p}_F)\right|}, \tag{4.37}$$

and N is the angle-resolved DOS

$$N(\boldsymbol{p}_F, \boldsymbol{R}; \epsilon) = -\frac{1}{2\pi} \operatorname{Im}\left[\operatorname{Tr}\left\{\hat{\tau}_3 \hat{g}^R(\boldsymbol{p}_F, \boldsymbol{R}; \epsilon)\right\}\right], \tag{4.38}$$

where the trace is over 4×4 Nambu-spin space, $\hat{\tau}_3$ is the third Pauli matrix in Nambu-spin space and $\hat{g}^R$ is the retarded Green function. The spectral current in Eq. (4.35) is a measure of the contributions of quasiparticle states at position $\boldsymbol{R}$, energy ϵ and momentum $\boldsymbol{p}_F$ to the current density. Thus, the total current density is obtained by multiplying the spectral current with the occupation distribution and integrating over both energies and the Fermi momentum. In equilibrium,

the occupation distribution is given by the Fermi-Dirac distribution f, and the Matsubara technique can be employed to obtain the current distribution as a sum

$$\begin{aligned} \boldsymbol{j}(\boldsymbol{R}) &= \int d\epsilon \int d\boldsymbol{p}_F \, (2f(\epsilon) - 1) \, \boldsymbol{j}(\boldsymbol{p}_F, \boldsymbol{R}; \epsilon) && (4.39) \\ &= \pi e N_F \int d\boldsymbol{p}_F \boldsymbol{v}_F(\boldsymbol{p}_F) k_B T \sum_{|\epsilon_n| < \epsilon_c} \frac{1}{2} \operatorname{Tr} \left\{ \hat{\tau}_3 \hat{g}^M(\boldsymbol{p}_F, \boldsymbol{R}; i\epsilon_n) \right\}, && (4.40) \end{aligned}$$

where ϵ_c is some cutoff, $\epsilon_n \equiv \pi k_B T_c (2n+1)$ are the Matsubara energies, and $\hat{g}^M$ is the Matsubara Green function. For the grains considered in this thesis

$$\operatorname{Tr} \left\{ \hat{\tau}_3 \hat{g}^M(\boldsymbol{p}_F, \boldsymbol{R}; z) \right\} = 4 g_0^M(\boldsymbol{p}_F, \boldsymbol{R}; z), \tag{4.41}$$

where 0 denotes the scalar component. Using the Matsubara symmetry derived in App. G, the sum can be converted to positive energies

$$\begin{aligned} \boldsymbol{j}(\boldsymbol{R}) &= 2\pi k_B T e N_F v_F \int d\boldsymbol{p}_F \sum_{0 < \epsilon_n < \epsilon_c} \hat{\boldsymbol{v}}_F \left(g_0^M(\boldsymbol{p}_F, \boldsymbol{R}; i\epsilon_n) + \left(g_s^M(\boldsymbol{p}_F, \boldsymbol{R}; i\epsilon_n) \right)^* \right), \\ &= 4\pi k_B T e N_F v_F \int d\boldsymbol{p}_F \sum_{0 < \epsilon_n < \epsilon_c} \hat{\boldsymbol{v}}_F g^M(\boldsymbol{p}_F, \boldsymbol{R}; i\epsilon_n), && (4.42) \end{aligned}$$

since j and g_s^M are real. Introducing the *depairing current*

$$j_d \equiv 4\pi k_B T_c |e| N_F v_F, \tag{4.43}$$

the current density can be written as a dimensionless equation

$$\frac{\boldsymbol{j}(\boldsymbol{R})}{j_d} = -\frac{T}{T_c} \int d\boldsymbol{p}_F \sum_{0 < \epsilon_n < \epsilon_c} \hat{\boldsymbol{v}}_F g_s^M(\boldsymbol{p}_F, \boldsymbol{R}; i\epsilon_n), \tag{4.44}$$

where the minus sign comes from the factor $e/|e|$.

4.3 Response to a uniform external magnetic field

In this section, the superconductivity phase diagram in an external magnetic field will be introduced. Furthermore, it will be shown that in the absence of spin dependence, an external magnetic field couples to the superconducting state through the magnetic vector potential as a Doppler shift to the self-energy. The vector potential is derived for two different cases, namely a uniform magnetic field through

(a) a homogeneous superconductor,

(b) a hole in a superconductor (i.e. a solenoid).

4.3.1 Superconductivity phase diagram and magnetic classification

There are two fundamental length scales in superconductivity; the superconducting coherence length (ξ), and the magnetic penetration depth (λ, also known as the London penetration depth). The superconducting order parameter usually varies on the first length-scale, while magnetic properties usually varies on the latter. These are commonly defined as

$$\xi(T) \equiv \frac{\hbar v_F}{\Delta(T)}, \tag{4.45}$$

$$\lambda(T) \equiv \sqrt{\frac{mc^2}{4\pi e^2 n_S(T)}}, \tag{4.46}$$

where n_S is the superfluid density. Note that both of these expressions might be modified by e.g. geometry and imperfections. In this thesis, the zero-temperature coherence length and penetration depth are used as length scales, defined as

$$\xi_0 \equiv \frac{\hbar v_F}{2\pi k_B T_c}, \tag{4.47}$$

$$\lambda_0 \equiv \sqrt{\frac{c^2}{4\pi e^2 N_F v_F^2}}, \tag{4.48}$$

respectively. The dimensionless ratio between the coherence length and the penetration depth is known as the Ginzburg-Landau parameter (κ) and is used to classify the magnetic-field response of a superconductor [108], according to

$$\kappa \equiv \frac{\lambda}{\xi} \quad \begin{cases} < \frac{1}{\sqrt{2}}, & \text{type-I superconductors} \\ > \frac{1}{\sqrt{2}}, & \text{type-II superconductors,} \end{cases} \tag{4.49}$$

where type-I (type-II) superconductors have a positive (negative) interface energy, making normal-superconducting interfaces energetically unfavorable (favorable). Frequently in this thesis, the ratio $\kappa_0 \equiv \lambda_0/\xi_0$ will be encountered. Figures. 4.2 (a) and (b) show the magnetic field response for a type-I and a type-II superconductor, respectively. As a result of the positive interface energy, type-I superconductors will strive for perfect[1] diamagnetism in the whole superconducting sample, with external fields being expelled exponentially with the distance from the boundary of the superconductor. This effect is referred to as the Meissner effect, and the phase is called the Meissner state, the latter which makes up the superconducting phase diagram until the thermodynamic critical field

$$H_c \propto \frac{\Phi_0}{\xi(T)\lambda(T)}. \tag{4.50}$$

Above this field, superconductivity is lost, and normal conduction ensues (see the phase diagram in Fig. 4.3). Type-II superconductors are in the Meissner state until the external field reaches the first critical field

$$H_{c,1} \propto \frac{\Phi_0}{\lambda^2(T)}. \tag{4.51}$$

Above $H_{c,1}$, Abrikosov vortices start to form. These vortices have a normal core (and thus a normal-superconducting interface), and exist up to the second critical field

$$H_{c,2} \propto \frac{\Phi_0}{\xi^2(T)}, \tag{4.52}$$

at which point superconductivity is lost. Note that this mainly applies for a bulk superconductor, and that the exact values of the critical fields generally

[1]The deviation from perfect diamagnetism is caused by the finite region at the boundary required to establish the diamagnetic supercurrent response.

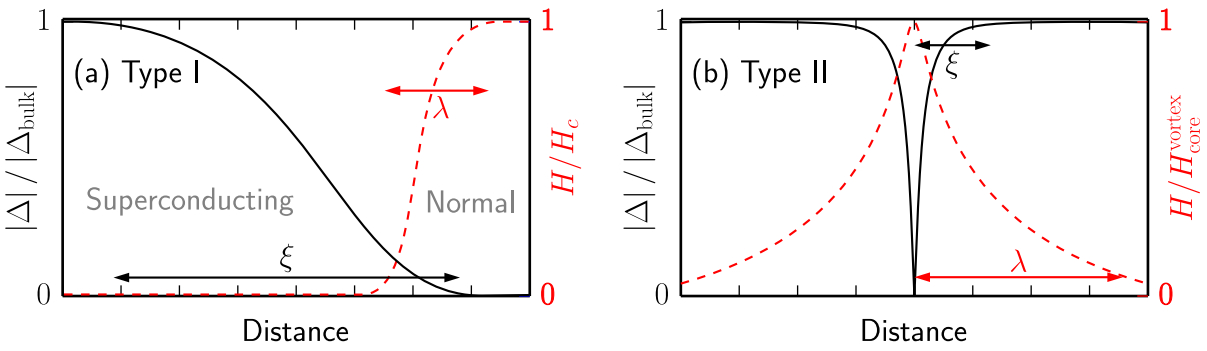

Figure 4.2: *(a) Meissner response at a normal-superconducting interface in a type-I superconductor. (b) Abrikosov vortex in a type-II superconductor. The solid line is the magnitude of the order parameter, and the dashed line the magnetic field.*

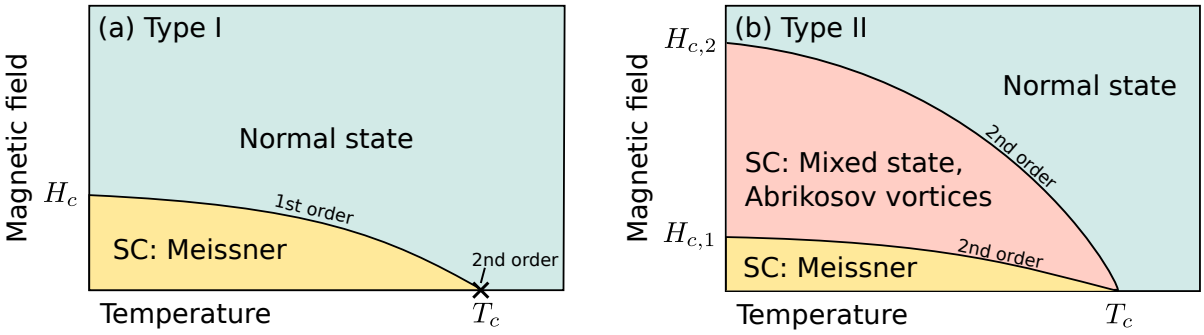

Figure 4.3: *Superconductivity phase diagram under a magnetic field. The order of the phase transition is labeled at each transition. (a) A type-I superconductor is superconducting and in the Meissner state up until the thermodynamic critical field* $H_c \propto \Phi_0/\xi(T)\lambda(T)$*, at which point superconductivity is lost. (b) A type-II superconductor is in the Meissner state up until the first critical field* $H_{c,1} \propto \Phi_0/\lambda^2(T)$*. Between* $H_{c,1}$ *and the second critical field* $H_{c,2} \propto \Phi_0/\xi^2(T)$*, the superconductor is in the mixed state and Abrikosov vortices are present. Above* $H_{c,2}$*, a type-II superconductor becomes normal conducting.*

depends on the geometry (among other things). For example, in a grain of area $\mathcal{A}$, then $H_{c,1}^{\text{grain}} \propto \Phi_0/\mathcal{A}$. Note that this thesis mainly studies unconventional superconductors in the extreme type-II limit, where $\lambda_0 \gg \xi_0$, like in the cuprates (where typically $\kappa_0 \approx 100$). In this limit, the penetration depth effectively drops out of the theory (as will be shown later). In paper I, it is shown that midgap states living on the boundaries of type-II superconductors give rise to a paramagnetic[2] response, and that as a result, the diamagnetic response is moved further into the bulk of the superconductor.

The following section shows how an external magnetic field couples to the superconducting state in quasiclassical theory.

4.3.2 Coupling to the superconducting state: a Doppler shift

There are two main contributions from an external magnetic field: a Lorentz force and a Doppler shift of the off-diagonal self-energies. The Lorentz term will affect electron and hole trajectories differently, and leads to a bending of quasiparticle trajectories. This term is generally beyond the scope of quasiclassical theory, but is fortunately often considered to be negligible [70], and is therefore omitted. In the following, the Doppler shift will be introduced.

Consider the Eilenberger equation (see Sec. 2.3),

$$i\hbar \boldsymbol{v}_F \cdot \boldsymbol{\nabla}_R \hat{g}(\boldsymbol{p}_F, \boldsymbol{R}; z) + \left[z'\hat{\tau}_3 - \hat{\Delta}(\boldsymbol{R}), \hat{g}(\boldsymbol{p}_F, \boldsymbol{R}; z)\right] = 0. \tag{4.53}$$

[2]Paramagnetic is a bit of a misnomer, as the midgap states will give the opposite response as the superfluid momentum: the midgap states will drive a paramagnetic current if the bulk is diamagnetic, while they will drive a diamagnetic current if the bulk is paramagnetic (e.g. the currents surrounding a vortex core).

In the presence of an external magnetic field, the momentum operator is modified in the full microscopic theories (the Gor'kov equations) as shown in Sec. 4.1.1, giving rise to an additional term proportional to the vector potential $\boldsymbol{A}$. This term transforms the same way as the energy

$$z' = z + \frac{e}{c}\boldsymbol{v}_F \cdot \boldsymbol{A}. \tag{4.54}$$

Here, $z = i\epsilon_n = i\pi k_B T_c(2n+1)$ in the case of Matsubara. The vector potential $\boldsymbol{A}$ is the full vector potential from external fields and induced due to currents,

$$\boldsymbol{A} = \boldsymbol{A}_{\text{ext}} + \boldsymbol{A}_{\text{ind}}. \tag{4.55}$$

Maxwell's equations relate $\boldsymbol{A}_{\text{ext}}$ to the external flux density $\boldsymbol{B}_{\text{ext}}$

$$\boldsymbol{B}_{\text{ext}} = \boldsymbol{\nabla} \times \boldsymbol{A}_{\text{ext}}, \tag{4.56}$$

while $\boldsymbol{A}_{\text{ind}}$ (derived in Sec. 4.4) is generated by the current density in the system. This current density is in turn generated by Doppler shifts due to phase gradients and superfluid momenta (as introduced in Sec. 4.2). To write the Eilenberger equation on a dimensionless form, it is divided by the energy $k_B T_c$, yielding

$$\begin{aligned} \frac{z'}{k_B T_c} &= \frac{z}{k_B T_c} + \frac{2\pi\hbar}{h}\frac{e v_F}{c}\frac{1}{k_B T_c}\hat{v}_F \cdot \boldsymbol{A} \\ &= \frac{z}{k_B T_c} - 2\pi^2 \frac{\hat{v}_F \cdot \boldsymbol{A}}{\Phi_0/\xi_0}, \end{aligned} \tag{4.57}$$

where the sign change comes from $e \to -|e|$ (introduced by Φ_0). Thus, there is a non-trivial pre-factor $2\pi^2$ (or π if using the modified coherence length $\zeta_0 \equiv 2\pi\xi_0$). This shift carries over trivially to the Riccati equations. It will now be shown how to calculate $\boldsymbol{A}_{\text{ext}}$ for the two systems in Fig. 4.4.

4.3.3 A superconductor without holes

Assuming a uniform external magnetic field as in Fig. 4.4 (a),

$$\boldsymbol{B}_{\text{ext}} = B_{\text{ext}}\hat{\boldsymbol{z}}, \tag{4.58}$$

where $\hat{\boldsymbol{z}}$ is perpendicular to the superconducting plane, $B_{\text{ext}} = \Phi_{\text{ext}}/\mathcal{A}$ and $\mathcal{A}$ is the area of the superconductor. A possible solution that satisfies Eq. (4.56) is (see for example Ch. 14 of Ref. [109])

$$\boldsymbol{A}_{\text{ext}} = \frac{1}{2}\boldsymbol{B}_{\text{ext}} \times \boldsymbol{\rho}, \tag{4.59}$$

where

$$\boldsymbol{\rho} = x\hat{\boldsymbol{x}} + y\hat{\boldsymbol{y}}, \tag{4.60}$$

$$\rho = \sqrt{x^2 + y^2}. \tag{4.61}$$

Written on a dimensionless form, the vector potential becomes

$$\frac{\boldsymbol{A}_{\text{ext}}}{\Phi_0/\xi_0} = \frac{1}{2}\frac{\boldsymbol{B}_{\text{ext}}}{\Phi_0/\xi_0^2} \times \frac{\boldsymbol{\rho}}{\xi_0} \tag{4.62}$$

$$= \frac{1}{2}\frac{\Phi_{\text{ext}}}{\Phi_0}\left(\frac{\mathcal{A}}{\xi_0^2}\right)^{-1}\left(-\frac{y}{\xi_0}\hat{\boldsymbol{x}} + \frac{x}{\xi_0}\hat{\boldsymbol{y}}\right). \tag{4.63}$$

4.3.4 A superconductor with a hole: a solenoid

Assume again a uniform external magnetic field, but that exists only in a cylinder of radius ρ_a, as in Fig. 4.4 (b), (see for example Ch. 5 of Ref. [110])

$$\boldsymbol{B}_{\text{ext}} = \begin{cases} B_{\text{ext}}\hat{\boldsymbol{z}}, & \rho < \rho_a \\ 0, & \text{otherwise.} \end{cases} \tag{4.64}$$

Assume also that this cylinder lies completely within a hole (of arbitrary shape) in a superconductor. This field gives rise to a vector potential which is non-zero for $\rho \geq \rho_a$. These fields are possible to realize by putting a solenoid in a hole of a (super)conductor. This system is for example considered to prove the famous Ahranov-Bohm effect (see for example Ch. 2.7 in Sakurai [107]), which was paramount in recognizing the physical importance of the vector potential $\boldsymbol{A}$ and the scalar potential ϕ as more than just mathematical supplements to $\boldsymbol{B}$ and $\boldsymbol{E}$, where $\boldsymbol{E}$ is the electric field.

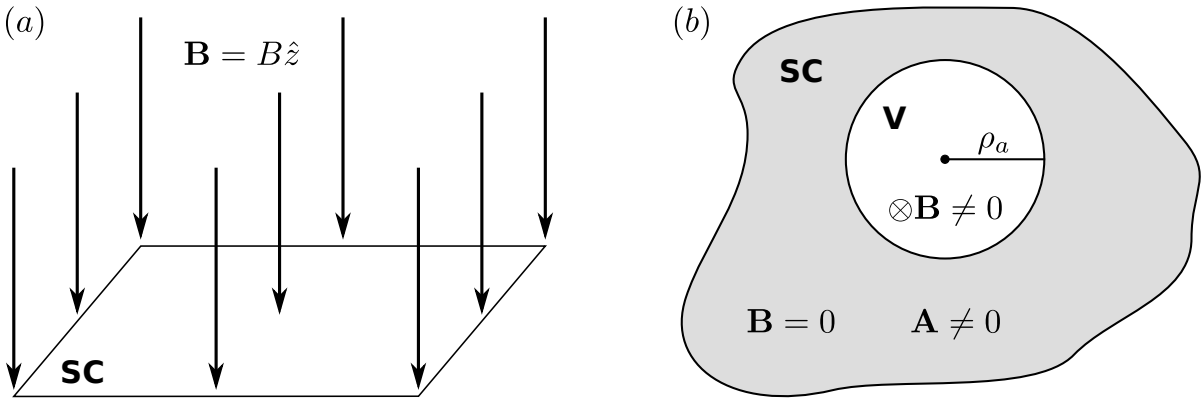

Figure 4.4: *Uniform magnetic flux penetrating (a) a homogeneous superconductor, and (b) a hole in a superconductor. In both cases, the superconductor lies in the xy-plane at $z = 0$. The vector $\hat{\boldsymbol{z}}$ points (a) down along the page, (b) into the page.*

Consider a circular path C of radius $\rho > \rho_a$ that lies in the superconducting region. Using Maxwell's equations and Stokes' theorem, it is found that

$$\oint_C \boldsymbol{A}_{\text{ext}} \cdot d\boldsymbol{l} = \int (\boldsymbol{\nabla} \times \boldsymbol{A}_{\text{ext}}) \cdot d\boldsymbol{S} = \int \boldsymbol{B}_{\text{ext}} \cdot d\boldsymbol{S} = \Phi_{\text{ext}}. \tag{4.65}$$

The line element is $d\boldsymbol{l} = \rho d\phi \hat{\boldsymbol{\phi}}$, and the first integral can be written

$$\begin{aligned} \oint_C \boldsymbol{A}_{\text{ext}} \cdot d\boldsymbol{l} &= \int_0^{2\pi} d\phi \boldsymbol{A}_{\text{ext}} \cdot \hat{\boldsymbol{\phi}} \rho \\ &= A_{\text{ext},\phi} 2\pi\rho. \end{aligned} \tag{4.66}$$

The surface element is $d\boldsymbol{S} = \hat{\boldsymbol{z}} \rho d\rho d\phi$, and the integral over $\boldsymbol{B}_{\text{ext}}$ becomes

$$\begin{aligned} \int \boldsymbol{B}_{\text{ext}} \cdot d\boldsymbol{S} &= \int_0^{\rho_a} d\rho \int_0^{2\pi} d\phi B_{\text{ext}} \rho \\ &= 2\pi B_{\text{ext}} \int_0^{\rho_a} d\rho \rho \\ &= B_{\text{ext}} \pi \rho_a^2. \end{aligned} \tag{4.67}$$

Combining the results, the vector potential is

$$\boldsymbol{A}_{\text{ext}} = \frac{B_{\text{ext}} \rho_a^2}{2\rho} \hat{\boldsymbol{\phi}}, \tag{4.68}$$

where

$$B_{\text{ext}} = \Phi_{\text{ext}} / \pi \rho_a^2, \tag{4.69}$$

$$\hat{\boldsymbol{\phi}} = -\sin(\phi)\hat{\boldsymbol{x}} + \cos(\phi)\hat{\boldsymbol{y}} = -y\hat{\boldsymbol{x}} + x\hat{\boldsymbol{y}}. \tag{4.70}$$

Finally, the vector potential can then be written on a dimensionless form as

$$\frac{\boldsymbol{A}_{\text{ext}}}{\Phi_0/\xi_0} = \frac{1}{2\pi} \left(\frac{\rho}{\xi_0} \right)^{-1} \frac{\Phi_{\text{ext}}}{\Phi_0} \hat{\boldsymbol{\phi}} \tag{4.71}$$

$$= \frac{1}{2\pi} \frac{\Phi_{\text{ext}}}{\Phi_0} \frac{-y\hat{\boldsymbol{x}} + x\hat{\boldsymbol{y}}}{x^2 + y^2} \xi_0. \tag{4.72}$$

4.4 Internally induced flux due to currents

In this section, the vector potential ($\boldsymbol{A}_{\text{ind}}$) induced by internal currents ($\boldsymbol{j}$) in a superconductor is derived. In principle, the vector potential has to be solved self-consistently together with the Green functions and the order parameter, as it couples back to the self-energy, according to Eqs. (4.53)–(4.55). It will be shown however that this back-coupling scales with $(\lambda_0/\xi_0)^{-2}$, which is an extremely small quantity for most unconventional superconductors, and therefore has a negligible influence. This has been verified for a variety of different systems, and seems to hold in most cases. Therefore, this backcoupling is ignored when obtaining the results in this thesis and in the appended papers. The following calculations are still important however, as they are used to obtain the induced magnetic flux density $\boldsymbol{B}_{\text{ind}}$, which is one of the main observables in the results. As a side note, the backcoupling seems to become non-negligible when applying strong external fields in the mixed state, and when $\lambda_0 \to \xi_0$.

4.4.1 Analytic solution and Poisson's equation

The current density $\boldsymbol{j}$ (introduced in Sec. 4.2) that is induced in the superconductor in turn gives rise to an induced magnetic flux density $\boldsymbol{B}_{\text{ind}}$ and a vector potential $\boldsymbol{A}_{\text{ind}}$. Ampère's circuit law and Maxwell's equations give that

$$\begin{aligned} \frac{4\pi}{c}\boldsymbol{j} &= \boldsymbol{\nabla} \times \boldsymbol{B}_{\text{ind}} \\ &= \boldsymbol{\nabla} \times \boldsymbol{\nabla} \times \boldsymbol{A}_{\text{ind}} \\ &= \boldsymbol{\nabla}\left(\boldsymbol{\nabla} \cdot \boldsymbol{A}_{\text{ind}}\right) - \boldsymbol{\nabla}^2 \boldsymbol{A}_{\text{ind}} \\ &= -\boldsymbol{\nabla}^2 \boldsymbol{A}_{\text{ind}}, \end{aligned} \tag{4.73}$$

where the last equality is obtained by assuming the Coulomb gauge (also known as the London gauge)

$$\boldsymbol{\nabla} \cdot \boldsymbol{A}_{\text{ind}} = 0. \tag{4.74}$$

Dividing Eq. (4.73) with the depairing current $j_d = 4\pi k_B T_c |e| N_F v_F$ from Sec. 4.2 and collecting terms on the right-hand side yields

$$\frac{\boldsymbol{j}}{j_d} = -\left(\xi_0 \boldsymbol{\nabla}\right)^2 \frac{\boldsymbol{A}_{\text{ind}}}{\Phi_0/\xi_0} \frac{1}{\xi_0^2} \left(\frac{\Phi_0}{\xi_0} \frac{c}{4\pi} \frac{1}{j_d}\right). \tag{4.75}$$

The last term can be rewritten as

$$\begin{aligned} \frac{\Phi_0}{\xi_0} \frac{c}{4\pi} \frac{1}{j_d} &= \frac{hc}{2|e|} \frac{4\pi k_B T_c}{\hbar v_F} \frac{c}{4\pi} \frac{1}{2\pi k_B T_c |e| N_F v_F} \\ &= \frac{\pi}{2} \frac{c^2}{4\pi e^2 N_F v_F^2}. \end{aligned} \tag{4.76}$$

Introducing the zero-temperature penetration depth

$$\lambda_0^2 \equiv \frac{c^2}{4\pi e^2 N_F v_F^2}, \tag{4.77}$$

makes it possible to rewrite Eq. (4.73) on a dimensionless form as

$$(\xi_0 \boldsymbol{\nabla})^2 \frac{\boldsymbol{A}_{\text{ind}}}{\Phi_0/\xi_0} = -2\frac{\kappa_0^{-2}}{\pi}\frac{\boldsymbol{j}}{j_d} \tag{4.78}$$

where $\kappa_0 \equiv \lambda_0/\xi_0$ is the Ginzburg-Landau parameter, as introduced in Sec. 4.3.1.

Taking a closer look at Eq. (4.78), it is seen that it is a Poisson equation of the form

$$\nabla^2 \phi(\boldsymbol{x}) = f(\boldsymbol{x}), \tag{4.79}$$

which can be solved by introducing the Green function (kernel) G_n of the Laplace operator $\triangle \equiv \nabla^2$ in n dimensions,

$$\nabla^2 G_n(\boldsymbol{x}, \boldsymbol{x}') = \delta^n(\boldsymbol{x}, \boldsymbol{x}'). \tag{4.80}$$

Assuming that it is allowed to differentiate under the integral sign,

$$\phi(\boldsymbol{x}) = \int d^2\boldsymbol{x}' G_n(\boldsymbol{x}, \boldsymbol{x}') f(\boldsymbol{x}'). \tag{4.81}$$

In two dimensions (like the grains considered in this thesis and the appended papers), the Green function G_2 is known to be

$$G_2(\boldsymbol{x}, \boldsymbol{x}') = -\frac{1}{2\pi} \ln |\boldsymbol{x} - \boldsymbol{x}'| . \tag{4.82}$$

With this, the induced vector potential due to the current density is found to be

$$\frac{\boldsymbol{A}_{\text{ind}}(\boldsymbol{x})}{\Phi_0/\xi_0} = \frac{\kappa_0^{-2}}{\pi^2} \int \frac{d^2\boldsymbol{x}'}{\xi_0^2} \frac{\boldsymbol{j}(\boldsymbol{x}')}{j_d} \ln \left| \frac{\boldsymbol{x} - \boldsymbol{x}'}{\xi_0} \right|, \tag{4.83}$$

where the factor ξ_0^{-2} under the integral sign comes from the factor $(\xi_0 \boldsymbol{\nabla})^2$. The induced magnetic flux density can then be obtained through Maxwell's equations

$$\boldsymbol{B}_{\text{ind}} = \boldsymbol{\nabla} \times \boldsymbol{A}_{\text{ind}}. \tag{4.84}$$

Thus, it is seen that the vector potential and the flux density due to currents scales with κ_0^{-2}, which is an extremely small quantity for most unconventional superconductors.

Equation (4.83) will now be considered in a discrete geometry. The reason why the discretized form is not just written down immediately is that there is an additional, non-trivial, term which comes from the singular point in the integrand.

4.4.2 Analytic solution in a discretized lattice

Consider a discrete lattice in two dimensions, as introduced in Sec. (3.1), with lattice spacing h. Let

$$\begin{aligned} \boldsymbol{x} &= (x, y), && (4.85)\\ \boldsymbol{x}' &= (x', y') = (x_i, y_i). && (4.86) \end{aligned}$$

Assuming that $\boldsymbol{j}$ is piecewise constant in each lattice cell, the integral in Eq. (4.83) can be written as a sum

$$\frac{\boldsymbol{A}_{\mathrm{ind}}(x,y)}{\Phi_0/\xi_0} = \frac{\kappa_0^{-2}}{\pi^2}\frac{h^2}{\xi_0^2}\sum_{x_i}\sum_{y_i}\frac{\boldsymbol{j}(x_i,y_i)}{j_d}\ln\frac{1}{\xi_0}\sqrt{(x-x_i)^2+(y-y_i)^2}. \tag{4.87}$$

The summand is singular in the point $(x, y) = (x_i, y_i)$, however. This point is treated separately by integrating over the lattice cell S'

$$S' = \left\{(x',y') : x' \in \left[x-\frac{h}{2}, x+\frac{h}{2}\right], \quad y' \in \left[y-\frac{h}{2}, y+\frac{h}{2}\right]\right\}. \tag{4.88}$$

Denote this integral (i.e. the point $(x = x_i, y = y_i)$ of the sum) as I

$$\begin{aligned} I &= \frac{1}{\xi_0^2}\int_{x-\frac{h}{2}}^{x+\frac{h}{2}} dx' \int_{y-\frac{h}{2}}^{y+\frac{h}{2}} dy' \frac{\boldsymbol{j}(x',y')}{j_d}\ln\frac{1}{\xi_0}\sqrt{(x-x')^2+(y-y')^2}\\ &= \left\{\begin{array}{rcl} \alpha &=& x-x' \\ \beta &=& y-y' \end{array}\right\}\\ &= \frac{\boldsymbol{j}(x,y)}{j_d}\frac{1}{\xi_0^2}\int_{-\frac{h}{2}}^{\frac{h}{2}} d\alpha \int_{-\frac{h}{2}}^{\frac{h}{2}} d\beta \ln\frac{1}{\xi_0}\sqrt{\alpha^2+\beta^2}\\ &= \frac{\boldsymbol{j}(x,y)}{j_d}\frac{h^2}{4\xi_0^2}\left(\pi - 6 + 2\ln\frac{h^2}{2\xi_0^2}\right). \end{aligned} \tag{4.89}$$

Combining the results, the induced vector potential in the discretized lattice is

$$\begin{aligned} \frac{\boldsymbol{A}_{\mathrm{ind}}(x,y)}{\Phi_0/\xi_0} &= \frac{\kappa_0^{-2}}{\pi^2}\left[\frac{\boldsymbol{j}(x,y)}{j_d}\frac{h^2}{4\xi_0^2}\left(\pi - 6 + 2\ln\frac{h^2}{2\xi_0^2}\right) + \right.\\ &\qquad \left. \frac{h^2}{\xi_0^2}\sum_{x\neq x_i}\sum_{y\neq y_i}\frac{\boldsymbol{j}(x_i,y_i)}{j_d}\ln\frac{1}{\xi_0}\sqrt{(x-x_i)^2+(y-y_i)^2}\right]. \end{aligned} \tag{4.90}$$

5 Thermodynamics

This chapter introduces a few important thermodynamic quantities, most notably the free energy[1] (F), the internal energy (U), the entropy (S) and the heat capacity (C). The goal is to show the procedure for calculating these thermodynamic quantities. In this work, the free energy is obtained from a microscopically derived free-energy functional. Using thermodynamic identities, the entropy and heat capacity are obtained as temperature derivatives of this free energy.

Together, these observables will be used in the thesis and in Paper I to study phases and phase transitions. In particular, the free energy indicates which phase is energetically more favorable. The entropy and heat capacity, defined as the first and second derivative of the free energy with respect to temperature, respectively, together indicates the order of a phase transition. This is because the order of a phase transition is defined as the order of the derivative which is discontinuous, according to Ehrenfest's classification. For example, the normal to superconducting phase transition is a second-order phase transition in temperature with a discontinuous heat capacity, and consequently no latent heat[2]. The resulting jump in the heat capacity (ΔC_{NS}) at the transition temperature (T_c) will be derived for both an s-wave and a d-wave bulk superconductor. Furthermore, the heat capacity is of particular interest as it is a commonly measured quantity in experiment. Therefore, it will be shown how the calculated heat capacity can be expressed in units of ΔC_{NS}.

[1]Here, F is the Helmholtz free energy in the absence of external magnetic fields, and the Gibbs free energy in the presence of external magnetic fields.

[2]For Type-I superconductors, this is only true in the absence of external magnetic fields. In the presence of such fields, the normal-superconducting transition is of first order, with an associated latent heat. For Type-II superconductors, the phase transition is of second order both when entering the Meissner state and the mixed state.

5.1 The free-energy functional

The goal of this section is to introduce two different equations used to calculate the free energy difference between the superconducting state and the normal state, through quasiclassical Green functions and self energies. The starting point is a general expression of the free energy, Ω, in terms of the grand partition function $\mathcal{Z}$. This expression can be manipulated into a Dyson equation, generating an expansion in interaction terms and hence energy. The quasiclassical approximation considers only the low-energy contributions, and absorbs high-energy corrections into terms that are either discarded or taken phenomenologically from experiment. This section is based on the lecture notes of Ref. [111]. The full derivation is beyond the scope of this thesis, but can be found in for example Refs.[69, 98, 112–114] and references therein. Note that Ω is also known in the literature as the grand potential, the thermodynamic potential, the Landau free energy, and the Landau potential, depending on which system is considered.

The free energy Ω depends on the chemical potential μ, volume $\mathcal{V}$ and temperature T, and is defined as

$$\Omega(\mu, \mathcal{V}, T) \equiv F - \mu N = U - TS - \mu N, \tag{5.1}$$

where F is the Helmholtz free energy, N the particle number, U the internal energy and S the entropy. An expression of Ω in terms of the grand partition function can be derived as

$$\Omega = -k_B T \ln(\mathcal{Z}), \tag{5.2}$$

where k_B is the Boltzmann constant. The grand partition function can be expressed in terms of expectational values with respect to Fock states

$$\mathcal{Z} = \sum_{E,N} e^{-\beta \langle E,N|H_0 - \mu\mathcal{N}|E,N\rangle}, \tag{5.3}$$

where $\mathcal{N}$ is the particle number operator, H_0 is the non-interacting Hamiltonian and E is the energy of the state. Considering an interacting Hamiltonian H_{int}, the free energy can be rewritten as

$$\Omega = -k_B T \langle e^{-\int_0^\beta d\tau H_{\text{int}}(\tau)} \rangle, \tag{5.4}$$

where τ is the imaginary energy $\tau \equiv i\epsilon$. This expression can be expanded diagrammatically in the energy close to the Fermi surface, but there is generally no nice way to sum these terms up as in the Dyson equation. An expression for the expansion was provided by Luttinger and Ward for normal state fermions [112], which was later generalized to superfluid systems by De Dominicis and Martin [113, 114], and to strongly correlated fermion superfluids by Serene and Rainer [69]. The expression supplied by Luttinger and Ward will now be presented, which will be used to estimate the free energy in bulk at zero temperature. This

is followed by a simplified "educated guess" by Eilenberger [82], which is the free energy functional which is used in this thesis. Subsequently, before studying the entropy and the heat capacity, the magnetic energy density is derived.

5.1.1 The Luttinger-Ward free-energy functional

Following Luttinger and Ward, the free energy functional can be expressed as

$$\Omega(\hat{G},\hat{\Sigma},\hat{V}) = -\mathrm{Tr}\left[\hat{\Sigma}\hat{G} + \ln\left(-\hat{G}_0^{-1} + \hat{V} + \hat{\Sigma}\right)\right] + \Phi\left[\hat{G}\right], \tag{5.5}$$

where *hat* denote a 2×2 matrix in Nambu space, $\hat{G}$ is the Green function, $\hat{V}$ is the interaction term and $\Phi[\hat{G}]$ is the "Φ-functional", which is connected with the self-energy functional $\hat{\Sigma}[\hat{G}]$ via

$$\delta\Phi[\hat{G}] = \mathrm{Tr}[\hat{\Sigma}\delta\hat{G}]. \tag{5.6}$$

The product between two of these Nambu matrices are understood as the Nambu-matrix product together with folding products in the $\boldsymbol{R}-\boldsymbol{p}$ variables. The operator Tr means

$$\mathrm{Tr}\left[\circ\right] = k_B T \sum_{|\epsilon_n|\leq\epsilon_c} \int \frac{d^3p}{(2\pi)^3} \int d^3R\ \mathrm{tr}_2\left[\circ\right]. \tag{5.7}$$

The momentum integral over p can here be replaced by a ξ-integration

$$\int \frac{d^3p}{(2\pi)^3}[\circ] \to \int N(\xi)d\xi\langle\circ\rangle_{F\xi} \sim N_F \int d\xi\langle\circ\rangle_{F\xi}, \tag{5.8}$$

where $\langle\circ\rangle_{F\xi}$ denotes the proper average in p-space over the surface, $\xi \equiv const$, and it is assumed that the density of states N is constant in a thin shell around the Fermi surface. N_F is the normal state density of states at the Fermi surface. The relation in Eq. (5.6) implies that Ω is stationary under variation of $\hat{G}$ with $\hat{\Sigma}$ and $\hat{V}$ constant. Additionally, Ω is also stationary with respect to variations of $\hat{\Sigma}$, yielding the Dyson equation

$$\hat{G} = \left(\hat{G}_0^{-1} - \hat{\Sigma} - \hat{V}\right)^{-1}. \tag{5.9}$$

This equations generates the Eilenberger equation in the quasiclassical approximation. The free energy difference between the superconducting state and the normal state (N) can be written as

$$\begin{aligned}\delta\Omega[\hat{G},\hat{\Sigma}] &= \Omega\left[\hat{G},\hat{\Sigma}\right] - \Omega_N\left[\hat{G},\hat{\Sigma}\right] \\ &= -\mathrm{Tr}\left[\hat{\Sigma}\hat{G} - \hat{\Sigma}_N\hat{G}_N + \ln\left(-\hat{G}_0^{-1} + \hat{V} + \hat{\Sigma}\right) - \ln\left(-\hat{G}_0^{-1} + \hat{V} + \hat{\Sigma}_N\right)\right] \\ &\quad + \Phi\left[\hat{G}\right] - \Phi\left[\hat{G}_N\right],\end{aligned} \tag{5.10}$$

where the same external interactions and temperature is assumed. Applying the quasiclassical approximation, the Luttinger-Ward free-energy functional is given by

$$\delta\Omega(T) = \int d\boldsymbol{R}\left\{\frac{\boldsymbol{B}_{\text{ind}}^2(\boldsymbol{R})}{8\pi} + N_F k_B T \frac{1}{2}\int_0^1 d\lambda \int \frac{d\Omega_{\boldsymbol{p}_F}}{4\pi}\sum_{\epsilon_n} \text{Tr}\left[\hat{\Delta}(\hat{g}_\lambda - \frac{1}{2}\hat{g})\right]\right\}, \quad (5.11)$$

where $\Omega_{\boldsymbol{p}_F}$ is the angle of the momentum $\boldsymbol{p}_F$ on the Fermi surface relative to the crystal a-axis, $\hat{g}_\lambda$ is the solution to the Eilenberger equation with the substitution $\hat{\Delta} \to \hat{\Delta}\lambda$, with λ being a "dummy variable". For a cylindrically symmetric Fermi surface in $2D$, $\int d\Omega_{\boldsymbol{p}_F}/4\pi = \int_0^{2\pi} d\theta_{\boldsymbol{p}_F}/2\pi$, where $\theta_{\boldsymbol{p}_F}$ is the corresponding angle in the crystal ab-plane. The first term in Eq. (5.11) is the magnetic energy density due to magnetic fields induced in the system (to be derived in Sec. 5.1.4). A dimensionless expression will now be derived for the free energy, by dividing it with $\mathcal{V}N_F(k_BT_c)^2$, where $\mathcal{V}$ is volume of the sample (replaced by the area $\mathcal{A}$ in 2D). Doing so leads to non-trivial scaling factors for the magnetic energy density, which are rarely written out in the literature. These scaling factors are found to be

$$\begin{aligned}
\frac{\boldsymbol{B}_{\text{ind}}^2}{8\pi N_F(k_BT_c)^2} &= \left(\frac{\boldsymbol{B}_{\text{ind}}}{\Phi_0/\xi_0^2}\right)^2 \frac{1}{\xi_0^2}\frac{\Phi_0^2}{\xi_0^2}\frac{1}{8\pi}\frac{1}{N_F(k_BT_c)^2} \\
&= \left(\frac{\boldsymbol{B}_{\text{ind}}}{\Phi_0/\xi_0^2}\right)^2 \frac{1}{\xi_0^2}\left(\frac{hc}{2e}\right)^2\left(\frac{2\pi k_BT_c}{\hbar v_F}\right)^2\frac{1}{8\pi}\frac{1}{N_F(k_BT_c)^2} \\
&= \left(\frac{\boldsymbol{B}_{\text{ind}}}{\Phi_0/\xi_0^2}\right)^2 2\pi^4\kappa_0^2, \qquad (5.12)
\end{aligned}$$

where $\kappa_0 \equiv \lambda_0/\xi_0$ is the dimensionless Ginzburg-Landau parameter ($\kappa_0 \approx 100$ for YBCO, introduced in Sec. 4.4.1). Note that $\boldsymbol{B}_{\text{ind}}^2 \propto \kappa_0^{-4}$ (as shown in Sec. 4.4.1), such that the term is small for the superconductors considered in this work. Finally, the Luttinger-Ward free energy can be written on a dimensionless form

$$\begin{aligned}
\frac{\delta\Omega(T)}{\mathcal{V}N_F(k_BT_c)^2} &= \int\frac{d\boldsymbol{R}}{\mathcal{V}}\left\{\left(\frac{\boldsymbol{B}_{\text{ind}}(\boldsymbol{R})}{\Phi_0/\xi_0^2}\right)^2 2\pi^4\kappa_0^2\right. \\
&\quad \left. + \frac{1}{2}\frac{T}{T_c}\int_0^1 d\lambda\int_0^{2\pi}\frac{d\theta_{\boldsymbol{p}_F}}{2\pi}\sum_{\epsilon_n}\text{Tr}\left[\frac{\hat{\Delta}}{k_BT_c}\left(\hat{g}_\lambda - \frac{1}{2}\hat{g}\right)\right]\right\}. \qquad (5.13)
\end{aligned}$$

5.1.2 Zero-temperature free energy

Consider a bulk superconductor at zero temperature. The trace in Eq. (5.13) simplifies to

$$\text{Tr}\left[\hat{\Delta}\left(\hat{g}_\lambda - \frac{1}{2}\hat{g}\right)\right] = 4\pi|\Delta|^2\left(\frac{1}{2\sqrt{|\Delta|^2 - \epsilon^2}} - \frac{\lambda}{\sqrt{|\Delta|^2\lambda^2 - \epsilon^2}}\right), \qquad (5.14)$$

where $\epsilon = i\epsilon_n = i2\pi k_B T(n + \frac{1}{2})$ for Matsubara and $\Delta = \Delta_\nu \eta_\nu(\theta_{\boldsymbol{p}_F})$ with ν being the basis function. At zero temperature,

$$\Delta\epsilon_n = 2\pi k_B T \xrightarrow[T\to 0]{} 0, \tag{5.15}$$

$$\epsilon_n \xrightarrow[T\to 0]{} x, \tag{5.16}$$

$$2\pi k_B T \sum_{|\epsilon_n|<\epsilon_c} \xrightarrow[T\to 0]{} \int_{-\epsilon_c}^{\epsilon_c} dx. \tag{5.17}$$

Letting $\epsilon_c \to \infty$, the free energy becomes

$$\begin{aligned}
\frac{\delta\Omega(T\to 0)}{\mathcal{V}N_F} &= \frac{1}{2}\int_0^1 d\lambda \frac{1}{2\pi}\int_{-\infty}^{\infty} dx \int_0^{2\pi} \frac{d\theta_{\boldsymbol{p}_F}}{2\pi} 4\pi|\Delta|^2 \left(\frac{1}{2\sqrt{|\Delta|^2+x^2}} - \frac{\lambda}{\sqrt{|\Delta|^2\lambda^2+x^2}}\right) \\
&= \int_{-\infty}^{\infty}\int_0^{2\pi} \frac{d\theta_{\boldsymbol{p}_F}}{2\pi}\left(\frac{|\Delta|^2}{2\sqrt{|\Delta|^2+x^2}} - \sqrt{|\Delta|^2+x^2} + |x|\right) \\
&= -\frac{1}{2}\int_0^{2\pi}\frac{d\theta_{\boldsymbol{p}_F}}{2\pi}|\Delta|^2 \\
&= -\frac{|\Delta_\nu|^2}{2}\int_0^{2\pi}\frac{d\theta_{\boldsymbol{p}_F}}{2\pi}|\eta_\nu(\theta_{\boldsymbol{p}_F})|^2.
\end{aligned} \tag{5.18}$$

For any basis function normalized as $\int_0^{2\pi} d\theta_{\boldsymbol{p}_F}|\eta_\nu(\theta_{\boldsymbol{p}_F})|^2/2\pi = 1$, the zero-temperature free energy becomes

$$\frac{\delta\Omega(T=0)}{\mathcal{V}N_F(k_BT_c)^2} = -\frac{1}{2}\frac{|\Delta_0|^2}{(k_BT_c)^2}, \tag{5.19}$$

where Δ_0 is the zero-temperature gap given by Eqs. (D.52) and (D.53) on p. 177. Inserting the numeric values of the gap,

$$\delta\Omega(T=0) \approx -2\mathcal{V}N_F(k_BT_c)^2. \tag{5.20}$$

These result are valid for s-, d- and unitary p-wave superconductors.

5.1.3 The Eilenberger free-energy functional

In the original paper introducing the Eilenberger equations [82], the following guess was made for the free-energy functional in Eq. (5.10)

$$\begin{aligned}
\delta\Omega(T) &= \int d\boldsymbol{R}\Bigg\{\frac{\boldsymbol{B}^2_{\text{ind}}(\boldsymbol{R})}{8\pi} + |\Delta(\boldsymbol{R})|^2 N_F \ln\frac{T}{T_c} \\
&\qquad + 2\pi N_F k_B T\sum_{\epsilon_n}\left[\frac{|\Delta(\boldsymbol{R})|^2}{\epsilon_n} + i\mathcal{I}(\boldsymbol{R};\epsilon_n)\right]\Bigg\},
\end{aligned} \tag{5.21}$$

$$\mathcal{I}(\boldsymbol{R};\epsilon_n) = \int\frac{d\theta_{\boldsymbol{p}_F}}{2\pi}\left[\tilde{\Delta}(\boldsymbol{p}_F,\boldsymbol{R})\gamma(\boldsymbol{p}_F,\boldsymbol{R};\epsilon_n) - \Delta(\boldsymbol{p}_F,\boldsymbol{R})\tilde{\gamma}(\boldsymbol{p}_F,\boldsymbol{R};\epsilon_n)\right]. \tag{5.22}$$

This form of the free energy is simpler to calculate than the Luttinger-Ward free energy, and is therefore used in this thesis and in the appended papers. It has been verified that this form of the free energy gives the same results as the Luttinger-Ward functional, for the loop-current phase studied in this thesis. Equivalent to the last section, dividing Eq. (5.21) with $\mathcal{V}N_F(k_BT_c)^2$ yields a dimensionless form of the Eilenberger free energy

$$\frac{\delta\Omega(T)}{\mathcal{V}N_F(k_BT_c)^2} = \int \frac{d\boldsymbol{R}}{\mathcal{V}}\Bigg\{ \left(\frac{\boldsymbol{B}_{\text{ind}}(\boldsymbol{R})}{\Phi_0/\xi_0^2}\right)^2 2\pi^4\kappa_0^2 + \frac{|\Delta(\boldsymbol{R})|^2}{(k_BT_c)^2}\ln\frac{T}{T_c} + 2\pi\frac{T}{T_c}\sum_{\epsilon_n}\left[\frac{|\Delta(\boldsymbol{R})|^2}{(k_BT_c)^2}\frac{k_BT_c}{\epsilon_n} + \frac{i\mathcal{I}(\boldsymbol{R};\epsilon_n)}{k_BT_c}\right]\Bigg\}. \tag{5.23}$$

5.1.4 The magnetic energy density

The term $\boldsymbol{B}^2_{\text{ind}}(\boldsymbol{R})/8\pi$ represents the magnetic energy density, which is the energy stored in the induced magnetic field (i.e. the work required to establish it). In the results and Paper I, this term is only evaluated in the superconducting plane ($z = 0$). In principle, however, there is magnetic flux outside the plane ($z \neq 0$), which contributes to this energy (although decreasing non-linearly with increazed z). The main reasons for not calculating this term for $z \neq 0$ is that

(a) the term is already vanishingly small (as is shown in the results in Sec. 7.1, Fig. 7.3), which is why it is often neglected in the literature,

(b) the external field and its response is translationally invariant along z (apart from possible fringe effects at surfaces),

(c) in a bulk system or a layered system (like the cuprates), the flux and vortices are often translationally invariant in z (flux tubes), and each layer (pancake) represents the system as a whole.

The calculated energy is therefore the average magnetic energy density of a pancake. Still, it might be of some interest to in the future extend the calculations to account for contributions from $z \neq 0$. Note that no energy exchange is assumed with any eventual external field (adiabacity).

The term $\boldsymbol{B}^2_{\text{ind}}(\boldsymbol{R})/8\pi$ will now be derived, closely following Ch. 5.16 of Jackson [115]. The calculations will initially be in SI units, but the results will later be converted into CGS units. Imagine a system with a steady-state current $\boldsymbol{J}$, where the current was switched on adiabatically such that $\boldsymbol{\nabla}\cdot\boldsymbol{J} = 0$ holds. The latter makes it possible to decompose the current distribution into current loops. Let $\Delta\sigma$, S, $\hat{n}$, C, be the cross-sectional area, the path, the enclosed surface and the surface normal, respectively, of a typical current loop. The Δ denotes that a single infinitesimal circuit loop is considered. The increase in work (against

the induced electromotive force), δW, in a loop can be written in terms of the magnetic flux density through the loop $\delta \boldsymbol{B}$

$$\Delta(\delta W) = J\Delta\sigma \int_S \hat{n} \cdot \delta \boldsymbol{B} dr, \tag{5.24}$$

where dr is an infinitesimal surface element, and the integral expresses the magnetic induction through the loop. Using Maxwell's equations and Stokes's theorem, Eq. (5.24) can be rewritten as

$$\begin{aligned} \Delta(\delta W) &= J\Delta\sigma \int_S \hat{n} \cdot (\boldsymbol{\nabla} \times \delta \boldsymbol{A}) dr \\ &= J\Delta\sigma \oint_C \delta \boldsymbol{A} \cdot d\boldsymbol{l}, \end{aligned} \tag{5.25}$$

where $d\boldsymbol{l}$ is an infinitesimal vector parallel to $\boldsymbol{J}$, which means that

$$J\Delta\sigma d\boldsymbol{l} = \boldsymbol{J} dR = \boldsymbol{\nabla} \times \boldsymbol{H} dR, \tag{5.26}$$

with dR being an infinitesimal volume element. The last step of Eq. (5.26) follows from Ampère's circuit law. Thus, the total incremental work done due to the incremental change $\delta \boldsymbol{A}$ is

$$\begin{aligned} \delta W &= \int \delta \boldsymbol{A} \cdot (\boldsymbol{\nabla} \times \boldsymbol{H}) dR \\ &= \int \left(\boldsymbol{H} \cdot (\boldsymbol{\nabla} \times \delta \boldsymbol{A}) + \boldsymbol{\nabla} \cdot (\boldsymbol{H} \times \delta \boldsymbol{A}) \right) dR \\ &= \int \boldsymbol{H} \cdot \delta \boldsymbol{B} dR + \int \boldsymbol{\nabla} \cdot (\boldsymbol{H} \times \delta \boldsymbol{A}) dR, \end{aligned} \tag{5.27}$$

where Maxwell's equations have been used, along with the vector identity

$$\boldsymbol{\nabla} \cdot (\boldsymbol{A} \times \boldsymbol{B}) = \boldsymbol{B} \cdot (\boldsymbol{\nabla} \times \boldsymbol{A}) - \boldsymbol{A} \cdot (\boldsymbol{\nabla} \times \boldsymbol{B}). \tag{5.28}$$

For a localized field distribution, the second integral in Eq. (5.27) vanishes. For systems where there exists a linear relation between the magnetic field $\boldsymbol{H}$ and the magnetic flux $\boldsymbol{B}$ (e.g. paramagnetic and diamagnetic media),

$$\boldsymbol{H} \cdot \delta \boldsymbol{B} = \frac{1}{2} \delta(\boldsymbol{H} \cdot \boldsymbol{B}) = \frac{\delta \boldsymbol{B}^2}{2\mu}, \tag{5.29}$$

where μ is the magnetic permeability. Summing over all infinitesimal changes up to the full magnetic field and flux, the total work required (i.e. the total magnetic energy density) becomes

$$E = \int \frac{\boldsymbol{B}^2}{2\mu} dR. \qquad \text{(SI)} \tag{5.30}$$

Recalling that the units of magnetic flux density and flux is

$$B = \frac{\Phi}{\mathcal{A}} = b\frac{\Phi_0}{\xi_0^2}, \tag{5.31}$$

$$\Phi_0 = \frac{h}{2|e|}, \qquad \text{(SI)} \tag{5.32}$$

$$\Phi_0 = \frac{hc}{2|e|}, \qquad \text{(CGS)} \tag{5.33}$$

and that when going from SI units to Gaussian CGS units $\mu \to 4\pi/c^2$ (see App. A), the magnetic energy density in Eq. (5.30) can be rewritten

$$\begin{aligned} \frac{\boldsymbol{B}^2}{2\mu} &= \left(\frac{\boldsymbol{b}}{\xi_0^2}\frac{h}{2e}\right)^2 \frac{1}{2\mu} && \text{(SI)} \\ &= \left(\frac{\boldsymbol{b}}{\xi_0^2}\frac{h}{2e}\right)^2 \frac{c^2}{8\pi} && \text{(CGS)} \\ &= \frac{\boldsymbol{B}^2}{8\pi}, && \text{(CGS)} \end{aligned} \tag{5.34}$$

which was to be shown.

5.2 Entropy

The statistical expression of the entropy is given by

$$S = -k_B \sum_{\boldsymbol{k},\sigma} \left[(1 - f_{\boldsymbol{k}}) \ln(1 - f_{\boldsymbol{k}}) + f_{\boldsymbol{k}} \ln f_{\boldsymbol{k}} \right], \tag{5.35}$$

where $\boldsymbol{k}$ denotes momentum and σ spin, $f_{\boldsymbol{k}} \equiv f(E_{\boldsymbol{k}}) = (e^{\beta(E_{\boldsymbol{k}}-\mu)} + 1)^{-1}$ is the Fermi-Dirac distribution at momentum $\boldsymbol{k}$, energy (dispersion) $E_{\boldsymbol{k}}$, chemical potential μ, and temperature T. Here, $\beta \equiv 1/k_B T$. The systems considered in this work are spin degenerate, yielding

$$S = -2k_B \sum_{\boldsymbol{k}} \left[(1 - f_{\boldsymbol{k}}) \ln(1 - f_{\boldsymbol{k}}) + f_{\boldsymbol{k}} \ln f_{\boldsymbol{k}} \right]. \tag{5.36}$$

This form of the entropy depends on the excitation spectrum of the system, and will be used for bulk and normal state systems. In this thesis, the thermodynamic definition is used instead to otbain the entropy and heat capacity as derivatives of the free energy functionals in Sec. 5.1. Following for example Ref. [116], the Helmholtz free-energy is defined as

$$F = U - TS, \tag{5.37}$$

where U is the internal energy, T the temperature and S the entropy. Under a differential variation,

$$\partial F = \partial U - S\partial T - T\partial S. \tag{5.38}$$

For reversible processes, the change in heat (Q) is related to a change in entropy

$$\partial Q = T\partial S. \tag{5.39}$$

Additionally, the first law of thermodynamics states that the change in heat is related to the change in work and internal energy

$$\partial Q = \partial R + \partial U, \tag{5.40}$$

where R is the work done per unit volume by the system on the surrounding. Substituting Eq. (5.40) into Eq. (5.39) and re-arranging slightly, yields

$$\partial U = T\partial S - \partial R. \tag{5.41}$$

Substituting Eq. (5.41) into Eq. (5.38) yields

$$\partial F = -\partial R - S\partial T. \tag{5.42}$$

The entropy can then be obtained as the temperature-derivative of the free energy

$$S = -\left(\frac{\partial F}{\partial T}\right)_R. \tag{5.43}$$

In the presence of external magnetic fields, it is more appropriate to use the Gibbs free energy. A similar expression can then be found under the assumption of stationary external fields.

5.3 Heat capacity

The heat capacity is an important and fundamental property of solids, which is typically measured with nanocalometric methods. It is an observable from which a great number of properties can be inferred, for example the transition temperature, the superconducting gap, the penetration depth, the coherence length, and the Fermi velocity [39].

This section starts by stating different kinds of heat capacities, and showing how the heat capacity is calculated from the entropy. Using the statistical expression of the entropy, the heat capacity is then calculated for a normal-state metal and for a bulk superconductor. The low- and high-temperature limit of the latter is examined, and the jump in heat capacity in the normal-superconducting phase transition (ΔC_{NS}) is derived for both an s-wave and a d-wave superconductor in bulk. Finally, ΔC_{NS} is used to form the dimensionless equations for calculating the heat capacity in mesoscopic systems with quasiclassics. Some of these calculations follow Refs. [4, 16, 73, 78, 116]

5.3.1 Different kinds of heat capacities: disambiguation

The heat capacity of a system is defined as the amount of heat Q needed to raise the temperature of the system, per degree temperature increase ΔT [117]

$$C \equiv Q/\Delta T. \tag{5.44}$$

The specific heat capacity (or *specific heat* in short) is the heat capacity per unit substance. Different units are used depending on the circumstance. For example, the volumetric heat capacity is the heat capacity per volume $C/\mathcal{V}$, the molar specific heat is the heat capacity per mole etcetera. In this thesis, the heat capacity for a given superconducting grain will exclusively be calculated, i.e. the grain heat capacity, or just heat capacity in short.

5.3.2 Thermodynamic definition

The second law of thermodynamics states that if an infinitesimal amount of heat δQ is added to a system at temperature T in a reversible manner, then the entropy change is

$$dS = \frac{\delta Q}{T}. \tag{5.45}$$

The definition of heat capacity states that

$$C = \frac{\delta Q}{dT}, \tag{5.46}$$

which means that

$$TdS = CdT, \tag{5.47}$$

and consequently

$$C = T\frac{dS}{dT}. \tag{5.48}$$

This can then be turned into a partial derivative if considering that certain parameters are held constant. In Sec. 5.2, it was shown that the entropy is related to the partial derivative of the Helmholtz free energy (or Gibbs free energy in the presence of external magnetic fields) through

$$S = -\left(\frac{\partial F}{\partial T}\right)_R, \tag{5.49}$$

which then means that the heat capacity at constant volume, for example, can be related to the free energy through

$$C_V = T\left(\frac{\partial S}{\partial T}\right)_V = -T\left(\frac{\partial^2 F}{\partial T^2}\right)_{R,V}. \tag{5.50}$$

5.3.3 Heat capacity in a normal-state metal

The heat capacity of a normal state metal, denoted C_N, has two main contributions C_N^{el} and C_N^{ph} from electrons and phonons, respectively,

$$C_N = C_N^{\mathrm{el}} + C_N^{\mathrm{ph}}. \tag{5.51}$$

The electronic part dominates at lower temperatures, and the phononic at higher temperatures. It is therefore customary to only consider the electronic contribution when studying the normal-superconducting phase transition for conventional low-T_c superconductors, and often also for unconventional high-T_c superconductors. Both the electronic and the phononic heat capacities will now be derived from the respective internal energy.

Electronic heat capacity (normal state)

The electronic heat capacity at constant volume is

$$C_N^{\mathrm{el}} = \left(\frac{\partial U_{n,e}}{\partial T}\right)_V. \tag{5.52}$$

The electronic internal energy $U_{n,e}$ is defined as

$$U_{n,e} = \sum_{\boldsymbol{k},\sigma} \xi_{\boldsymbol{k}} f_{\boldsymbol{k}} = 2\sum_{\boldsymbol{k}} \xi_{\boldsymbol{k}} f_{\boldsymbol{k}}, \tag{5.53}$$

Considering a bulk system in thermodynamic equilibrium, the chemical potential is an arbitrary reference which can be set to zero. By noting that

$$\frac{df_{\boldsymbol{k}}}{dT} = \frac{d}{dT}(e^{\xi_{\boldsymbol{k}}/k_BT}+1)^{-1} = \frac{\xi_{\boldsymbol{k}}}{k_BT^2} f_{\boldsymbol{k}}(1-f_{\boldsymbol{k}}), \tag{5.54}$$

the heat capacity can be written as

$$C_N^{\text{el}} = \frac{2}{k_B T^2} \sum_{\boldsymbol{k}} \xi_{\boldsymbol{k}}^2 f_{\boldsymbol{k}}(1 - f_{\boldsymbol{k}}). \tag{5.55}$$

Using the density of states $N(\xi)$ for a system of volume $\mathcal{V}$, the sum is converted into an integral over energy (see App. C)

$$C_N^{\text{el}} = \frac{2}{k_B T^2} \sum_{\boldsymbol{k}} \xi_{\boldsymbol{k}}^2 f_{\boldsymbol{k}}(1 - f_{\boldsymbol{k}}) \quad \longrightarrow \quad \frac{2\mathcal{V}}{k_B T^2} \int_{-\infty}^{\infty} d\xi N(\xi) \xi^2 f(\xi)[1 - f(\xi)], \tag{5.56}$$

The Fermi-Dirac distribution is a step function centered around μ (which was previously set to zero, meaning that ξ is an energy relative to the Fermi energy), which at finite temperatures is smeared. The expression $f(1 - f)$ comes from the derivative of f, and describes a peak around μ that drops off rapidly on an energy scale $k_B T \ll \epsilon_F$, where ϵ_F is the Fermi energy. Since the density of states $N(\xi)$ varies on an energy-scale ϵ_F, it can be considered to be constant $N(\epsilon) \approx N(0) \equiv N_0$ in the domain where $f(1-f)$ is non-zero, and therefore pulled out of the integral. Thus,

$$C_N^{\text{el}} = \frac{2\mathcal{V} N_0}{k_B T^2} \int_{-\infty}^{\infty} d\xi \frac{\xi^2 e^{\xi/k_B T}}{(e^{\xi/k_B T} + 1)^2}, \tag{5.57}$$

With a change of variables $x = \xi/k_B T$, the integral becomes

$$C_N^{\text{el}} = 2k_B^2 T \mathcal{V} N_0 \int_{-\infty}^{\infty} dx \frac{x^2 e^x}{(e^x + 1)^2}. \tag{5.58}$$

This integral has the solution

$$\int_{-\infty}^{\infty} dx \frac{x^2 e^x}{(e^x + 1)^2} = \frac{\pi^2}{3}. \tag{5.59}$$

Finally, the electronic heat capacity at constant volume $\mathcal{V}$ turns out to be

$$C_N^{\text{el}} = \gamma T, \tag{5.60}$$

$$\gamma \equiv \frac{2\pi^2 k_B^2 \mathcal{V} N_0}{3}. \tag{5.61}$$

Phononic heat capacity (normal state)

As a solid is heated, energy is stored in phonons. The energy E of a phonon mode follows the expression of a harmonic oscillator

$$E(\omega) = \hbar\omega \left(\frac{1}{2} + n \right), \tag{5.62}$$

where ω is the frequency and n the number of phonons in the mode according to the Bose-Einstein distribution

$$n(\omega, T) = \frac{1}{e^{\hbar\omega/k_B T} - 1}. \tag{5.63}$$

For simplicity, the density of phonon states is assumed to follow the Debye model

$$G(\omega) = \begin{cases} 9\mathcal{V}N\frac{\omega^2}{\omega_D^3}, & \omega < \omega_D \\ 0, & \omega > \omega_D, \end{cases} \tag{5.64}$$

where ω_D is the Debye frequency and $N = D/\mathcal{V}$ is the density of states per volume. The phononic internal energy is then

$$\begin{aligned} U_{n,ph} &= \int_0^\infty E(\omega)G(\omega)d\omega \\ &= \int_0^{\omega_D} \hbar\omega \left(\frac{1}{2} + \frac{1}{e^{\hbar\omega/k_B T} - 1}\right) \frac{9\mathcal{V}N}{\omega_D^3}\omega^2 d\omega \\ &= \frac{9\mathcal{V}N\hbar\omega_D}{8} + \frac{9\hbar N}{\omega_D^3}\int_0^{\omega_D} \frac{\omega^3}{e^{\hbar\omega/k_B T}} d\omega. \end{aligned} \tag{5.65}$$

With the substitutions

$$y = \frac{\hbar\omega}{k_B T}, \tag{5.66}$$

$$x = \frac{\hbar\omega_D}{k_B T}, \tag{5.67}$$

the integral can be written

$$\begin{aligned} \frac{9\hbar\mathcal{V}N}{\omega_D^3}\int_0^{\omega_D} \frac{\omega^3}{e^{\hbar\omega/k_B T}} d\omega &= \frac{9\mathcal{V}N\hbar}{\omega_D^3}\left(\frac{k_B T}{\hbar\omega_D}\right)^4 \int_0^x \frac{y^3}{e^y - 1} dy \\ &= 3\mathcal{V}Nk_B T\frac{3}{x^3}\int_0^x \frac{y^3}{e^y - 1} dy \\ &= 3\mathcal{V}Nk_B T D(x), \end{aligned} \tag{5.68}$$

where

$$D(x) \equiv \frac{3}{x^3}\int_0^x \frac{y^3}{e^y - 1} dy. \tag{5.69}$$

Finally, the internal energy can be written

$$U_{n,ph} = \frac{9\mathcal{V}N\hbar\omega_D}{8} + 3\mathcal{V}Nk_B T D(x). \tag{5.70}$$

The phononic heat capacity at constant volume $\mathcal{V}$ is

$$\begin{aligned} C_N^{\text{ph}} &= \left(\frac{\partial U_{n,ph}}{\partial T}\right)_V \\ &= 3\mathcal{V}Nk_B\left(D(x)T\frac{\partial D(x)}{\partial T}\frac{\partial x}{\partial T}\right) \\ &= = 3\mathcal{V}Nk_B\left(D(x) - x\frac{\partial D(x)}{\partial T}\right). \end{aligned} \tag{5.71}$$

Here,

$$\frac{\partial D(x)}{\partial T} = -\frac{3}{x}D(x) + \frac{3}{e^x - 1}, \tag{5.72}$$

yielding

$$C_N^{\text{ph}} = 3\mathcal{V}Nk_B\left(4D(x) - \frac{3x}{e^x - 1}\right). \tag{5.73}$$

For large temperatures ($x, y \to 0$),

$$\frac{3y}{e^y - 1} \xrightarrow[y\to 0]{} 3, \tag{5.74}$$

$$D(x) \xrightarrow[y\to 0]{} \frac{3}{x^3}\int_0^x \frac{y^3}{y}dy = 1. \tag{5.75}$$

For small temperatures ($x, y \to \infty$),

$$\frac{3y}{e^y - 1} \xrightarrow[y\to 0]{} 0, \tag{5.76}$$

$$D(x) \xrightarrow[y\to 0]{} \frac{3}{x^3}\int_0^\infty \frac{y^3}{e^y - 1}dy = \frac{k_B^3\pi^4}{5(\hbar\omega_D)^3}T^3. \tag{5.77}$$

Combining these results, the phononic heat capacity becomes

$$C_N^{\text{ph}} \xrightarrow[T\to 0]{} \frac{12\pi^4\mathcal{V}Nk_B^4}{5(\hbar\omega_D)^3}T^3, \tag{5.78}$$

$$C_N^{\text{ph}} \xrightarrow[T\to\infty]{} 3\mathcal{V}Nk_B. \tag{5.79}$$

Hence, it is seen that for low temperatures, the phononic heat capacity goes to zero as T^3, compared to the linear T-dependence of the electronic heat capacity.

5.3.4 Heat capacity in a bulk superconductor

The electronic heat capacity of a bulk superconductor, denoted C_S will now be derived from the statistical expression of the entropy. The thermodynamic definition of the heat capacity in Eq. (5.48) gives that

$$C \equiv T\frac{dS}{dT} = T\frac{dS}{d\beta}\frac{dT}{d\beta} = -\beta\frac{dS}{d\beta}. \tag{5.80}$$

In a bulk superconductor, the excitation energy required to create a quasiparticle of momentum k is

$$E_{\boldsymbol{k}} = \sqrt{(\xi_{\boldsymbol{k}} - \mu)^2 + \Delta_{\boldsymbol{k}}^2}, \tag{5.81}$$

where $\xi_{\boldsymbol{k}}$ is the single-particle energy measured relative to the Fermi energy in the normal state. In this formalism, μ is the energy shift of the chemical potential between the normal and superconducting states. The energy shift fulfills $\mu = 0$ for systems with a particle-hole symmetry close to the Fermi surface. In fact, this is quite generally a good approximation [71], which is why $\mu = 0$ is assumed in the rest of this calculation. With Eq. (5.36), the heat capacity is

$$\begin{aligned} C &= 2\beta k_B \sum_{\boldsymbol{k}} \frac{d}{d\beta} \left[(1 - f_{\boldsymbol{k}}) \ln(1 - f_{\boldsymbol{k}}) + f_{\boldsymbol{k}} \ln f_{\boldsymbol{k}}\right] \\ &= 2\beta k_B \sum_{\boldsymbol{k}} \left[-\frac{df}{d\beta} \ln(1 - f_{\boldsymbol{k}}) + (1 - f_{\boldsymbol{k}}) \frac{\frac{-df}{d\beta}}{1 - f_{\boldsymbol{k}}} + \frac{df}{d\beta} \ln f_{\boldsymbol{k}} + f_{\boldsymbol{k}} \frac{1}{f_{\boldsymbol{k}}} \frac{df}{d\beta} \right] \\ &= 2\beta k_B \sum_{\boldsymbol{k}} \frac{df}{d\beta} \ln \frac{f_{\boldsymbol{k}}}{1 - f_{\boldsymbol{k}}}, \end{aligned} \tag{5.82}$$

where

$$\ln \frac{f_{\boldsymbol{k}}}{1 - f_{\boldsymbol{k}}} = \ln \frac{\frac{1}{e^{\beta E_{\boldsymbol{k}}} + 1}}{1 - \frac{1}{e^{\beta E_{\boldsymbol{k}}} + 1}} = \ln e^{-\beta E_{\boldsymbol{k}}} = -\beta E_{\boldsymbol{k}}. \tag{5.83}$$

Substituting this result into Eq. (5.82) yields

$$C = -2\beta^2 k_B \sum_{\boldsymbol{k}} E_{\boldsymbol{k}} \frac{df}{d\beta}. \tag{5.84}$$

This expression can be processed further by assuming a particular form of $E_{\boldsymbol{k}}$ and evaluating the total derivative

$$\frac{df}{d\beta} = \frac{\partial f_{\boldsymbol{k}}}{\partial \beta} \frac{d\beta}{d\beta} + \frac{\partial f_{\boldsymbol{k}}}{\partial E_{\boldsymbol{k}}} \frac{dE_{\boldsymbol{k}}}{d\beta}. \tag{5.85}$$

Assuming a bulk superconductor with an excitation spectrum given by Eq. (5.81), the terms in the total derivative in Eq. (5.85) are

$$\frac{\partial f_{\boldsymbol{k}}}{\partial E_{\boldsymbol{k}}} = \frac{\partial}{\partial E_{\boldsymbol{k}}} (e^{\beta E_{\boldsymbol{k}}} + 1)^{-1} = -\beta \frac{e^{\beta E_{\boldsymbol{k}}}}{(e^{\beta E_{\boldsymbol{k}}} + 1)^2} = -\beta f_{\boldsymbol{k}}(1 - f_{\boldsymbol{k}}), \tag{5.86}$$

$$\frac{\partial f_{\boldsymbol{k}}}{\partial \beta} = \frac{\partial}{\partial \beta} (e^{\beta E_{\boldsymbol{k}}} + 1)^{-1} = -E_{\boldsymbol{k}} \frac{e^{\beta E_{\boldsymbol{k}}}}{(e^{\beta E_{\boldsymbol{k}}} + 1)^2} = \frac{E_{\boldsymbol{k}}}{\beta} \frac{\partial f_{\boldsymbol{k}}}{\partial E_{\boldsymbol{k}}}, \tag{5.87}$$

$$\frac{dE_{\boldsymbol{k}}}{d\beta} = \frac{d}{d\beta} \sqrt{\xi_{\boldsymbol{k}}^2 + \Delta_{\boldsymbol{k}}^2(T)} = \frac{1}{2\sqrt{\xi_{\boldsymbol{k}}^2 + \Delta_{\boldsymbol{k}}^2}} \frac{d|\Delta_{\boldsymbol{k}}|^2}{d\beta} = \frac{1}{2E_{\boldsymbol{k}}} \frac{d|\Delta_{\boldsymbol{k}}|^2}{d\beta}, \tag{5.88}$$

which gives

$$\frac{df}{d\beta} = \frac{\partial f_{\boldsymbol{k}}}{\partial E_{\boldsymbol{k}}}\left(\frac{E_{\boldsymbol{k}}}{\beta} + \frac{1}{2E_{\boldsymbol{k}}}\frac{d|\Delta_{\boldsymbol{k}}|^2}{d\beta}\right) = -f_{\boldsymbol{k}}(1-f_{\boldsymbol{k}})\left(E_{\boldsymbol{k}} + \frac{\beta}{2E_{\boldsymbol{k}}}\frac{d|\Delta_{\boldsymbol{k}}|^2}{d\beta}\right). \tag{5.89}$$

Substituting this result back into the heat capacity in Eq. (5.84) yields the electronic heat capacity for a bulk superconductor

$$C_S = 2\beta^2 k_B \sum_{\boldsymbol{k}} f_{\boldsymbol{k}}(1-f_{\boldsymbol{k}})\left(E_{\boldsymbol{k}}^2 + \frac{\beta}{2}\frac{d|\Delta_{\boldsymbol{k}}|^2}{d\beta}\right). \tag{5.90}$$

Turning this expression into an integral over energies (see App. C) by using the density of states per volume $N(\xi)$

$$C_S = 2\beta^2 k_B \mathcal{V} \int d\Omega \int_{-\infty}^{\infty} d\xi N(\xi) f(E)\left[1-f(E)\right]\left(E^2 + \frac{\beta}{2}\frac{d|\Delta|^2}{d\beta}\right), \tag{5.91}$$

where $E = \sqrt{\xi^2+\Delta^2}$, $\Delta = \Delta_0\eta(\Omega)$ and $\mathcal{V}$ is the volume of the sample. Using the same argument as in Sec. 5.3.3, the density of states varies on an energy scale ϵ_F which is typically much larger than the energy scale where $f(1-f)$ is non-zero (i.e. $k_B T_c$ in this case), so that $N(\epsilon) \simeq N(0) \equiv N_F$, yielding

$$C_S \approx 2\beta^2 k_B \mathcal{V} N_F \int d\Omega \int_{-\infty}^{\infty} d\xi f(E)\left[1-f(E)\right]\left(E^2 + \frac{\beta}{2}\frac{d|\Delta|^2}{d\beta}\right). \tag{5.92}$$

This expression will now be examined in the limits $T \to 0$ and $T \to T_c$.

C_S at low temperatures: fully gapped superconductors

It will now be shown that the heat capacity C_S goes to zero exponentially as $T \to 0$ for s-wave and unitary p-wave superconductors. This is a result which is quite general for all systems with an energy gap for excitations [9].

Starting from Eq. (5.92), the second term in the sum in C_S can be written as

$$\frac{\beta}{2}\frac{d|\Delta|^2}{d\beta} = \frac{dT}{d\beta}\frac{d|\Delta|^2}{dT} = -\frac{T}{\beta}\frac{d|\Delta|^2}{dT}, \tag{5.93}$$

where

$$\frac{T}{\beta} = k_B T^2 \xrightarrow[T\to 0]{} 0, \tag{5.94}$$

$$\frac{d|\Delta|^2}{dT} \xrightarrow[T\to 0]{} 0. \tag{5.95}$$

Noting that for low temperatures,

$$\begin{aligned} f(E)\left[1-f(E)\right] &= \frac{1}{e^{\beta E}+1}\left(1-\frac{1}{e^{\beta E}+1}\right) \\ &= e^{-\beta E}\left(1+2e^{-\beta E}+e^{-2\beta E}\right)^{-1} \\ &\approx e^{-\beta E}, \end{aligned} \tag{5.96}$$

the heat capacity can be rewritten as

$$\begin{aligned} C_S &\approx 2\beta^2 k_B \mathcal{V} N_F \int d\Omega \int_{-\infty}^{\infty} d\xi e^{-\beta\sqrt{\xi^2+\Delta^2}}\left(\xi^2+\Delta^2\right) \\ &\approx 2\beta^2 k_B \mathcal{V} N_F \int d\Omega e^{-\beta\Delta} \int_{-\infty}^{\infty} d\xi e^{-\beta\xi^2/2\Delta}\left(\xi^2+\Delta^2\right) \\ &= 2\beta^2 k_B \mathcal{V} N_F \int d\Omega e^{-\beta\Delta}\left(\sqrt{\frac{\pi}{4}}\left(\frac{2\Delta}{\beta}\right)^{3/2}+\Delta^2\sqrt{\frac{2\pi\Delta}{\beta}}\right). \end{aligned} \tag{5.97}$$

The first term goes to zero faster as $T \to 0$ than the second, and is therefore neglected. Assuming that the angular integral only gives rise to a trivial prefactor (in fact, $\int d\Omega = 1$ for s-wave),

$$\frac{C_S}{k_B^2 T_c \mathcal{V} N_F} \approx \sqrt{8\pi}\left(\frac{\Delta}{k_B T}\right)^{5/2} e^{-\Delta/k_B T} \xrightarrow[T\to 0]{} 0, \tag{5.98}$$

exponentially due to the factor $e^{-\Delta_0/k_B T}$, as expected [73].

C_S at low temperatures: d-wave

It will now be shown that the heat capacity C_S goes to zero like T^2 as $T \to 0$ for d-wave superconductors. The deviation from an exponential suppression is caused by the line nodes on the Fermi surface (i.e. due to the gapless density of states) [37].

Starting from Eq. (5.92), applying Eqs.(5.93)–(5.96), and inserting the d-wave order parameter $\Delta_d = \Delta_0\eta(\theta) = \Delta_0\cos(2\theta)$, where $\Delta_0 \approx 2.14 k_B T_c$ at $T = 0$ [118],

$$C_S = 2\beta^2 k_B \mathcal{V} N_F \int_0^{2\pi} \frac{d\theta}{2\pi} \int_{-\infty}^{\infty} d\xi e^{-\beta E} E^2. \tag{5.99}$$

Note that a cylindrically symmetric Fermi surface has been assumed with $d\Omega = d\theta/2\pi$. Changing integration to $E = \sqrt{\xi^2+\Delta^2}$, the integral becomes

$$C_S = 2\beta^2 k_B \mathcal{V} N_F \int_0^{2\pi} \frac{d\theta}{2\pi} \int_{-\mu}^{\infty} dE e^{-\beta E} E^3 \frac{\Theta\left(|E|-|\Delta_0\cos(2\theta)|\right)}{\sqrt{E^2-\Delta_0^2\cos^2(2\theta)}}, \tag{5.100}$$

where Θ is the Heaviside step function. Setting $\mu = 0$ and $x = E/\Delta_0$ yields

$$\begin{aligned} C_S &= 2\beta^2 k_B \mathcal{V} N_F \Delta_0^3 \int_0^\infty dx e^{-\beta\Delta_0 x} x^2 \int_0^{2\pi} \frac{d\theta}{2\pi} \frac{\Theta\left(|x| - |\cos(2\theta)|\right)}{\sqrt{1 - \frac{\cos^2(2\theta)}{x^2}}} \\ &= 2\beta^2 k_B \mathcal{V} N_F \Delta_0^3 \int_0^\infty dx e^{-\beta\Delta_0 x} x^2 \frac{4}{2\pi} \Bigg[xK(x)\Theta(1-x) \\ &\qquad + K\left(\frac{1}{x}\right)\Theta(x-1)\Bigg], \end{aligned} \tag{5.101}$$

where $K(x)$ is the complete elliptic integral of the first kind, defined as[3]

$$K(x) \equiv \int_0^{\pi/2} d\theta \frac{1}{\sqrt{1 - x^2 \sin^2(\theta)}}. \tag{5.102}$$

The aim is to get the leading temperature dependence. Therefore, $K(x)$ is expanded to lowest order $K(x) \approx \pi/2$, and the second term $K(\frac{1}{x})$ is discarded. The heat capacity becomes

$$\begin{aligned} C_S &\approx \frac{4}{\pi}\beta^2 k_B \mathcal{V} N_F \Delta_0^3 \int_0^1 dx e^{-\beta\Delta_0 x} x^3 \frac{\pi}{2} \\ &= 2\beta^2 k_B \mathcal{V} N_F \Delta_0^3 6 (\beta\Delta_0)^{-4} \\ &= 12 k_B \mathcal{V} N_F \frac{(k_B T)^2}{\Delta_0}, \end{aligned} \tag{5.103}$$

which was to be shown. Inserting $\Delta_0 \approx 2.14 k_B T_c$, as derived in App. D.4, yields

$$\frac{C_S}{k_B^2 T_c \mathcal{V} N_F} = 12 \frac{(k_B T)^2}{k_B T_c \Delta_0} \approx 6 \left(\frac{T}{T_c}\right)^2. \tag{5.104}$$

C_S at the transition temperature T_c

As $T \to T_c$, then $\Delta \to 0$, and $E \to \xi$. Starting from the integral expression for the superconducting heat capacity in Eq. (5.92),

$$C_S \xrightarrow[T \to T_c^-]{} 2\beta^2 k_B \int d\Omega \int_{-\infty}^{\infty} d\xi N(\xi) f(\xi)\left[1 - f(\xi)\right] \left(\xi^2 + \frac{\beta}{2} \frac{d|\Delta_{\boldsymbol{k}}|^2}{d\beta}\bigg|_{T_c}\right). \tag{5.105}$$

The first term is simply C_N^{el}. Thus,

$$\left(C_S - C_N^{\text{el}}\right)\Big|_{T_c} = 2\beta^2 k_B \int d\Omega \int_{-\infty}^{\infty} d\xi N(\xi) f(\xi)\left[1 - f(\xi)\right] \frac{\beta}{2} \frac{d|\Delta_{\boldsymbol{k}}|^2}{d\beta}\bigg|_{T_c}. \tag{5.106}$$

[3]Note that in the Wolfram Language (e.g. Mathematica, Wolfram Alpha), $K(x)$ is replaced with $K(x^2)$.

5.3.5 Heat capacity jump in the N-S phase transition

In this section, the jump in heat capacity at the normal-superconducting phase transition will be derived analytically for both an s and a d-wave bulk superconductor. Combining C_N^{el} from Eq. (5.55) and C_S from Eq. (5.90), an expression for this jump can be formed

$$\Delta C_{NS} \equiv (C_S - C_N^{\mathrm{el}})\Big|_{T_c} = \beta^3 k_B \sum_{\boldsymbol{k}} f_{\boldsymbol{k}}(1-f_{\boldsymbol{k}}) \frac{d|\Delta_{\boldsymbol{k}}|^2}{d\beta}\bigg|_{T_c}. \tag{5.107}$$

To evaluate this sum, an analytic expression of the order parameter close to T_c has been derived in Eq. (D.80) in App. D.5 on p. 180. The slope of the order parameter close to T_c was then found to be (Eq. (D.84) on p. 180)

$$\frac{d\Delta_0^2}{d\beta}\bigg|_{T_c} = \alpha\tilde{\eta}^{-1}(k_B T_c)^3, \tag{5.108}$$

where

$$\begin{aligned}
\Delta_{\boldsymbol{k}} &= \Delta(\theta_{\boldsymbol{k}}) = \Delta\eta_\nu(\theta_{\boldsymbol{k}}), && (5.109)\\
\eta_\nu(\theta_{\boldsymbol{k}}) &= \begin{cases} 1, & \nu = s, \\ \sqrt{2}\cos(2\theta_{\boldsymbol{k}}), & \nu = d_{x^2-y^2}, \end{cases} && (5.110)\\
\Delta_0 &\equiv \Delta\big|_{T_c}, && (5.111)\\
\alpha &\equiv \frac{8\pi^2}{7\zeta(3)} \approx 9.4, && (5.112)\\
\tilde{\eta} &\equiv \int_0^{2\pi} \frac{d\theta_{\boldsymbol{k}}|\eta_\nu(\theta_{\boldsymbol{k}})|^4}{2\pi} = \begin{cases} 1, & \nu = s, \\ \frac{3}{2}, & \nu = d_{x^2-y^2}, \end{cases} && (5.113)\\
\tilde{\alpha} &\equiv \alpha\tilde{\eta}^{-1}. && (5.114)
\end{aligned}$$

Inserting this result into ΔC_{NS}, evaluating at $T \to T_c^-$, and turning the sum into an integral over energy (see App. C) through the density of states per volume $N(\epsilon)$, yields

$$\begin{aligned}
\Delta C_{NS} &= \frac{1}{k_B^2 T_c^3} \sum_{\boldsymbol{k}} f_{\boldsymbol{k}}(1-f_{\boldsymbol{k}})\tilde{\alpha}(k_B T_c)^3 |\eta_\nu(\theta_{\boldsymbol{k}})|^2 \\
&= \tilde{\alpha} k_B \sum_{\boldsymbol{k}} f_{\boldsymbol{k}}(1-f_{\boldsymbol{k}})|\eta_\nu(\theta_{\boldsymbol{k}})|^2 \\
&= \tilde{\alpha} k_B \mathcal{V} \int_0^{2\pi} \frac{d\theta}{2\pi}|\eta_\nu(\theta)|^2 \int_{-\infty}^{\infty} d\xi N(\xi) f(\xi)\left[1-f(\xi)\right] \\
&= \tilde{\alpha} k_B \mathcal{V} \int_{-\infty}^{\infty} d\xi N(\xi) f(\xi)\left[1-f(\xi)\right], && (5.115)
\end{aligned}$$

where the angular integral is unity due to normalization. Using the same argument as in Sec. 5.3.3, the density of states varies on an energy scale ϵ_F which is typically much larger than the energy scale where $f(1-f)$ is non-zero (i.e. $k_B T_c$ in this case), so that $N(\epsilon) \simeq N(0) \equiv N_F$. Introducing the substitution

$$x = \frac{\xi}{k_B T_c}, \tag{5.116}$$

$$dx = \frac{d\xi}{k_B T_c}, \tag{5.117}$$

the heat capacity jump becomes

$$\begin{aligned} \Delta C_{NS} &= \tilde{\alpha} k_B \mathcal{V} N_F \int_{-\infty}^{\infty} dx (k_B T_c) \frac{1}{e^x + 1} \left(1 - \frac{1}{e^x + 1}\right) \\ &= \tilde{\alpha} k_B^2 T_c \mathcal{V} N_F. \end{aligned} \tag{5.118}$$

Thus, for an s- and a d-wave superconductor, the jump equals to

$$\Delta C_{NS}^s = \alpha k_B^2 T_c \mathcal{V} N_F \approx 9.38 k_B^2 T_c \mathcal{V} N_F, \tag{5.119}$$

$$\Delta C_{NS}^d = \frac{2}{3} \Delta C_{NS}^s \approx 6.26 k_B^2 T_c \mathcal{V} N_F, \tag{5.120}$$

respectively, where $\alpha \equiv 8\pi^2/7\zeta(3)$. In terms of the electronic normal-state heat capacity (at the transition temperature) C_N^{el} from Eq. (5.60), the jumps become the constants

$$\frac{\Delta C_{NS}^s}{C_N^{\mathrm{el}}(T_c)} = \frac{12}{7\zeta(3)} \approx 1.43, \tag{5.121}$$

$$\frac{\Delta C_{NS}^d}{C_N^{\mathrm{el}}(T_c)} = \frac{2}{3} \frac{12}{7\zeta(3)} \approx 0.95, \tag{5.122}$$

which are well-known values for weak-coupling superconductors [119].

5.3.6 Calculating heat capacity in quasiclassics

It is possible to calculate the heat capacity in quasiclassics with two different methods: from a statistical or a thermodynamic expression of the entropy. The statistical method relies on a first-order derivative of the entropy with respect to temperature, and the evaluation of an integral over the LDOS [120]. The thermodynamic method relies on a numerical second-order derivative of the free-energy functional. The latter method is much faster numerically, but requires an adequate resolution in temperature and a much higher numerical stability. The latter method is used in this work. Both of these methods will now be described.

Heat capacity from the entropy and LDOS

The heat capacity in a bulk supercondcutor was derived in Eq. (5.90) from the statistical expression of the entropy. It is possible to get an expression valid for non-bulk system, by rewriting the entropy in Eq. (5.36) as an integral over energy through the density of states (see App. C)

$$\begin{aligned} S &= -2k_B \sum_{\boldsymbol{k}} \left[(1-f_{\boldsymbol{k}})\ln(1-f_{\boldsymbol{k}}) + f_{\boldsymbol{k}} \ln f_{\boldsymbol{k}}\right] \\ &= -2\mathcal{V} \int_{-\infty}^{\infty} d\xi N(\xi) \left[(1-f(\xi))\ln\left(1-f(\xi)\right) + f(\xi)\ln f(\xi)\right], \end{aligned} \tag{5.123}$$

where the density of states $N(\xi)$ is related to the angle-resolved DOS

$$N(\xi) = \int d\hat{\boldsymbol{p}} N(\xi, \hat{\boldsymbol{p}}), \tag{5.124}$$

$$\frac{N(\xi,\hat{\boldsymbol{p}})}{N_F(\hat{\boldsymbol{p}})} = -\frac{1}{\pi} \operatorname{Im} g^R(\hat{\boldsymbol{p}}, \xi). \tag{5.125}$$

Here, g^R is the retarded Green function. The heat capacity was shown in Eq. (5.48) to be $C = TdS/dT$. Under the assumption that the DOS and the order parameter are weakly temperature dependent, the heat capacity is obtained by differentiating only the Fermi-Dirac distribution in Eq. (5.123), yielding

$$C(T, \boldsymbol{H}) \approx 2k_B \mathcal{V} \int_{-\infty}^{\infty} d\xi \frac{\xi^2}{(2k_B T)^2} \frac{N(T, \boldsymbol{H}, \xi)}{\cosh^2(\xi/2k_B T)}. \tag{5.126}$$

This approximation is generally good enough far from T_c [120].

Heat capacity from the free-energy functional

The method that will be used in this work is based on the second-order derivative of the free-energy functional with respect to temperature. The free-energy functional was introduced in Sec. 5.1, providing a method to calculate the free-energy difference between the superconducting and normal states, denoted $\delta\Omega$. The heat capacity difference between superconducting and normal states can then be calculated from the free energy according to Eq. (5.50), i.e.

$$\delta C = -T \left(\frac{\partial^2 \delta\Omega}{\partial^2 T} \right)_{R,V}. \tag{5.127}$$

In this work, the free-energy difference between different superconducting states will be of more interest. This will be in order to determine which state is energetically more favorable, and has the added benefit of canceling some systematic errors. The free-energy difference between two superconducting states 1 and 2 is thus

$$\Delta\Omega \equiv \delta\Omega_1 - \delta\Omega_2 = (\Omega_{S,1} - \Omega_N) - (\Omega_{S,2} - \Omega_N) = \Omega_{S,1} - \Omega_{S,2}. \tag{5.128}$$

This means that the contribution from the normal state cancels. To study the heat capacity jump in second-order phase transitions, ΔC is calculated from $\Delta\Omega$ through Eq. (5.127). As a scale for the heat capacity, the jump in the heat capacity in the superconducting-normal state transition will be used. In particular, the analytically derived jumps for bulk systems in Eqs. (5.119) and (5.120) will be used.

A dimensionless equation for the heat capacity in quasiclassics will now be derived. Starting from the Eilenberger free-energy functional in Eq. (5.21)

$$\begin{aligned}\delta C &= T\frac{\partial^2}{\partial T^2}\delta\Omega(T) \\ &= T\frac{\partial^2}{\partial T^2}\int d\boldsymbol{R}\Bigg\{\frac{\boldsymbol{B}_{\mathrm{ind}}^2(\boldsymbol{R})}{8\pi} + |\Delta(\boldsymbol{R})|^2 N_F \ln\frac{T}{T_c} \\ &\qquad +2\pi N_F k_B T\sum_{\epsilon_n}\left[\frac{|\Delta(\boldsymbol{R})|^2}{\epsilon_n} + i\langle\mathcal{I}(\boldsymbol{p}_F,\boldsymbol{R};\epsilon_n)\rangle_{\boldsymbol{p}_F}\right]\Bigg\},\end{aligned} \tag{5.129}$$

Noting that heat capacity has the dimension $[C] = J/K$, i.e.

$$\delta C = T\frac{\partial T}{\partial T^2}\delta\Omega = \frac{1}{T_c}\frac{T}{T_c}\frac{\partial^2}{\partial(T/T_c)^2}\delta\Omega. \tag{5.130}$$

Recalling that $[N_F] = \#\text{states}/(\text{energy}\times\text{volume})$, the heat capacity can be made dimensionless by dividing with $\mathcal{V}N_F k_B^2 T_c$, where $\mathcal{V}$ is the volume

$$\begin{aligned}\frac{\delta C}{\mathcal{V}N_F k_B^2 T_c} &= \frac{T}{T_c}\frac{\partial^2}{\partial(T/T_c)^2}\int\frac{d\boldsymbol{R}}{\mathcal{V}}\Bigg\{\left(\frac{\boldsymbol{B}(\boldsymbol{R})}{\Phi_0/\xi_0^2}\right)^2 2\pi^4\kappa_0^2 + \frac{|\Delta(\boldsymbol{R})|^2}{(k_B T_c)^2}\ln\frac{T}{T_c} \\ &\qquad +2\pi\frac{T}{T_c}\sum_{\epsilon_n}\left[\frac{|\Delta(\boldsymbol{R})|^2}{(k_B T_c)^2}\frac{k_B T_c}{\epsilon_n} + i\frac{\langle\mathcal{I}(\boldsymbol{p}_F,\boldsymbol{R};\epsilon_n)\rangle_{\boldsymbol{p}_F}}{k_B T_c}\right]\Bigg\}.\end{aligned} \tag{5.131}$$

Thus, by dividing with the heat capacity jump at the normal-superconducting phase transition from Eq. (5.118), $\Delta C_{NS} \equiv \tilde{\alpha}k_B^2 T_c\mathcal{V}N_F$, a dimensionless form with a relevant scale is obtained

$$\begin{aligned}\frac{\delta C}{\Delta C_{NS}} &= \frac{1}{\tilde{\alpha}}\frac{T}{T_c}\frac{\partial^2}{\partial(T/T_c)^2}\int\frac{d\boldsymbol{R}}{\mathcal{V}}\Bigg\{\left(\frac{\boldsymbol{B}(\boldsymbol{R})}{\Phi_0/\xi_0^2}\right)^2 2\pi^4\kappa_0^2 + \frac{|\Delta(\boldsymbol{R})|^2}{(k_B T_c)^2}\ln\frac{T}{T_c} \\ &\qquad +2\pi\frac{T}{T_c}\sum_{\epsilon_n}\left[\frac{|\Delta(\boldsymbol{R})|^2}{(k_B T_c)^2}\frac{k_B T_c}{\epsilon_n} + i\frac{\langle\mathcal{I}(\boldsymbol{p}_F,\boldsymbol{R};\epsilon_n)\rangle_{\boldsymbol{p}_F}}{k_B T_c}\right]\Bigg\},\end{aligned} \tag{5.132}$$

where

$$\tilde{\alpha} \equiv \begin{cases}\frac{8\pi^2}{7\zeta(3)} \approx 9.4, & \text{s-wave},\\ \frac{2}{3}\frac{8\pi^2}{7\zeta(3)} \approx 6.3, & \text{d-wave}.\end{cases} \tag{5.133}$$

6 Mesoscopic superconductivity

This chapter studies the thermodynamics and electrodynamics of mesoscopic grains with s, d and p-wave pairing symmetries. The first section shows that in the absence of external fields, bulk behavior is essentially obtained for grains that have an isotropic s-wave pairing or an anisotropic d-wave pairing with ab-axes aligned with the grain edges. The thermodynamics and gap profiles of such systems are benchmarked against the analytic expressions derived in this thesis, with an excellent agreement. It is then shown that in the presence of external fields, or when the ab-axes of a d-wave grain are misaligned with the grain edges, mesoscopic effects are obtained which are not present in bulk samples. In the case of the external fields, this has to do with the grain size being small compared to the magnetic relaxation length, i.e. the penetration depth. For d-wave grains with misaligned ab-axes relative to the grain edges, the deviation from bulk behavior is due to pairbreaking at the edges, giving rise to quasiparticle states in the middle of the superconducting gap. The second section studies Abrikosov vortices in d-wave and s-wave grains. Mesoscopic effects are verified, such as exotic vortex-antivortex pairs [121–123], the vortex shell effect [124–127], and midgap states in vortex cores [128]. The third section verifies flux quantization and its thermodynamics in superconductors with holes. The fourth section studies surface currents in chiral p-wave superconductors [129–131], with preliminary results on peculiar current and flux phenomena.

6.1 Bulk versus mesoscopic behavior: Midgap states and benchmark of thermodynamics

In this section, square superconducting grains of varying sidelengths D and temperatures $T = 0$–$1T_c$ will be considered for s-wave and d-wave pairing symmetries. The grains are assumed to be clean, meaning that quasiparticles scatter specularly at the edges of the grain. For an s-wave superconductor, the order parameter is isotropic and the grain essentially behaves like a bulk system with a BCS gap, as shown in Figs. 6.1 (a) and (d). A d-wave order parameter, on the other hand, is anisotropic, which means that it makes a difference how the edges of the grain are cut with respect to the crystal ab-axes (and thus the positive and negative lobes of the order parameter). Let the angle between the edge and the ab-axes be denoted as θ. For a perfect alignment ($\theta = 0$), quasiparticles are scattered from positive to

positive or negative to negative lobes, and the system is essentially a bulk system, as shown in Figs. 6.1 (b) and (e). As θ increases, however, quasiparticles are scattered from positive to negative lobes and vice versa, which means that the order parameter changes sign. Thus, the single-valued order parameter is suppressed on a length scale of $\sim \xi_0$ from the edge. Here, the superconducting pairs are broken up into quasiparticle states with energies in the middle of the superconducting gap exactly at the Fermi energy, referred to as midgap states (MGS). Thus, these edges are referred to as pairbreaking. As $\theta \to 45°$, the edges are maximally pairbreaking, leading to a huge density of MGS, as shown in Figs. 6.1 (c) and (f). It will now be shown that these midgap states give rise to a deviation from standard bulk behavior, by studying the gap profile, the free energy, the entropy, and the heat capacity.

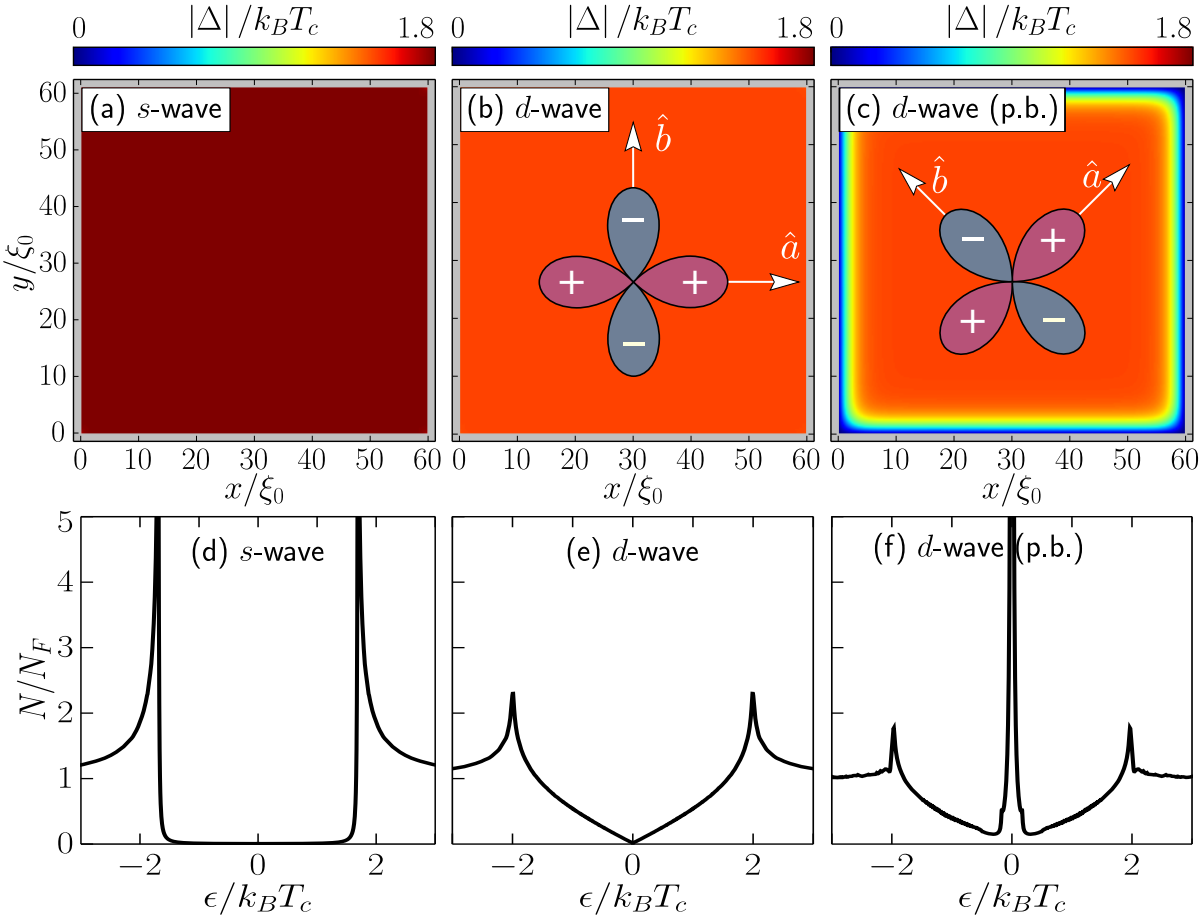

Figure 6.1: *The spatial dependence of the order parameter magnitude in grains with (a) an s-wave and (b)–(c) a d-wave pairing symmetry. In panels (b) and (c), the crystal ab-axes are perfectly aligned and misaligned with the grain edges, respectively, as shown by the graphics. Panels (d)–(f) shows the LDOS at the edge for the same grains. The misaligned edges are pairbreaking, giving rise to a huge density of midgap states exactly at the Fermi energy, as seen in the LDOS in panel (f).*

Figure 6.2 shows the temperature-dependent gap and various thermodynamic quantities for the same grains above with $D = 60\xi_0$ (dashed lines) and $D = 10\xi_0$ (solid lines). Panels (a)–(c) show the temperature dependence of the grain-averaged order-parameter magnitude, (d)–(f) the free-energy difference, (g)–(i) the entropy difference, and (j)–(l) the heat-capacity difference, with respect to the normal state. Here,

$$\Omega_{\mathcal{A}} \equiv \mathcal{A}N_F(k_BT_c)^2, \tag{6.1}$$
$$S_{\mathcal{A}} \equiv \mathcal{A}N_F k_B^2 T_c, \tag{6.2}$$
$$C_{\mathcal{A}} \equiv \mathcal{A}N_F k_B^2 T_c. \tag{6.3}$$

For the first two columns, there is virtually no difference between the two grain sizes. This indicates that there is no size dependence. Compare the left column with for example the plots and bulk values in Ch. 3.6 of Tinkham [73]. Indeed, it is seen that the two left columns perfectly reproduce values expected for a bulk system. For example, the gaps at zero temperature has the values $\Delta_s(T=0) \approx 1.76k_BT_c$ and $\Delta_d(T=0) \approx 1.51k_BT_c$, as derived in Eqs. (D.52) and (D.53) on p. 177. The free-energy difference at zero temperature is also reproduced from Eq. (5.19) on p. 67, i.e.

$$\frac{\delta\Omega(T=0)}{\Omega_{\mathcal{A}}} = -\frac{1}{2}\frac{\Delta^2(T=0)}{(k_BT_c)^2}, \tag{6.4}$$
$$\frac{\delta\Omega_s(T=0)}{\Omega_{\mathcal{A}}} \approx -\frac{1.76^2}{2} \approx -1.55, \tag{6.5}$$
$$\frac{\delta\Omega_d(T=0)}{\Omega_{\mathcal{A}}} \approx -\frac{1.51^2}{2} \approx -1.14. \tag{6.6}$$

Furthermore, the heat-capacity jump at the transition temperature T_c in Eqs. (5.119) and (5.120) on p. 82 is also reproduced as

$$\frac{\Delta C_s}{C_{\mathcal{A}}} \approx 9.4, \tag{6.7}$$
$$\frac{\Delta C_d}{C_{\mathcal{A}}} \approx 6.3. \tag{6.8}$$

The right column shows a significant deviation from bulk behavior, however, which grows as the grain becomes smaller. This is due to the fact that at $D = 10\xi_0$, a substantial portion of the grain hosts non-superconducting quasiparticle states. It will be shown in Ch. 7 that these midgap states enable spontaneous symmetry breaking, since it is energetically favorable to shift them to finite energies. The deviation from bulk behavior is further pronounced in the presence of external fields, which will be studied in the following section.

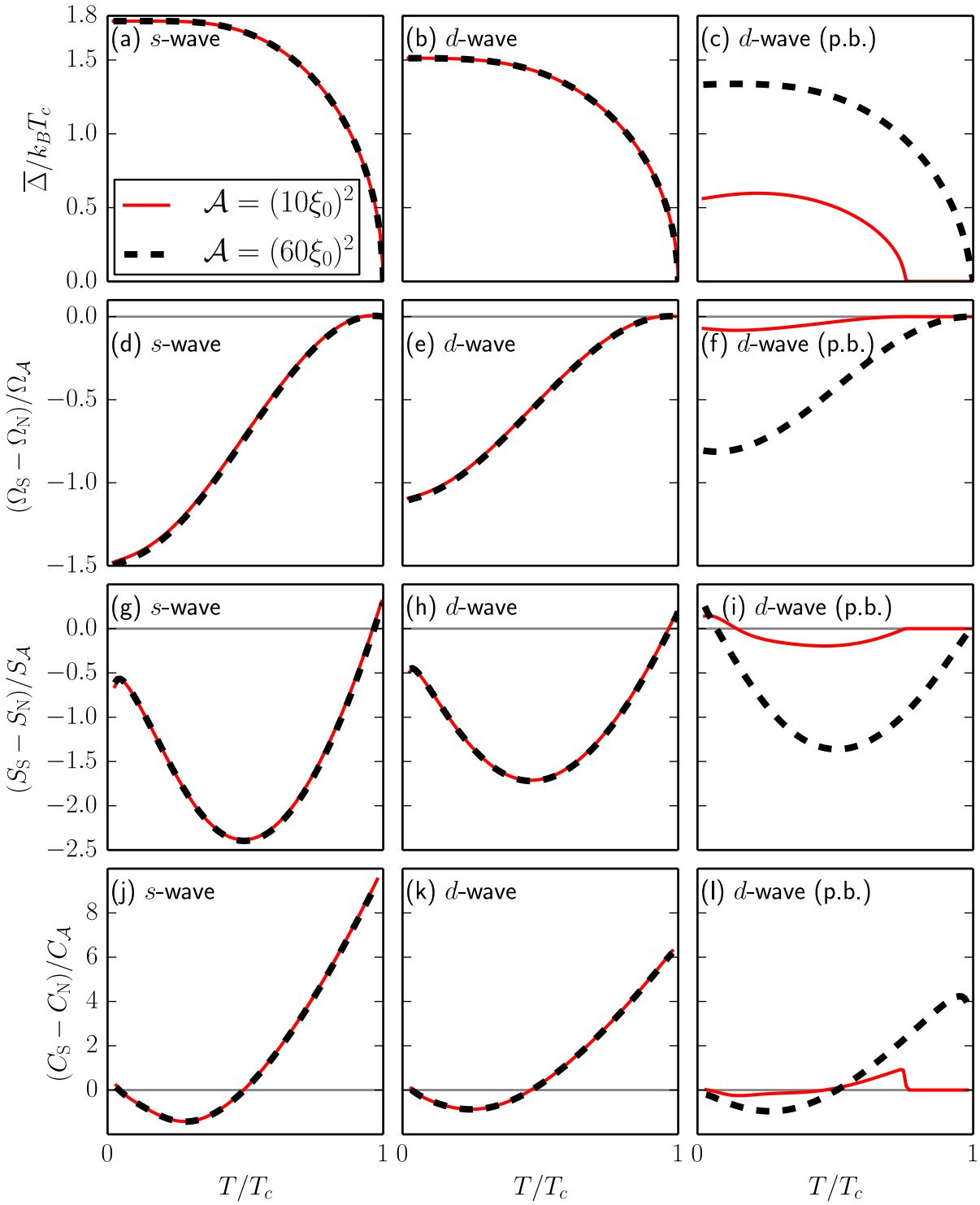

Figure 6.2: *Gap and thermodynamic observables in a square grain of area $\mathcal{A}$, as indicated by the legend, with different pairing symmetries as indicated by the labels. (a)–(c) grain-averaged gap, (d)–(f) free-energy difference w.r.t. the normal state with $\Omega_\mathcal{A} = \mathcal{A}N_F(k_BT_c)^2$, (g)–(i) entropy difference w.r.t. the normal state with $S_\mathcal{A} = \mathcal{A}N_Fk_B^2T_c$, and (j)–(l) heat-capacity difference w.r.t. the normal state with $C_\mathcal{A} = \mathcal{A}N_Fk_B^2T_c$.*

6.2 Abrikosov vortices

This section studies Abrikosov vortices in s-wave and d-wave superconductors. Figure 6.3 shows vortex lattices for external fields $B_{\text{ext}} = n\Phi_0/\mathcal{A}$ in d-wave grains of area $\mathcal{A} = 180\xi_0 \times 180\xi_0$, with integer flux quanta $n = 1$–6 and a corresponding winding of the superconducting phase $\chi \equiv \text{Arg}\{\Delta\}$. The figure also shows that it is possible to stabilize exotic vortex-antivortex pairs, for example for external flux $\Phi_{\text{ext}} = 3\Phi_0$, where there is no unique geometric configuration minimizing the free energy for three vortices. Here, there are four vortices and one antivortex, such that the winding number and the external flux quanta are both still $n = 3$. This vortex configuration was predicted by Ref. [121]. Usually vortices and antivortices attract and annihilate, but in a mesoscopic grain, the existence of both allows a more symmetric vortex arrangement leading to a thermodynamically stable ground state. Indications of vortex-antivortex pairs have been seen in experiment, see for example Refs. [122, 123] and references therein. Figure 6.4 demonstrates the vortex "shell effect" in circular and square grains with s-wave pairing symmetry, with area $\mathcal{A} \approx 180\xi_0 \times 180\xi_0$ and at temperature $T = 0.5T_c$. The vortex shell effect is a mesoscopic effect, where for higher flux quanta, vortices do not necessarily enter a grain one-by-one, but rather in "shells", see Refs. [124–127] and references therein. Seen in the same figure is another mesoscopic effect where the geometry of the vortex lattice reflects the geometry of the grain, which has been shown experimentally for example in disc-shaped grains [124], square-shaped grains [125], and in triangular-shaped grains [126]. Figure 6.5 plots the LDOS for a vortex lattice, showing pronounced midgap states in each vortex core, and continuum states far from the centers. The midgap states are known to be responsible for driving the currents that lies within a few coherence lengths from the vortex cores, while continuum states carry the currents further away [132]. This is verified by the spectral currents in Fig. 6.6.

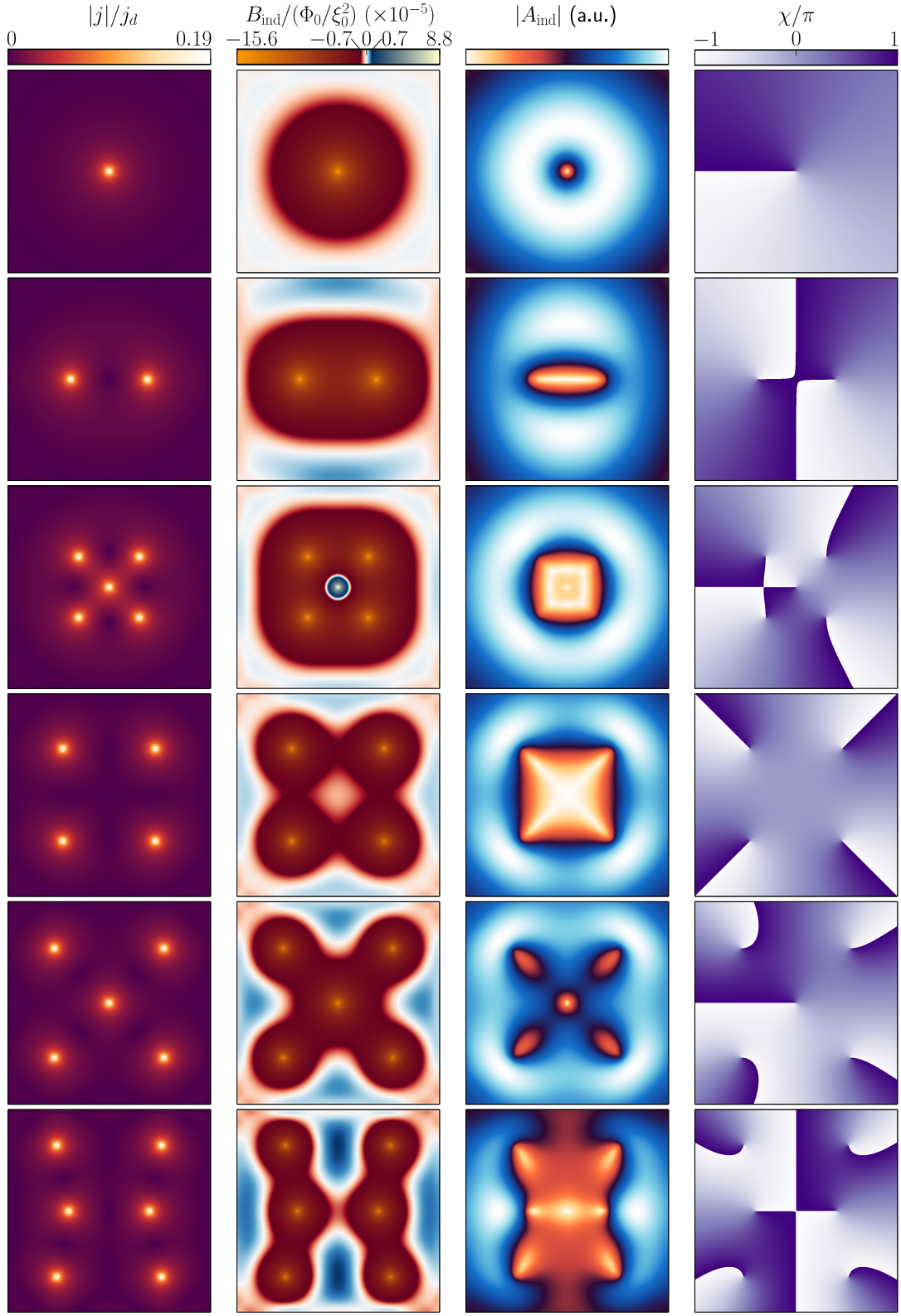

Figure 6.3: *Abrikosov vortex lattices in d-wave grains for different external flux densities* $B_{ext} = n\Phi_0/\mathcal{A}$*, where* $\mathcal{A} = 180\xi_0 \times 180\xi_0$ *is the grain area and* n *is an integer ranging between* $n = 1$–6 *from top to bottom row. The first column shows the induced current density, the second the magnetic flux density due to these currents, the third the induced magnetic vector potential and the fourth column shows the superconducting phase. The penetration depth is* $\lambda_0 = 100\xi_0$*, and the temperature is* $T = 0.2T_c$*. The red-to-blue color scale (*-0.7–$0.7 \times 10^{-5}\Phi_0/\xi_0^2$*) in the induced magnetic flux is the typical scale of the fluxes due to the loop-current phase in Ch. 7.*

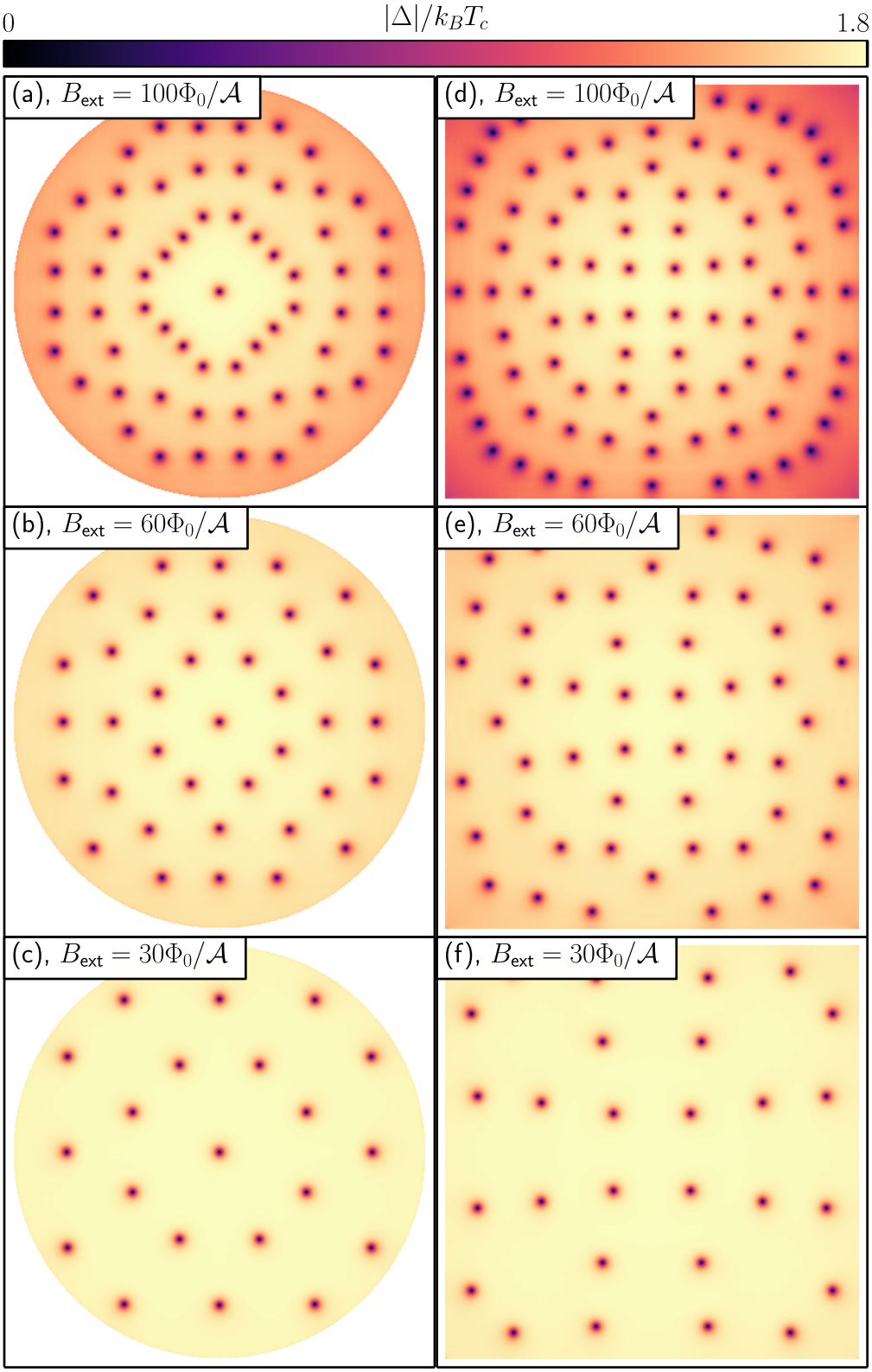

Figure 6.4: *Order-parameter magnitude in (left column) circular and (right column) square grains with an s-wave pairing symmetry. The dark spots are Abrikosov vortices. From top to bottom row, an external flux of* $\Phi_{ext} = 100\Phi_0, 60\Phi_0, 30\Phi_0$ *is applied, respectively. The temperature is* $T = 0.5T_c$ *and the sidelength is* $180\xi_0$*. The figures illustrate that vortices enter in shells, with a distribution which reflects the geometry of the grain, e.g. in the left column layers of circles with centers at the corners of the panels are seen.*

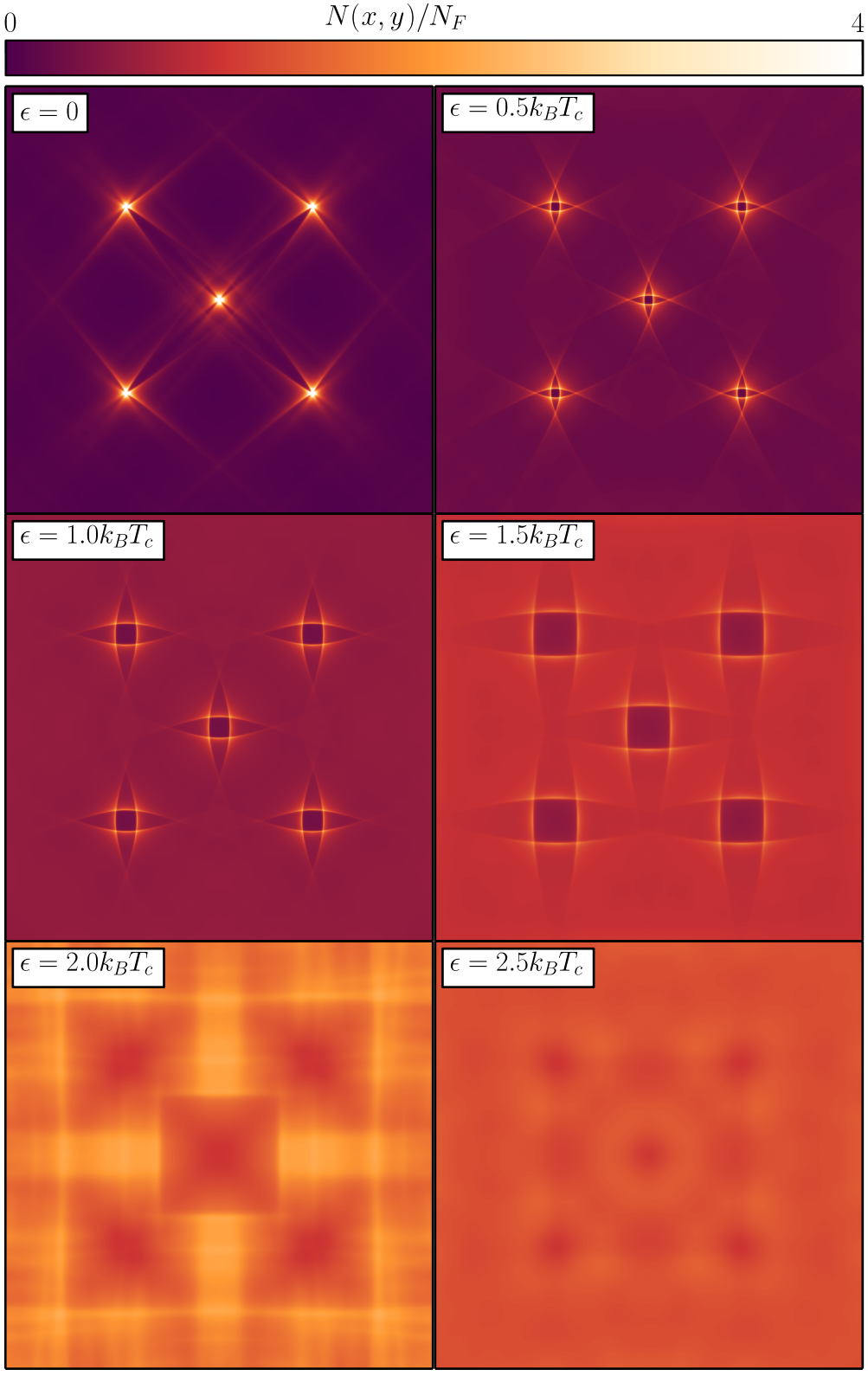

Figure 6.5: *Local density of states in a $60\xi_0 \times 60\xi_0$ large d-wave grain (non-pairbreaking) with 5 Abrikosov vortices, at temperature $T = 0.5T_c$. Each figure represents a certain energy, as indicated by the labels. At zero energy, there is a high density of midgap states exactly in the core of each vortex. For higher energies, the states are spread out more evenly across the grain. There are profiles in the LDOS that reflect the d-wave pairing symmetry, as well as the geometry of the grain. A cutoff of $N_{max} = 4N_F$ has been chosen for increased visibility, although the LDOS at zero energy in each vortex core is roughly an order of magnitude larger.*

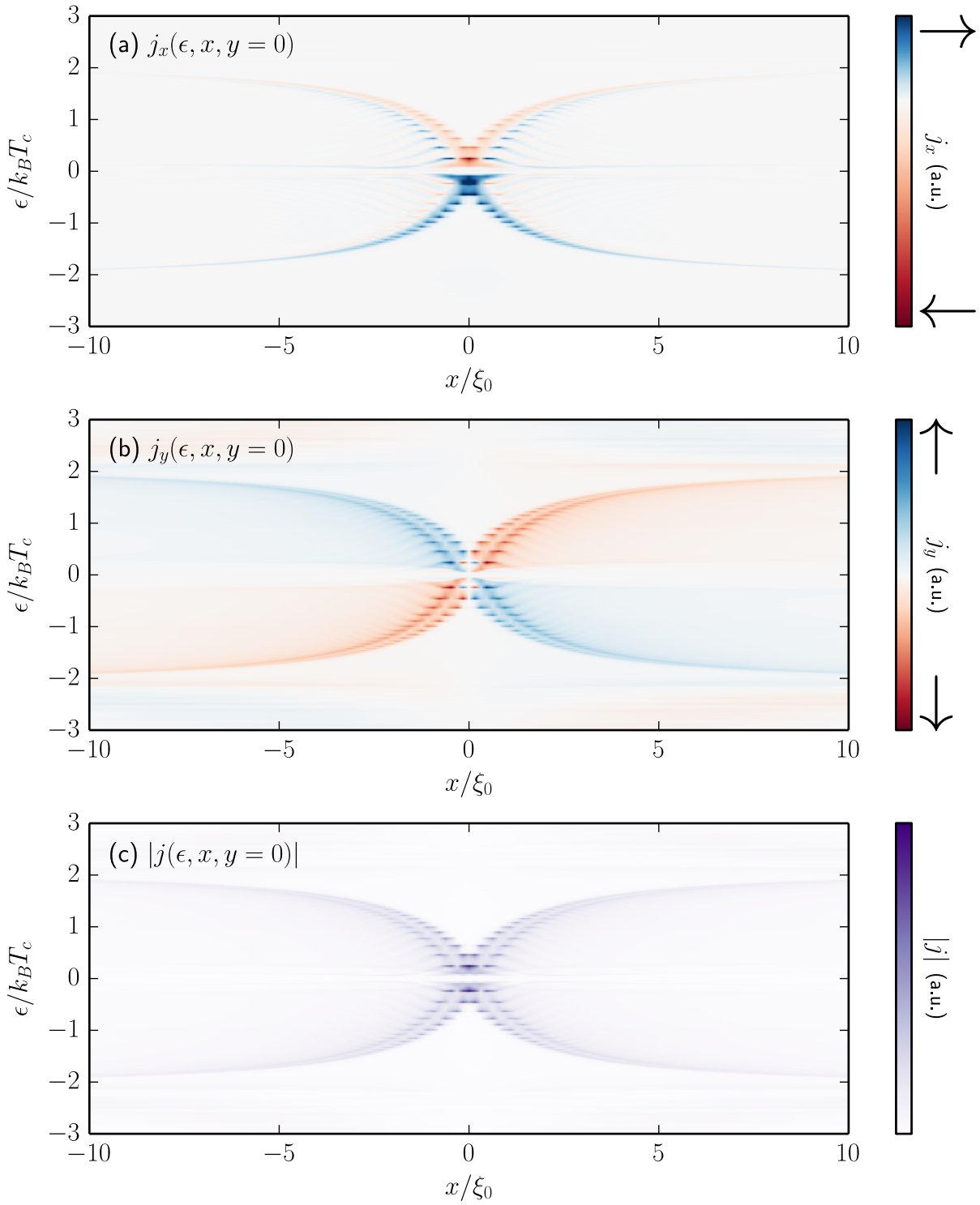

Figure 6.6: *Spatial dependence and energy dependence of the spectral current (j) along a line-cut ($y = 0$) through a d-wave Abrikosov vortex at temperature $T = 0.17T_c$. (a) The x-component, (b) the y-component and (c) absolute value of the spectral current. The figure shows that midgap states are responsible for carrying the current up until a distance $\sim 1\xi_0$ from the vortex core, while continuum states carry the current further away.*

6.3 Solenoids and flux quantization

In this section, an s-wave superconductor with a hole is studied at $T = 0.75T_c$, subject to a uniform external magnetic flux $\Phi_{\text{ext}} = (n + \delta)\Phi_0$. This flux is perpendicular to the superconducting plane, is non-zero in the hole and zero in the superconductor itself (i.e. a solenoid, see Sec. 4.3.4 for the derivation of the corresponding vector potential). Here, n represents the number of flux quanta and is varied in integer steps from 0 to 10, while δ is a "shift" varied from -2 to 2 in steps of 0.1. Figure 6.7 shows how the superconducting phase $\chi \equiv \text{Arg}\{\Delta\}$ looks for different values of n (while $\delta = 0$). The configuration with the lowest free energy is when the phase matches the number of flux quanta through the solenoid, i.e. when the phase winds as $\chi = 2\pi n$ around the hole. This is illustrated in Fig. 6.8 (a) where the free energy is plotted versus Φ_{ext}. The solid and dashed parabolas are fits to the calculated free energies, with and without the magnetic

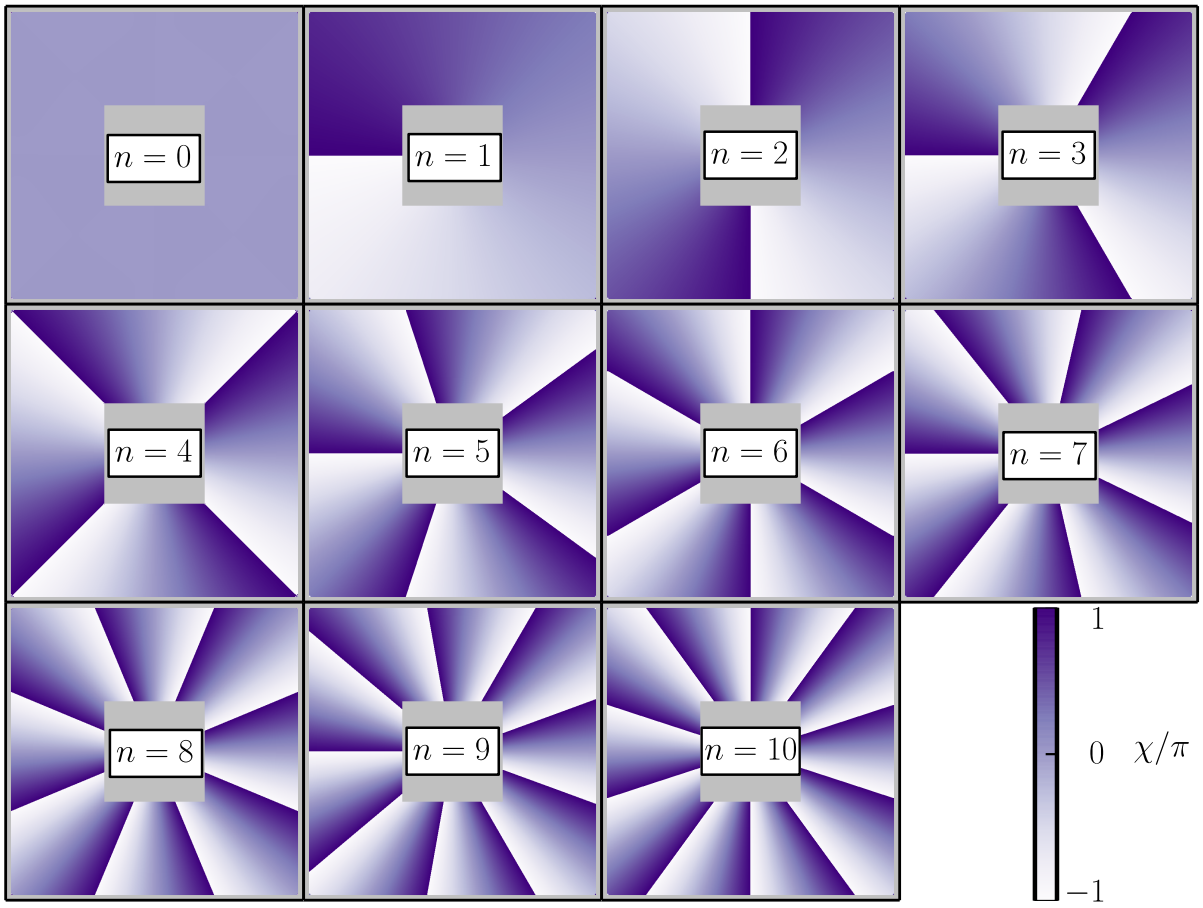

Figure 6.7: *The superconducting phase $\chi \equiv \text{Arg}\{\Delta\}$ in a grain with sidelength $60\xi_0$, for different strengths of an external "solenoid" magnetic flux $\Phi_{ext} = n\Phi_0$. Here, the external flux is non-zero in the hole and zero in the grain, and is perpendicular to the grain. The figure shows the phase winding with the lowest free energy, which corresponds to $\chi = 2\pi n$ around the hole (see Fig. 6.8).*

energy density taken into account, respectively. Figure 6.8 (b) shows that the minima in Fig. 6.8 (a) follows a parabola. In principle, the minima should lie exactly at n, but as the figures show, there is a slight deviation which grows with n. This deviation has also been verified for solenoids of various shapes at different temperatures, and for other pairing symmetries. The deviation is most probably tied to discretization errors, as shown in Fig. 6.9, where (a) the size D and (b) the discretization resolution N_x are varied. The deviation gets smaller as the lattice spacing $h \propto D/(N_x - 1)$ gets smaller. Thus, a higher spatial resolution decreases the error.

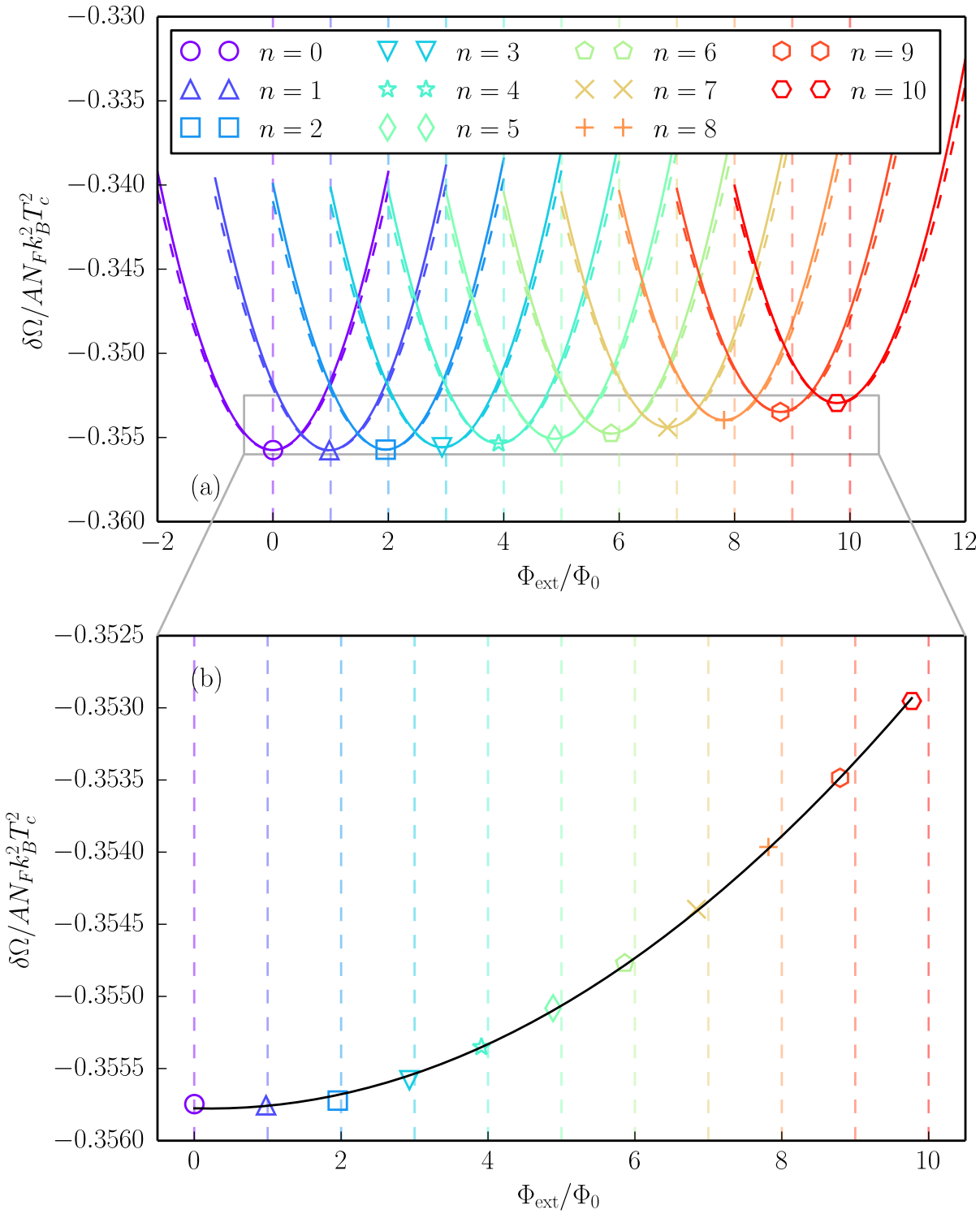

Figure 6.8: *(a) Free energy versus external magnetic flux* $\Phi = (n + \delta)\Phi_0$*, in a grain with sidelength* $60\xi_0$ *and a hole in the middle (as shown in Fig. 6.7). The external magnetic field is a "solenoid field" perpendicular to the sample (non-zero in the hole, zero in the grain). Here,* n *is varied from* 0 *to* 10*, and for each value,* δ *is varied between* ± 2 *in steps of* 0.1*, while the initial guess is an order parameter with a* $2\pi n$ *phase winding around the hole. Solid and dashed parabolas correspond to fits to the calculated free energies with and without the magnetic energy density taken into account, respectively. As is shown, the configuration with the lowest free energy is when the phase winding matches the flux quantum of the external field. (b) Parabolic fit to the minimum of each parabola in (a), the latter which is marked by the corresponding symbols.*

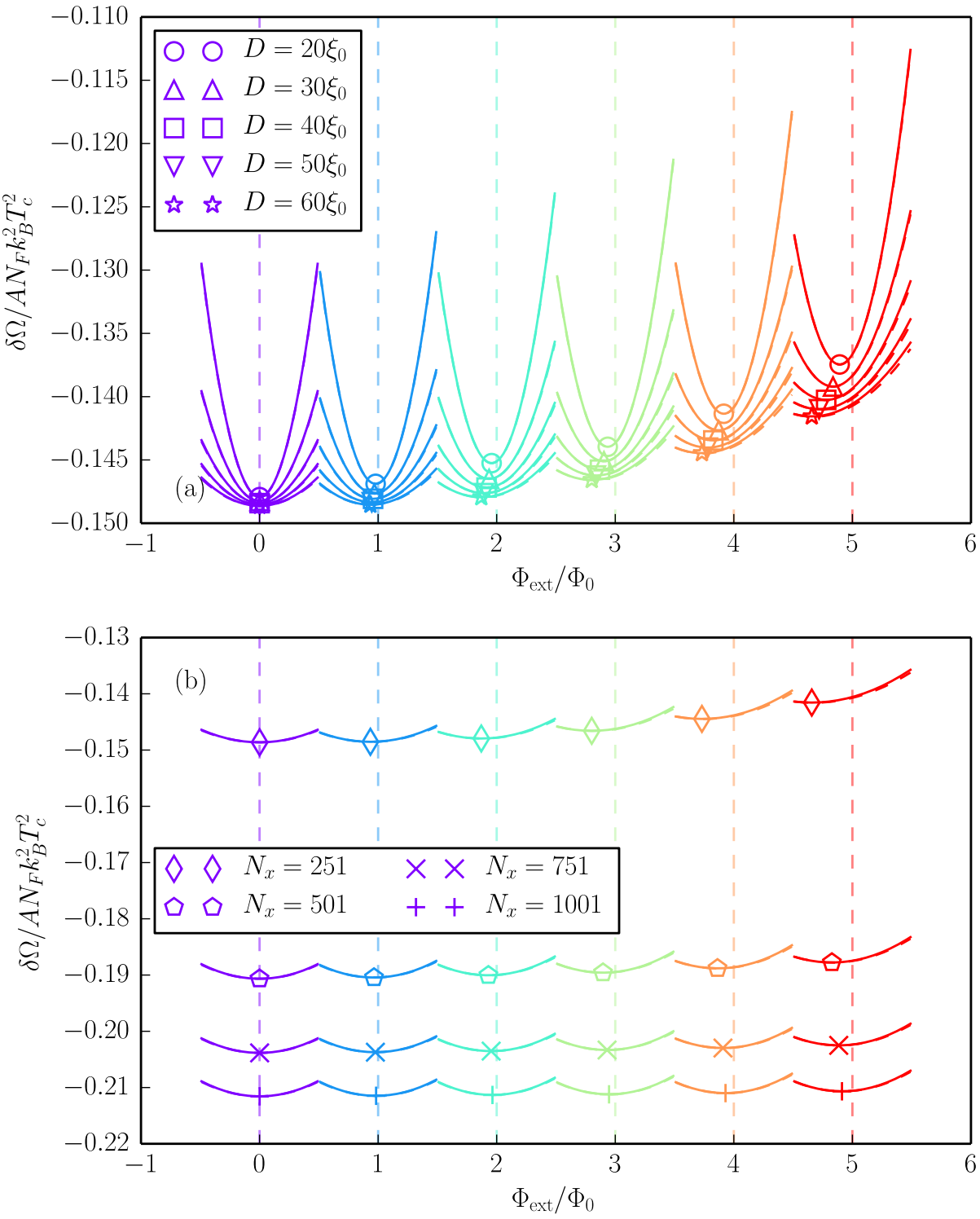

Figure 6.9: *Free energy versus external magnetic flux* $\Phi = (n + \delta)\Phi_0$*, in a grain with varying (a) sidelength* D*, and (b) discretization resolution* N_x*, as indicated by the symbols. In (b), the system side length is* $60\xi_0$*. While the free energy minimum in principle should be centered exactly at units of flux quanta, there is a deviation which scales with* n*. The figure shows that this deviation gets smaller as the lattice spacing* $h \propto D/(N_x - 1)$ *gets smaller.*

6.4 Chiral spin-triplet superconductors

This section considers a spin-triplet superconducting grain in vacuum and equilibrium. See App. F for a brief description of the quasiclassical Green functions and the Riccati equations for spin-triplet superconductors. The order parameter is assumed to have the $\hat{p}_x \pm i\hat{p}_y$ pairing symmetry

$$\Delta_{\alpha\beta}(\boldsymbol{p}_F, \boldsymbol{R}) = \boldsymbol{\Delta}_t(\boldsymbol{p}_F, \boldsymbol{R}) \cdot (\boldsymbol{\sigma} i\sigma_2)_{\alpha\beta}\,, \tag{6.9}$$

$$\boldsymbol{\Delta}_t(\boldsymbol{p}_F, \boldsymbol{R}) = \sum_\nu \Delta_\nu(\boldsymbol{R}) \boldsymbol{\eta}_{\Gamma_\nu}(\boldsymbol{p}_F), \tag{6.10}$$

$$\boldsymbol{\eta}_{p_x \pm i p_y}(\boldsymbol{p}_F) = (\hat{p}_x \pm i\hat{p}_y)\, \boldsymbol{d}, \tag{6.11}$$

$$\boldsymbol{d} = \hat{\boldsymbol{z}}, \tag{6.12}$$

where σ, σ' are spins, $\boldsymbol{p}_F$ is the Fermi momentum, $\hat{p}_x \pm i\hat{p}_y$ is the basis function in Cartesian form, and $\hat{\boldsymbol{z}}$ is perpendicular to the superconducting plane. This describes a chiral superconductor which is predicted to host spontaneous surface currents [129, 130]. The sign in Eq. 6.11 sets the chirality and thus the direction of the surface currents. Figure 6.10 shows the current magnitude in two grains of different signs, and hence different current circulation. The chiral currents follow the edge of the grain even when the shape varies, which is illustrated in Figs. 6.11 (a) and (b) for grains with holes and mesoscopic edge roughness. The circulation is opposite for internal and external boundaries, as evident in panel (a). Figures 6.11

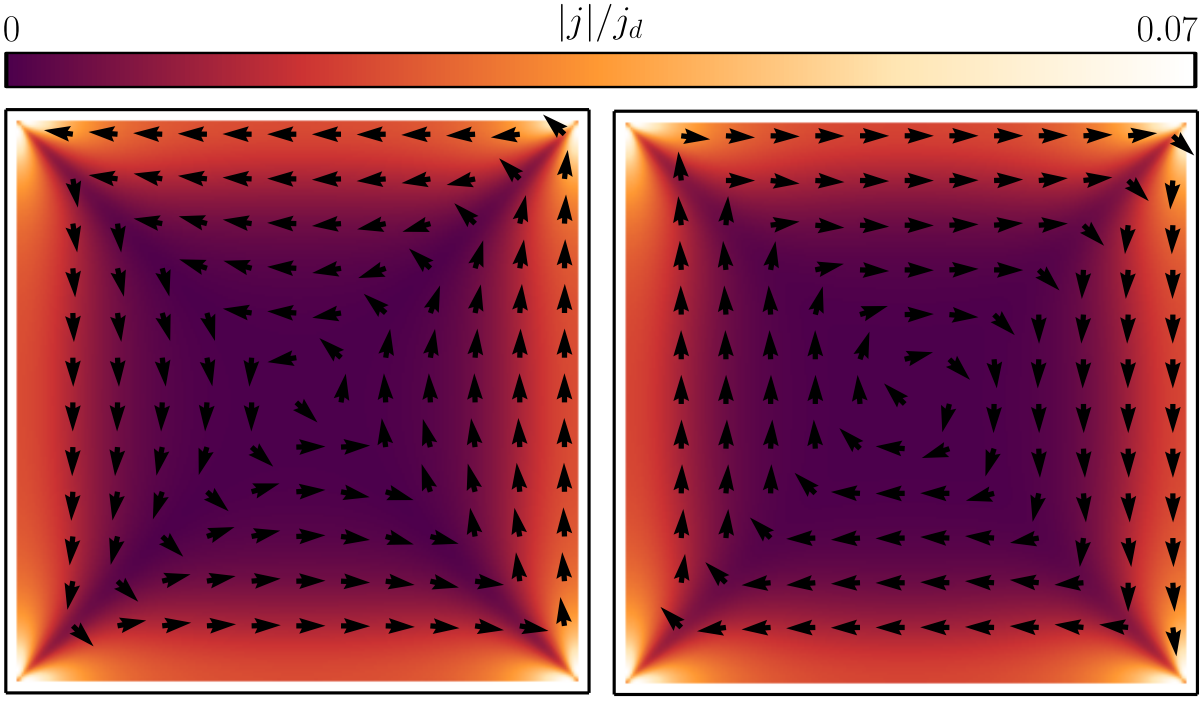

Figure 6.10: *Chiral currents in $\hat{p}_x \pm i\hat{p}_y$ spin-triplet grains. The sign, and hence the current direction, differs between the left and the right grain.*

(c) and (d) show the chiral currents in grains with an external magnetic flux applied along $-\hat{\boldsymbol{z}}$. Panel (d) shows flux entering the grain from the left and right side in a peculiar manner. To study this peculiarity further, Figure 6.12 shows the induced currents in a grain with varying external flux density in each panel. Here, the external field varies up to several flux quanta. The response is anomalous compared to the response in the spin-singlet superconductors studied in the rest of this thesis. This illustrates that there might be interesting flux quantization and magnetic field effects even when considering relatively simple mesoscopic p-wave

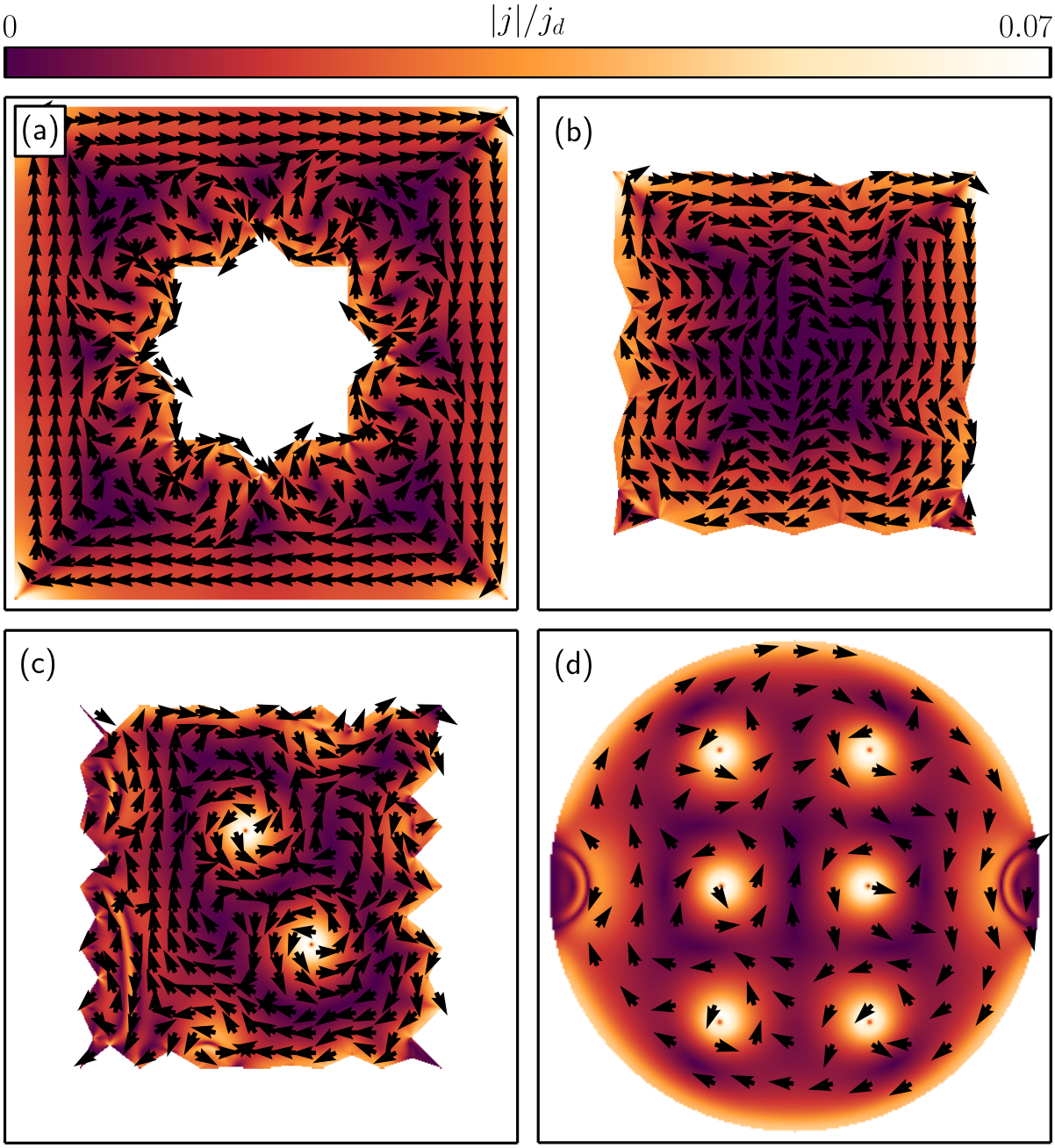

Figure 6.11: *Chiral currents in spin-triplet p-wave grains.*

grains. At the present, there is no good explanation for the behavior in the figure, and further studies are required to describe it. It is worth mentioning that these simulations were run without any self-consistency in the induced vector potential. Note that for chiral p-wave superconductors like Sr_2RuO_4 [131]

$$\kappa_0 \equiv \frac{\lambda_0}{\xi_0} = \frac{190 \text{ nm}}{66 \text{ nm}} \approx 2.6. \tag{6.13}$$

Furthermore, Sr_2RuO_4 is a multi-band superconductor [129, 130]. It is therefore questionable which systems the simple simulations above apply to.

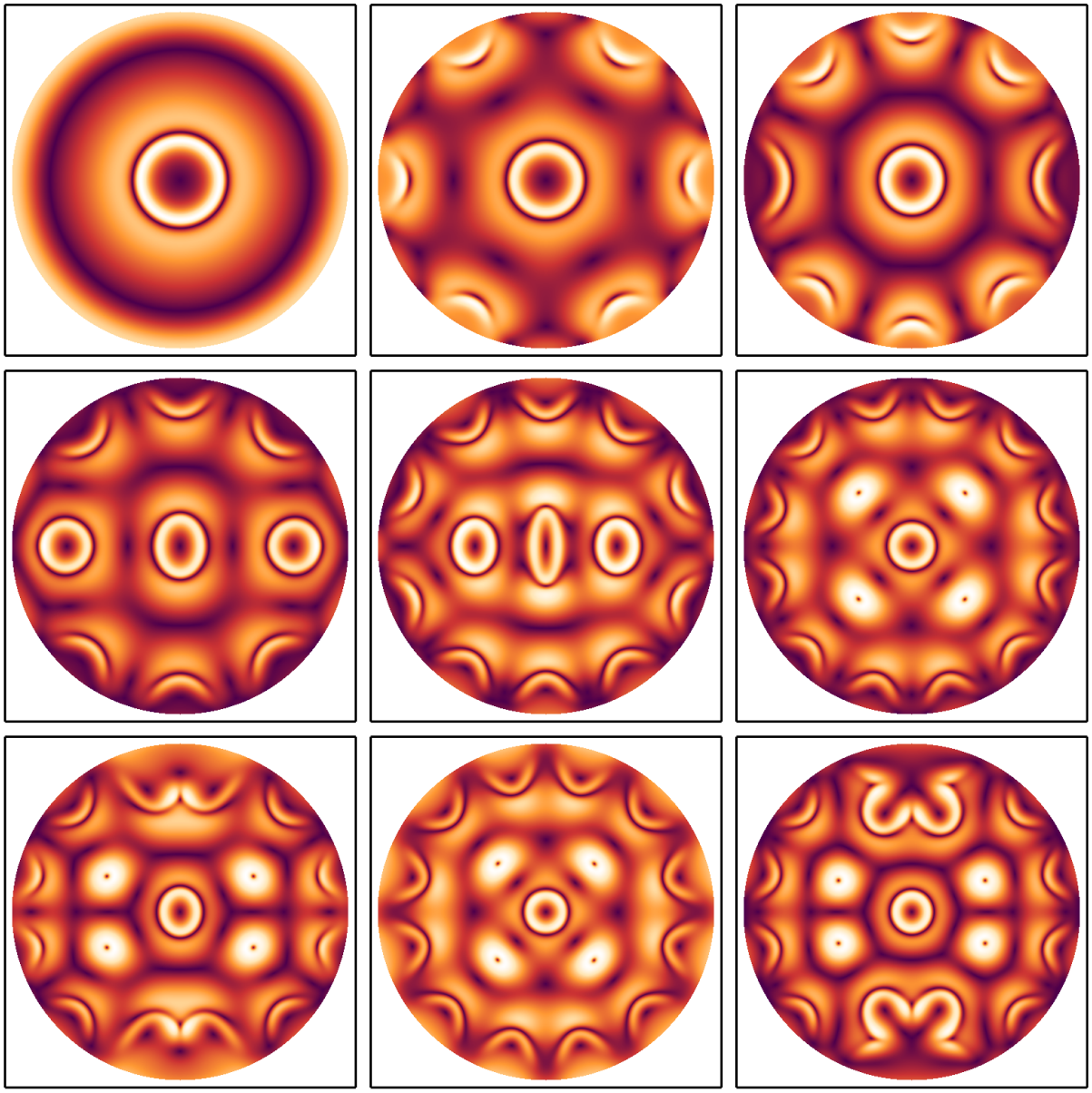

Figure 6.12: *The current magnitude when applying an external flux that increases from the top left to the bottom right panel. Several concentric rings of circulating currents can be seen, as well as "half rings" at the edges.*

7 The loop-current phase

The previous chapter showed that interfaces which are misaligned with respect to the order parameter lobes in an anisotropic superconductor (e.g. the crystal ab-axes in a d-wave superconductor), lead to a suppression of the order parameter and the breaking of superconducting pairs on a length scale of the superconducting coherence length. Such pairbreaking interfaces give rise to a high density of midgap states, also known as Andreev states, exactly at the Fermi energy [41–43]. It is energetically favorable to shift these states to finite energies, hence broadening the MGS and possibly even opening up a new gap. A mechanism providing such a shift can induce a phase transition into a new ground state with an associated broken symmetry, and thus according to Landaus theory of phase transitions, a new order parameter [44, 45]. The recently discovered phase that is the topic of this chapter, referred to as the "loop-current phase" [46–48], is related to spontaneous breaking of translational and time-reversal symmetries. It is but one out of several mechanisms proposed over the last decades [46–48, 50–54]. Many tunneling experiments show results in favor of such mechanisms [55–61], but direct experimental observation, in particular of the associated spontaneously induced magnetic fields, remains controversial [62, 63]. The loop-current phase is interesting because it offers a possible explanation to this controversy, as it predicts that the symmetry-breaking phase manifests itself as a "necklace" of circulating and counter-circulating current loops[1], that due to their intrinsic properties are very difficult to measure experimentally. Furthermore, the introduction of paper I and paper II briefly argues why this phase is believed to be a competitive mechanism. Two reasons stated are the relatively high transition temperature of $T^* \approx 0.18T_c$, and the robustness against other coupling constants, e.g. a relatively strong sub-dominant s-wave pairing channel as studied in Ref. [46].

The chapter starts by summarizing and cataloging the basic properties of the circulating currents, explaining why and how they arise. In short, the most fundamental property of the phase is a new order parameter characterized by a spontaneous superfluid momentum due to translational symmetry breaking, which drives the circulating currents. The superfluid momentum provides an energetically favorable Doppler shift to the midgap states, and is associated with a non-trivial

[1]These circulating loop currents were previously called fractional vortices and antivortices. This nomenclature is controversial, however, since it will be seen in this chapter that each circulating current has a phase winding of less than π, and a microscopic flux density. Remnants of the old terminology might still linger in a few places.

planar vector field with sources and sinks with Poincaré index (winding number) $n = 1/2$, and saddle points with $n = -1$. The latter was found out after this chapter was written and is ongoing research, which is why it will not be mentioned in this chapter. Instead, see paper I for more details. The chapter also studies how the phase is affected by different geometrical effects and external magnetic fields, as well as at extremely low temperatures. Finally, the possibility of experimental verification of the phase is discussed.

The system studied here is a clean superconducting grain in the weak-coupling limit with spin degeneracy, that is in vacuum and equilibrium, with perfectly specular boundary conditions. No spin-orbit coupling is assumed, and the order parameter is assumed to have a unitary $d_{x^2-y^2}$ pairing symmetry, where the ab-axes in general are maximally misaligned with the grain edges. The Fermi surface is assumed to be cylindrically symmetric.

7.1 What, why and how

The loop-current phase breaks translational and time-reversal symmetries through the spontaneous generation of circulating and counter-circulating current loops along the pairbreaking interfaces, as illustrated in Fig. 7.1, at temperatures below $T^* \approx 0.18T_c$. These current loops do not contain a full flux quantum, and have a phase winding that is only a fraction of 2π, as will be seen later in this section. The loop diameter of $\sim 6\xi_0$ and the period of $\sim 12.5\xi_0$ generally does not vary, neither with temperature nor with the size of the pairbreaking interface. Therefore, the number of current loops is generally proportional to the length of a pairbreaking interface. Exceptions to this due to geometric effects is studied in Sec. 7.2, and in specific circumstances due to an external magnetic field in Sec. 7.3. Note that the application of an external magnetic field breaks time-reversal symmetry explicitly. The survival of the phase under such a field (the topic of paper I), illustrates that

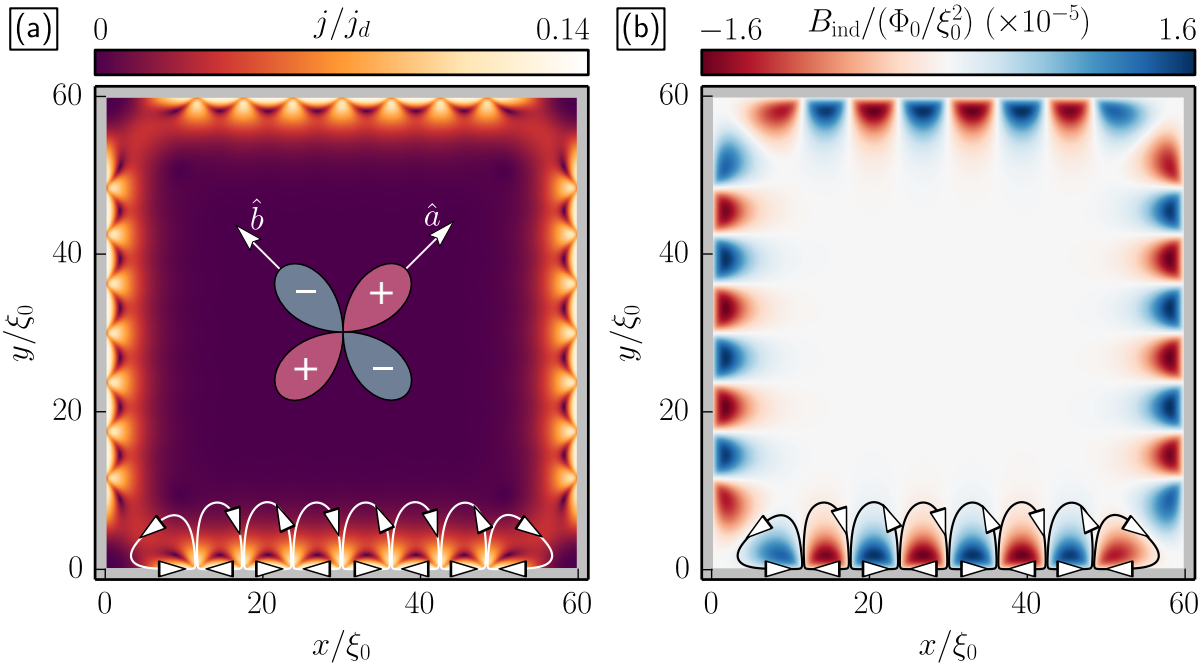

Figure 7.1: *The the circulating and counter-circulating loop current pairs of the loop-current phase in a square d-wave grain (order parameter lobes and crystal axes indicated by the graphics), with pairbreaking edges of sidelengths $D = 60\xi_0$ and at temperature $T = 0.1T_c < T^* \approx 0.18T_c$. Panel (a) shows the current density, and panel (b) the magnetic flux density induced by these currents. Lines and arrows mark the flow of the particle current (the charge current is in the opposite direction). The diameter of each current loop is roughly 5–6ξ_0. Here, the depairing current is $j_d \equiv 4\pi k_B T_c |e| N_F v_F$, and $\Phi_0 \equiv hc/2|e|$, yielding a flux of each vortex of roughly $\Phi_0 \approx 10^{-6}$–$10^{-5}\Phi_0/\xi_0$, depending on temperature. For YBCO ($\xi_0 \approx 2$ nm), this corresponds to a magnetic field of roughly 1–10 mT, distributed over an area of roughly (10 nm) × (10 nm).*

it is the translation symmetry breaking which is the fundamental property of the phase. Noether's theorem states that translation symmetry breaking leads to non-conservation of momentum. Accordingly, the order parameter of the phase is the superfluid momentum $\boldsymbol{p}_S \equiv \hbar\boldsymbol{\nabla}\chi/2 - e\boldsymbol{A}/c$ which drives the loop currents (non-locally). The temperature dependence of $p_S \equiv |\boldsymbol{p}_S|$ is shown in Fig 7.2 (a), and the energetically favorable shift of the MGS in Fig 7.2 (b). Here, the new gap is proportional to the Doppler shift

$$\delta_\epsilon \propto \boldsymbol{v}_F \cdot \boldsymbol{p}_S. \tag{7.1}$$

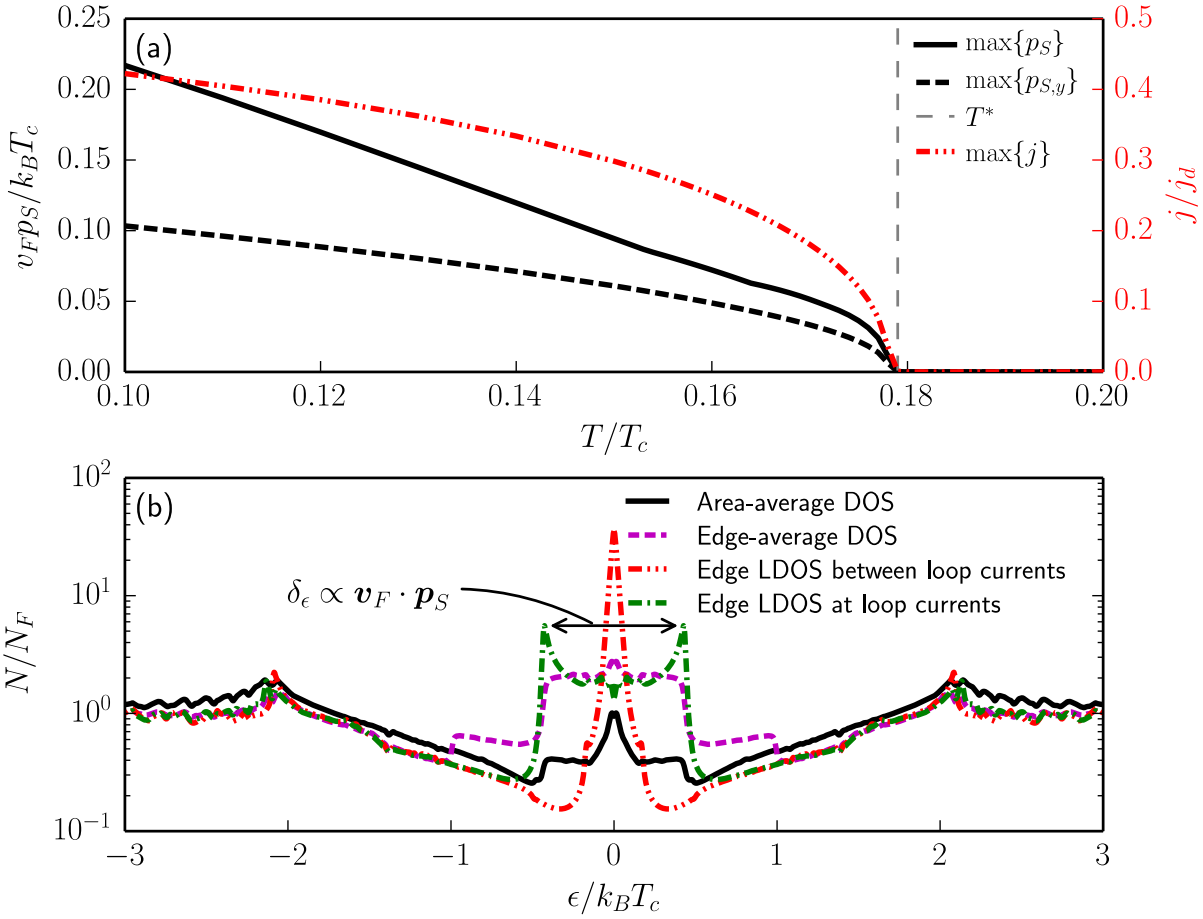

Figure 7.2: *(a) Temperature-dependence of the maximum value of the (left axis) superfluid momentum, and (right axis) current density of the loop currents, both along the edge of a maximally pairbreaking $60\xi_0 \times 60\xi_0$ grain. The superfluid momentum is the new order parameter of the loop-current phase. (b) The density of states (DOS) averaged over the same grain (solid line), and along the edge (dashed line), at $T = 0.1T_c$. Dot-dashed lines show the local density of states (LDOS) on the edge at the loop currents and between them, respectively. These dot-dashed lines show that there are MGS between the loops, and that these MGS are Doppler-shifted to finite energies. The new gap is proportional to $|\boldsymbol{v}_F \cdot \boldsymbol{p}_S|$.*

To understand why this shift is energetically favorable, consider the internal energy, which can be expressed as an energy-integral over the density of states and the occupation distribution $U \sim \int dE N(E) f(E) E$. A huge MGS peak centered at the Fermi energy with finite occupation leads to a high internal energy. Shifting these MGS symmetrically about the Fermi energy means that half of the states will be unoccupied and half occupied at a lower energy, leading to a lowering of the free energy. As Fig. 7.2 (a) showed, the magnitude of the superfluid momentum grows as the temperature is lowered, which means a stronger Doppler shift and a higher energy gain. To quantify how favorable the shift is, and to learn more about the phase-transition, Fig. 7.3 (a)–(b) shows the free energy difference, (c)–(d) the entropy difference and (e)–(f) the heat capacity difference, as a function of temperature in a grain of area $\mathcal{A} = 60\xi_0 \times 60\xi_0$. The difference is with respect to the normal state in the left column, and with respect to the metastable state (ms) in the right column. The metastable state[2] refers to a grain where the loop currents do not appear for any temperature, and thus have a higher free energy than the loop-current phase (the ground state). Results are shown both with and without an external magnetic field, and both with and without taking the magnetic energy density (MED) into account, as indicated by the legend. The overlapping of the latter results illustrates the fact that the MED gives a negligible contribution, as expected, due to a scaling with $\kappa_0^{-2} \equiv (\xi_0/\lambda_0)^2$, which is extremely small for the type-II superconductors considered. The sudden lowering of the free energy at T^* leads to a sudden change in the slope of the entropy, and hence a discontinuity in the heat capacity. The loop-current phase is thus a second-order phase transition in temperature, without an associated latent heat. The jump is a few percent of the heat capacity jump in the normal-superconducting phase transition for a d-wave superconductor (ΔC_d). The transition temperature is extracted from the heat capacity discontinuity to be

$$T^*(B_{\text{ext}} = 0, D = 60\xi_0) \approx 0.179T_c \pm 0.002T_c, \tag{7.2}$$

$$T^*(B_{\text{ext}} = 0.5B_{g1}, D = 60\xi_0) \approx 0.176T_c \pm 0.002T_c, \tag{7.3}$$

where $B_{g1} \equiv \Phi_0/\mathcal{A}$ is the first critical field of the grain. The exact method for extracting T^* is explained in detail in Sec. 7.2.4, where the heat capacity jump and T^* are found as a function of the grain size.

In the following, the different observables will be studied at $T = 0.1T_c$ in a double unit cell of the loop-current necklace. Figure 7.4 (a) shows the magnitude of the superfluid momentum, (b) the current density, (c) the induced magnetic flux density and (d) the induced vector potential. Here, $r_\parallel$ and $r_\perp$ denote coordinates

[2]Such a metastable state can be simulated by assuming a completely real order parameter, which will remain completely real throughout the self-consistent iterations as long as there is no perturbation present, for example external magnetic fields and other effects leading to phase fluctuations. Nucleating the loop-current phase thus relies on a complex order parameter and such perturbations. The phase remains if the perturbations are removed.

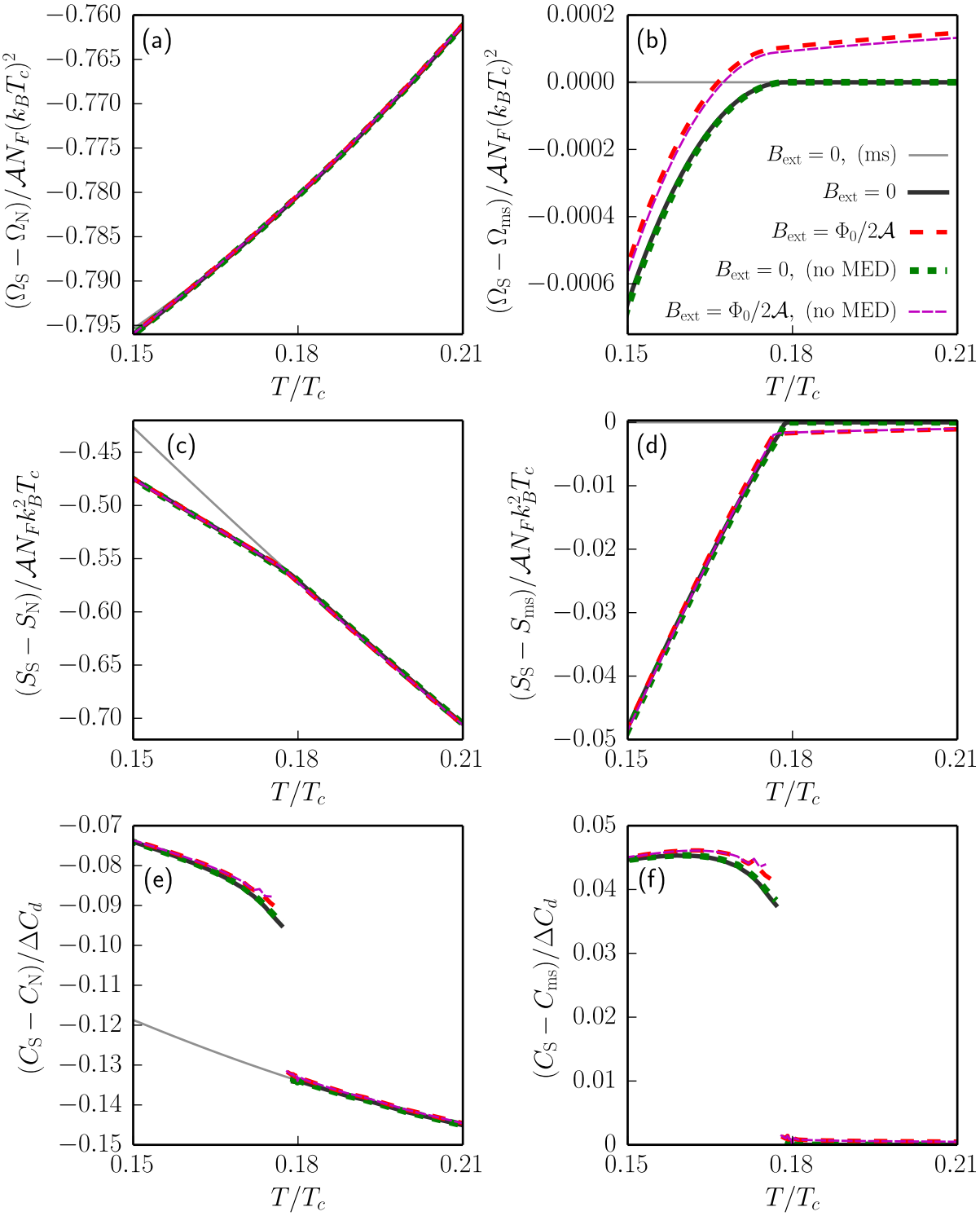

Figure 7.3: *Temperature dependence of the (a)–(b) the free energy difference, (c)–(d) entropy difference and (e)–(f) heat capacity difference. In the left column, the difference is with respect to the normal state, in the right column with respect to the metastable state (ms). Here, the meta stable state (fine solid line) does not have any loop currents at any temperature, and thus a higher free energy than the loop-current phase. Results are shown both with and without an external field of half a flux quantum spread across the grain area $\mathcal{A} = 60\xi_0 \times 60\xi_0$, as indicated by the legend. Results are also shown without taking the magnetic energy density (MED) into account. The heat capacity is in units of ΔC_d, denoting the heat-capacity jump in the normal-superconducting phase transition in a bulk sample of area $\mathcal{A}$.*

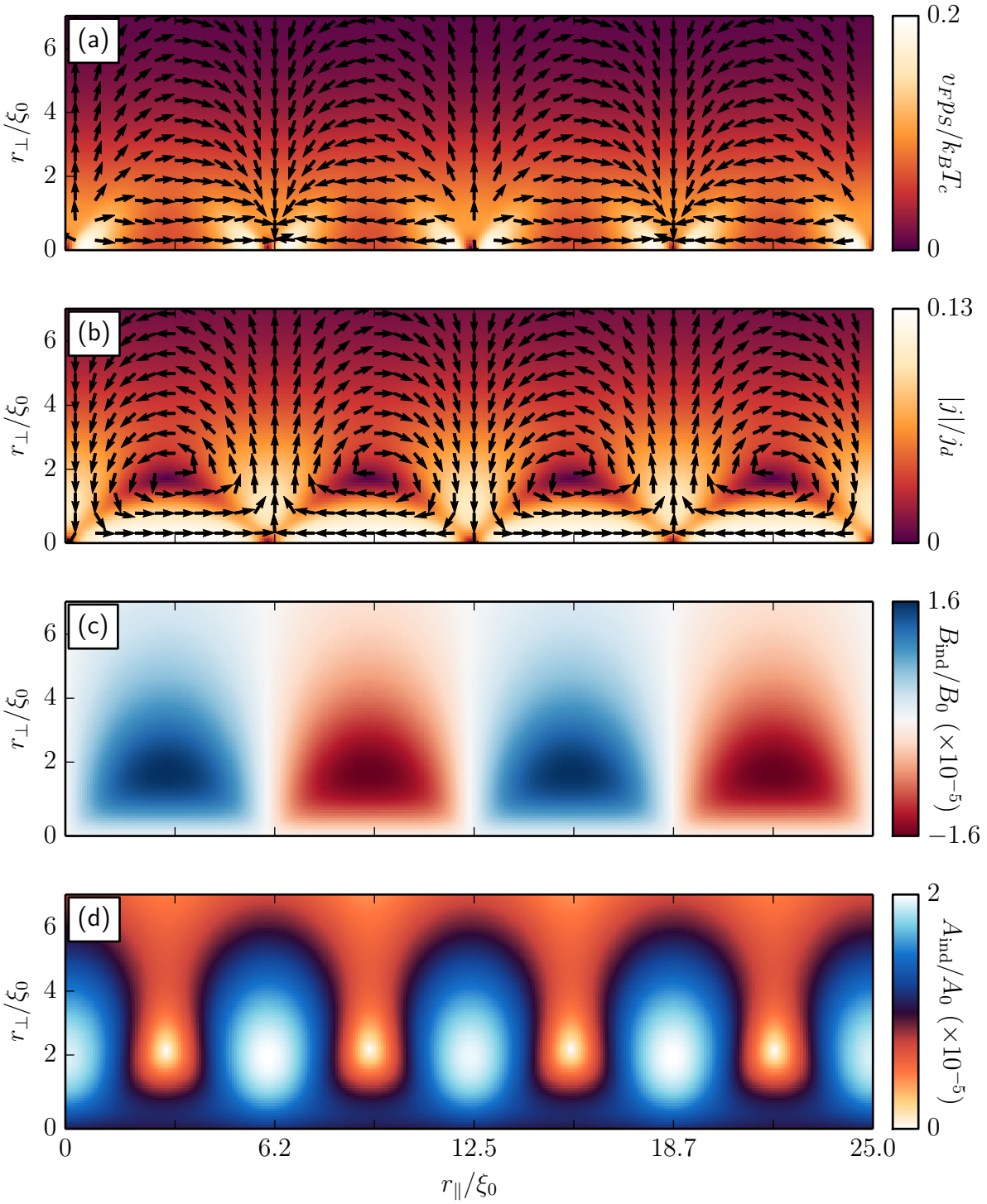

Figure 7.4: *Two loop-current unit cells at $T = 0.1T_c$, showing the (a) superfluid momentum, (b) current density, (c) induced magnetic flux density, (d) induced vector potential. Here, $B_0 \equiv \Phi_0/\xi_0^2$ and $A_0 \equiv \Phi_0/\xi_0$. Arrows mark the vector field of the respective observable.*

parallel and perpendicular to the pairbreaking interface, respectively. Arrows mark vector field of the corresponding observable. In the case of the current density, it marks the particle current, following the right-hand-rule with respect to the induced fields (the charge current is in the opposite direction). As can be seen, nodes and anti-nodes form on and between loop currents, respectively. This is where MGS are shifted and unshifted, respectively, as will be seen later in this section. It is interesting to note that there is a chain of sources and sinks in the superfluid momentum, generating a vector field which looks exactly the same as the vector field due to a chain of dipoles. The stiffness of the vector field increases with decreasing temperature. The "charge" and the source-sink-separation distance are the two fundamental parameters of the field, and the question is how to interpret and derive these analytically. Furthermore, there is a non-local response in the current density due to the superfluid momentum. Again, it is seen in panel (c) that the flux density per loop is on the scale of $10^{-5}\Phi_0/\xi_0^2$ (at higher temperatures $T = 0.17T_c$, it is on the scale of $10^{-6}\Phi_0/\xi_0^2$). Figures 7.5 (a) and (b) show the corresponding parallel and perpendicular components of the superfluid momentum, and Figs. 7.5 (c) and (d) the same but for the current density. Here, positive values (blue) implies flow to the right for the parallel component and up (away from the pairbreaking interface) for the perpendicular component, and the opposite directions for negative values (red). The superconducting order parameter magnitude, phase, real part and imaginary part are shown in Figs. 7.6 (a)–(d), respectively. There is an oscillation in both the magnitude and the phase of the order parameter, somewhat similar to the Fulde-Ferrell-Larkin-Ovchinnikov phase [133–135]. Note that the phase winds less than 2π, which indicates that the loop currents are not associated with e.g. Abrikosov vortices. The instability mainly arises in the imaginary part. This because the solution was converged by starting with a completely real order parameter, which was converged to the bulk value with machine precision, followed by a perturbation with magnetic field annealing. The oscillations are arguably easier to see in line plots, which is why the magnitude and phase are plotted in Figs. 7.7 (a) and (b), respectively, and the real and imaginary parts in Figs. 7.8 (a) and (b), respectively. Here, the color of the line indicates the value of $r_\perp$ for the respective line cut. Vertical solid and dashed lines show nodes and anti-nodes, between and through loop currents, where where MGS are shifted and unshifted, respectively. Exactly at the edge and in the corners, superconductivity is suppressed. The line $r_\perp = 0$ contains noise and appropriately has white color and is therefore not visible. This noise is most probably caused by interpolation errors exactly at the edge, and the major inhibitor in the convergence of the self-consistent iterations. Note that the phase is not entirely sinusoidal, as it contains some higher modes. Closer to the transition temperature, however, the oscillations in the phase, and therefore the superfluid momentum, can be well-approximated by sinusoids. This is a useful ansatz in making an analytic approach to studying this phase.

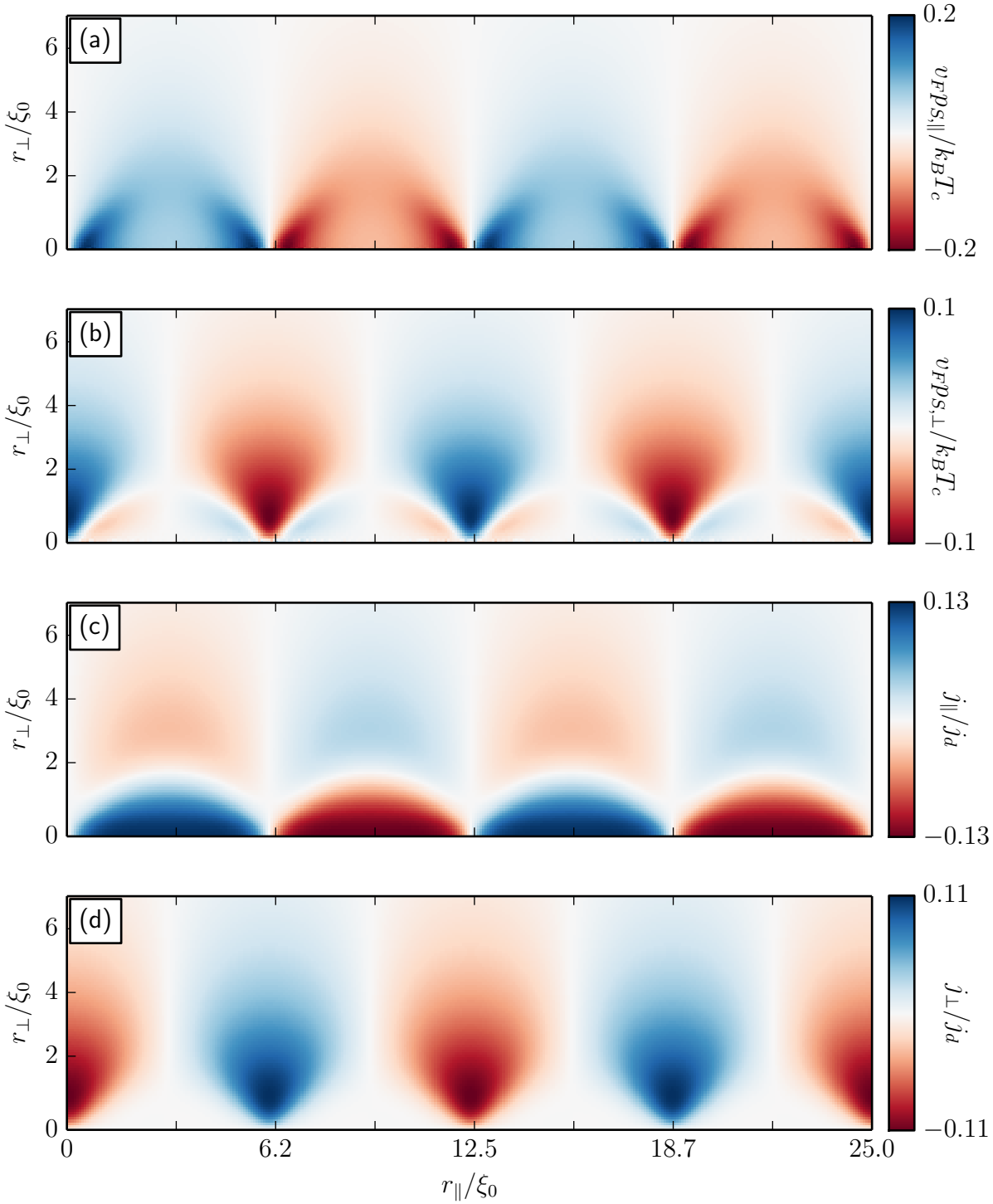

Figure 7.5: *Two loop-current necklace unit cells at $T = 0.1T_c$, showing the parallel and perpendicular (to the pairbreaking interface) components of the (a)–(b) superfluid momentum, (c)–(d) current density. Positive values (blue) mark flow to the right and up away from the interface for the parallel and perpendicular components, respectively, and the opposite directions for negative values (red).*

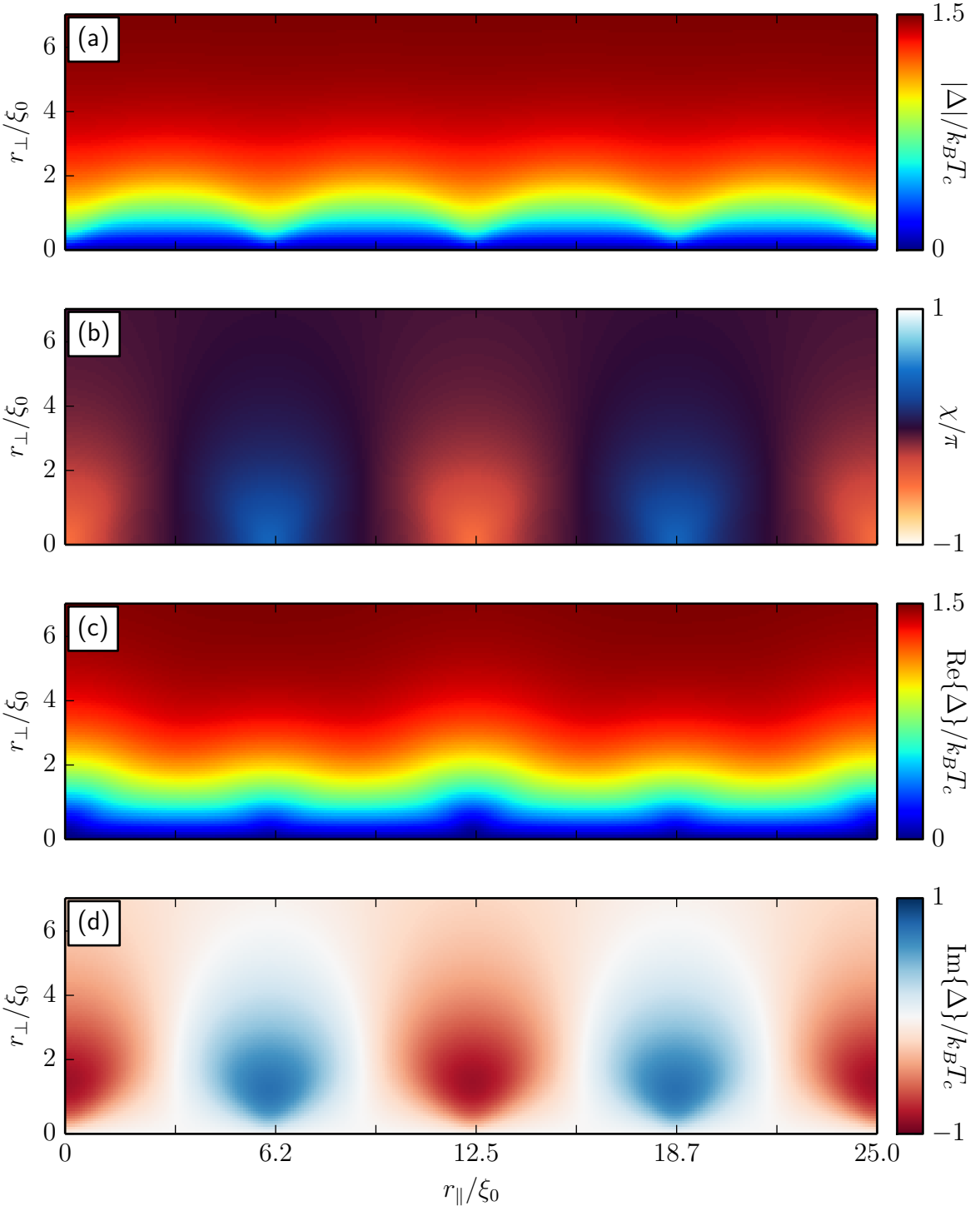

Figure 7.6: *Two loop-current necklace unit cells at $T = 0.1T_c$, showing the superconducting order parameter (a) magnitude, (b) phase, (c) real part, (d) imaginary part. Note that the phase winding is less than 2π, and that the bulk d-wave value is $\Delta_0 \approx 1.51 k_B T_c$. The maximal gap is a factor $\sqrt{2}$ larger than this, i.e. $\max\{|\Delta_d|\} \approx 2.14 k_B T_c$. This is because the factor $\sqrt{2}$ is absorbed in the basis function to make it normalized.*

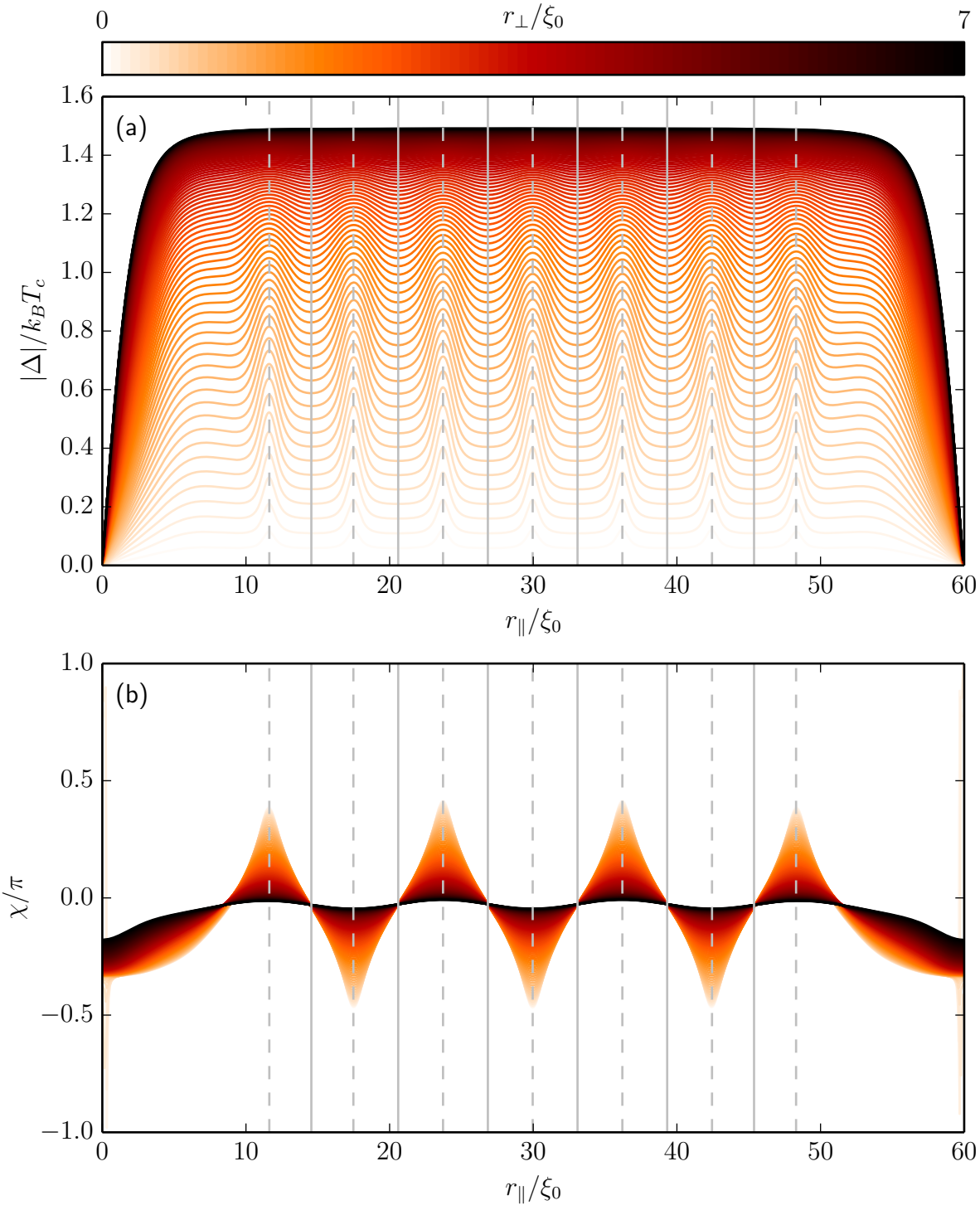

Figure 7.7: *The superconducting order parameter (a) magnitude and (b) phase along a pairbreaking interface, at different distances from the interface, as indicated by the colors. The grain is* $60\xi_0 \times 60\xi_0$*, and the temperature is* $T = 0.1T_c$*. Vertical solid and dashed lines indicate cuts through and between loop currents, referred to as nodes and anti-nodes, respectively.*

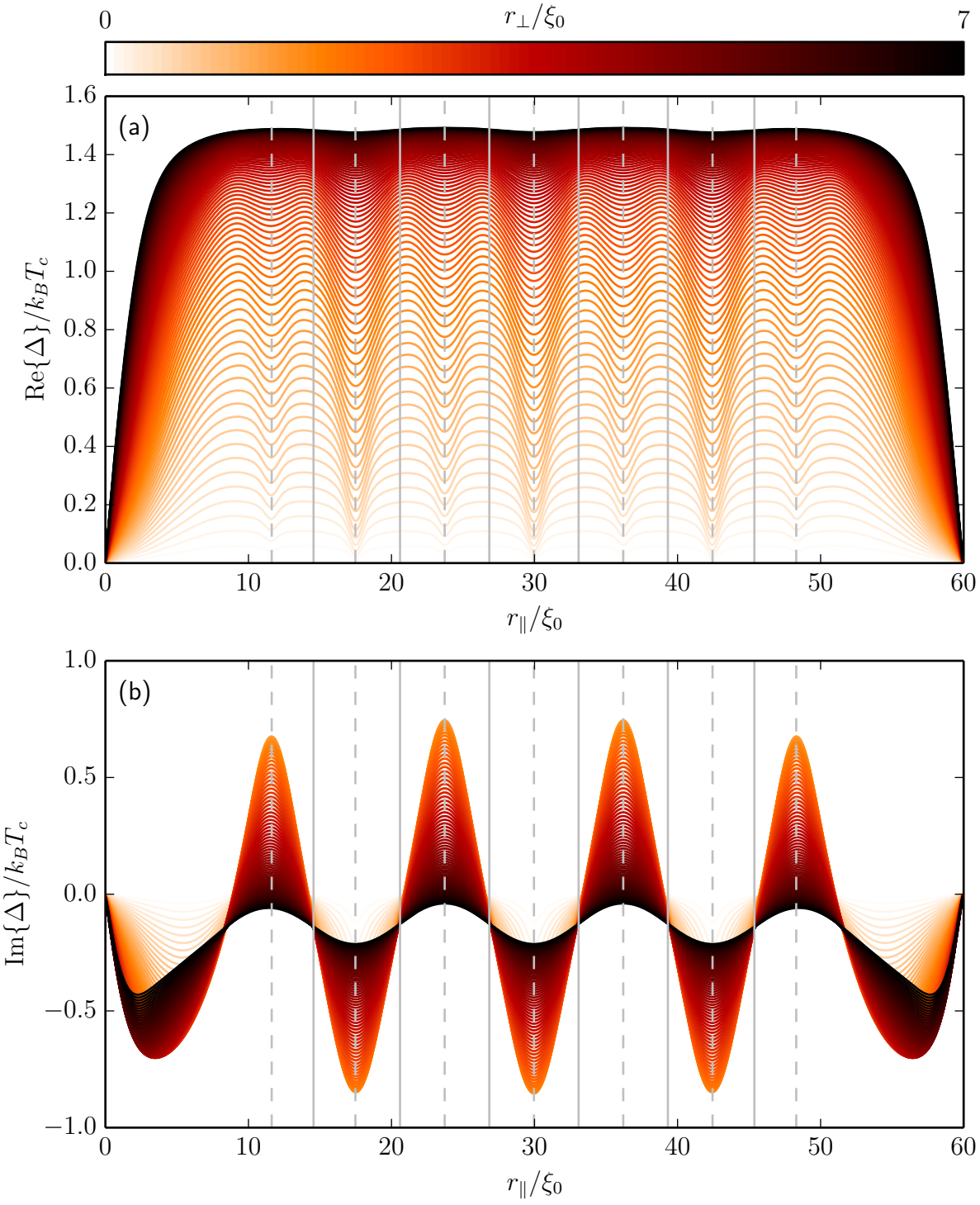

Figure 7.8: *The order parameter (a) real part and (b) imaginary part along a pairbreaking interface, at different distances from the interface, as indicated by the colors. The grain is* $60\xi_0 \times 60\xi_0$*, and the temperature is* $T = 0.1T_c$*. Vertical solid and dashed lines indicate cuts through and between loop currents, referred to as nodes and anti-nodes, respectively.*

Finally, the spectral observables are studied. Figure 7.9 shows the LDOS versus $r_\parallel$ and $r_\perp$ at different energies $\epsilon = 0$–$0.5 k_B T_c$ as indicated by the labels, and Fig. 7.10 shows the LDOS versus $r_\parallel$ and ϵ, at different values of $r_\perp$ as indicated by the labels. At low energies, there are huge densities of MGS between loop currents. At higher energies, the states shift toward the loop currents, and finally gets smeared more or less homogeneously across the sample. Figure 7.11 shows the spectral current component that is parallel to the interface ($j_\parallel$) versus $r_\parallel$ and $r_\perp$ at different energies $\epsilon = 0.1$–$0.5 k_B T_c$ as indicated by the labels, and Fig. 7.12 shows $j_\parallel$ versus $r_\parallel$ and ϵ, at different values of $r_\perp$ as indicated by the labels.

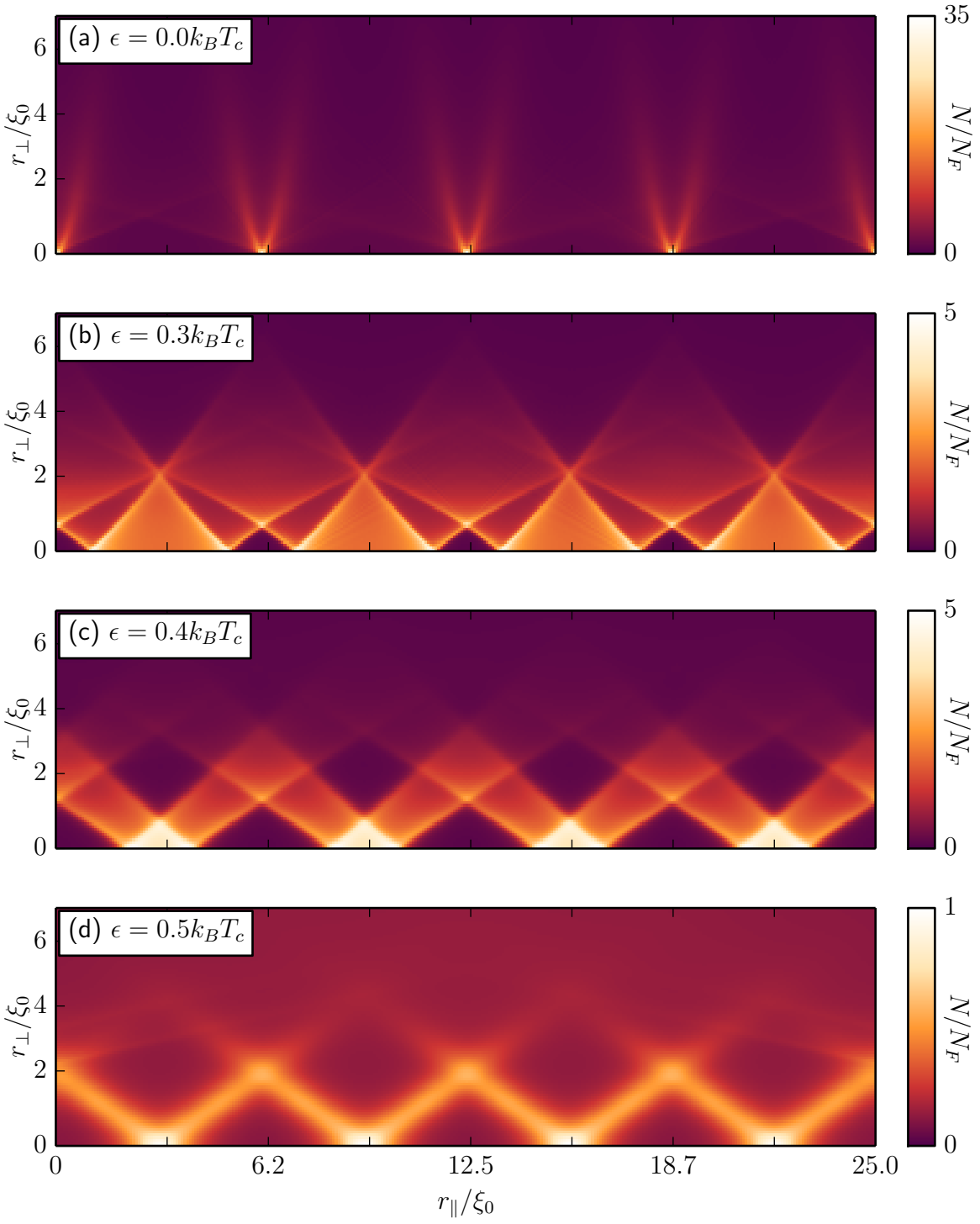

Figure 7.9: *Two loop-current necklace unit cells at $T = 0.1T_c$, showing the LDOS at different energies, as indicated by the labels. Note the varying color scales.*

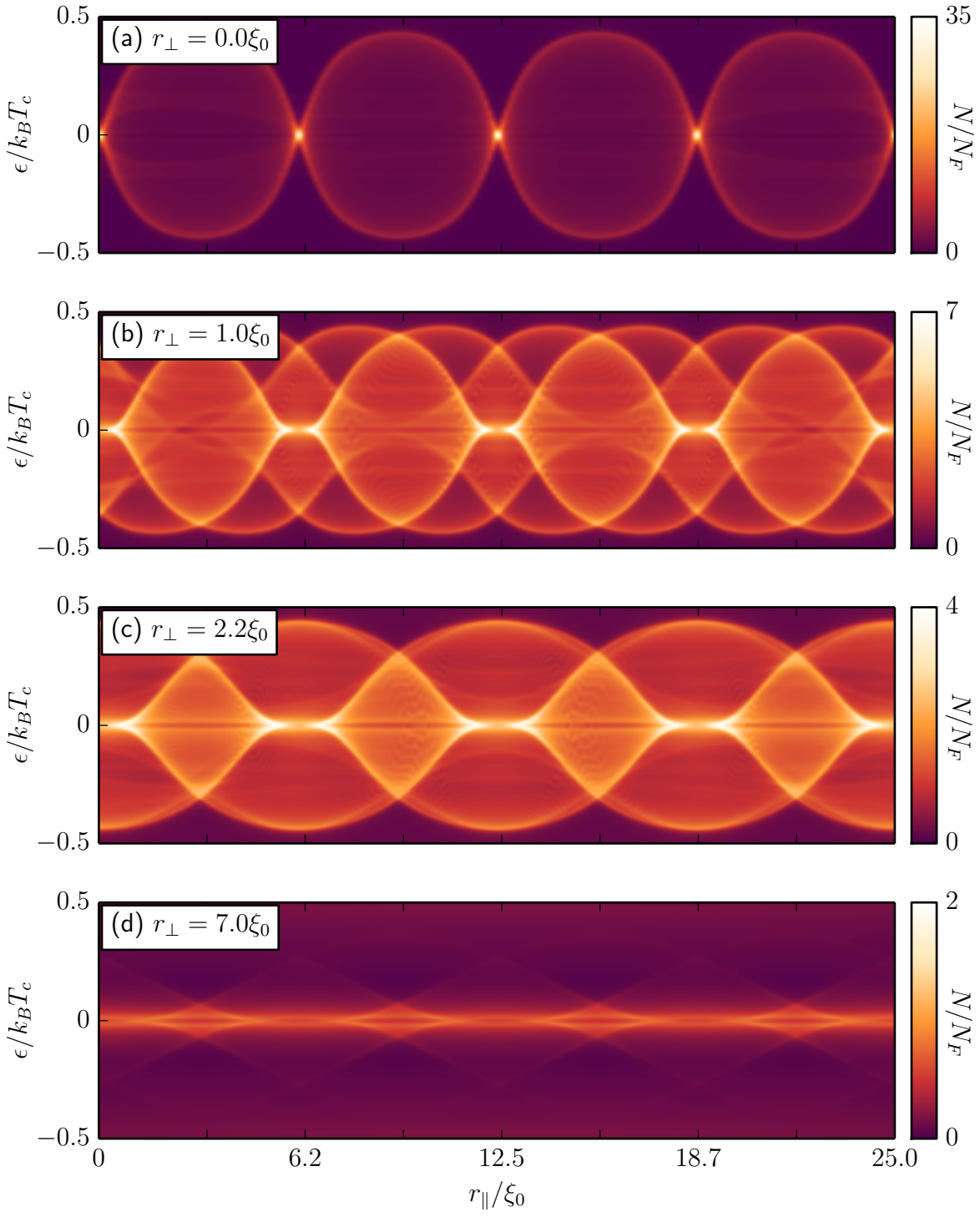

Figure 7.10: *The LDOS versus energy and along the pairbreaking interface, at different distances from the pairbreaking interface as indicated by the labels. Note the varying color scales.*

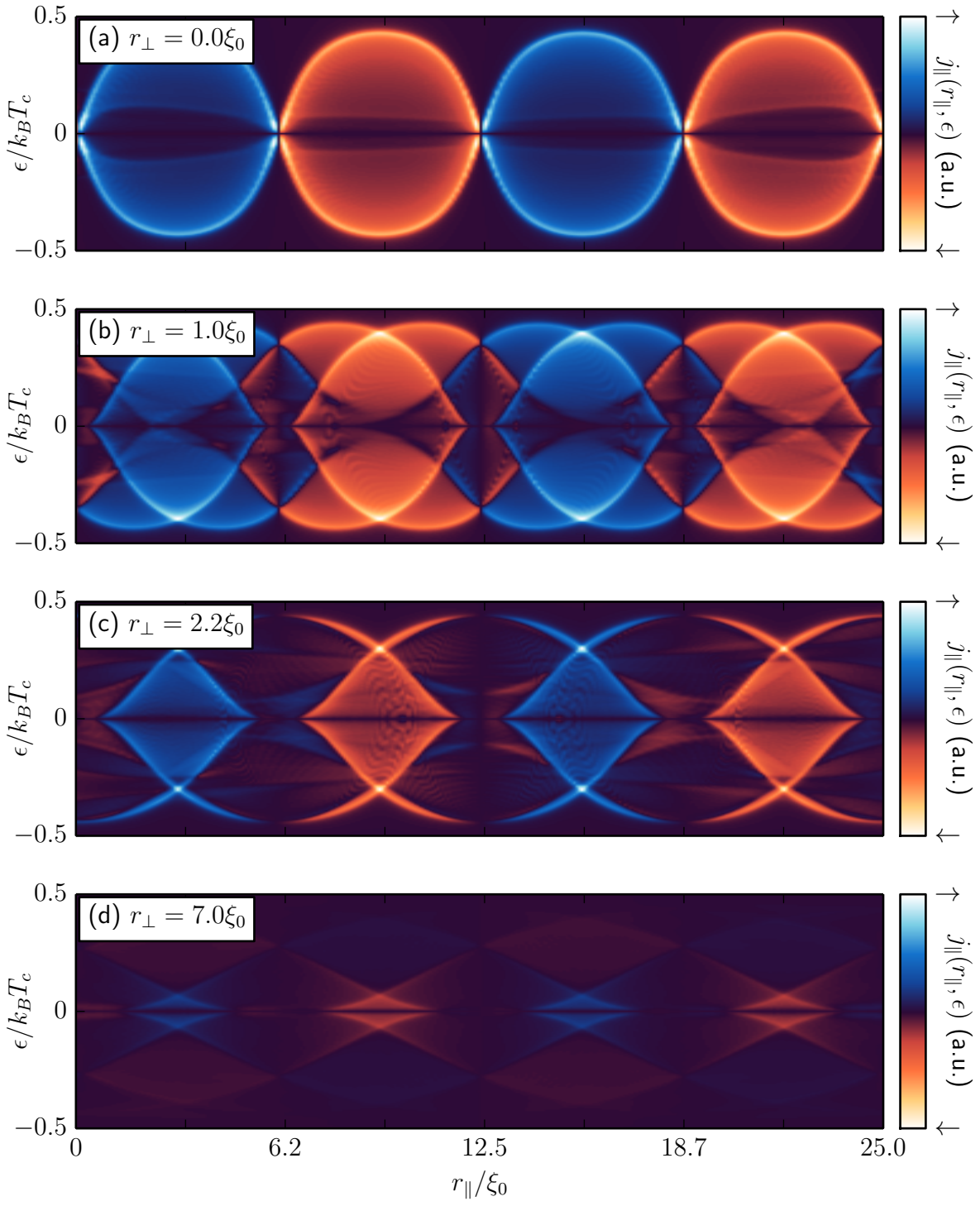

Figure 7.11: *Two loop-current necklace unit cells at $T = 0.1T_c$, showing the spectral current component that is parallel to the interface ($j_\parallel$), at different energies, as indicated by the labels. Colors indicate the direction of the current.*

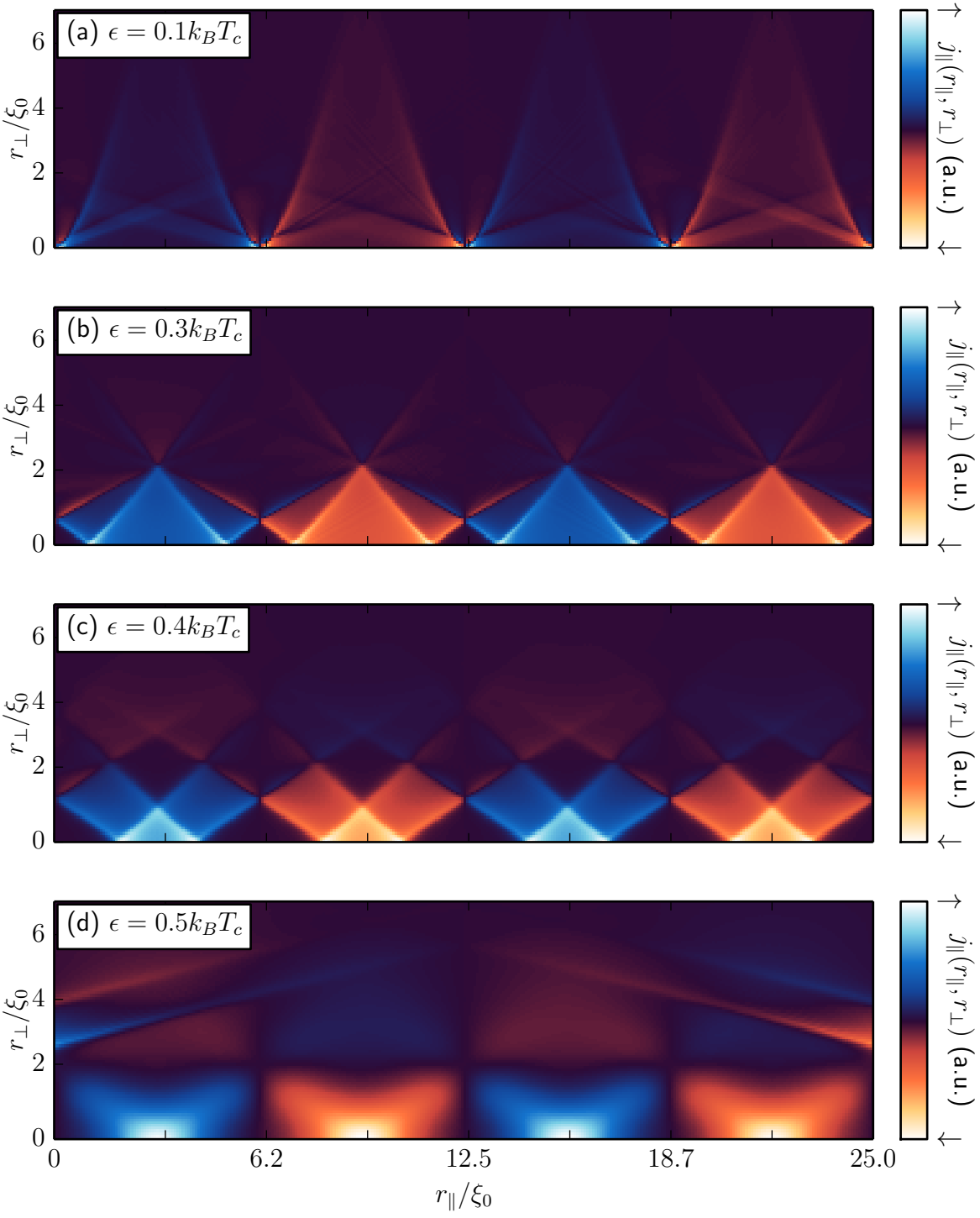

Figure 7.12: *The spectral current component that is parallel to the interface ($j_\parallel$), versus energy, at different distances from the pairbreaking interface as indicated by the labels. Colors indicate the direction of the current.*

7.2 Geometric effects

This section studies how the loop currents are affected by grain shape, surface roughness, the edges-to-crystal-axis angle (denoted θ), as well as the grain size. The first two effects are studied in a more qualitative way, to illustrate that the phase can exist even when the system does not have perfect edges. The latter two effects will be studied to quantify this fact through phase diagrams. Finally, the size-dependence of a single pairbreaking interface is studied, which is the main topic of paper II. The main conclusion is that the phase has a tendency to form at *any* pairbreaking interface, as long as

- the interface is sufficiently mis-aligned with the crystal *ab*-axis,
- there is sufficient space around the interface for the loop currents to nucleate.

A main result is also that the system will try to average out the induced flux to zero (in the absence of external fields), but that when forced to, it will rather shift midgap states at the expense of having a net flux.

7.2.1 Different shapes

Figure 7.13 shows the current distribution in superconducting grains shaped like the logotype of the Chalmers Department of Microtechnology and Nanoscience (MC2). This is a qualitative demonstration that the simulation tool used can create superconducting grains of any two-dimensional shape that is simply connected (with or without holes). Figure 7.14 shows the induced magnetic flux density in different systems at temperature $T = 0.1T_c < T^*$. The flux is induced spontaneously by loop currents. In each system, the crystal *ab*-axis are rotated 45° relative to the figure. What is clearly seen is that the loop currents appear at any interface that has an angle $\theta \sim 45°$ to the crystal *ab*-axis (more specifically, $25° < \theta < 70°$, as will be seen in Sec. 7.2.3), even if the interface is rounded or irregular. This is illustrated more profoundly in the next sections.

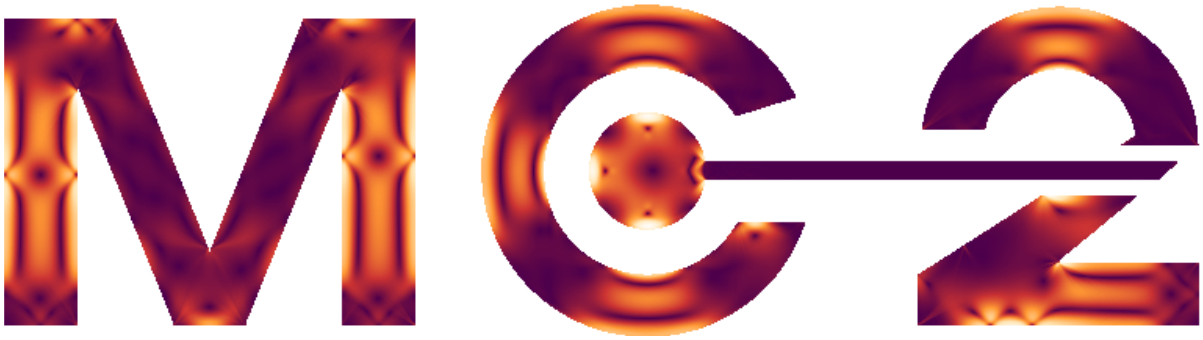

Figure 7.13: *Current distribution in SC grains shaped like the Chalmers MC2 logo.*

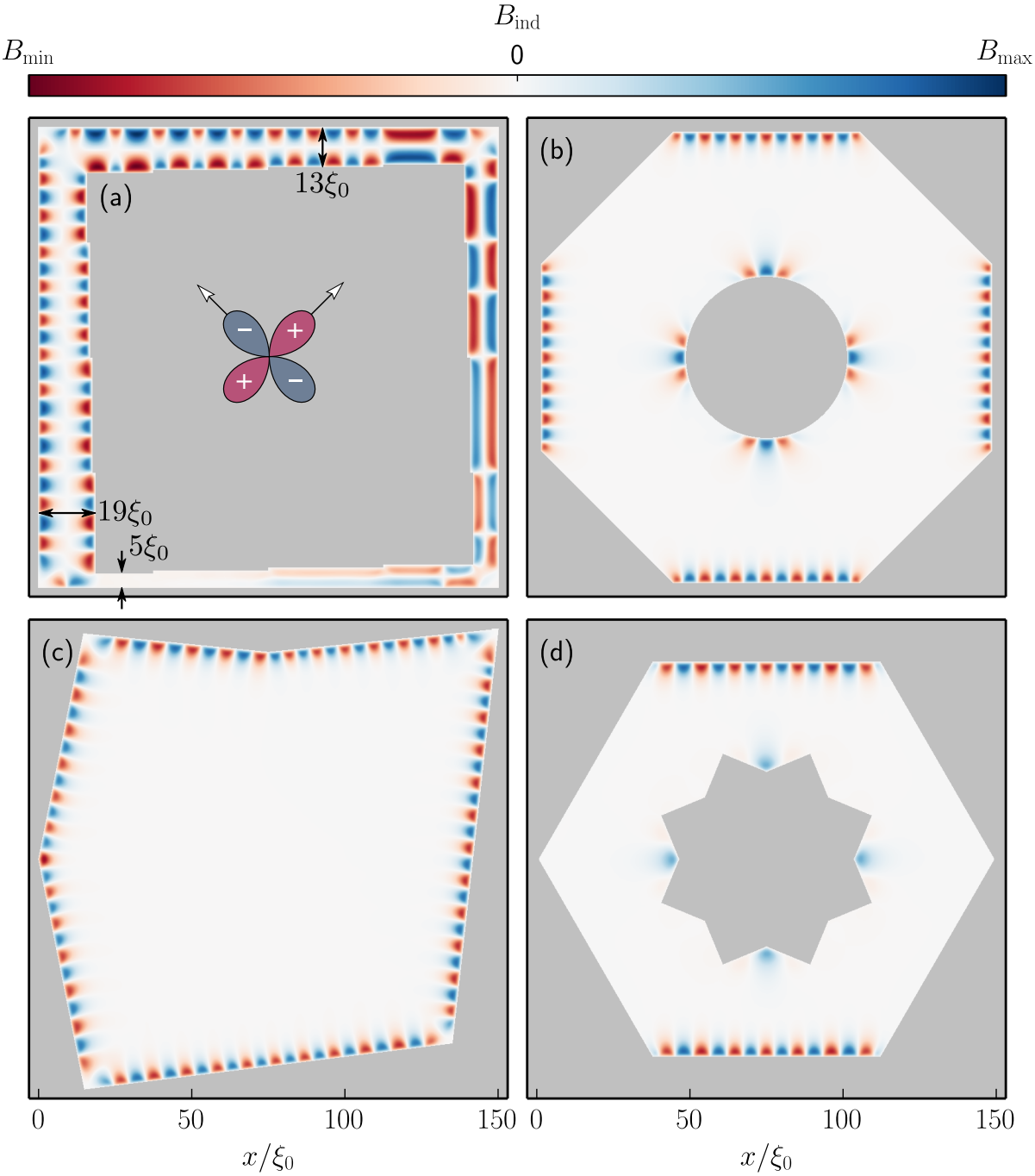

Figure 7.14: *Induced flux density in grains of various shapes, at temperature* $T = 0.1T_c$. *The gray area around and inside each grain is vacuum, and the crystal ab-axis is rotated* 45° *relative to the edges of the page, as indicated in panel (a). In panel (a) the SC grain is a square with a square hole, with a thickness that varies around the grain, from* $4.7\xi_0$ *to* $18.7\xi_0$. *In the bottom and right parts, the system is in the Vorontsov phase, but as the thickness increases to* $> 12.5 \pm 0.5\xi_0$, *the loop-current phase is induced. Note that the critical thickness of* $\sim 12.5\xi_0$ *is consistent with previous results [46], and is the size of one loop-current unit cell along the pairbreaking edge. In panel (a)* $B_{min,max} \approx \pm 2 \times 10^{-5}\Phi_0/\xi_0^2$, *and in panels (b)–(d)* $B_{min,max} \approx \pm 6 \times 10^{-6}\Phi_0/\xi_0^2$.

7.2.2 Surface roughness

This section briefly studies how the loop-current phase is affected by mesoscopic surface roughness, referring to surface irregularities that scatter specularly and have a size comparable to the superconducting coherence length, as illustrated in Fig. 7.15 (a). Figures 7.16 and 7.17 show several systems with mesoscopic surface roughness of varying shape and regularity, with side-lengths $150\xi_0$ and $60\xi_0$, respectively. It turns out that the relevant parameters for the loop currents to form are the edge-to-crystal-axes angle, as well as the size of the irregularities [Fig. 7.15 (b)].

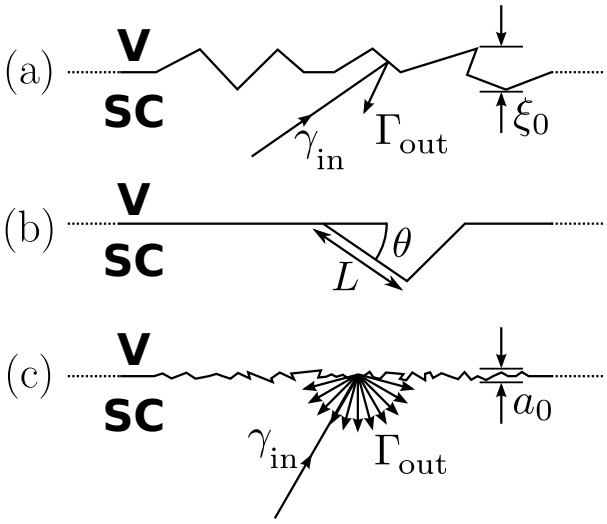

Figure 7.15: *(b) Mesoscopic roughness on the order of the superconducting coherence length, where the roughness consists of surface irregularities that scatter specularly. (b) For the loop-current phase, the relevant parameters of the mesoscopic roughness are the size of the irregularities and the angle with respect to the crystal ab-axis. (c) Microscopic roughness, coupling every incoming scattering trajectory to every outgoing one.*

Microscopic roughness, in contrast, refer to irregularities on the atomic scale [Fig. 7.15 (c)]. The atomic scale is generally beyond the scope of quasiclassical theory, but microscopic surface roughness can still be modeled as a diffuse boundary condition, where each incoming trajectory is scattered into every possible outgoing trajectory (with some weight distribution) [40, 136–140]. A specularity parameter can be introduced to quantify the degree of microscopic roughness, with a value ranging from 0 to 1 corresponding to completely diffuse and specular reflection, respectively. Such a parametrization was used to study the Vorontsov phase [53], showing a gradual suppression of the phase for reduced specularity, and a complete suppression below $\sim 20\%$ specularity [65]. It would be surprising if the loop-current phase showed a different dependence, since what seems to be important for both phases is the amount of midgap states. As the system becomes more diffuse or dirty, these MGS are broadened. What probably happens is that for higher diffusivity, there are not enough states close to zero energy to shift, and there will be no symmetry-breaking phase (with this reasoning, systems with non-magnetic impurities might behave the same way). This is exactly what happens when the angle between the crystal *ab*-axis and the system edge varies, which will be shown in the following section.

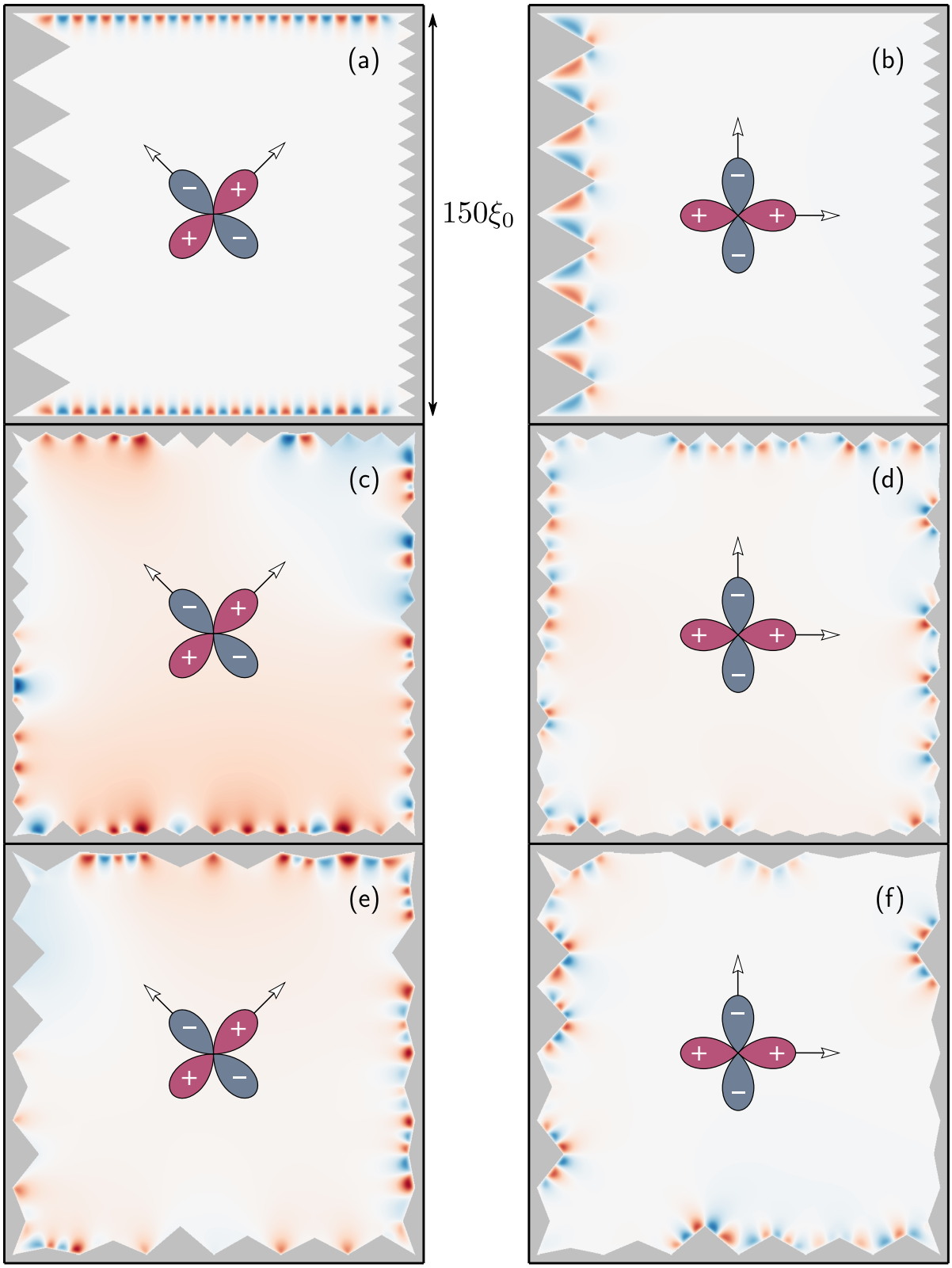

Figure 7.16: *Induced flux density in grains with mesoscopic surface roughness, at temperature $T = 0.1T_c$. The maximum induced flux density is roughly $10^{-5}\Phi_0/\xi_0^2$. Loop currents form wherever there is enough space and the edge is sufficiently misaligned with respect to the crystal ab-axis. The large red regions in panel (c) are probably remnants from the magnetic field used to nucleate the loop currents.*

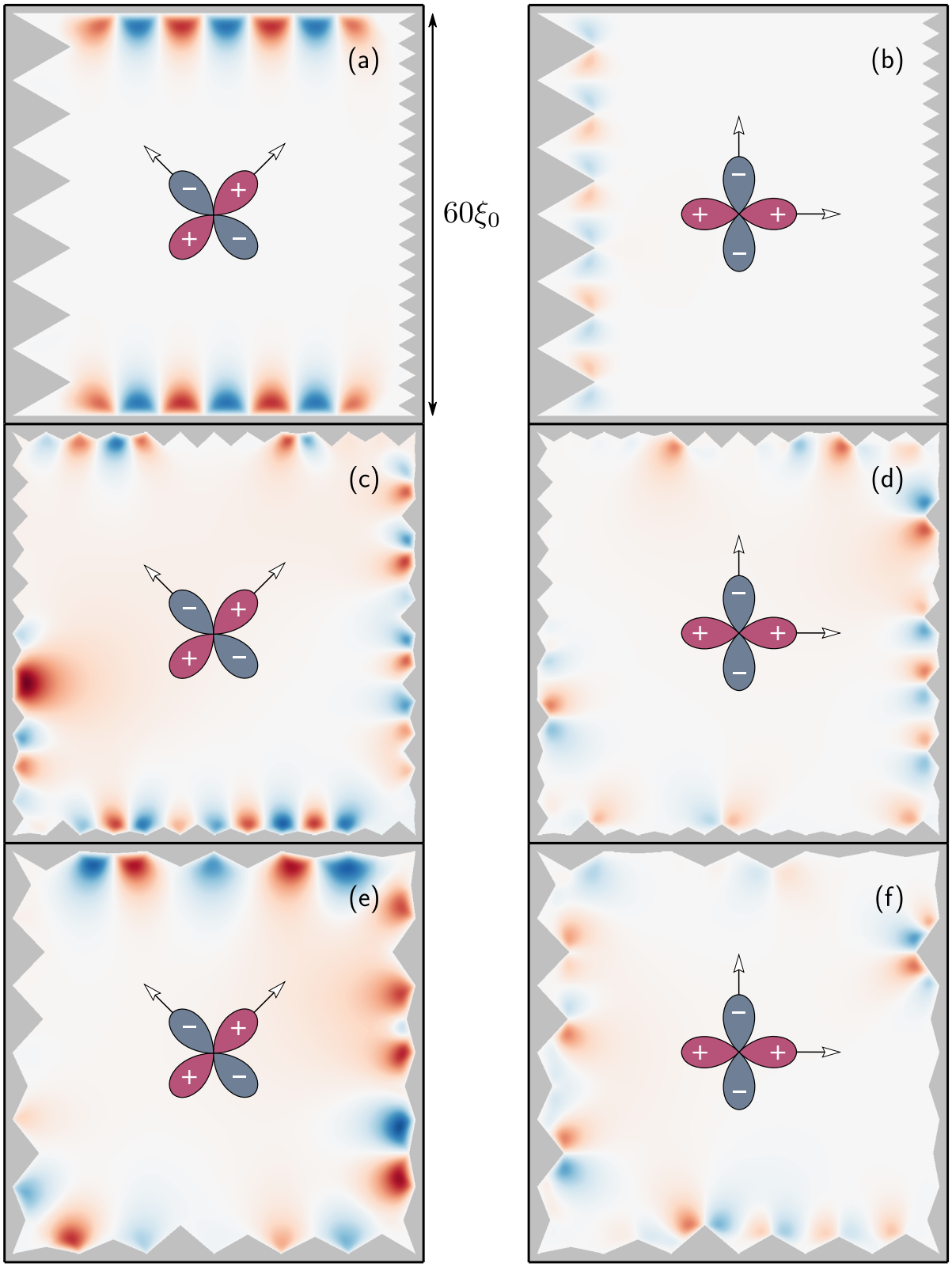

Figure 7.17: *Induced flux density in grains with mesoscopic surface roughness, at temperature $T = 0.1T_c$. The maximum induced flux density is roughly $10^{-5}\Phi_0/\xi_0^2$. Loop currents form wherever there is enough space and the edge is sufficiently misaligned with respect to the crystal ab-axis.*

7.2.3 Edge-to-crystal-axis angle

A square grain with sidelength $60\xi_0$ is studied at temperatures $T = 0.1$–$0.2T_c$, while varying the angle θ between the edge and the crystal ab-axis from $\theta = 0°$ (non-pairbreaking edges) to $\theta = 45°$ (maximally pairbreaking edges). Two start-guesses are converged for each angle: a completely real order parameter, and an order-parameter with the loop-current phase present. The free energy is then compared between these two guesses, and the system with the lowest free energy is chosen as the ground state. Figures 7.18 (a) and (b) show the free energy difference between the ground state and the system with the real order parameter at $T = 0.17T_c$ and $T = 0.1T_c$, respectively. The completely real order parameter has the lowest free energy at lower angles, up to some critical angle $\theta^*(T)$, where the loop-current phase is favorable. Figures 7.18 (c)–(d) show the total induced current magnitude versus θ. As the angle increases, the edges become more pairbreaking, leading to more MGS, as illustrated by the DOS and order parameter in Figs. 7.19 and 7.20, respectively.

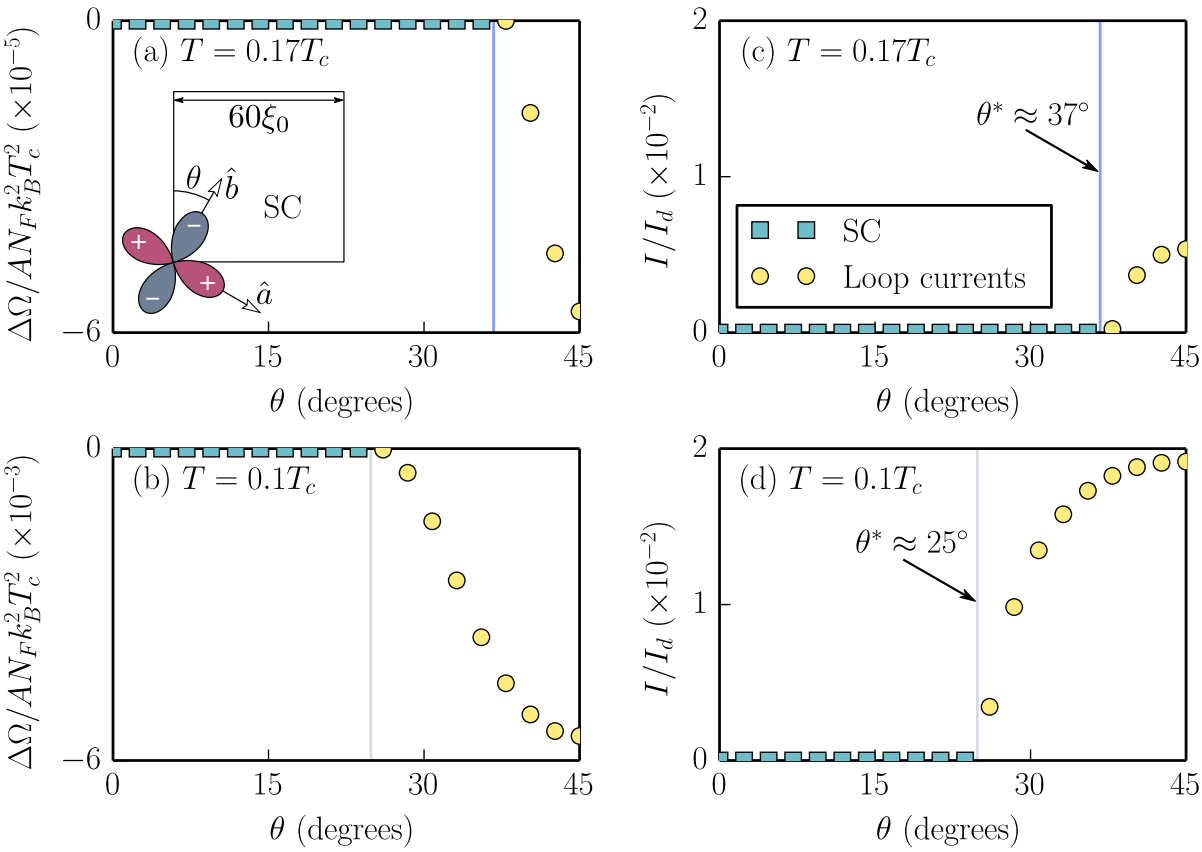

Figure 7.18: *Dependence on edge-to-crystal-axis angle (θ) of the loop-current phase, in a square grain with sidelength $60\xi_0$. (a)–(b) Free-energy difference with respect to a phase without loop currents. Note the different scales in the two panels. (c)–(d) Current density integrated over the grain area, where $I = \int |\boldsymbol{j}|\, d\boldsymbol{R}$ and $I_d = \int j_d d\boldsymbol{R}$.*

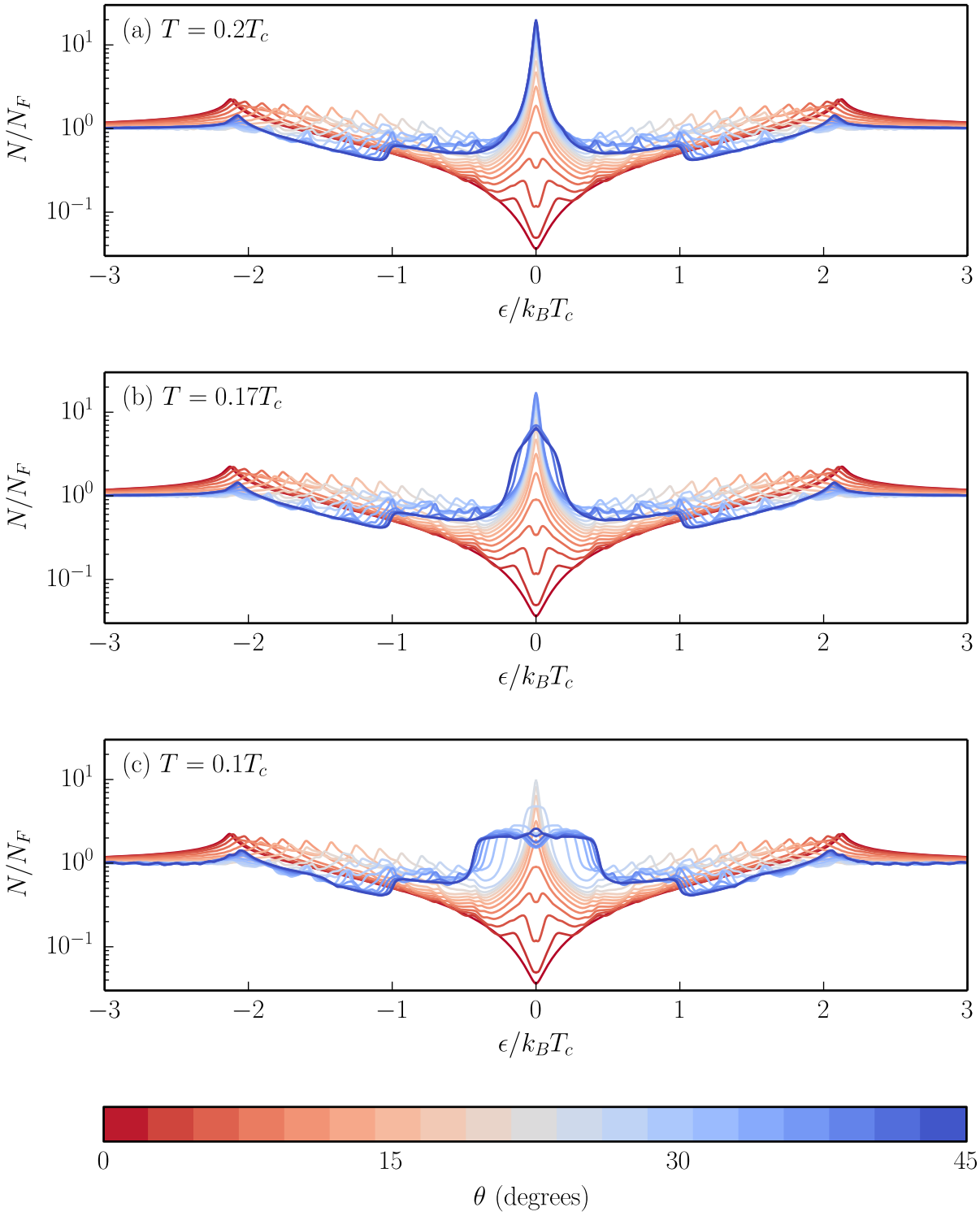

Figure 7.19: *Edge-averaged DOS dependence on edge-to-crystal-axis angle (θ) of the loop-current phase, in a square grain with sidelength $60\xi_0$, where each panel represents a different temperature (see annotation). The smearing factor is $\delta = 0.02$. The interpretation is that as θ increases, the edges become more pairbreaking, generating more MGS. Below T^*, there is a critical angle θ^* where there are enough zero-energy MGS to make a Doppler shift to finite energies energetically favorable. Note that the ordinate is on a logarithmic scale.*

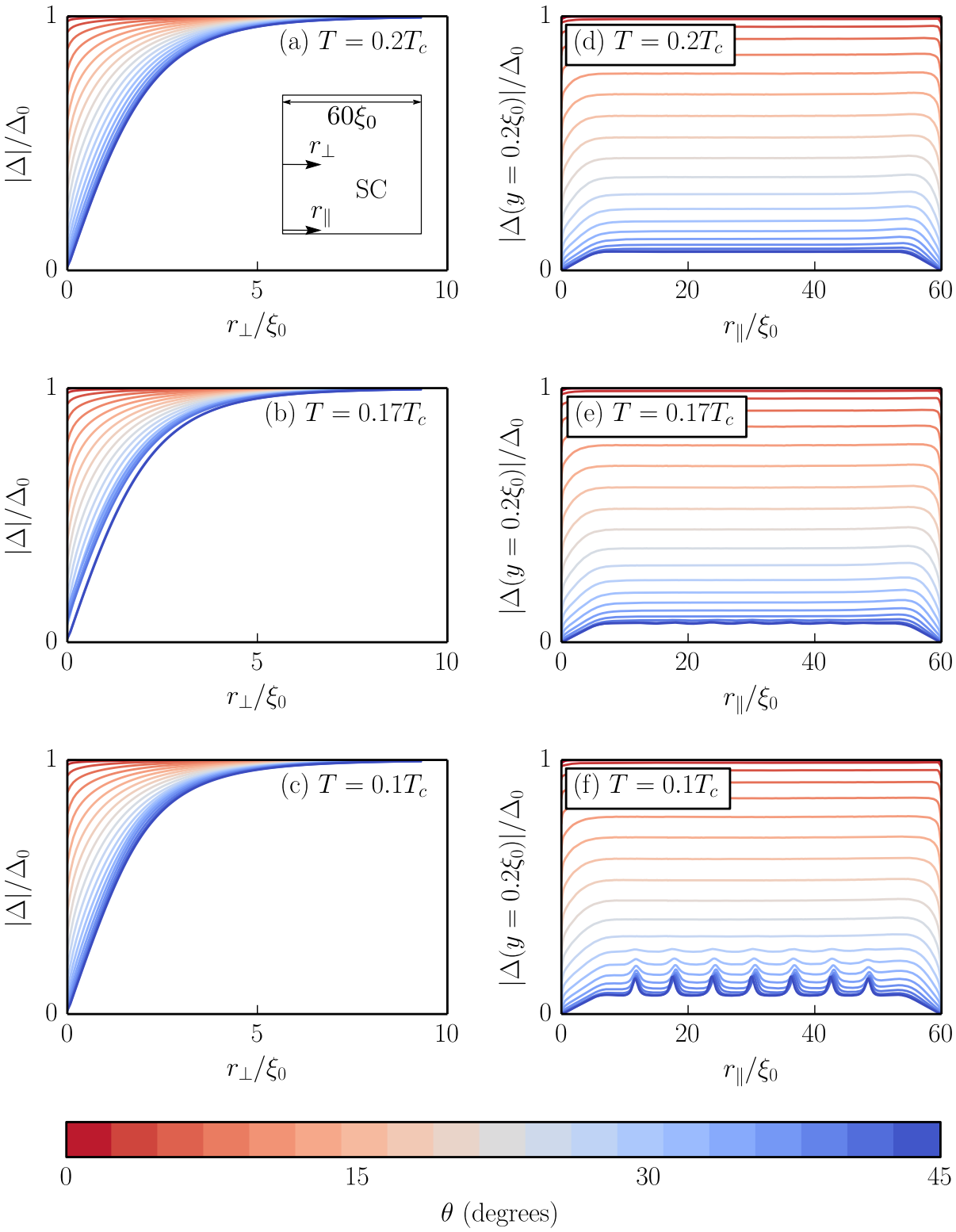

Figure 7.20: *Order parameter dependence on edge-to-crystal-axis angle (θ) of the loop-current phase (a)–(c) perpendicular to the edge starting at an anti-node (between loop currents) and (d)–(f) parallel to the edge at $y \approx 0.2\xi_0$ (to avoid noise exactly at the edge). The superconductor is a square grain with sidelength $60\xi_0$ as shown in the inset in panel (a), at different temperatures (see annotation). Here, $\Delta_0 \approx 1.51 k_B T_c$ is the bulk d-wave gap.*

Once there are enough MGS, there is a non-negligible free energy reduction in shifting these states to finite energies. Figures 7.20 (a)–(c) show the order parameter magnitude as a function of the distance to a system edge, and (d)–(f) along the edge. In the loop-current phase, the order parameter starts oscillating along the edge, due to suppression and recovery at the nodes and anti-nodes, respectively. The order parameter recovers to the bulk value roughly 5–6ξ_0 from the edge of the system (which happens to coincide with the loop-current size). Finally, Fig. 7.21 shows the critical angle as a function of temperature (circles with error bars), together with a linear fit. The critical angle was obtained from a logarithmic fit to the $I(\theta)/I_d$ data (i.e. Fig. 7.18) for each temperature. However, $I(\theta)/I_d$ has a shape that closely resembles the temperature dependence of a BCS gap, since it is directly related to the order parameter of the loop-current phase, namely the superfluid momentum p_S. Therefore, it is probably more appropriate to fit $I(\theta)/I_d$ with typical functions used to approximate the BCS gap, like $\mathrm{Re}\{\sqrt{\theta/\theta^* - 1}\}$ or $\tanh\big(\mathrm{Re}\{\sqrt{\theta/\theta^* - 1}\}\big)$, but the logarithmic function turned out to be easier to fit and captured the essential features. Error bars are due to the discrete resolution in the number of angles.

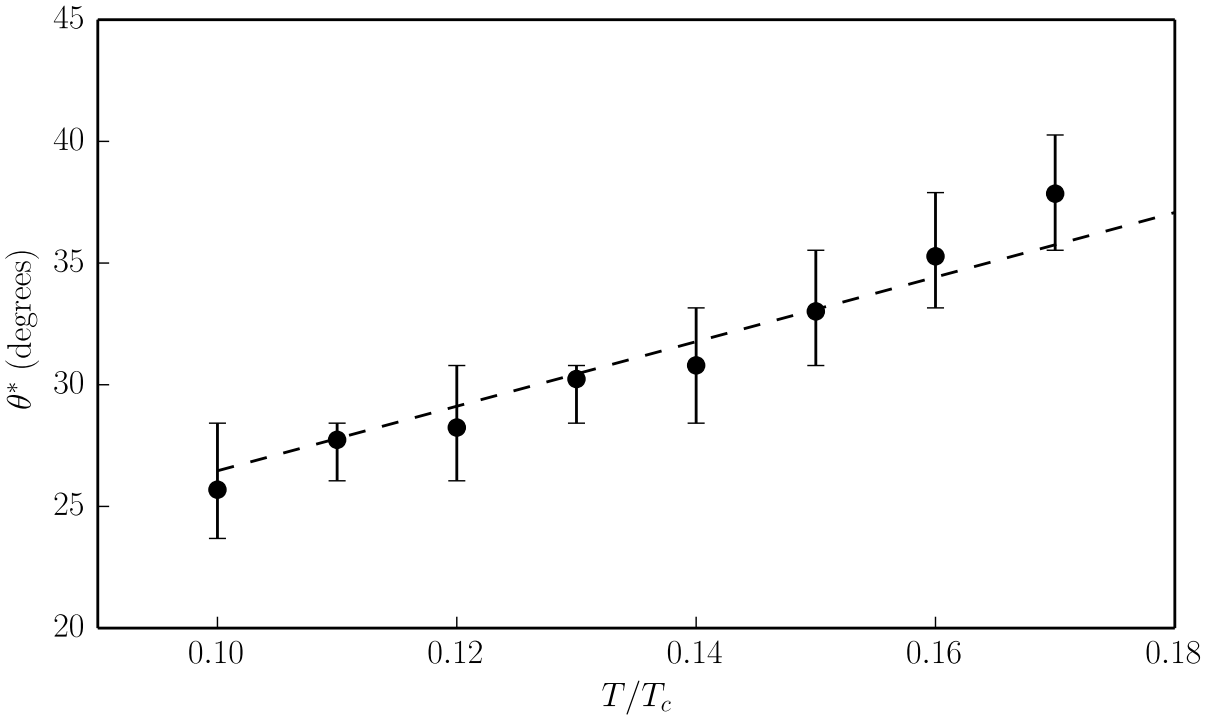

Figure 7.21: *The critical edge-to-crystal-axis angle θ^* below which the loop-current phase is induced, as a function of temperature. The error bars are from the discrete resolution in temperature, and the fit is $\theta^*_{fit}(T) = 132.7°T/T_c + 13.2°$. The formula is valid below the critical temperature $T^* \approx 0.179T_c$ (at $\theta = 45°$), and it is unclear if it is valid for very low temperatures.*

7.2.4 System size

In this section, a square grain is studied with a varying side-length D from $20\xi_0$ to $210\xi_0$, in steps of $10\xi_0$. Similar studies of size-dependence was carried out by Vorontsov [53] and Håkansson et al. [46]. The former author had a semi-infinite thin film with translation invariance along the film, and varied the film thickness. A relatively strong temperature-dependence was found in the maximum and minimum critical thickness between which the "Vorontsov phase" occurs (spontaneous breaking of time-reversal, with a translation-invariant current along the pairbreaking edges). The latter authors had a rectangular shape with one sidelength fixed at a relatively large value (large enough for several loop-current periods), while the other sidelength was varied, leading to a critical thickness $D^*_{\text{slab}} \approx 4\pi\xi_0$, above which the loop currents are induced. Below this critical thickness, the Vorontsov phase is retained. Thus, these studies constrained one dimension, while the present study constrains both. Sharper finite-size effects are therefore expected for small sizes. Of main interest is to see how the transition temperature varies with size, and to find the critical size D^*_{square} at which the phase disappears. Since the transition into the phase is of second order, and the transition temperature T^* can therefore be obtained as the temperature where the heat capacity has a discontinuity. Figure 7.22 shows the heat capacity difference with respect to the normal state, at $D = 60\xi_0$ and zero external field. The heat capacity is normalized with the heat capacity jump in the normal-superconducting phase transition for a bulk d-wave superconductor, $\Delta C_d \approx 6.3 k_B^2 T_c N_F$ (derived in Sec. 5.3.5). Open circles correspond to simulations where the start guess is a well-converged solution with the loop currents present at $T < T^*$, and the solid line a completely real order parameter which does not enter this phase at any temperature (labeled metastable as it exhibits a higher free energy at $T < T^*$). The solid line follows a second-order polynomial, which is expected for a d-wave superconductor at low temperatures (the line is negative due to the subtraction of the larger and linear heat capacity of the normal state, see Sec. 5.3.4). Note that there is an additional $1/T^2$ dependence due to midgap states, but that this effect becomes smaller as the grain becomes larger, since it is a sidelength-to-area effect. The jump at $T \approx 0.179 T_c$ is due to a lowering of the free energies by the spontaneously induced superfluid momentum. The jump in the heat capacity is a few percent of ΔC_d, and is defined as the difference between the two curves at T^*. Since the transition shows a smearing, there is a small uncertainty in the transition temperature and the heat capacity jump. ΔC_2 marks the heat capacity closest to the transition, but it is probably lower than the sought jump ΔC, as it might be reduced due to the smearing. Therefore, the heat capacity is calculated as the mean value between ΔC_2 and ΔC_1, with symmetric error bars

$$\Delta C = \Delta C_2 + \frac{\Delta C_1 - \Delta C_2}{2} \pm \frac{\Delta C_1 - \Delta C_2}{2}, \tag{7.4}$$

where ΔC_1 is the maximal heat-capacity jump in the vicinity of T^*. The transition temperature is extracted as the point where the heat capacity has increased $\Delta C/2$ from the metastable heat capacity, with an uncertainty corresponding to the width of the smearing (i.e. the points marked p_1 and p_2). This procedure is then followed for different grain sidelengths D, both with and without an external field.

Figures 7.23 (a) and (b) show the transition temperature as a function of grain size, with and without an external field, respectively. The external field is $B_{\text{ext}} = \Phi_0/2\mathcal{A}$, where $\mathcal{A} = D^2$ is the grain area. Note that this is half the first critical field $B_{g1} = \Phi_0/\mathcal{A}$, at which point Abrikosov vortices form inside the grain. For small grains, the transition temperature shows a strong suppression with $T^* \to 0$ as $D \to D^*$, while it should level off to a constant value for larger grains. The suppression is stronger with an external field, probably since the field interferes with the formation of the loop currents (sources, sinks and saddle points of the superfluid momentum are constricted to a smaller and smaller area, such that

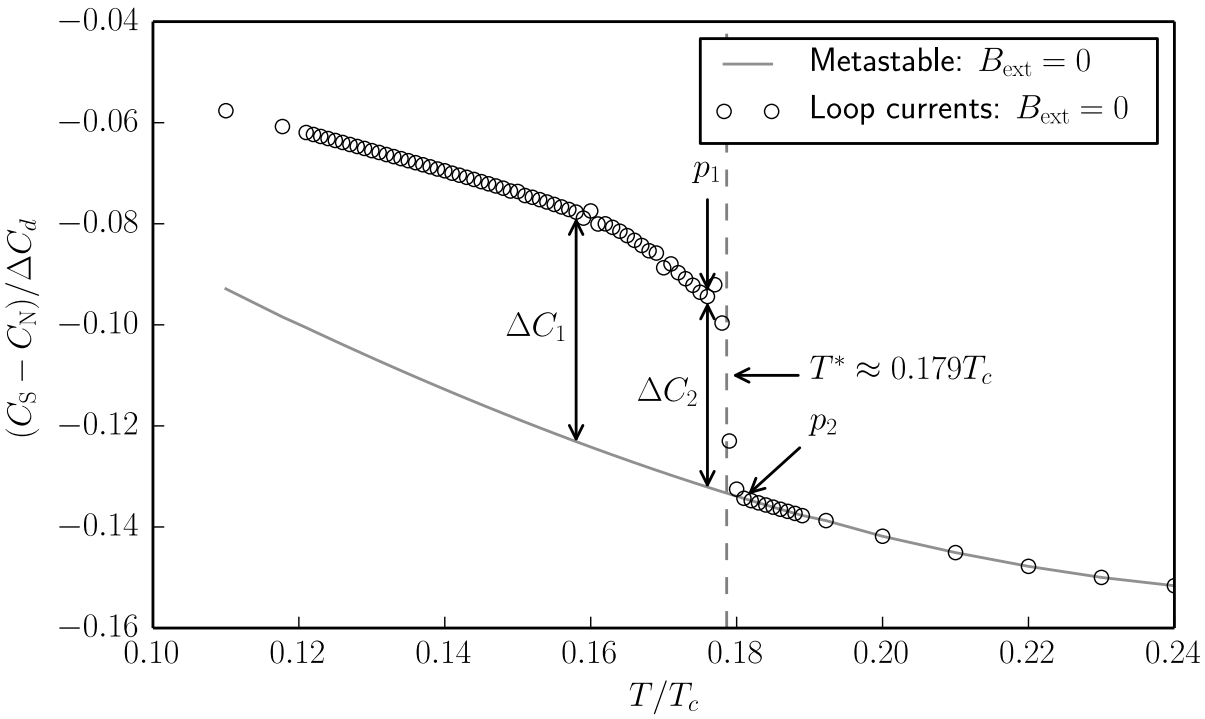

Figure 7.22: *Temperature-dependence of the heat capacity difference between the normal and the superconducting state, in a square grain of side-length $D = 60\xi_0$ with maximally pairbreaking edges. Here, ΔC_d is the heat capacity jump between the normal-superconducting phase transition for a bulk d-wave superconductor. The solid line corresponds to a purely real order parameter which does not exhibit loop currents, while the open circles correspond to a grain with an order parameter that does at some transition temperature $T^* \approx 0.179 T_c$. A smearing in the transition presents an uncertainty in T^*, marked by the points p_1 and p_2, and an uncertainty in the heat capacity jump, marked by ΔC_1 and ΔC_2.*

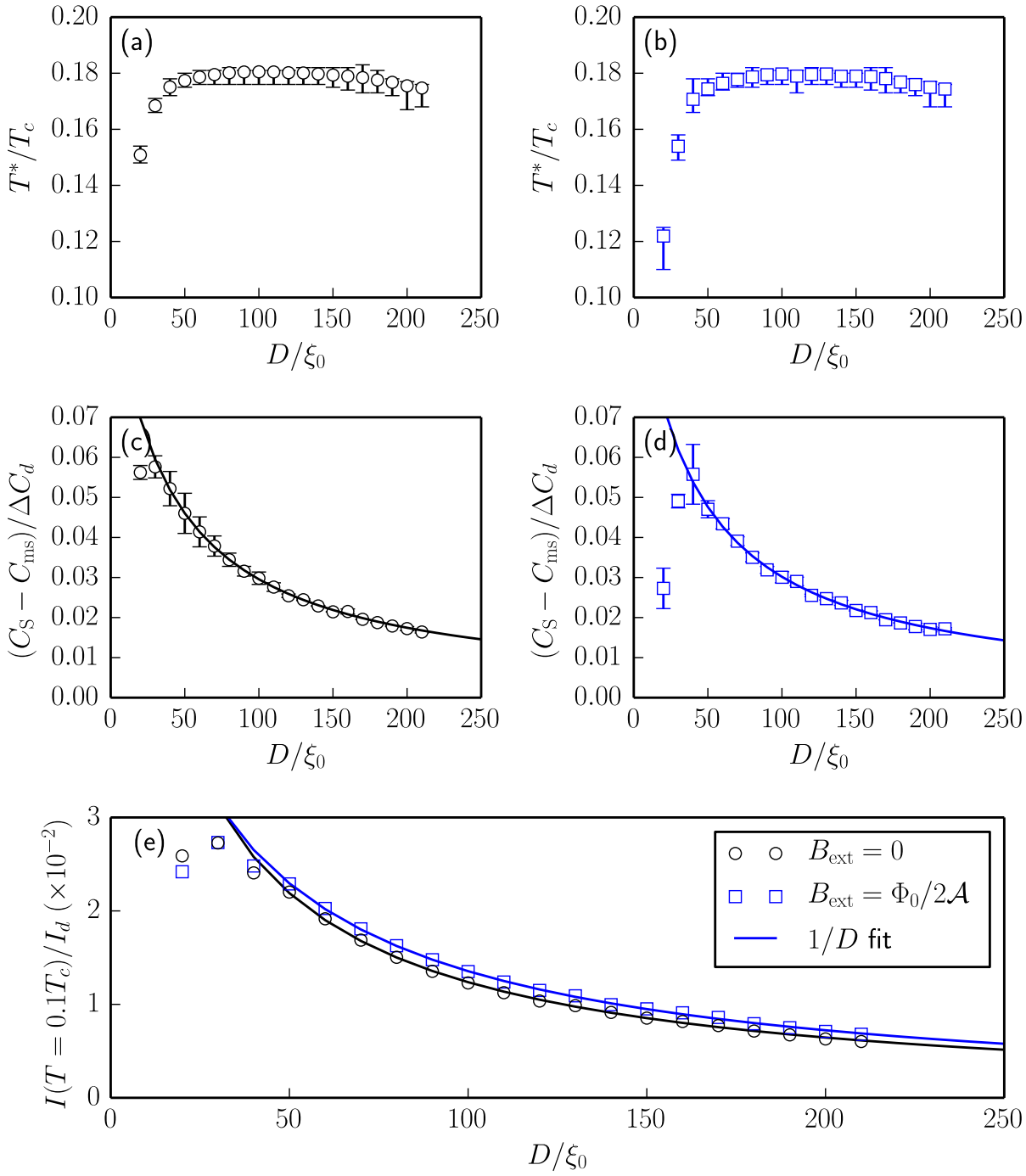

Figure 7.23: *The sidelength dependence of the (a)–(b) transition temperature, (c)–(d) heat-capacity jump, and (e) total induced current in the loop-current phase. Here, $T = 0.1T_c$ and $I = \int |\boldsymbol{j}| d\boldsymbol{R}$ with $I_d = \int j_d d\boldsymbol{R}$. Open circles are without an external field, while open squares are with an external field $B_{ext} = \Phi_0/2\mathcal{A}$ where $\mathcal{A} \equiv D^2$ is the grain area. Solid lines are $1/D$ fits to the data. See text for interpretation.*

they more easily annihilate). Furthermore, the external field already shifts midgap states (albeit a rather minuscule shift). Figures 7.23 (c) and (d) show the jump in heat with respect to the metastable state, with and without an external field, respectively. There are finite-size effects for smaller grains, and a convergence to a $1/D$-dependence for larger grains, as shown by the fit (solid lines). This is expected since the density of midgap states scales with the sidelength, as does then the total Doppler shift. This means that the free energy gain, and therefore also the heat capacity, scales with one over length as the area increases. The area-integrated current density exhibits a similar dependence, as shown in Fig 7.23 (e). Here, $I = \int |\boldsymbol{j}| d\boldsymbol{R}$ and $I_d = \int j_d d\boldsymbol{R}$.

In principle, the critical grain size D^*_{square} below which the loop-current phase disappears could be obtained as the point where ΔC or T^* goes to zero. It is rather difficult to do numerically though, for several reasons. For instance, as the grain shrinks, it is unclear whether the system is actually in the loop-current phase (even if there appears to be a heat capacity jump and a transition temperature), as illustrated in Figs. 7.24 and 7.25 showing the induced magnetic flux density for different grain sizes at temperature $T = 0.15T_c$, with and without an external field, respectively. More importantly, the arrangement of circulating and counter-circulating loop currents becomes incommensurate and difficult to converge in small grains, and the heat capacity data gets very noisy as a result. The best estimate with the available data is that the critical sidelength D_{square} is

$$D^*_{\text{slab}} \approx 4\pi\xi_0 < D^*_{\text{square}} < 20\xi_0, \tag{7.5}$$

and that it should decrease with increased external field. Figure 7.24 also illustrates that the loop size generally does not scale with the system size. Therefore, the number of loops scales more or less linearly with the sidelength, with some additional staggering when the variation of the sidelength is smaller than the typical loop size. This is the topic of the following section, as well as Paper II. The conclusion is that although the necklace of loop currents seems to disappear below the critical size, there still seems to be a phase transition with spontaneous flux present. Thus, even if the grain cannot accommodate the circulating current pairs, it is still energetically favorable to shift midgap states through some manifestation of spontaneous flux.

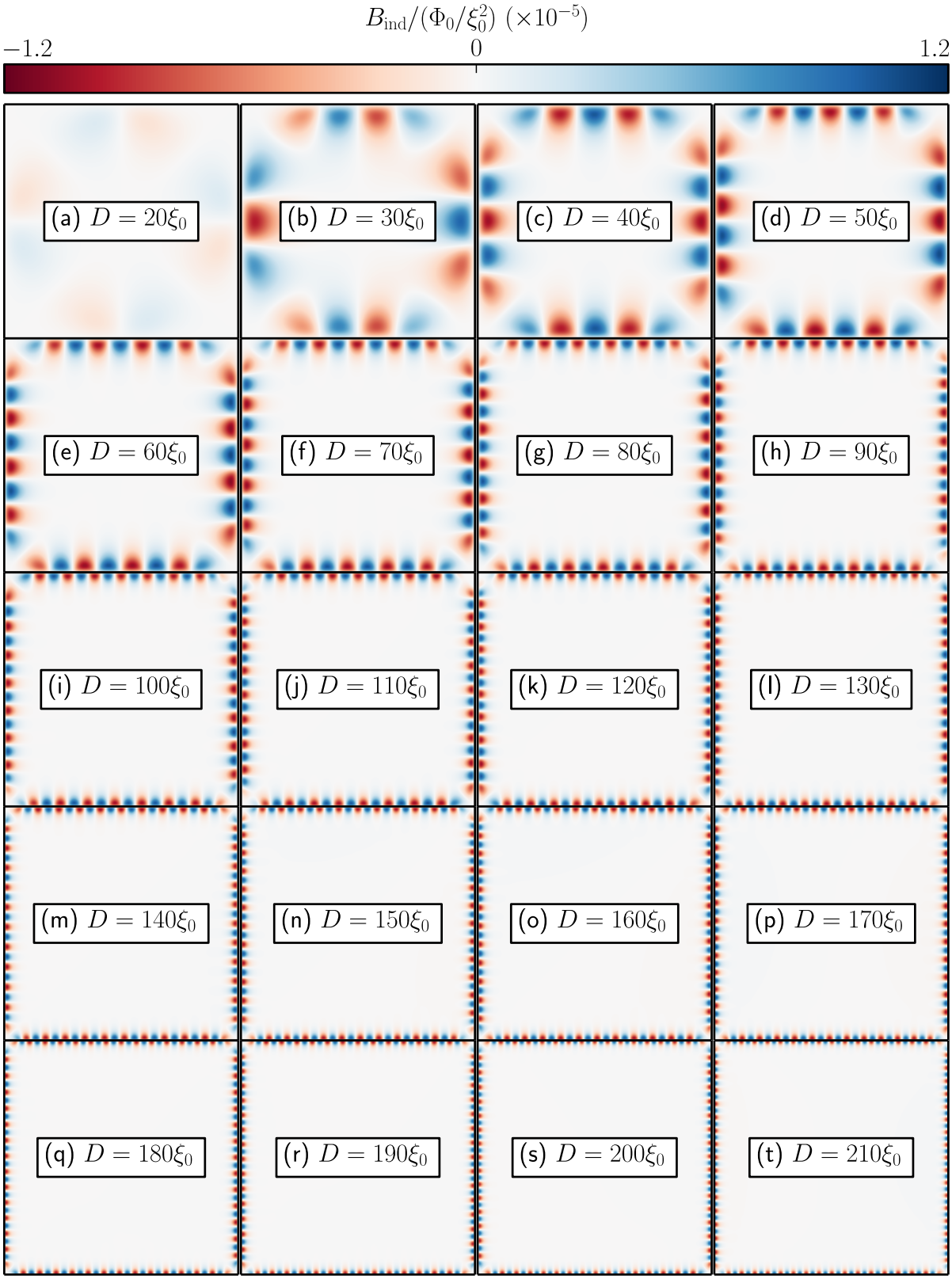

Figure 7.24: *The induced magnetic field due to spontaneous loop currents in grains with varying side-length D, from $D = 20\xi_0$ in panel (a) to $D = 210\xi_0$ in panel (t). The temperature is $T = 0.15T_c$, and there is no external field.*

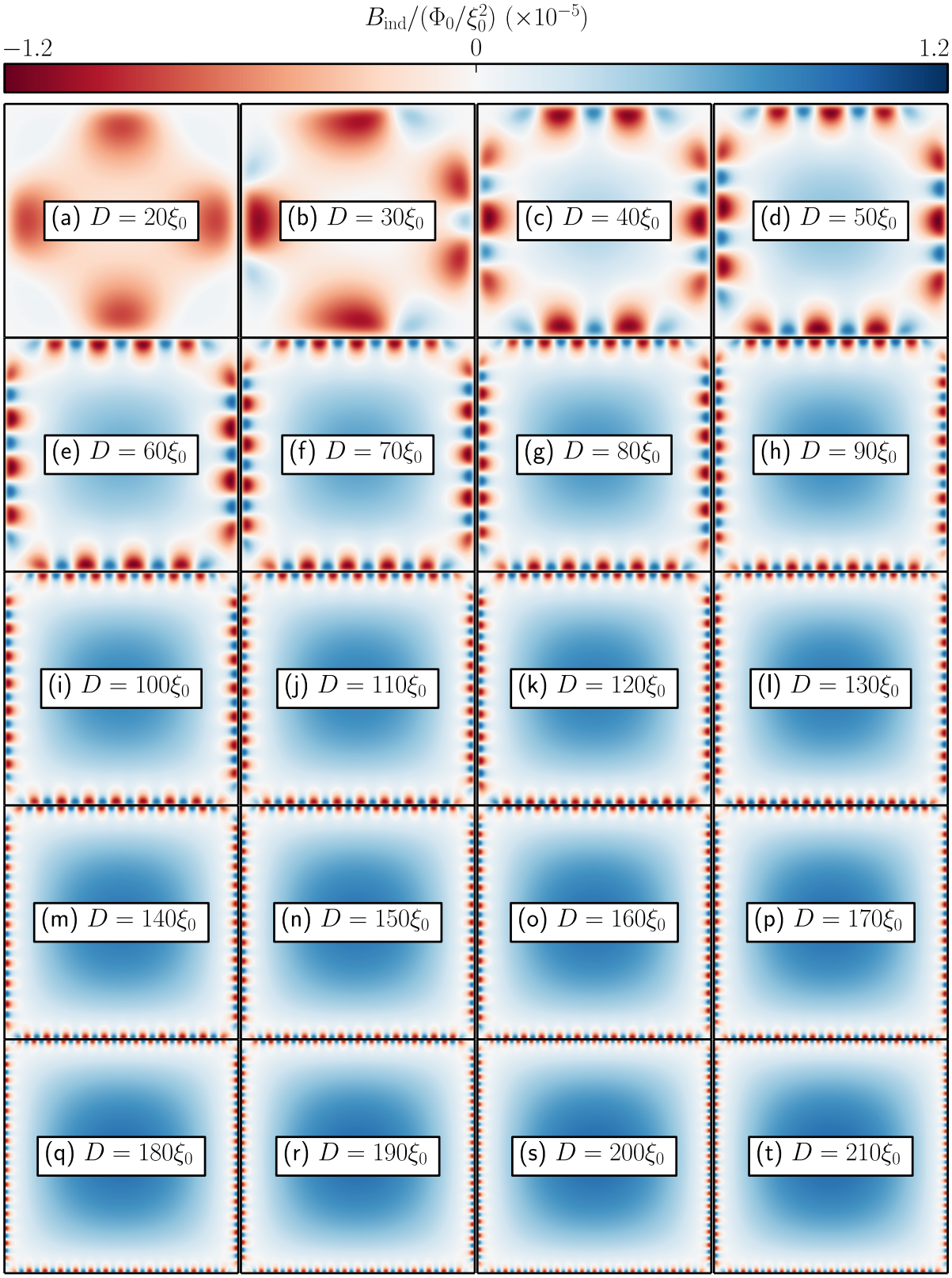

Figure 7.25: *The induced magnetic field due to spontaneous loop currents in grains with varying side-length D, from $D = 20\xi_0$ in panel (a) to $D = 210\xi_0$ in panel (t). The temperature is $T = 0.15T_c$ and there is a homogeneous external magnetic field perpendicular to the grain with magnitude $B_{ext} = \Phi_0/2\mathcal{A}$, where $\mathcal{A} \equiv D^2$ is the area of the grain. There is a diamagnetic response in the bulk of the grain (blue) carried by the condensate, and a paramagnetic response at the edges carried by quasiparticles. The latter gives rise to an asymmetry between the circulating and counter-circulating loop currents (see Sec. 7.3).*

7.2.5 Paper II: A single pairbreaking interface

Paper II deals with a mesoscopic grain with a single pairbreaking interface, as illustrated in Fig. 7.26, where the length of the interface is varied. The main conclusion is that the loop-current phase is *not* a mesoscopic effect in the sense that it does not require the proximity of two pairbreaking edges, in contrast to the Vorontsov phase. Thus, systems with any pairbreaking interface should be unstable to the formation of the loop currents and lead to a broadening of zero-bias conductance peaks, unless if there is a competing phase which is even more favorable. Another conclusion is that the loops have a fairly constant diameter of roughly 5–6ξ_0, except the outermost loops. These are generally smaller, until the pairbreaking edge becomes so large that additional loops enter the system. There might also be an asymmetry in the number of circulating to counter-circulating loops, although the total flux density sums to zero. The only exception is for pairbreaking edges smaller than the typical loop size. Thus, the system finds it energetically favorable to Doppler shift midgap states, at the expense of having a net flux (note that since the flux lines must close on themselves, the corresponding flux of opposite sign lies outside the grain). Hence, although the loop-current phase "disappears" for smaller grain sizes, there is still a spontaneous breaking of time-reversal symmetry.

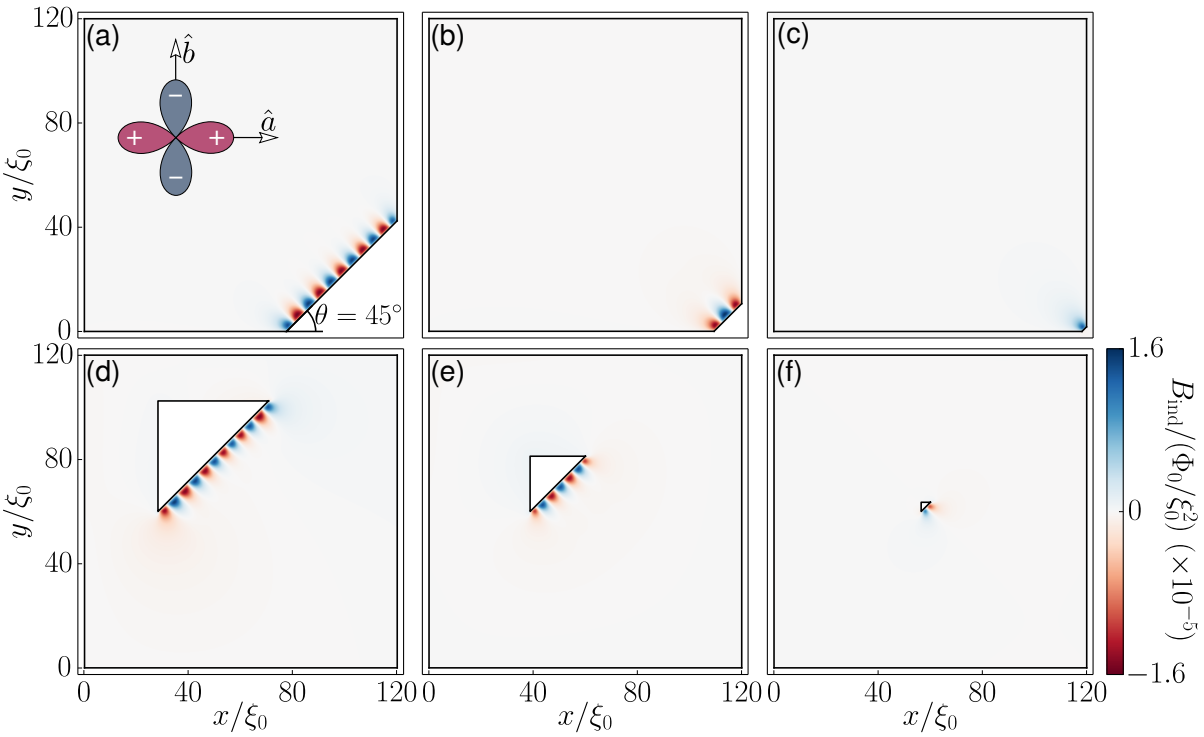

Figure 7.26: *Square grains with a triangular section cut out either at the corner (top row) or inside the grain (bottom row), creating a grain with a single pairbreaking edge.*

7.3 Response to an external magnetic field

This section studies how three different kinds of external magnetic fields affects the loop-current phase. All fields are considered to be perpendicular to the superconducting plane. The first kind of field is a uniform field in the Meissner state of magnitude $B_{\text{ext}} \leq B_{g1}$, and is the main topic of paper I. Here, B_{g1} is proportional to the first critical field of the grain, and is defined as

$$B_{g1} \equiv \frac{\Phi_0}{\mathcal{A}}, \tag{7.6}$$

where $\mathcal{A}$ is the area of the grain. Note that in a bulk sample, the first critical field is

$$B_{c1} \propto \frac{\Phi_0}{\lambda^2}, \tag{7.7}$$

which for the type-II grains considered is smaller than B_{g1}, since $\lambda \approx 100\xi$ and typically $\mathcal{A} = D^2$ with $D = 60\xi_0$. The second kind of field considered is in the mixed state with magnitude $B_{g1} < B_{\text{ext}} < B_{g2}$, such that an Abrikosov-vortex lattice is induced. Here, B_{g2} is the second critical field of the grain, and should be roughly equal to the second bulk critical field B_{c2}, where any difference owes to finite-size effects

$$B_{g2} \approx B_{c2} \propto \frac{\Phi_0}{\xi^2}. \tag{7.8}$$

The third kind of field considered enters through a hole in the superconductor, i.e. a solenoid. Thus, there is no flux in the superconductor itself in this case, but a non-zero vector potential like in the Ahranov-Bohm problem. The final part of this section goes through the field distribution induced by the loop currents, and discusses the distribution in the context of NMR measurements.

7.3.1 Paper I: a weak uniform external field

This is a summary of paper I, which studies the loop-current phase in an external magnetic field $B_{\text{ext}} \leq 1.5B_{g1}$. When applying a uniform magnetic field perpendicular to a grain, there is a diamagnetic response in the interior of the grain carried by the condensate. There is also a paramagnetic response at pairbreaking edges carried by quasiparticle states. This paramagnetic response occurs due to an energetically favorable Doppler shift of midgap states to finite energies. It is thus a competing mechanism to the loop current phase. The shift caused by the paramagnetic response is relatively small and varies very little with temperature, while the shift caused by the spontaneous superfluid momentum is large and increases highly non-linearly with lowered temperature. Therefore, the loop-current phase is more energetically favorable at lower temperatures. The paramagnetic response is however still superimposed with the loop currents, leading to a shape asymmetry between the circulating and counter-circulating loop currents. Another effect

of the paramagnetic response is that as it already shifts the midgap states, it leads to a minor decrease in the transition temperature T^* with increased external field. This is because it requires slightly stronger loop currents to increase the Doppler shift, which occurs at lower temperatures. Consequently, paper I shows that the phase is robust both in the Meissner state and for the mixed state.

The external field breaks time-reversal symmetry explicitly. Therefore, the loop-current phase only breaks continuous translational symmetry in an external field. The breaking of translational symmetry is illustrated by oscillations in the magnitude and phase of the order parameter, as seen in Figs. 7.27 (a) and (b), respectively. The figure shows that the oscillation do not occur when only time-reversal symmetry is broken at $B_{\text{ext}} > 0$ and $T > T^*$, but rather when the spontaneous superfluid momentum arises and breaks translational symmetry at $T < T^*$. Thus, it is translational symmetry-breaking and the appearance of a spontaneous superfluid momentum which are the most important ingredients of the loop-current phase.

Below $T < T^*$, the paramagnetic current is broken up into circulating and counter-circulating parts. This is illustrated by the x-component of the spectral current in Fig. 7.28, i.e. the component parallel to the edge, at $y = 0$. As illustrated, all the spectral currents at the edge are carried by midgap states. Above T^*, there is a translation-invariant paramagnetic current following the edge. As $T \approx T^*$, the current starts oscillating up and down in the y-direction at certain nodes and anti-nodes. As $T < T^*$, these are the same nodes and anti-nodes where the circulating and counter-circulating loop currents develop, and there is a Doppler shift in the energy spectrum. Since the Doppler shift is proportional to $\boldsymbol{v}_F \cdot \boldsymbol{A}$,the current direction determines the sign of the Doppler shift. Furthermore, the spectral current is directly related to the density of states. The latter is shown for the same temperatures and external fields in Fig. 7.29. Again, above $T > T^*$, there is a small shift of MGS due to a paramagnetic response at the pairbreaking interface. As $T \approx T^*$, nodes and anti-nodes develop where the shift is enhanced and suppressed, respectively. Below T^*, there are considerable shifts due to loop currents. The cuts indicated in (c) are plotted in Fig. 7.30 (a). Figure 7.30 (b) shows a typical area-averaged (solid line) and edge-averaged (dashed line) DOS.

In conclusion, paper I presents the phase diagram for the loop current phase in the Meissner state and for one Abrikosov vortex in the mixed state. The question arises what happens at stronger fields in the mixed state. This question is answered in the following sections.

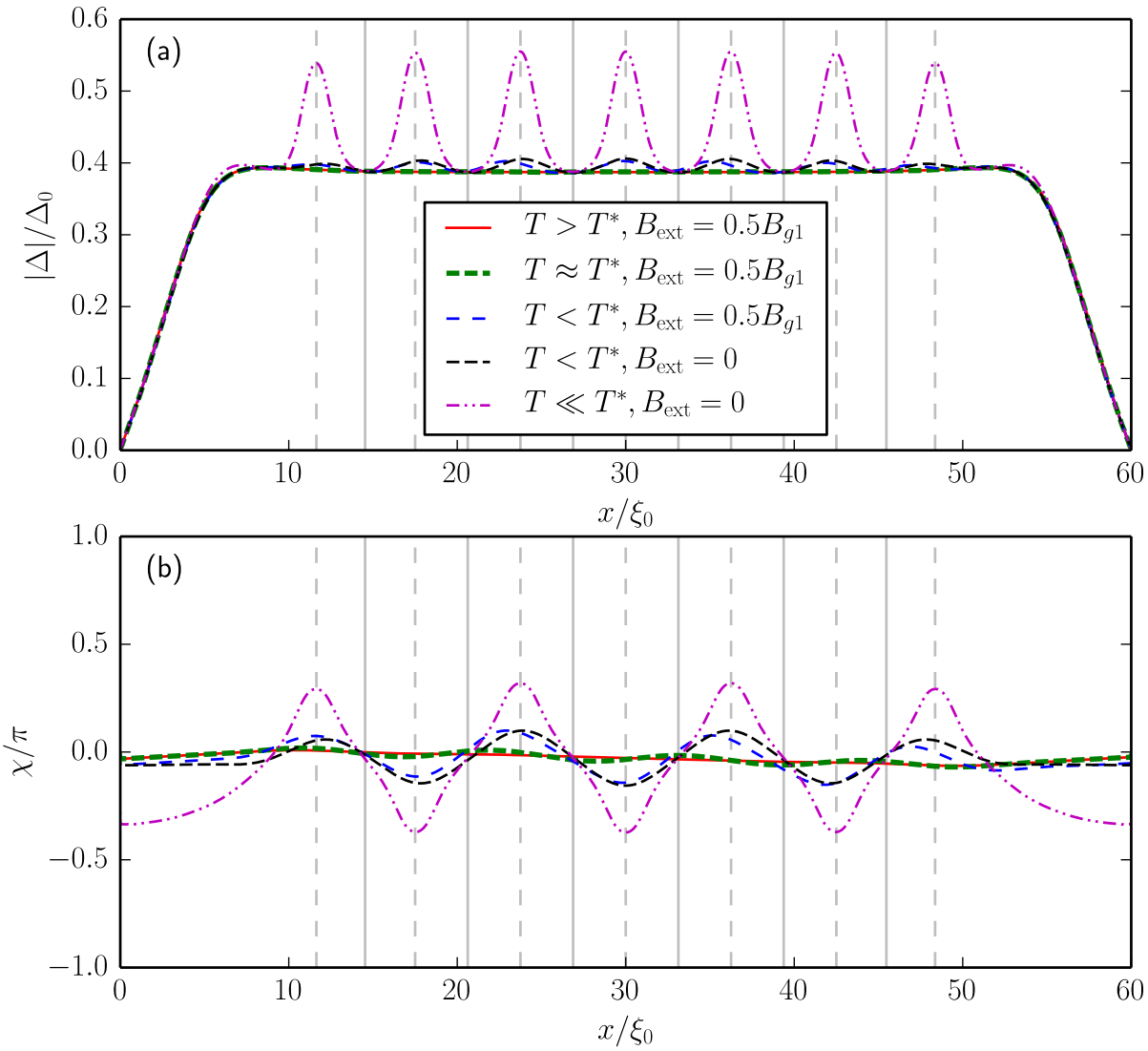

Figure 7.27: *Order parameter (a) magnitude and (b) phase along a pairbreaking interface, at different temperatures and external fields (see labels). Here, x is parallel to the interface, $y = 1\xi_0$, and $\Delta_0 \approx 1.5k_BT_c$ is the d-wave bulk value. At the corners of the system ($x = 0\xi_0$ and $x = 60\xi_0$), the order parameter is suppressed. Along the pairbreaking edges, however, both the magnitude and phase of the order parameter oscillates. The oscillation commences first when $T < T^*$, not when time-reversal symmetry is broken at $B_{ext} > 0$ and $T < T^*$. Note that the phase winds roughly π rather than 2π radians, indicating that the loop currents are not vortices. Vertical solid and dashed lines indicate cuts through and between loop currents, referred to as nodes and anti-nodes, respectively.*

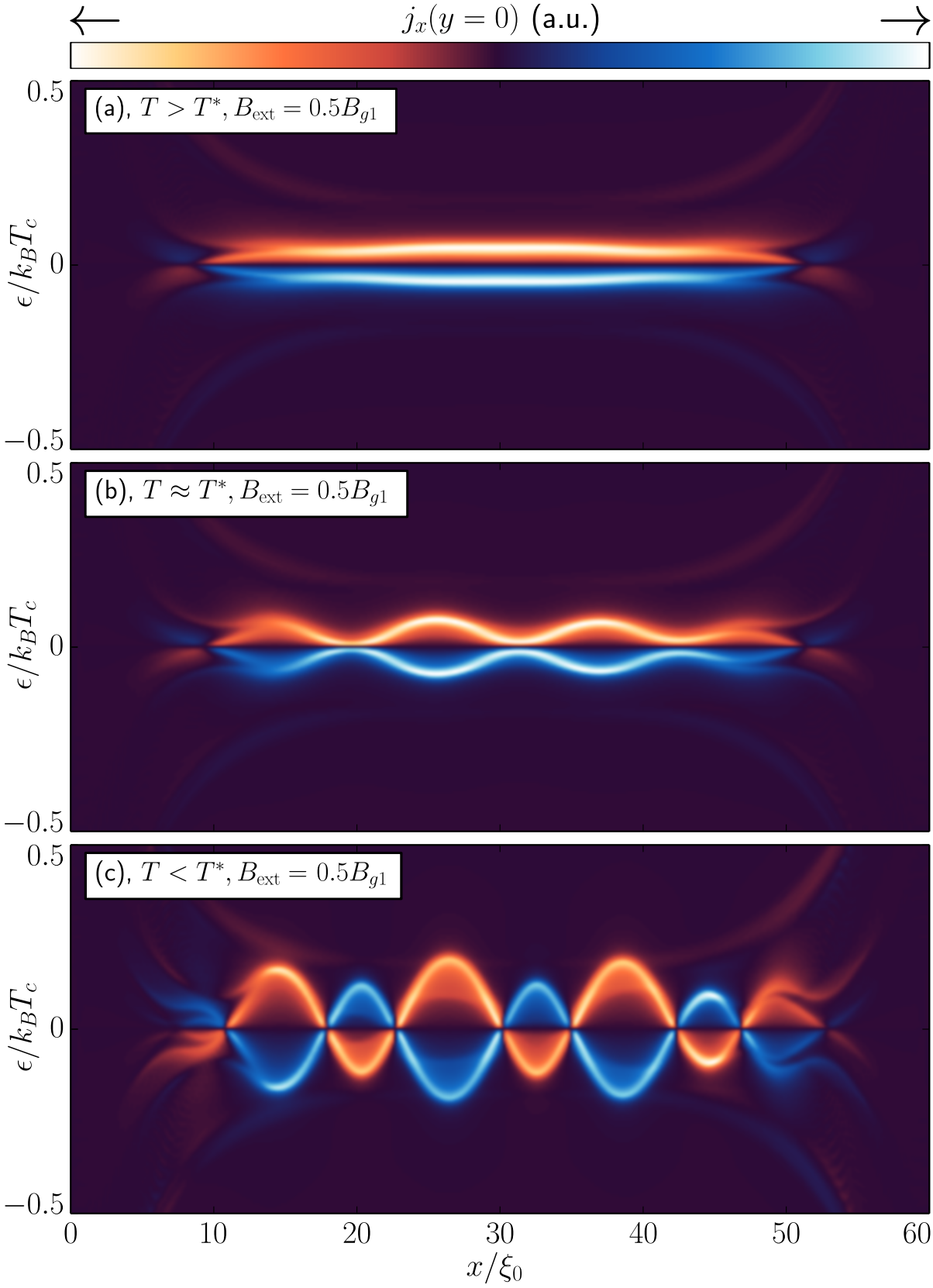

Figure 7.28: *The x-component of the spectral current parallel to a pairbreaking interface ($y = 0$). Colors indicate the direction of the currents. The different panels corresponds to different temperatures and external fields (see labels).*

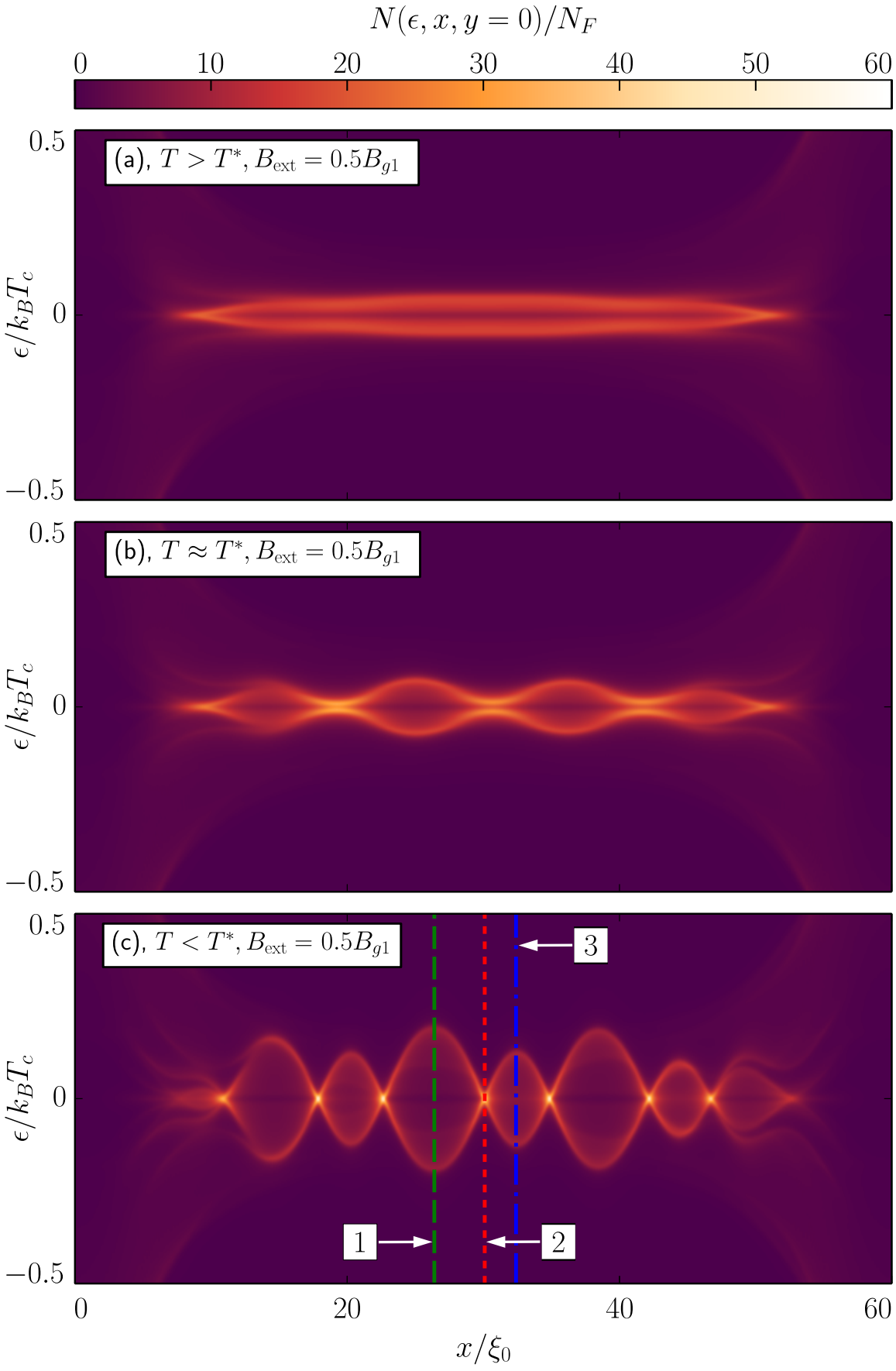

Figure 7.29: *The LDOS versus temperature along a pairbreaking edge, at different temperatures and external fields (see labels). Here, x is parallel to the edge and $y = 0$. The LDOS along the vertical lines marked by 1, 2 and 3 are plotted in Fig. 7.30 (b).*

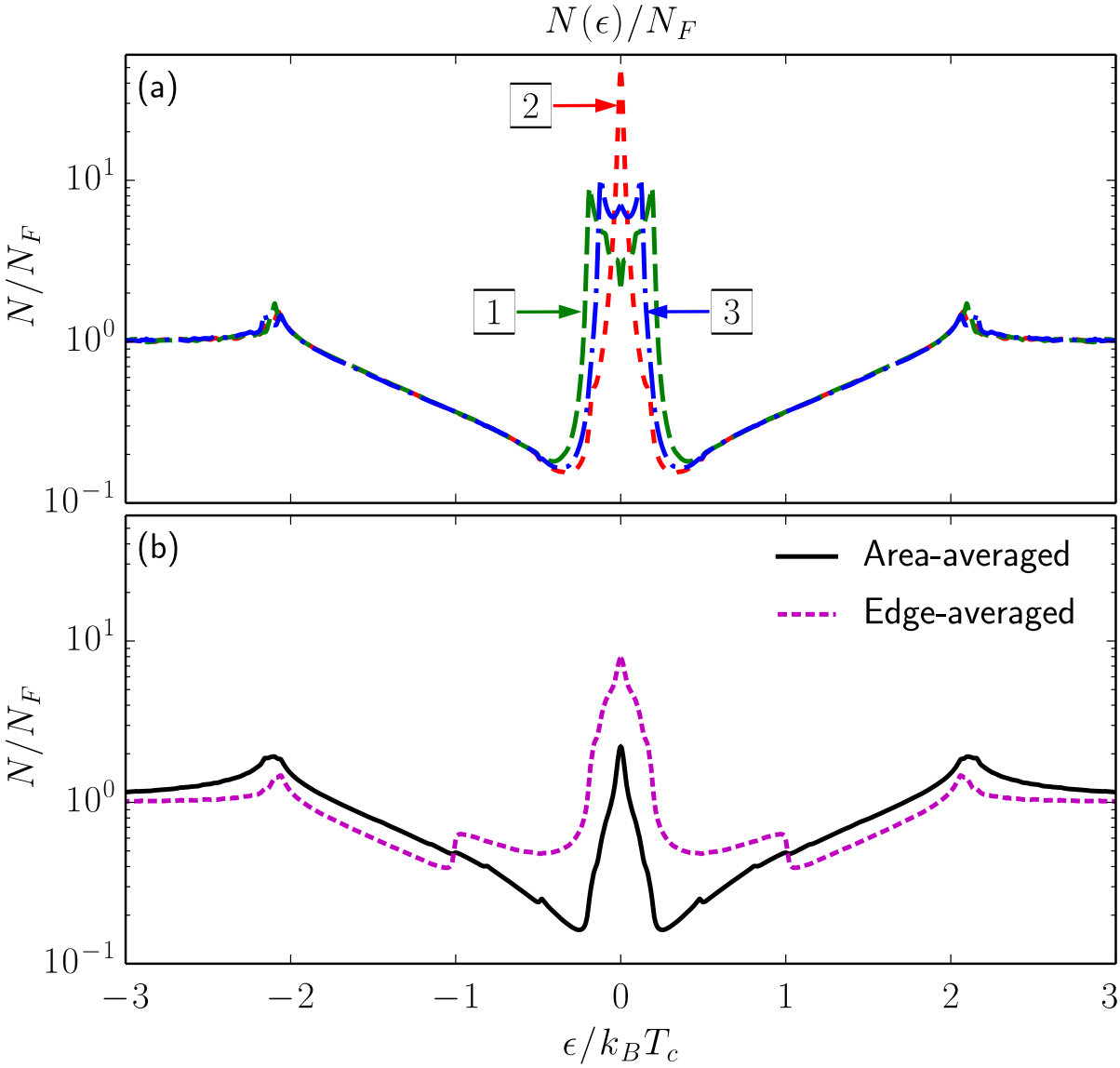

Figure 7.30: *(a) The LDOS along the cuts indicated by the same numbers and line styles in Fig. 7.29. The high peak at zero energy (2) is at an anti-node between loop currents. This peak is split by the large (1) and (3) small loop currents that are aligned and anti-aligned with the diamagnetic response to the external fields, respectively. (b) The area-averaged DOS (solid line) and edge-averaged DOS (dashed line) in a typical pair-breaking grain at $T < T^*$. The midgap state peak at zero energy is broadened by circulating loop currents.*

7.3.2 Stronger fields: Abrikosov vortex lattices

When applying a uniform magnetic flux density $B_{g1} < B_{\text{ext}} < B_{g2}$ perpendicular to a grain, Abrikosov vortices start to form in the interior of the grain. The number of vortices n scales as $n = \text{int}\,(B_{g1}/B_{\text{ext}})$ in a bulk sample. As discussed in Sec. 6.2, this relation might not always hold in grains due to finite-size effects. For higher n, for example, it also becomes increasingly more difficult to find the vortex lattice configuration which minimizes the free energy. The following results on what happens to the loop-current phase in the mixed vortex phase are preliminary, and some of the figures presented do not show a vortex configuration corresponding to the free energy minimum, although they are believed to closely resemble such configurations. However, there seems to be a good understanding of what happens to the phase in the mixed state. The following results are obtained without solving the induced vector potential self-consistently. As discussed below, a more careful analysis should do so as the self-consistency becomes relevant at higher fields.

Figure 7.31 shows (from left to right row) the current density, induced magnetic flux density, induced vector potential and the phase of the order parameter. The side-length is $D = 180\xi_0$, the temperature $T = 0.1T_c$, and the external magnetic flux density is $B_{\text{ext}} = nB_{g1}$, with $n = 1$–6 from top to bottom row, respectively. For small n, the loop currents at the pairbreaking edges seem to be relatively unaffected. At $n = 6$, there is a minor distortion in the loop currents closest to the Abrikosov vortices. Figure 7.32 shows the same observables but with $n = 100$ and $D = 60\xi_0$. As can be clearly seen, there are no loop currents left. The interpretation is that since the Abrikosov vortices are repelled from the edges, there is minimal interaction between the Abrikosov vortices and the loop currents for small n. As n increases, however, the mutual repulsion between Abrikosov vortices pushes them closer towards the edges. As they "squeeze" towards the edges, the vector potential due to the vortices become non-negligible, and the circulating and counter-circulating loop currents are ripped apart. At a critical value, the loop-current phase is lost in favor of a phase where there are long translation invariant (along the pairbreaking edge) currents. The critical field B^*_{ext}, i.e. critical vector potential A^*_{ext}, for which the loop currents are lost should be when the vector potential overcomes the Doppler shift from the superfluid momentum driving the loop currents, i.e. when

$$\frac{A^*_{\text{ext}}}{\Phi_0/\xi_0} \approx \frac{\boldsymbol{v}_F \cdot \boldsymbol{p}_S}{2\pi k_B T_c}. \tag{7.9}$$

The corresponding critical external flux $B_{g1} < B^*_{\text{ext}} < B_{g2}$ is

$$\frac{B^*_{\text{ext}}}{\Phi_0/\xi_0^2} = \left| (\xi_0 \boldsymbol{\nabla}) \times \frac{\boldsymbol{A}^*_{\text{ext}}}{\Phi_0/\xi_0} \right|. \tag{7.10}$$

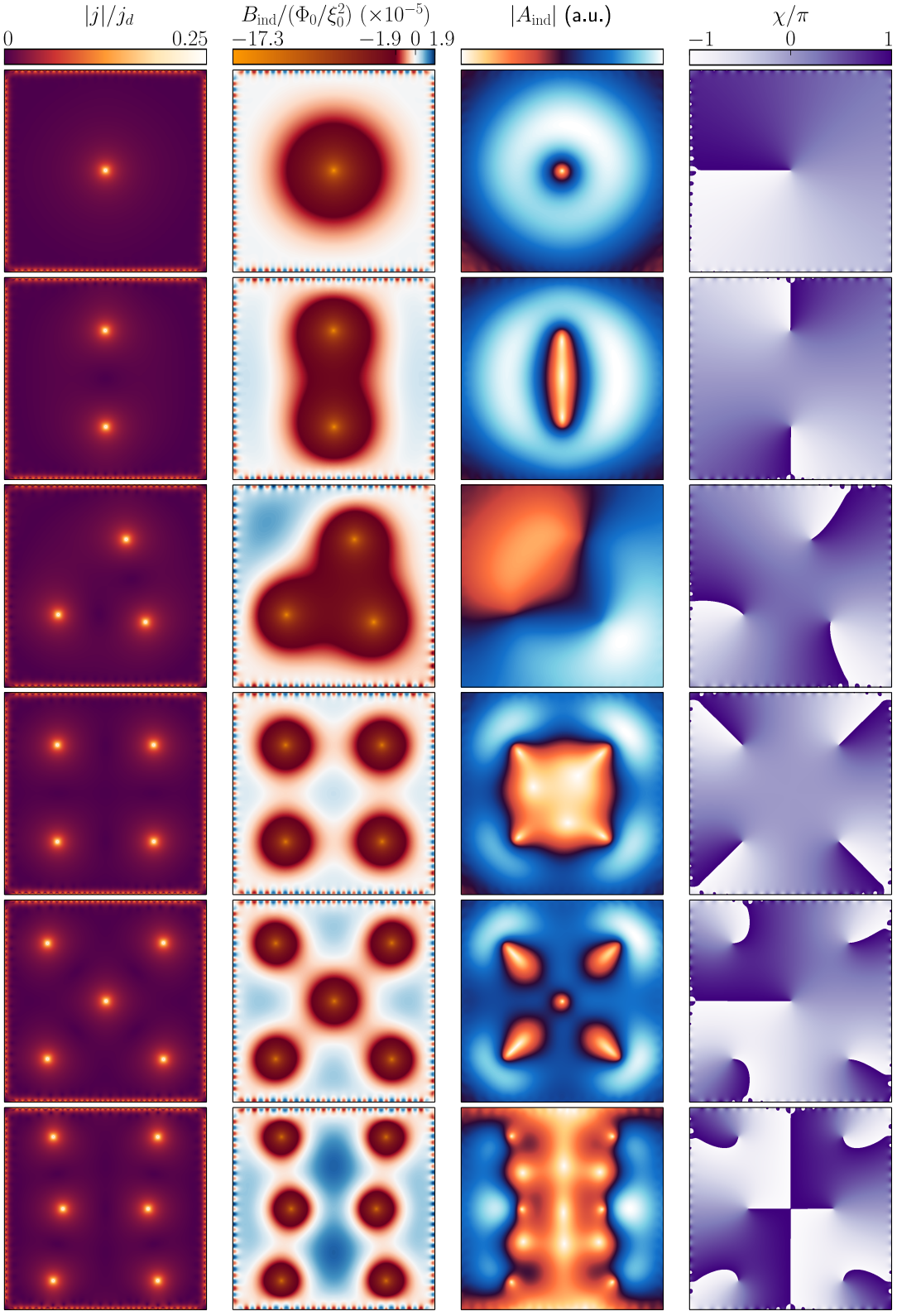

Figure 7.31: *Abrikosov vortex lattices for different external flux densities* $B_{ext} = n\Phi_0/\mathcal{A}$*, where* $\mathcal{A} = 180\xi_0 \times 180\xi_0$ *is the grain area and* n *is an integer ranging between* $n = 1$–6 *from top to bottom row. The first column shows the induced current density, the second the magnetic flux density due to these currents, the third the induced magnetic vector potential and the fourth column shows the order parameter phase. The penetration depth is* $\lambda_0 = 100\xi_0$*, and the temperature is* $T = 0.1T_c$*. The loop-current phase survives until some critical external field* B^* *in the mixed state:* $B_{g1} < B^* \lesssim B_{g2}$

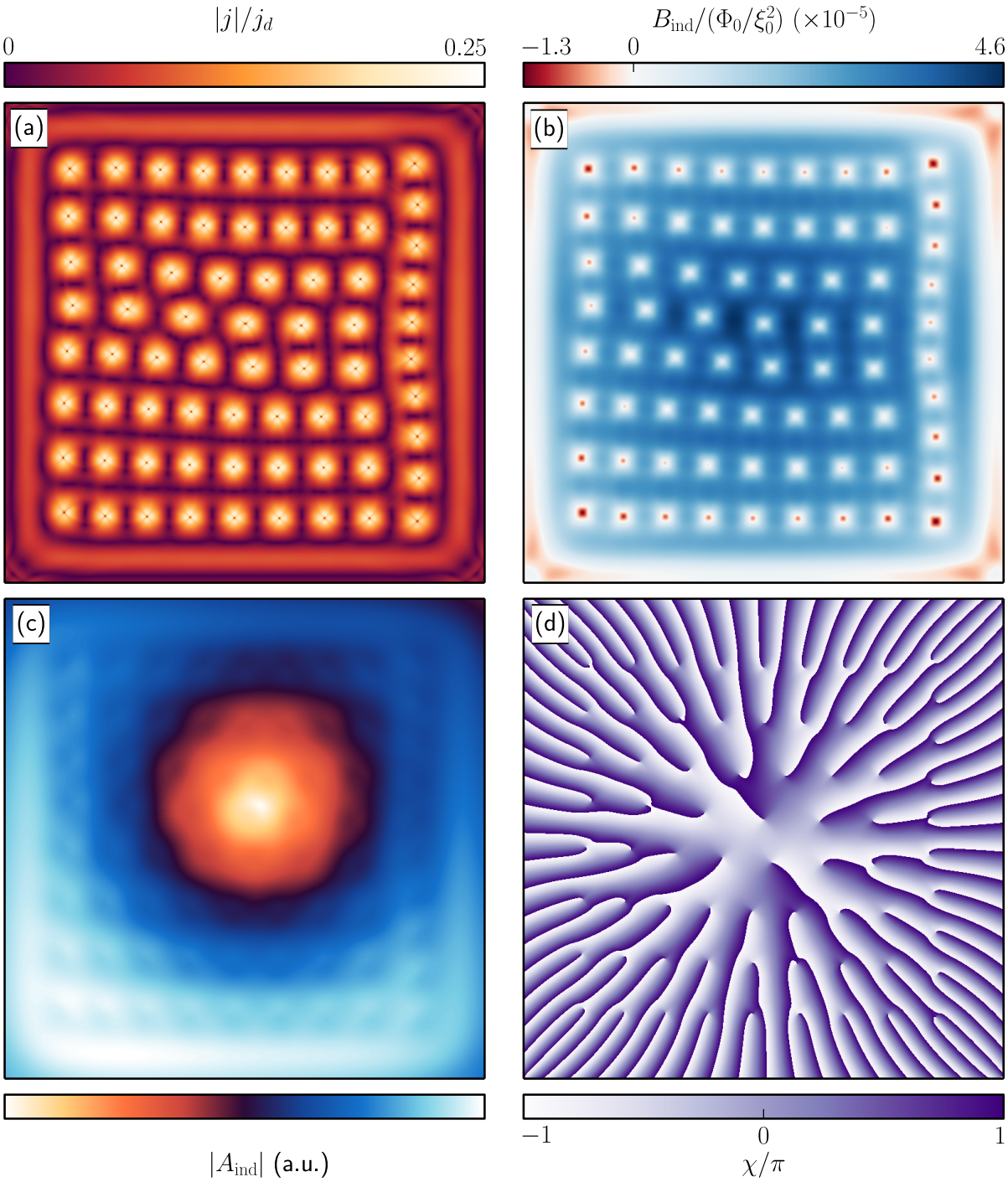

Figure 7.32: *An Abrikosov vortex lattice suppressing the loop-current phase. (a) The current density, (b) induced flux density due to the currents, (c) induced vector potential, (d) phase of the order parameter. The vortex lattice is not fully converged as illustrated by the irregularities. The penetration depth is $\lambda_0 = 100\xi_0$, the temperature is $T = 0.1T_c$, and the external flux density is $B_{ext} = 100\Phi_0/\mathcal{A}$, where $\mathcal{A} = 60\xi_0 \times 60\xi_0$ is the area of the grain.*

Judging by the preliminary results, not all of which are shown here, it is believed that $B^*_{\rm ext}$ lies closer to B_{g1} than B_{g2}, and that for grains of size $D = 60$–$200\xi_0$, the critical field is somewhere around

$$B^*_{\rm ext} \lessapprox 10\frac{\Phi_0}{\xi_0^2}. \tag{7.11}$$

The critical field $B^*_{\rm ext}$ also seems to depend strongly on the grain size. The size dependence should be more important when including the self-consistency[3] in the induced vector potential. With the self-consistency included, there should be different regimes depending on the ratio D/λ, i.e. there should be different kinds of behavior for $D/\lambda \ll 1$ and $D/\lambda \gg 1$. Another indication that the self-consistency becomes more important is that at an external field $B_{\rm ext} = \Phi_0/2\mathcal{A}$, the induced vector potential due to currents is less than a permille of the external vector potential, while already at $B_{\rm ext} = \Phi_0/\mathcal{A}$, the induced vector potential is several percent of the external vector potential. Thus, it is therefore believed that the self-consistency in the vector potential becomes relevant at higher fields in the mixed state, even for extreme type-II superconductors.

7.3.3 Stronger fields: solenoids

This section presents a preliminary study of what happens to the loop current phase when a magnetic field is applied through a hole in the center of a square grain. The field is applied in such a manner that it is zero in the grain, but the vector potential is non-zero (e.g. a solenoid). The grain area is $\mathcal{A} = 60\xi_0 \times 60\xi_0$ and the temperature is $T = 0.17T_c$. Figure 7.33 shows the induced current density (left columns) and phase winding (right columns) for an external flux $\Phi_{\rm ext} = \Phi_0(n + \delta)$ where n is the integer phase-winding number and δ is a shift (which is zero in this figure). The phase shows only minor modifications even at $n = 10$. Figure 7.34 shows that as δ is increased, the circulating and counter-circulating loop currents are lost in favor of longer currents that are translational invariant along the pairbreaking edges. These figures illustrate that as long as the winding number matches the external flux, the loop currents survive an external solenoid field that is higher than the critical field found for the uniform grain in the previous section. This is true even though the temperature is $T = 0.17T_c$, which is relatively close to T^*. The interpretation is that the winding number compensates the vector potential by the external field. If the field is increased without increasing the winding number, however, the phase cannot compensate the vector potential, and the latter increases considerably leading to a competitive Doppler shift of the midgap states. However, it was shown in Fig. 6.8 in Sec. 6.3 that this corresponds

[3]Recall that no self-consistency in the induced vector potential means that $\lambda_0 \to \infty$ and that the penetration depth drops out of the theory (except when calculating the induced magnetic flux density).

to an energetically unfavorable situation. Figure 7.35 (a) shows that the same applies to the loop current phase, since the free energy follows a parabola (solid lines) centered at each integer winding number. The minimum of free energy therefore switches to a new parabola between flux quanta. The minimum of each parabola also follows a parabola (dashed lines). Figure 7.35 (b) shows a similar dependence for the grain-averaged magnitude of the induced current density I/I_d, where $I = \int |\boldsymbol{j}|\, d\boldsymbol{R}$ and $I_d = \int j_d d\boldsymbol{R}$. Figure 7.35 (c) shows the induced flux density due to these currents.

The question is if it is possible to design an experiment with such solenoid fields, i.e. with the capability of both staying on a single parabola or following the minimum. For example, applying a high field far above the phase, it should be possible for the order parameter to develop the corresponding phase winding. Upon cooling, the phase would be induced with the phase winding already present.

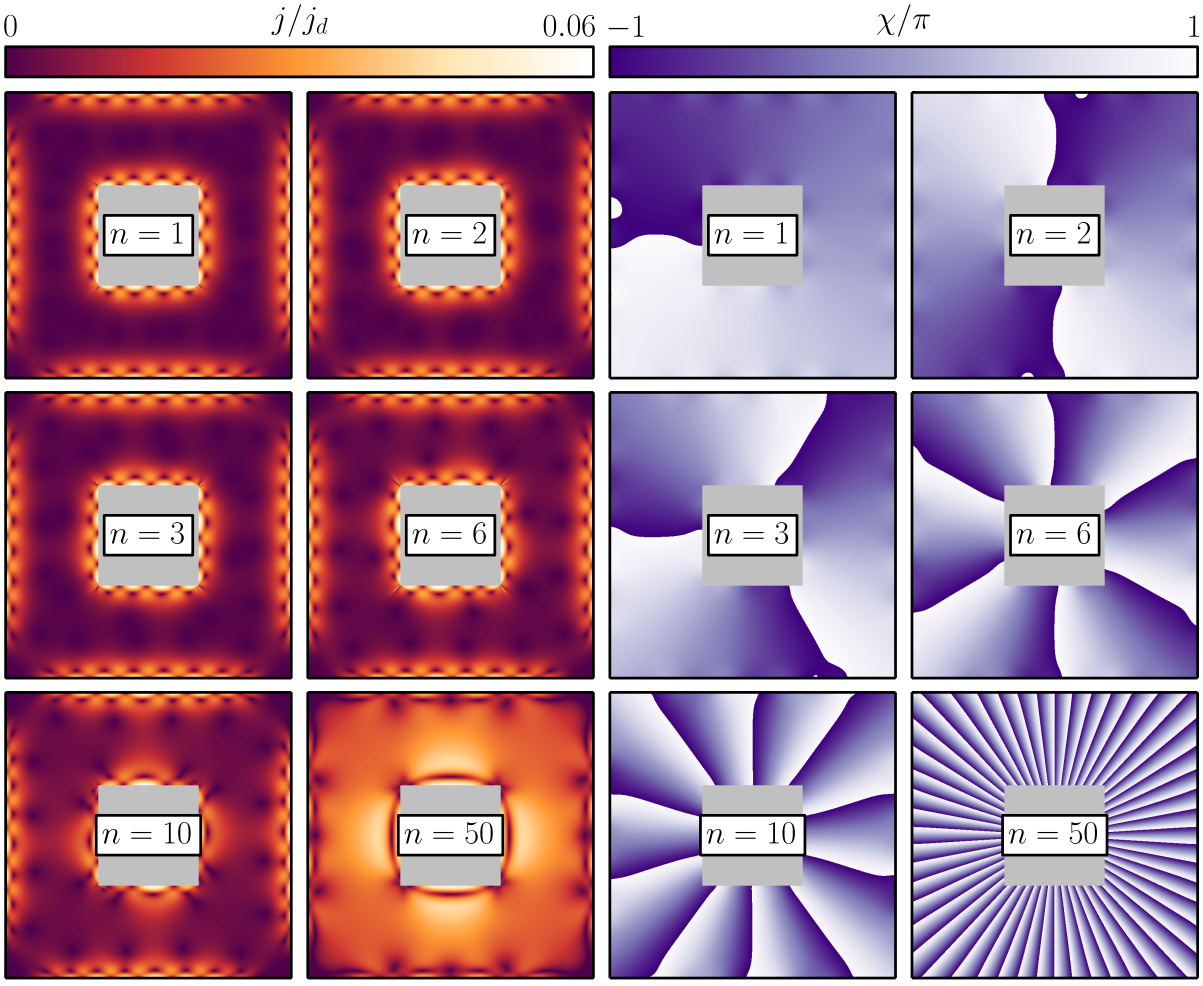

Figure 7.33: *Induced current density (left columns) and phase winding (right columns) for an external flux $\Phi_{ext} = \Phi_0 n$ applied through a hole in the center of a grain, where n is the integer phase-winding number (as labeled in each figure). The area of each grain is $\mathcal{A} = 60\xi_0 \times 60\xi_0$ and the temperature is $T = 0.17T_c \lesssim T^*$.*

If instead the field is applied once the phase is already induced, there might be rigidity due to the circulating currents which prevents the phase winding to occur. If there is a possibility to study both these scenarios, it raises the question of if there are any observables that differ significantly when the loop currents are lost. This could be interesting both as a way of tuning the properties of a grain, but also as a means to verifying the existence of the phase. To answer these question, further studies have to be carried out.

7.3.4 Magnetic-field distribution and NMR measurements

By using the nuclear magnetic resonance (NMR) technique, it is possible to study various vortex properties in the mixed state (see for example Ref. [141] and references therein), like vortex phase transitions [142]. In particular, it can be used as a sensitive magnetic probe of spontaneous magnetic fields close to an interface [143]. For example, when applying a magnetic field to a sample, the induced magnetic-field distribution can be obtained as a function of the induced field magnitude. It is the aim of this section to study the magnetic-field distribution induced by the loop currents, to see which signatures might be observable in NMR measurements. This is done by making a histogram of the induced magnetic flux density as a function of its magnitude. This is in turn done by dividing the magnitude into discrete intervals (binning), and counting the occurrence of each magnitude interval (bin) in the discretized grain. For grains, the histogram generally depends on the geometry and the strength of the external field, since different responses and effects, (e.g. diamagnetic, paramagnetic, Abrikosov vortices, and the loop currents) give rise to different signatures in the histogram. Each of these effects

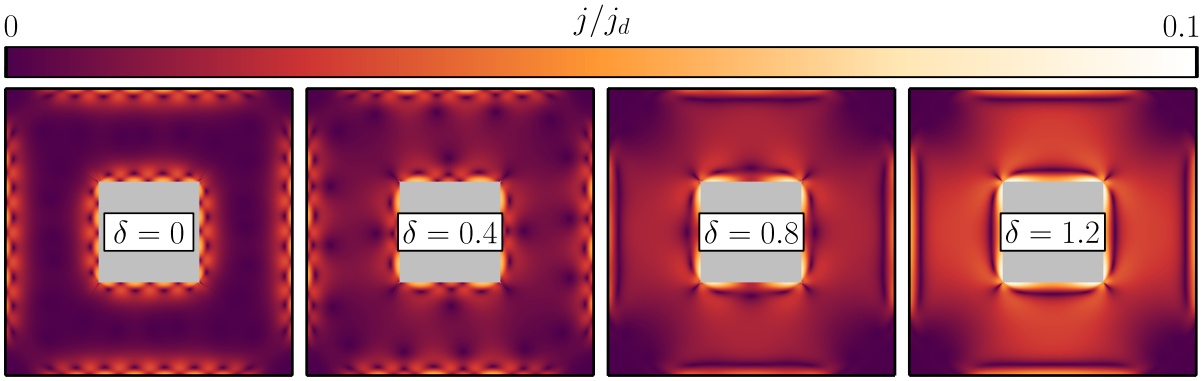

Figure 7.34: *Induced current density for an external flux* $\Phi_{ext} = \Phi_0(n + \delta)$ *applied through a hole in the center of a grain. Here,* n *is the integer phase-winding number and* δ *is a shift, as labeled in each figure. Note that the behavior is the same regardless of* $n \in [1, 6]$*, where* $n = 6$ *is the highest winding number simulated with a shift. The area of each grain is* $\mathcal{A} = 60\xi_0 \times 60\xi_0$ *and the temperature is* $T = 0.17T_c \lesssim T^*$*. The circulating loop currents are lost when* $\delta \gtrsim 0.8$*. At lower temperatures, the loop-current phase can withstand a higher shift.*

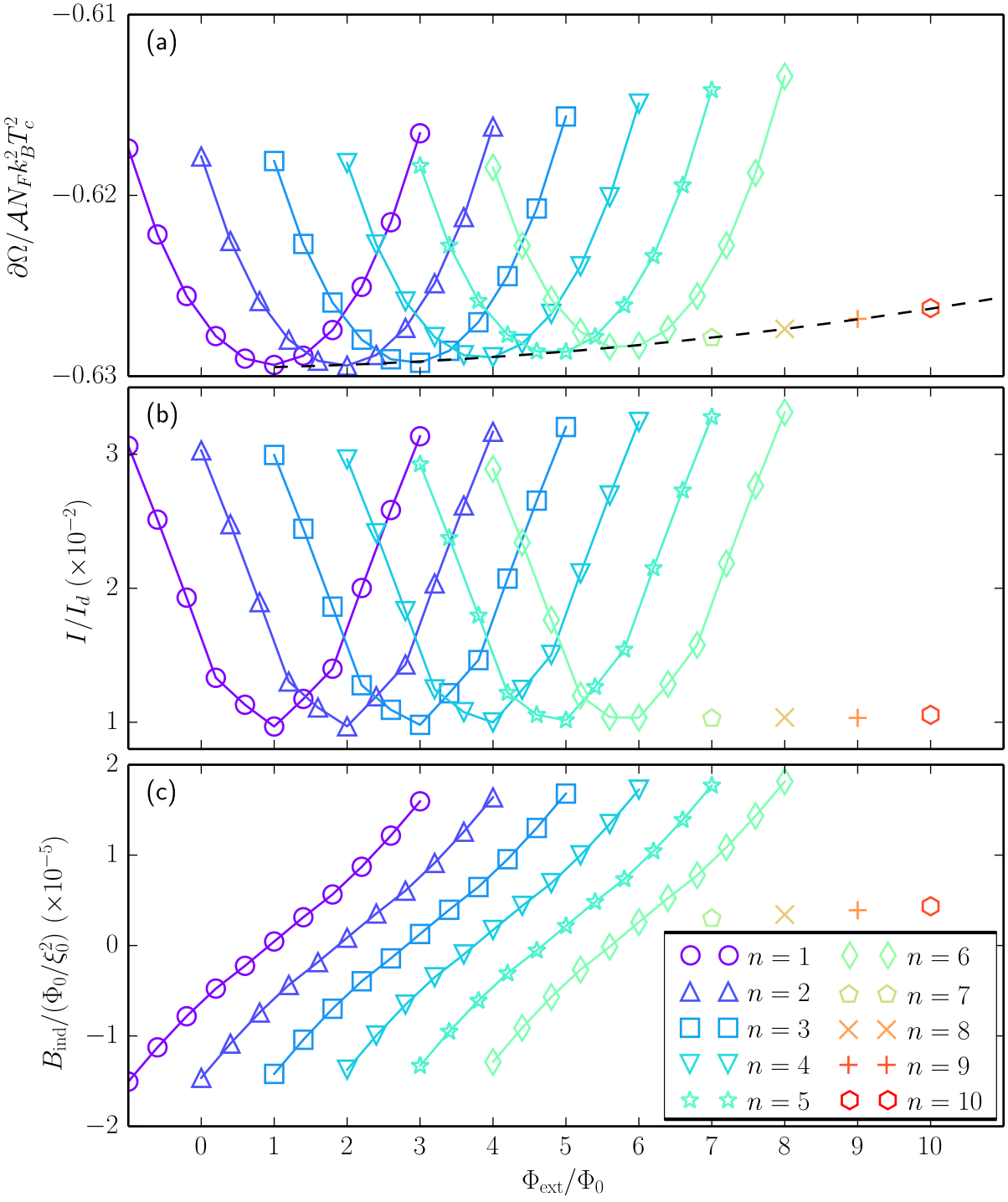

Figure 7.35: *Area-integrated (a) free energy, (b) current density and (c) induced flux density, versus an external solenoid flux $\Phi_{ext} = \Phi_0(n+\delta)$, where n is the integer phase-winding number and δ is a shift. As δ is varied, the quantities follows certain functional behavior, as indicated by the lines. In panel (a), the dashed line is a second-order polynomial fit to the minimum of each free-energy parabola.*

will now be studied separately in order to understand the full distribution, which is a superposition of all the signatures. The analysis shown here is preliminary. The next step in the analysis would be to apply proper statistical fits, and study scenarios that can be compared with experiments, e.g. vortex lattices.

Starting with the Meissner state outside the loop current phase, Fig. 7.36 (a) shows the induced magnetic flux histogram in a d-wave grain with maximally pairbreaking edges of length $D = 60\xi_0$ at temperature $T = 0.2T_c > T^*$ and $B_{\text{ext}} = 0.5B_{g1}$. Here, $B_{g1} \equiv \Phi_0/\mathcal{A}$ is the first critical field in the grain of area $\mathcal{A} = D^2$, and the external field is applied perpendicular to the grain along $-\hat{\boldsymbol{z}}$. Figure 7.36 shows the response, i.e. the induced magnetic flux density, with a dashed line corresponding to the contour $B_{\text{ind}} = 0$. The histogram shows two distributions, coming from the diamagnetic ($B_{\text{ind}} > 0$) and paramagnetic ($B_{\text{ind}} < 0$) responses lying inside and outside the contour, respectively. The corresponding histograms are shown in Figs. 7.36 (c) and (e), and the induced flux densities in Figs. 7.36 (d) and (f). The histograms are exponentially decaying, possibly with Poisson or Lorentzian distributions, with a constant offset. Figure 7.37 (a) shows the histogram for the same grain but at $T = 0.1T_c < T^*$ and $B_{\text{ext}} = 0$, such that the entire distribution is from the loop currents, the latter which are illustrated in Fig. 7.37 (b). Figure 7.37 (c) and (d) shows the same but at $B_{\text{ext}} = 0.5B_{g1}$, such that the distribution is a superposition of the diamagnetic, paramagnetic and loop current fluxes. The loop currents seem to have an exponentially decaying distribution $\sim \exp(-a|B_{\text{ind}}|)$, where a is some decay constant. This distribution gives rise to a peak at zero field and a sharp edge at the maximal B_{ind} of the loop currents, as indicated by the arrows in the figures.

In the mixed state, Abrikosov vortices gives rise to an exponentially decaying distribution, as illustrated in Figs. 7.38 (a) and (b) for a system without pairbreaking edges. Fig. 7.38 (c) and (d) show how this distribution is superimposed with the loop-current distribution. Arrows again mark the peak and edge of the latter. The question arises if these signatures are strong enough to be seen in NMR measurements. Local measurements close to the interface and in low external fields would improve the chances of seeing the signatures, as this reduces the background distribution from other sources. Even if the signature is swallowed by the background, it might be possible to extract it through statistical fitting.

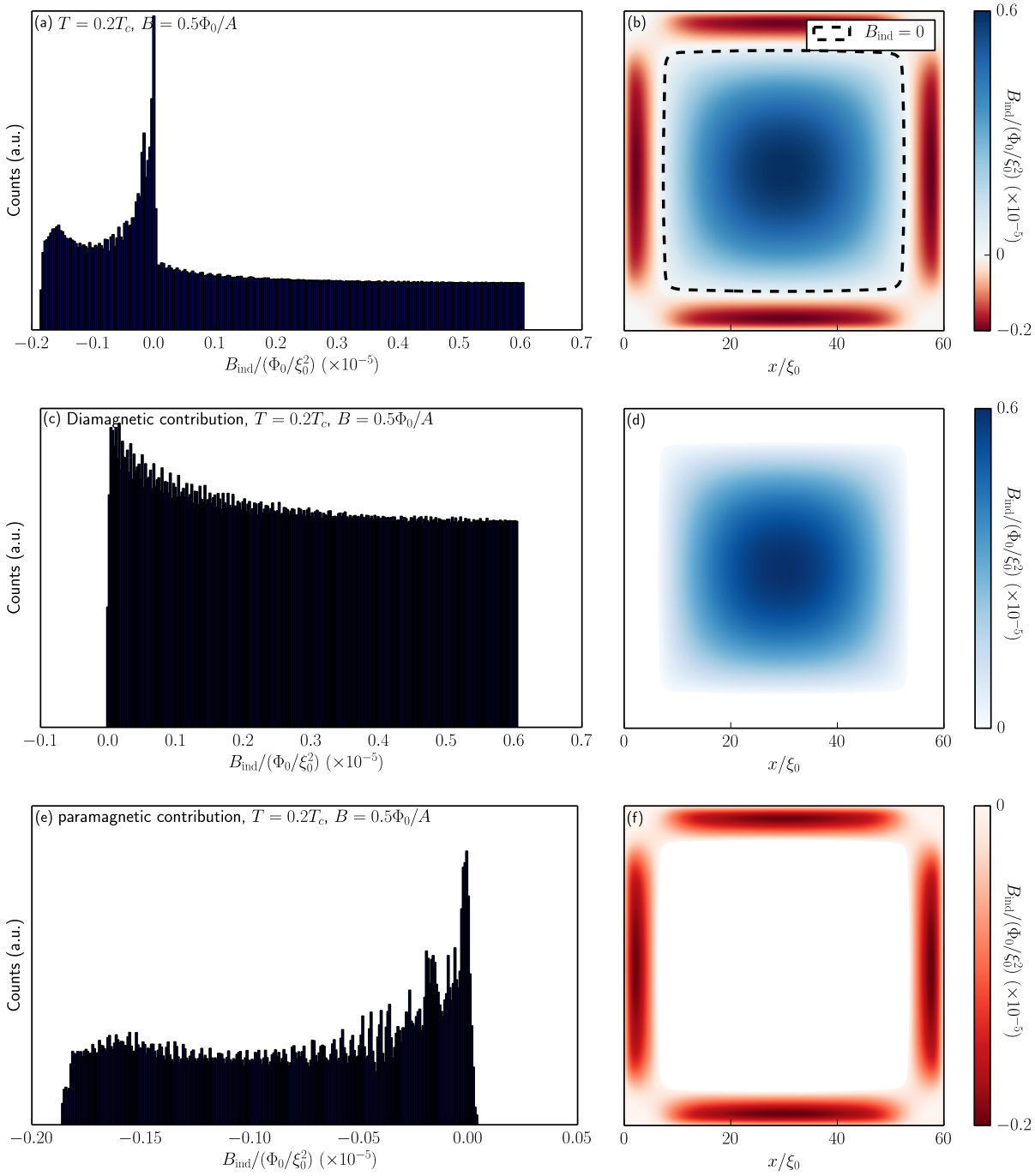

Figure 7.36: *Panels (a), (c) and (e) show histograms of the magnetic-field distribution for the induced magnetic flux densities in panels in panels (b), (d) and (f), respectively. The diamagnetic response (blue) and the paramagnetic response (red) are separated by the dashed line $B_{ind} = 0$. The grains are maximally pairbreaking d-wave grains, at temperature $T = 0.2T_c$ and external field $B_{ext} = 0.5\Phi_0/\mathcal{A}$, where $\mathcal{A} = (60\xi_0)^2$ is the area of the grain.*

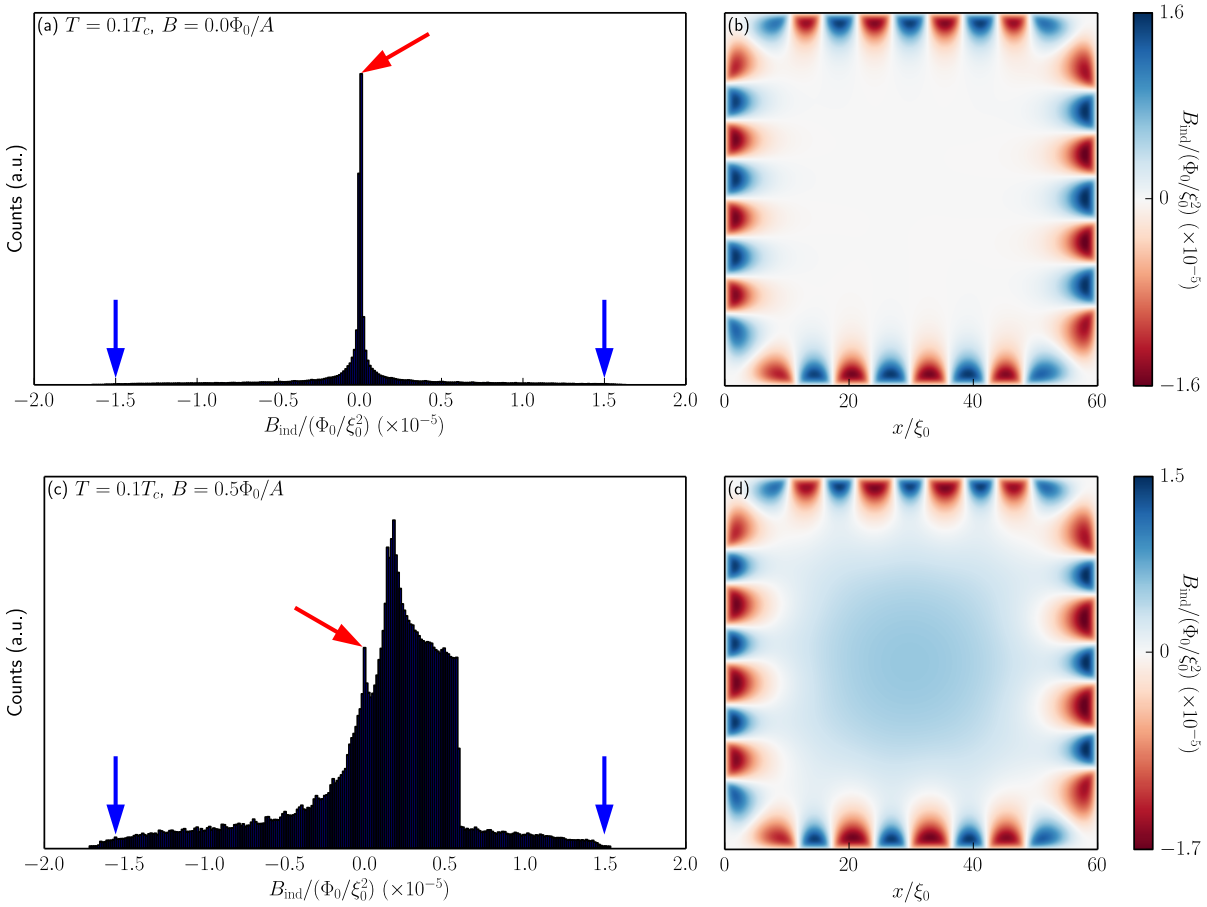

Figure 7.37: *(a) Histogram of the magnetic-field distribution in in panel (b), in a maximally pairbreaking d-wave grain at temperature $T = 0.1T_c$ and no external field. The distribution seems to be exponentially decaying as $\sim \exp(-a|B_{ind}|)$, where a is some decay constant. The sharp peak exactly at zero (red arrow) is due to singular points, and might not be present in a real sample. (c) In an external field $B_{ext} = 0.5\Phi_0/\mathcal{A}$, the histogram is a superposition of the signatures from the loop currents, the diamagnetic response as well as the paramagnetic response, shown in panel (d). Blue arrows mark the edges of the distribution of the loop current.*

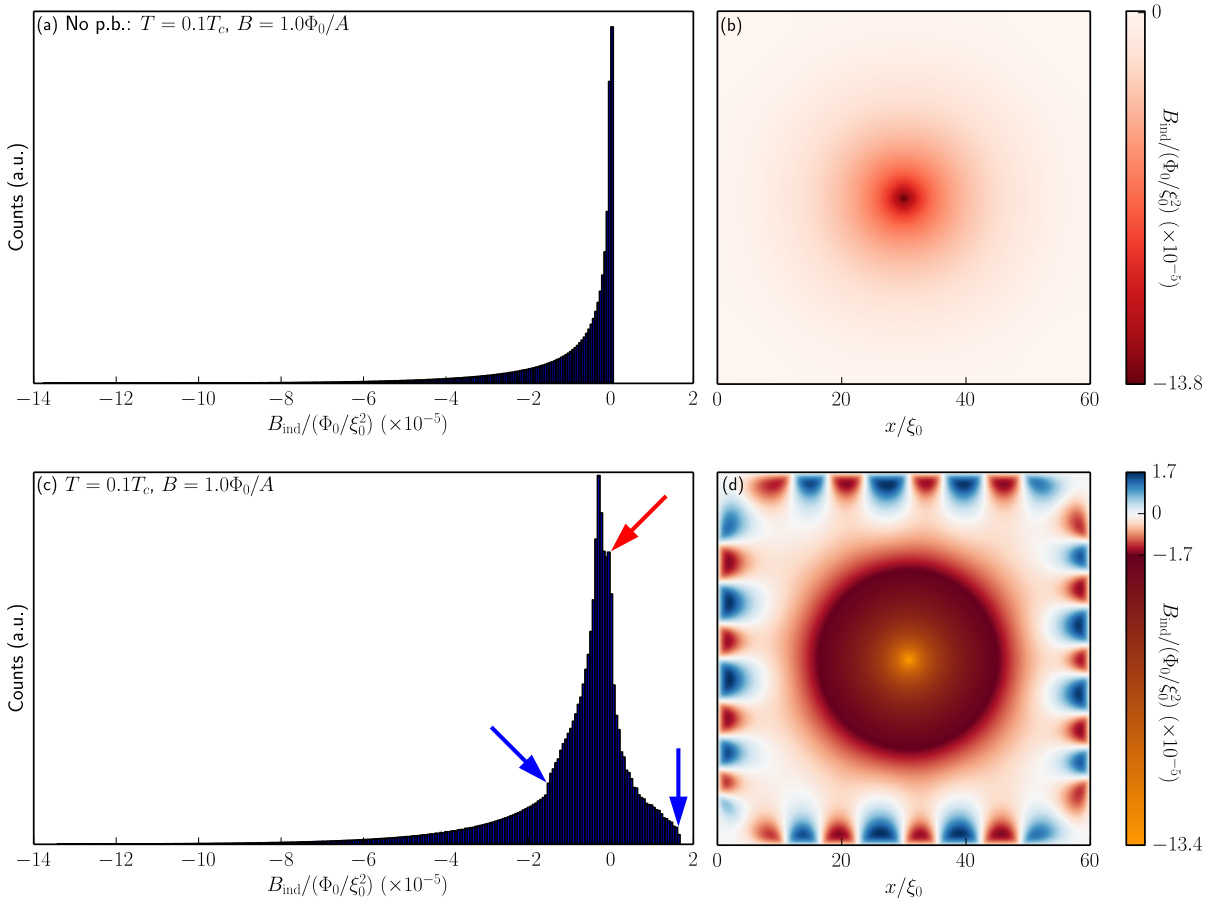

Figure 7.38: *(a) Histogram of the magnetic-field distribution due to the Abrikosov vortex shown in panel (b), in a grain without pairbreaking edges, at temperature* $T = 0.1T_c$ *and external field* $B_{ext} = \Phi_0/\mathcal{A}$*. (c) With pairbreaking edges, the distribution is superimposed with that of the loop currents, shown in panel (d). Arrows mark the peak (red) and edges (blue) of the loop current distribution.*

7.4 Extremely low temperatures

Extremely low temperatures of $T = 0.01T_c$ and $T = 0.001T_c$ have been studied, to see if the phase survives or shows any qualitative changes. To study such low temperatures, the Ozaki technique is employed (see Sec. 3.5), with a cutoff of $N_O = 100$. Figure 7.39 shows the (a) current density and (b) induced flux density, at $T = 0.001T_c$, illustrating that the phase is intact with no major changes. The only change in going to lower temperatures seems to be an increased "stiffness" in the vector field of the superfluid momentum, hence also the current density (compare against Fig. 7.1 on p. 103). As a start guess for these simulations, a well-converged solution at temperature $T = 0.1T_c$ was used. It has also been verified that the phase is found when starting from a completely real order parameter at extremely low temperatures and then annealing with an external field to nucleate the circulating currents. It is however much more difficult to converge to a high degree due to the increased simulation time, as well as an increased difficulty for the system to rearrange circulating and counter-circulating currents. The latter might be due to the increased stiffness.

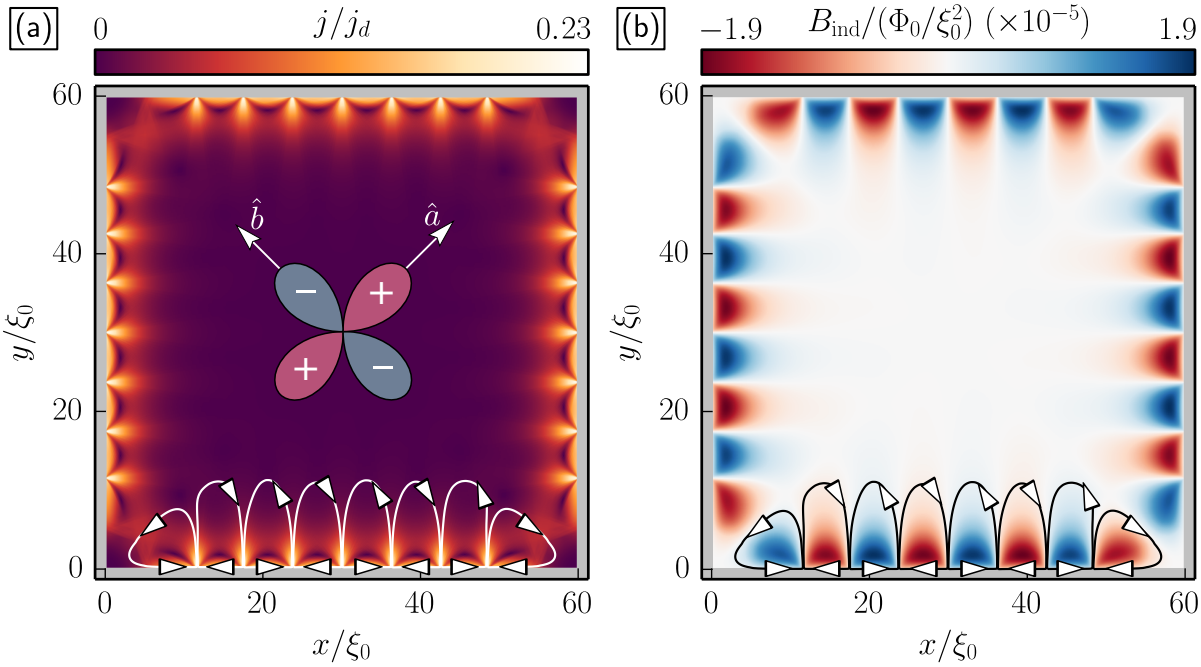

Figure 7.39: *(a) Spontaneous loop currents and (b) induced flux density, at $T = 0.001T_c$. The phase shows no major changes at low temperatures, except an increased stiffness. Arrows mark the circulation of the particle currents.*

7.5 Discussion: experimental verification

The loop currents of the loop-current phase lead to "blobs" of magnetic fluxes with magnitudes on the order of $10^{-5}\Phi_0/\xi_0^2$, which increases at lower temperatures, and is distributed over areas of roughly $5\xi_0 \times 5\xi_0$ (yielding a field on the order of 1 mT in YBCO with $\xi_0 \approx 2$ nm). This is in stark contrast to typical magnetic phenomena in superconductors, with integer flux quanta that are distributed on a length scale of the penetration depth, i.e. two orders of magnitude longer than the superconducting coherence length in type-II superconductors. The most commonly used probes, like the superconducting quantum interference device (SQUID), typically have active areas of hundreds of coherence lengths. Thus, detecting the fluxes generated in the loop-current phase should be extremely challenging with conventional tools. Direct detection is further complicated by two facts, the first being that there generally is an equal amount of positive and negative flux through the grain. This means that the flux measured with a larger probe should average to zero. The second fact is that neighboring fluxes have opposite sign, which implies that the flux lines probably bend and close on themselves very near the surface of the grain. Therefore, direct detection of the induced flux ought to rely on very local probes, like recently developed nano-SQUIDs [144], nitrogen-vacancy cantilevers [145], scanning tunneling microscope tips [146–148], and magnetic resonance force microscopes [149]. Even if the probe is slightly larger than the typical blob size, it can be swept across the interface, giving rise to a modulation in the measured flux depending on the asymmetry of positive to negative flux covered. As mentioned in Sec. 7.3.4, another route might be to try to detect the characteristic magnetic field distribution of the current loops in NMR measurements. These NMR measurements should also be as localized to the pair breaking interfaces as possible.

As argued in paper I, the situation might be somewhat improved when applying an external magnetic field. It is shown that an external magnetic field in the Meissner phase leads to a net induced magnetic field, with both a paramagnetic and a diamagnetic response. As the temperature is lowered below the transition temperature T^* of the loop-current phase, the loop currents induces a "kink" in the grain-total induced magnetic flux, on the order of $10^{-7}\Phi_0/\xi_0^2$, which for YBCO ($\xi_0 \approx 2$ nm) corresponds to a magnetic field of ~ 0.1 mT. Such a kink ought to be observable as long as the probe can be put close enough to the grain. Furthermore, the loop currents lead to a sudden disappearance of the paramagnetic response, which might be detectable in a penetration-depth experiment.

One of the most promising ways to indirectly verify the phase, however, would be by measuring the heat capacity jump with nano-calorimetry [39]. The jump was shown in Sec. 7.2.4 and paper I to be a few percent of the heat-capacity jump in the normal-superconducting phase transition. To improve the chances of observing the jump, an array of grains could be measured.

8 Conclusions

In summary, the purpose of this thesis has been to study mesoscopic unconventional superconductors. In particular, the aim has been to study the "loop-current phase" in greater detail. This is a phase which spontaneously breaks translational and time-reversal symmetries along pairbreaking interfaces in d-wave superconductors. Along such interfaces, midgap states are formed exactly at the Fermi energy from broken superconducting pairs as a result of a sign inversion in the order parameter. It is energetically favorable to shift such states to finite energies, and the loop-current phase is one possible mechanism that provides such a shift. This is done through a spontaneous generation of a superfluid momentum p_S, with a repeated pattern of sources and sinks separated by a distance of $\sim 6\xi_0$, where ξ_0 is the superconducting coherence length. This superfluid momentum generates a necklace of circulating and counter-circulating current loops, and provides an energetically favorable Doppler shift of the midgap states. The transition temperature into this phase is $T^* \approx 0.18T_c$, where T_c is the superconducting transition temperature. Various properties of the phase were cataloged. The main research goal was to study the stability of the phase against external magnetic fields and different geometric effects.

It was shown in paper I that the phase survives in the entire Meissner state and for low fields in the mixed state. An external field explicitly breaks time-reversal symmetry, and leads to a paramagnetic response carried by midgap states at pairbreaking interfaces. The paramagnetic response is a competing mechanism to shift the midgap states, with a shift which grows linearly with decreased temperature. The spontaneous superfluid momentum induces a shift which grows highly non-linearly, however, and is therefore the winning mechanism. The competition slightly lowers the transition temperature with increased external field, and gives rise to observables which might be measured in experiment. The phase also survives strong fields in a solenoid as long as there is a phase winding corresponding to the flux quanta of the external field. For stronger fields with Abrikosov vortices, or with low winding numbers in solenoids, the external field eventually develops a vector potential which gives a more energetically favorable shift of the midgap states than the spontaneous superfluid momentum.

Similarly, it was shown that geometric effects that induce a significant broadening of the spectrum also lead to a suppression of the phase. These effects were related to the shape of the grain, its surface roughness, as well as to the angle between the crystal ab-axes and the grain edges. The purpose of paper II was to

illustrate that the phase does not rely on finite-size effects, in contrast to similar phases studied previously in the literature.

Experimental verification of the phase was discussed. The manner in which the spontaneous currents and flux appear makes them challenging to observe experimentally, and provides a possible explanation why detection of such predicted symmetry-broken phases has been controversial. The effects associated with the phase scale with the surface-to-volume ratio, or edge-to-area ratio, and is therefore easier to see in small mesoscopic grains. To observe the phase, it is suggested to look for the jump in the heat capacity with nanocalorimetry. Direct observation relies on techniques which can resolve a microscopic flux distributed over small areas of roughly $5\xi_0 \times 5\xi_0$. Examples of such techniques are nano SQUIDs, diamond cantilevers, STMs, and magnetic resonance force microscopes. It might also be possible to detect signatures of the phase in NMR measurements.

In conclusion, the loop-current phase gives rise to a spectral broadening which is consistent with current experimental observations. With its potential explanation of longstanding contradictions regarding spontaneous symmetry-breaking phases, it offers an interesting topic for further research in both experiment and theory.

8.1 Open questions

The field of mesoscopic superconductivity is today an active area of research, with many questions that remain open surrounding the nature of the superconducting state in this regime. Perhaps most relevant to this thesis are the properties of midgap states. This thesis and its appended papers mainly focus on how these midgap states enable spontaneous breaking of translational and time-reversal symmetries, in phases that are here referred to as the Vorontsov phase [53] and the loop-current phase [46]. Many questions were answered about the nature of the latter phase, but even more questions remain. Some of them are listed in the following, together with questions relevant to mesoscopic superconductors in general.

Why does the circulating currents have a size of roughly $5\xi_0$, and why is the transition temperature into the phase $T^* \sim \frac{1}{5}T_c$? To answer these questions, small perturbations close to T^* will be studied.

The Vorontsov phase has previously been studied with respect to different effects and perturbations, e.g. external magnetic fields [64], microscopic surface roughness [65], temperature fluctuations [66], and fermi-surface nesting [67]. Do these effects show a similar behavior in the loop-current phase?

Another question is what happens to the phase as the penetration depth $\lambda_0 \to \xi_0$, and when the induced vector potential is solved self consistently? Preliminary studies have been made, which shows negligible influence on the phase even as $\lambda \simeq \xi_0$, assuming no external field. Higher external fields, and in particular in the mixed state, might give rise to different results. On the same topic, the

penetration depth might be affected by the phase, which is something that could be studied in a linear-response regime for weak external fields. It was shown that the phase is robust against external fields in the Meissner state, but that the phase breaks down somewhere in the mixed state. It would be relevant to produce the full phase diagram.

The influence of various geometric effects was studied, with the conclusion that the phase survives as long as the midgap states are not broadened significantly. Such results should carry over to grains with microscopic roughness (i.e. diffuse boundary conditions), and perhaps to non-magnetic impurities as well. The effect of magnetic impurities is also of interest, as many real materials host these. The manifestation of the phase in $3D$ is completely unknown. The preliminary guess is that, similar to general vortex phenomena, there might be translational invariance along the third dimension. Of course, the results might vary depending on the type of superconductor considered, e.g. layered superconductors and "real" $3D$ superconductors.

With spin-dependence, it is possible to have in-plane fields which couples to the spin. The effect of such a coupling is unknown.

p-wave superconductors have been studied (in particular $p_x + ip_y$), without any direct sign of the phase. This ought to be due to the strong chiral currents inherent in these superconductors. More detailed studies might reveal hints of similar phases though. More generally, it is predicted that p-wave superconductors host interesting states like half-quantum and double-quantum vortices. By simulating recently developed Sr_2RuO_4 grains, it should be possible to study such states.

Of great relevance to real devices is the effects of non-equilibrium and time-dependence. Such effects would require a significant modification of the formalism developed here (and the software used), but would open the doors to many new research topics. Similarly, the effects of coupling the grain to other materials, such that junctions and transport can be studied, is of great interest.

Appendices

Appendix A

Units

This thesis combines theory with numerical implementation, and on occasion compares results with experiment. To make all of this easier, the (mal)practice of using natural units ("setting" units like c and $\hbar$ to 1) is avoided, except in some lengthier calculations. Instead, this thesis uses Gaussian centimeter-gram-second units (CGS), unless otherwise specified, in line with most superconductivity literature. Equations are generally written on a dimensionless form by normalization with standard units. This appendix goes through these units and dimensions, and makes a short comparison between International System units (SI, or mksa) and CGS units. Note that in this thesis, the sign convention for the elementary charge is

$$e = -|e|\,. \tag{A.1}$$

For a more elaborate discussion on units and dimensions, see for example the appendices of Tinkham [73] and Jackson [115].

A.1 Systems of units: SI versus Gaussian CGS

In Tab. A.1, a conversion from SI to CGS systems is provided for a few important expressions and quantities. Quantities that are not specifically of an electromagnetic nature (e.g. force, length, mass, time, etc.) remain the same in both systems. In summary, the most important substitution in going from SI to CGS units is

$$\mu \to \frac{4\pi}{c^2}. \tag{A.2}$$

Table A.1: *Conversion between SI and Gaussian units for various electrodynamic expressions.*

Expression	**SI** (mksa)	**Gaussian CGS**
Speed of Light	$\frac{1}{\sqrt{\epsilon_0 \mu_0}}$	c
Flux Quantum (Φ_0)	$\frac{h}{2\lvert e\rvert}$	$\frac{hc}{2\lvert e\rvert}$
London penetration depth (λ)	$\sqrt{\frac{m}{\mu_0 e^2 n_s}}$	$\sqrt{\frac{mc^2}{4\pi e^2 n_S}}$
Ampère's Circuit Law	$\boldsymbol{\nabla} \times \boldsymbol{B} = \mu_0 \boldsymbol{j}$	$\boldsymbol{\nabla} \times \boldsymbol{B} = \frac{4\pi}{c}\boldsymbol{j}$
Lorentz Force	$\boldsymbol{F} = q\left(\boldsymbol{E} + \boldsymbol{v} \times \boldsymbol{B}\right)$	$\boldsymbol{F} = q\left(\boldsymbol{E} + \frac{1}{c}\boldsymbol{v} \times \boldsymbol{B}\right)$
Magnetic $\boldsymbol{B}$ field, flux, vector potential	$\sqrt{\frac{4\pi}{\mu_0}}(\boldsymbol{B}, \Phi_m, \boldsymbol{A})$	$(\boldsymbol{B}, \Phi_m, \boldsymbol{A})$
Magnetic $\boldsymbol{H}$ field	$\sqrt{4\pi\mu_0}\boldsymbol{H}$	$\boldsymbol{H}$
Magnetic moment, Magnetization	$\sqrt{\frac{\mu_0}{4\pi}}(\boldsymbol{m}, \boldsymbol{M})$	$(\boldsymbol{m}, \boldsymbol{M})$
Electric field, Electric potential	$\sqrt{4\pi\epsilon_0}(\boldsymbol{E}, \varphi)$	$(\boldsymbol{E}, \varphi)$
Electric displacement field	$\sqrt{\frac{4\pi}{\epsilon_0}}\boldsymbol{D}$	$\boldsymbol{D}$
Dielectric constant	$\frac{\epsilon}{\epsilon_0}$	ϵ
Permeability	$\frac{\mu}{\mu_0}$	μ
Electric susceptibility, Magnetic Susceptibility	$\frac{1}{4\pi}(\chi_e, \chi_m)$	(χ_e, χ_m)
Conductivity, Conductance, Capacitance	$\frac{1}{4\pi\epsilon_0}(\sigma, S, C)$	(σ, S, C)
Resistivity, Resistance, Inductance	$4\pi\epsilon_0(\rho, R, L)$	(ρ, R, L)
Charge, Charge density, Current, Current density, Polarization density, Electric dipole moment	$\frac{1}{\sqrt{4\pi\epsilon_0}}(g, \rho, I, \boldsymbol{J}, \boldsymbol{P}, \boldsymbol{p})$	$(g, \rho, I, \boldsymbol{J}, \boldsymbol{P}, \boldsymbol{p})$

A.2 Table of normalization units

Table A.2 shows the normalization units which are used in the results and in order to make equations dimensionless in the thesis. In the table, k_B is the Boltzmann constant, T_c the superconducting transition temperature, $\int_{\mathrm{FS}}$ denotes an integral over the Fermi surface (FS), v_F the Fermi velocity, p_F the Fermi momentum, h the Planck constant, $\hbar$ the reduced Planck constant, c the speed of light, $e = -|e|$ the elementary charge, $\alpha \equiv 8\pi^2/7\zeta(3)$, and ΔC_{NS} is the heat-capacity jump between the normal to superconducting (NS) phase transition in bulk (derived in Sec. 5.3.5). Note that it is common to find both literature with and without the factor of 2π in ϵ_0 and in the denominator of ξ_0. Unfortunately, the combination chosen here that $\left[E\right] = k_B T_c$ with $\xi_0 = \hbar v_F / 2\pi k_B T_c$ leads to additional factors of 2π in many equations, but this choice is more consistent with relevant literature. Note that the notation for the dimensions of the density of states often varies in the literature, from number of states per energy and volume, to just number of states per volume. In this thesis, the former notation is chosen except for when deriving the gap equation. In particular, N_F is per spin and has the dimensions

$$\left[N_F\right] = \frac{(\#\text{states})}{(\text{energy}) \times (\text{volume})} = \frac{1}{Jm^3}. \tag{A.3}$$

Table A.2: *Normalization units used for different dimensions/expressions.*

Dimension/expression	**Comment**	**Symbol definition**
Energy		$\epsilon_0 \equiv k_B T_c$
Density of states	Normal-state DOS at F.S.	$N_F \equiv \int_{\mathrm{FS}} \frac{d^2 p_F}{(2\pi\hbar)^3 \lvert \boldsymbol{v}_F(\boldsymbol{p}_F)\rvert}$
Length (order parameter)	coherence length ($T = 0$)	$\xi_0 \equiv \frac{\hbar v_F}{2\pi k_B T_c}$
Length (magnetic)	penetration depth ($T = 0$)	$\lambda_0 \equiv \sqrt{\frac{c^2}{4\pi e^2 N_F v_F^2}}$
Momentum	superfluid momentum	$p_0 \equiv \frac{k_B T_c}{v_F}$
Current density	depairing current	$j_d \equiv 4\pi k_B T_c \lvert e\rvert N_F v_F$
Magnetic flux	magnetic flux quantum	$\Phi_0 \equiv \frac{hc}{2\lvert e\rvert}$
Magnetic flux density		$B_0 \equiv \frac{\Phi_0}{\xi_0^2}$
Magnetic vector potential		$A_0 \equiv B_0 \xi_0 = \frac{\Phi_0}{\xi_0}$
Heat Capacity (s-wave)	NS-jump (d-wave)	$\Delta C_{NS}^s \equiv \alpha k_B^2 T_c \mathcal{V} N_F$
Heat Capacity (d-wave)	NS-jump (d-wave)	$\Delta C_{NS}^d \equiv \frac{2}{3} \Delta C_{NS}^s$

Appendix B

Summary of dimensionless equations

This appendix summarizes the most relevant equations on dimensionless forms.

The Eilenberger equation is (Sec. 2.3)

$$i2\pi\hat{\boldsymbol{v}}_F\cdot(\xi_0\boldsymbol{\nabla}_R)\hat{g}+\left[\left(\frac{z}{k_BT_c}-2\pi^2\frac{\hat{\boldsymbol{v}}_F\cdot\boldsymbol{A}}{\Phi_0/\xi_0}\right)\hat{\tau}_3-\frac{\hat{\Delta}}{k_BT_c},\hat{g}\right]_{\otimes}=0, \tag{B.1}$$

with a minus sign relative to the previous formulation due to $e=-|e|$ in Φ_0. The Eilenberger equation is rewritten into the Riccati equations (Sec. 2.5)

$$\left[i2\pi\hat{\boldsymbol{v}}_F\cdot(\xi_0\boldsymbol{\nabla})+2\left(\frac{z}{k_BT_c}-2\pi^2\frac{\hat{\boldsymbol{v}}_F\cdot\boldsymbol{A}}{\Phi_0/\xi_0}\right)\right]\gamma = \frac{\tilde{\Delta}}{k_BT_c}\gamma^2-\frac{\Delta}{k_BT_c}, \tag{B.2}$$

$$\left[i2\pi\hat{\boldsymbol{v}}_F\cdot(\xi_0\boldsymbol{\nabla})-2\left(\frac{z}{k_BT_c}-2\pi^2\frac{\hat{\boldsymbol{v}}_F\cdot\boldsymbol{A}}{\Phi_0/\xi_0}\right)\right]\tilde{\gamma} = \frac{\Delta}{k_BT_c}\tilde{\gamma}^2-\frac{\tilde{\Delta}}{k_BT_c}. \tag{B.3}$$

Note that these Riccati equations are in spin-space, rendering a sign difference with respect to the scalar Riccati equations introduced later on the appendices.The gap equation for a spin-singlet order parameter is (Sec. 2.4.1)

$$\frac{\Delta_{s,t}}{k_BT_c}=V_{s,t}\frac{T}{T_c}\int\frac{d\theta_{\boldsymbol{p}_F}}{2\pi}\eta^*_{\Gamma_{s,t}}(\boldsymbol{p}_F)\sum_{\epsilon_n>0}^{\Omega_c}\left(f_{s,t}(\boldsymbol{p}_F,\boldsymbol{R};\epsilon_n)\pm\tilde{f}^*_{s,t}(\boldsymbol{p}_F,\boldsymbol{R};\epsilon_n)\right), \tag{B.4}$$

with $+$ for singlet (s) and $-$ for triplet (t). The dimensionless angle-resolved LDOS is (Sec. 4.2)

$$\mathcal{N}(\boldsymbol{p}_F,\boldsymbol{R};\epsilon) = -\frac{1}{2\pi}\,\mathrm{Im}\left[\mathrm{Tr}\left\{\hat{g}^R(\boldsymbol{p}_F,\boldsymbol{R};\epsilon)\right\}\right] \tag{B.5}$$

$$= -\frac{2}{\pi}\,\mathrm{Im}\left[g_0^R(\boldsymbol{p}_F,\boldsymbol{R};\epsilon)\right], \tag{B.6}$$

and the angle-averaged LDOS is (Sec. 2.4.2)

$$\frac{N(\boldsymbol{R};\epsilon)}{N_F}=-\frac{2}{\pi}\int\frac{d\theta_{\boldsymbol{p}_F}}{2\pi}\,\mathrm{Im}\left[g_0^R(\boldsymbol{p}_F,\boldsymbol{R};\epsilon)\right]. \tag{B.7}$$

Here, the normal-state DOS at the Fermi surface (FS) is defined as

$$N_F = \int_{\mathrm{FS}} \frac{d^2 p_F}{(2\pi\hbar)^3 \left|\boldsymbol{v}_F(\boldsymbol{p}_F)\right|}. \tag{B.8}$$

The current density is (Sec. 4.2)

$$\frac{\boldsymbol{j}(\boldsymbol{R})}{j_d} = -\frac{T}{T_c} \int d\boldsymbol{p}_F \sum_{0<\epsilon_n<\epsilon_c} \hat{\boldsymbol{v}}_F g_0^M(\boldsymbol{p}_F, \boldsymbol{R}; i\epsilon_n), \tag{B.9}$$

where $j_d \equiv 4\pi k_B T_c e N_F v_F$ is the depairing current. The energy shift due to the presence of a magnetic vector potential $\boldsymbol{A}$ is (Sec. 4.3.2)

$$\frac{z}{k_B T_c} \to \frac{z}{k_B T_c} - 2\pi^2 \frac{\hat{v}_F \cdot \boldsymbol{A}}{\Phi_0/\xi_0}, \tag{B.10}$$

where z is a complex energy and the vector potential can be separated into one part that is coupled to external magnetic flux ($\boldsymbol{A}_{\mathrm{ext}}$), and another due to induced currents in the systems ($\boldsymbol{A}_{\mathrm{ind}}$), according to

$$\boldsymbol{A} = \boldsymbol{A}_{\mathrm{ext}} + \boldsymbol{A}_{\mathrm{ind}}. \tag{B.11}$$

The vector potential also enters the gauge invariant expression of the superfluid momentum

$$\frac{1}{2\pi}\frac{\boldsymbol{p}_s}{p_0} = \frac{1}{2}\left(\xi_0 \boldsymbol{\nabla}\right)\chi + \pi \frac{\boldsymbol{A}}{\Phi_0/\xi_0}, \tag{B.12}$$

$$p_0 \equiv \frac{k_B T_c}{v_F}. \tag{B.13}$$

In homogeneus superconductors without holes, a uniform external flux perpendicular to the SC ($\boldsymbol{B}_{\mathrm{ext}} = B_{\mathrm{ext}}\hat{\boldsymbol{z}}$) gives rise to a vector potential (Sec. 4.3.3)

$$\frac{\boldsymbol{A}_{\mathrm{ext}}}{\Phi_0/\xi_0} = \frac{1}{2}\frac{\boldsymbol{B}_{\mathrm{ext}}}{\Phi_0/\xi_0^2} \times \frac{\boldsymbol{\rho}}{\xi_0} \tag{B.14}$$

$$= \frac{1}{2}\frac{\Phi_{\mathrm{ext}}}{\Phi_0}\left(\frac{\mathcal{A}}{\xi_0^2}\right)^{-1}\left(-\frac{y}{\xi_0}\hat{\boldsymbol{x}} + \frac{x}{\xi_0}\hat{\boldsymbol{y}}\right). \tag{B.15}$$

If the superconductor has holes, and there is a uniform magnetic flux inside the hole of radius ρ_a, but no flux in the superconductor itself, (Sec. 4.3.4) the vector potential can be written

$$\frac{\boldsymbol{A}_{\mathrm{ext}}}{\Phi_0/\xi_0} = \frac{1}{2\pi}\left(\frac{\rho}{\xi_0}\right)^{-1}\frac{\Phi_{\mathrm{ext}}}{\Phi_0}\hat{\boldsymbol{\phi}} \tag{B.16}$$

$$= \frac{1}{2\pi}\frac{\Phi_{\mathrm{ext}}}{\Phi_0}\frac{-y\hat{\boldsymbol{x}} + x\hat{\boldsymbol{y}}}{x^2+y^2}\xi_0. \tag{B.17}$$

Currents in the system give rise to an induced vector potential and an induced flux density (Sec. 4.4.1)

$$\frac{\boldsymbol{A}_{\rm ind}(\boldsymbol{x})}{\Phi_0/\xi_0} = \frac{\kappa_0^{-2}}{\pi^2}\int\frac{d^2\boldsymbol{x}'}{\xi_0^2}\frac{\boldsymbol{j}(\boldsymbol{x}')}{j_d}\ln\left|\frac{\boldsymbol{x}-\boldsymbol{x}'}{\xi_0}\right|, \tag{B.18}$$

$$\frac{\boldsymbol{B}_{\rm ind}}{\Phi_0/\xi_0^2} = (\xi_0\boldsymbol{\nabla})\times\frac{\boldsymbol{A}_{\rm ind}}{\Phi_0/\xi_0}, \tag{B.19}$$

respectively, where $\kappa_0 \equiv \lambda_0/\xi_0$ is the dimensionless Ginzburg-Landau parameter. The free-energy difference between the normal and superconducting states is given by the Luttinger-Ward functional (Sec. 5.1.1)

$$\frac{\delta\Omega(T)}{\mathcal{V}N_F(k_BT_c)^2} = \int\frac{d\boldsymbol{R}}{\mathcal{V}}\Bigg\{\left(\frac{\boldsymbol{B}_{\rm ind}(\boldsymbol{R})}{\Phi_0/\xi_0^2}\right)^2 2\pi^4\kappa_0^2 + \frac{1}{2}\frac{T}{T_c}\int_0^1 d\lambda\int_0^{2\pi}\frac{d\theta_{\boldsymbol{p}_F}}{2\pi}\sum_{\epsilon_n}\mathrm{Tr}\left[\frac{\hat{\Delta}}{k_BT_c}\left(\hat{g}_\lambda - \frac{1}{2}\hat{g}\right)\right]\Bigg\} \tag{B.20}$$

or the Eilenberger functional (Sec. 5.1.3)

$$\frac{\delta\Omega(T)}{\mathcal{V}N_F(k_BT_c)^2} = \int\frac{d\boldsymbol{R}}{\mathcal{V}}\Bigg\{\left(\frac{\boldsymbol{B}_{\rm ind}(\boldsymbol{R})}{\Phi_0/\xi_0^2}\right)^2 2\pi^4\kappa_0^2 + \frac{|\Delta(\boldsymbol{R})|^2}{(k_BT_c)^2}\ln\frac{T}{T_c} + 2\pi\frac{T}{T_c}\sum_{\epsilon_n}\left[\frac{|\Delta(\boldsymbol{R})|^2}{(k_BT_c)^2}\frac{k_BT_c}{\epsilon_n} + \frac{i\mathcal{I}(\boldsymbol{R};\epsilon_n)}{k_BT_c}\right]\Bigg\}, \tag{B.21}$$

$$\mathcal{I}(\boldsymbol{R};\epsilon_n) = \int\frac{d\theta_{\boldsymbol{p}_F}}{2\pi}\Big[\tilde{\Delta}(\boldsymbol{p}_F,\boldsymbol{R})\gamma(\boldsymbol{p}_F,\boldsymbol{R};\epsilon_n) - \Delta(\boldsymbol{p}_F,\boldsymbol{R})\tilde{\gamma}(\boldsymbol{p}_F,\boldsymbol{R};\epsilon_n)\Big]. \tag{B.22}$$

The heat capacity difference with respect to the normal state is calculated as the second-derivative of the Eilenberger free energy (Sec. 5.3.6)

$$\frac{\delta C_V}{\mathcal{V}\Delta C_{NS}} = \frac{1}{\tilde{\alpha}}\frac{T}{T_c}\frac{\partial^2}{\partial(T/T_c)^2}\int\frac{d\boldsymbol{R}}{\mathcal{V}}\Bigg\{\left(\frac{\boldsymbol{B}(\boldsymbol{R})}{\Phi_0/\xi_0^2}\right)^2 2\pi^4\kappa_0^2 + \frac{|\Delta(\boldsymbol{R})|^2}{(k_BT_c)^2}\ln\frac{T}{T_c} + 2\pi\frac{T}{T_c}\sum_{\epsilon_n}\left[\frac{|\Delta(\boldsymbol{R})|^2}{(k_BT_c)^2}\frac{k_BT_c}{\epsilon_n} + i\frac{\langle\mathcal{I}(\boldsymbol{p}_F,\boldsymbol{R};\epsilon_n)\rangle_{\boldsymbol{p}_F}}{k_BT_c}\right]\Bigg\}, \tag{B.23}$$

where ΔC_{NS} is the heat capacity jump in the normal-superconducting phase transition, and

$$\tilde{\alpha} \equiv \begin{cases}\frac{8\pi^2}{7\zeta(3)} \approx 9.4, & \text{s-wave},\\ \frac{2}{3}\frac{8\pi^2}{7\zeta(3)} \approx 6.3, & \text{d-wave}.\end{cases} \tag{B.24}$$

Appendix C

From summation over momenta to integration over energies

In this appendix, it is shown how a sum over states in momentum space can be converted into an integral over energies, through introducing the density of states, following e.g. Ref [4]. This is an extremely common procedure in quantum mechanics, and especially in condensed matter physics. In contrast to most similar derivations in the literature, this derivation will keep the angular dependence, which will come in handy when studying systems that are anisotropic in momentum space, like d-wave superconductors.

Consider a bulk system, in which it is appropriate to assume periodic boundary conditions (i.e. Born-von Karman boundary conditions) for a wave function of interest. Let $\mathcal{L}$ be length of the period in spatial space. The components of the wave vector $\boldsymbol{k}$ then take on the form

$$k_i = \frac{2\pi}{\mathcal{L}} n_i, \quad n_i \text{ integers}, \tag{C.1}$$

such that each state in k space occupies a cell of volume

$$\Delta \boldsymbol{k} \equiv \Delta k^d = \left(\frac{2\pi}{\mathcal{L}}\right)^d = \frac{(2\pi)^d}{\mathcal{V}}, \tag{C.2}$$

where d is the dimension and $\mathcal{V} = \mathcal{L}^d$ is the corresponding volume in spatial space. Consider a system of volume Ω. The number of states n in Ω will approximately be the "total volume divided by volume per k-state", i.e.

$$n \approx \frac{\Omega}{\Delta k^d} = \frac{\Omega \mathcal{V}}{(2\pi)^d}. \tag{C.3}$$

The density of k-states N is then

$$N = \frac{n}{\Omega} = \frac{\mathcal{V}}{(2\pi)^d}. \tag{C.4}$$

The sheer amount of states in a typical condensed matter system makes the approximation very good. For Fermions with γ number of internal degrees of freedom, the density of states is $2^\gamma N$, due to the Pauli exclusion principle. Consider the sum over momentum states for a smooth function $F_{\boldsymbol{k}}$

$$\sum_{\boldsymbol{k}} F_{\boldsymbol{k}} = \sum_{\boldsymbol{k}} F_{\boldsymbol{k}} \frac{\Delta \boldsymbol{k}}{\Delta \boldsymbol{k}} = \frac{\mathcal{V}}{(2\pi)^d} \sum_{\boldsymbol{k}} F_{\boldsymbol{k}} \Delta \boldsymbol{k}. \tag{C.5}$$

For a very large system, taking the limit $\mathcal{V} \to \infty$ corresponds to $\Delta \boldsymbol{k} \to 0$, and an integral expression will be obtained through the Riemann sum

$$\lim_{\mathcal{V}\to\infty} \sum_{\boldsymbol{k}} F_{\boldsymbol{k}} = \lim_{\Delta \boldsymbol{k}\to 0} \frac{\mathcal{V}}{(2\pi)^d} \sum_{\boldsymbol{k}} F_{\boldsymbol{k}} \Delta \boldsymbol{k} = \mathcal{V} \int \frac{d\boldsymbol{k}}{(2\pi)^d} F(\boldsymbol{k}). \tag{C.6}$$

Let S_ξ denote a surface of constant energy ξ, such that the integration measure can be decomposed as

$$d\boldsymbol{k} \equiv \prod_i^d dk_i = dS_\xi dk_\perp, \tag{C.7}$$

where $dk_\perp$ is the perpendicular distance between the surface ξ = constant, and the surface $(\xi + d\xi)$ = constant. Perpendicular to these surfaces is also $\boldsymbol{\nabla}_{\boldsymbol{k}}\xi$, which is the gradient of ξ with respect to k

$$dk_\perp = dk_\perp \frac{d\xi}{d\xi} = \frac{dk_\perp}{d\xi} d\xi = \frac{d\xi}{|\boldsymbol{\nabla}_{\boldsymbol{k}}\xi|}. \tag{C.8}$$

In spherical coordinates, for example, $dS_\xi dk_\perp = \sin(\theta) k^2 dk d\theta d\phi$, and for a plane-wave dispersion

$$|\boldsymbol{\nabla}_{\boldsymbol{k}}\xi| = \frac{d}{dk}\frac{\hbar^2 k^2}{2m} = \frac{\hbar k}{m}. \tag{C.9}$$

The integral over $F(\boldsymbol{k})$ is rewritten

$$\begin{aligned} \int \frac{d\boldsymbol{k}}{(2\pi)^d} F(\boldsymbol{k}) &= \frac{1}{(2\pi)^d} \int dS_\xi \int dk F(\boldsymbol{k}) \\ &= \frac{1}{(2\pi)^d} \int dS_\xi \int \frac{d\xi}{|\boldsymbol{\nabla}_{\boldsymbol{k}}\xi|} F(\boldsymbol{k}). \end{aligned} \tag{C.10}$$

The density of states states $D(\xi)$ in a small interval $d\xi$ is defined as

$$D(\xi) d\xi \equiv \frac{\mathcal{V}}{(2\pi)^d} \int \frac{dS_\xi}{|\boldsymbol{\nabla}_{\boldsymbol{k}}\xi|} d\xi, \tag{C.11}$$

where $[D(\xi)]$ = #states/energy. Defining the density of states per unit volume $N(\xi)$

$$N(\xi) \equiv \frac{D(\xi)}{\mathcal{V}} = \frac{1}{(2\pi)^d} \int \frac{dS_\xi}{|\boldsymbol{\nabla}_{\boldsymbol{k}}\xi|}. \tag{C.12}$$

In the case that $F(\boldsymbol{k})$ only depends on the magnitude of the wave vector (i.e. isotropic like usual s-wave superconductors), the sum over $\boldsymbol{k}$ thus reduces to

$$\sum_{\boldsymbol{k}} F_{\boldsymbol{k}} \xrightarrow[\Delta\boldsymbol{k}\to 0]{} \mathcal{V} \int d\xi N(\xi) F(\xi) \qquad \text{(isotropic case).} \tag{C.13}$$

In the case that $F(\boldsymbol{k})$ is anisotropic, the dispersion relation either needs to be known or at least isotropic. Under such conditions, $\frac{1}{|\boldsymbol{\nabla}_{\boldsymbol{k}}\xi|}$ can be evaluated or pulled out from the integral over dS_ξ, and substituted for $N(\xi)$, yielding

$$\sum_{\boldsymbol{k}} F_{\boldsymbol{k}} \xrightarrow[\Delta\boldsymbol{k}\to 0]{} \mathcal{V} \int dS_\xi \int d\xi N(\xi) F(\xi) \qquad \text{(anisotropic case).} \tag{C.14}$$

Note that most literature sets $\mathcal{V} \to 1$ to keep a compact notation.

The normal-state density of states at the Fermi surface, denoted N_F, commonly occurs in this thesis. It is defined as

$$N_F = \int_{\mathrm{FS}} \frac{d^2 p_F}{(2\pi\hbar)^3 \left|\boldsymbol{v}_F(\boldsymbol{p}_F)\right|}, \tag{C.15}$$

where the Fermi velocity $\boldsymbol{v_F}$ at the Fermi momentum p_F takes the role of $\boldsymbol{\nabla}_{\boldsymbol{k}}\xi$.

Appendix D

The BCS gap and analytic solutions

In this appendix, the BCS gap equation will be derived from the expectation value of the BCS Hamiltonian using a variational method, similar to Tinkham [73]. An integral expression will then be derived, which is valid for different pairing symmetries, like s and d-wave superconductors with a single order parameter (i.e. no mixtures like $s + id$). After that, an expression of T_c will be derived in the weak-coupling limit, together with analytic expressions of the BCS gap at $T = 0$ and close to T_c. The slope of the gap will also be derived close to T_c. The latter result is used in Ch. 5 to get an analytic expression for the jump in the heat capacity ΔC, in the normal-superconductor phase transition (in bulk). Some of these derivations follow Refs. [16, 73, 78]

D.1 Derivation of the BCS gap equation

The BCS Hamiltonian is usually written (see for example Schrieffer [71], de Gennes [72] and Tinkham [73]) as a sum over spin indices σ and momenta k, q, of fermionic creation ($c^\dagger$) and annihilation (c) operators

$$\mathcal{H}_{\text{BCS}} = \sum_{\boldsymbol{k},\sigma} \xi_{\boldsymbol{k}} c^\dagger_{\boldsymbol{k},\sigma} c_{\boldsymbol{k},\sigma} + \frac{1}{2} \sum_{\boldsymbol{k}_1,\sigma_1,\boldsymbol{k}_2,\sigma_2,\boldsymbol{q}} c^\dagger_{\boldsymbol{k}_1+\boldsymbol{q},\sigma_1} c^\dagger_{\boldsymbol{k}_2-\boldsymbol{q},\sigma_2} V_{\boldsymbol{k}_1,\boldsymbol{k}_2,\boldsymbol{q}} c_{\boldsymbol{k}_1,\sigma_1} c_{\boldsymbol{k}_2,\sigma_2}, \tag{D.1}$$

where the first term is the kinetic energy term with kinetic energies $\xi_{\boldsymbol{k}}$, and the second term is the interaction term with the potential V. The interaction term describes scattering from momentum states $\boldsymbol{k}_1, \boldsymbol{k}_2$ to $\boldsymbol{k}_1 + \boldsymbol{q}, \boldsymbol{k}_2 - \boldsymbol{q}$. The BCS ground state of Cooper pairs is similarly written as a product of creation operators acting on the vacuum state $|0\rangle$

$$|\Psi_{\text{BCS}}\rangle = \prod_{\boldsymbol{k}} \left(u_{\boldsymbol{k}} + e^{i\chi} v_{\boldsymbol{k}} c^\dagger_{\boldsymbol{k}+\boldsymbol{s},\uparrow} c^\dagger_{-\boldsymbol{k}+\boldsymbol{s},\downarrow} \right) |0\rangle \,, \tag{D.2}$$

where χ is the phase of the superfluid, $\boldsymbol{s}$ is the center-of-mass momentum for the Cooper pair, and $u^2_{\boldsymbol{k}}$ and $v^2_{\boldsymbol{k}}$ are the probabilities of a state being empty or occupied, respectively, such that $\left| u^2_{\boldsymbol{k}} + v^2_{\boldsymbol{k}} \right| = 1$. Equation (D.2) thus describes

pairwise creation of particles of momentum $\boldsymbol{k}+\boldsymbol{s}$ and $-\boldsymbol{k}+\boldsymbol{s}$ of opposite spin. The expectation value of the BCS Hamiltonian can be written

$$\begin{aligned}\langle E\rangle &= \langle\Psi_{\mathrm{BCS}}|\,\mathcal{H}_{\mathrm{BCS}}\,|\Psi_{\mathrm{BCS}}\rangle \\ &= \sum_{\boldsymbol{k}} 2v_{\boldsymbol{k}}^2\xi_{\boldsymbol{k}} + \sum_{\boldsymbol{kl}} v_{\boldsymbol{k}}u_{\boldsymbol{l}}u_{\boldsymbol{k}}v_{\boldsymbol{l}}V_{\boldsymbol{kl}} \\ &= \sum_{\boldsymbol{k}} 2v_{\boldsymbol{k}}^2\xi_{\boldsymbol{k}} + \sum_{\boldsymbol{k}} v_{\boldsymbol{k}}u_{\boldsymbol{k}}2\sum_{\boldsymbol{l}} u_{\boldsymbol{l}}v_{\boldsymbol{l}}V_{\boldsymbol{kl}} \\ &= \sum_{\boldsymbol{k}} \left(2v_{\boldsymbol{k}}^2\xi_{\boldsymbol{k}} - 2v_{\boldsymbol{k}}u_{\boldsymbol{k}}\Delta_{\boldsymbol{k}}\right), \end{aligned} \tag{D.3}$$

where opposite spin and momentum pairing has been assumed, and

$$\Delta_{\boldsymbol{k}} \equiv -\sum_{\boldsymbol{l}} u_{\boldsymbol{l}}v_{\boldsymbol{l}}V_{\boldsymbol{kl}}. \tag{D.4}$$

The BCS gap equation will be derived by minimizing Eq. (D.3) by variation of $u_{\boldsymbol{k}}, v_{\boldsymbol{k}}$

$$d\langle E\rangle = \frac{\partial\langle E\rangle}{\partial v_{\boldsymbol{k}}}dv_{\boldsymbol{k}} + \frac{\partial\langle E\rangle}{\partial u_{\boldsymbol{k}}}du_{\boldsymbol{k}} = 0. \tag{D.5}$$

Rewriting,

$$d\langle E\rangle = \sum_{\boldsymbol{k}} \left(4v_{\boldsymbol{k}}\xi_{\boldsymbol{k}} - 2u_{\boldsymbol{k}}\Delta_{\boldsymbol{k}}\right)dv_{\boldsymbol{k}} - 2\sum_{\boldsymbol{k}} v_{\boldsymbol{k}}\Delta_{\boldsymbol{k}}du_{\boldsymbol{k}} = 0. \tag{D.6}$$

Using the fact that $u_{\boldsymbol{k}}^2 + v_{\boldsymbol{k}}^2 = 1$, it is possible to rewrite $u_{\boldsymbol{k}}$ in terms of $v_{\boldsymbol{k}}$

$$u_{\boldsymbol{k}} = \sqrt{1-v_{\boldsymbol{k}}^2}, \tag{D.7}$$

$$du_{\boldsymbol{k}} = \frac{-v_{\boldsymbol{k}}}{u_{\boldsymbol{k}}}dv_{\boldsymbol{k}} = \frac{-v_{\boldsymbol{k}}}{\sqrt{1-v_{\boldsymbol{k}}^2}}dv_{\boldsymbol{k}}. \tag{D.8}$$

Substituting these expressions into Eq. (D.6) yields

$$0 = \sum_{\boldsymbol{k}} \left[4v_{\boldsymbol{k}}\xi_{\boldsymbol{k}}dv_{\boldsymbol{k}} - 2\Delta_{\boldsymbol{k}}u_{\boldsymbol{k}}dv_{\boldsymbol{k}} + 2\Delta_{\boldsymbol{k}}v_{\boldsymbol{k}}\frac{v_{\boldsymbol{k}}}{u_{\boldsymbol{k}}}dv_{\boldsymbol{k}}\right]. \tag{D.9}$$

This is multiplied with $u_{\boldsymbol{k}}/2dv_{\boldsymbol{k}}$ to obtain

$$0 = \sum_{\boldsymbol{k}} \left[2v_{\boldsymbol{k}}u_{\boldsymbol{k}}\xi_{\boldsymbol{k}} - (u_{\boldsymbol{k}}^2 - v_{\boldsymbol{k}}^2)\Delta_{\boldsymbol{k}}\right]. \tag{D.10}$$

One minimum is obviously if the summand in Eq. (D.10) is zero, which in fact turns out to be the global minimum. Solving for $\Delta_{\boldsymbol{k}}$,

$$\Delta_{\boldsymbol{k}} = \frac{2u_{\boldsymbol{k}}v_{\boldsymbol{k}}\xi_{\boldsymbol{k}}}{u_{\boldsymbol{k}}^2 - v_{\boldsymbol{k}}^2}. \tag{D.11}$$

Introducing the new parameter $E_{\boldsymbol{k}}$ (the excitaiton energy, i.e. the energy of unpaired electrons relative to that of the supercondensate), the probability amplitudes can be written

$$v_{\boldsymbol{k}}^2 = \frac{1}{2}\left(1 - \frac{\xi_{\boldsymbol{k}}}{E_{\boldsymbol{k}}}\right), \tag{D.12}$$

$$u_{\boldsymbol{k}}^2 = \frac{1}{2}\left(1 + \frac{\xi_{\boldsymbol{k}}}{E_{\boldsymbol{k}}}\right), \tag{D.13}$$

such that

$$u_{\boldsymbol{k}}^2 - v_{\boldsymbol{k}}^2 = \frac{\xi_{\boldsymbol{k}}}{E_{\boldsymbol{k}}}, \tag{D.14}$$

$$u_{\boldsymbol{k}}^2 v_{\boldsymbol{k}}^2 = \frac{1}{4}\left(1 - \frac{\xi_{\boldsymbol{k}}^2}{E_{\boldsymbol{k}}^2}\right), \tag{D.15}$$

$$u_{\boldsymbol{k}} v_{\boldsymbol{k}} = \frac{1}{2}\sqrt{1 - \frac{\xi_{\boldsymbol{k}}^2}{E_{\boldsymbol{k}}^2}}. \tag{D.16}$$

This allows $\Delta_{\boldsymbol{k}}$ to be rewritten as

$$\Delta_{\boldsymbol{k}} = \frac{2\xi_{\boldsymbol{k}}\frac{1}{2}\sqrt{1 - \frac{\xi_{\boldsymbol{k}}^2}{E_{\boldsymbol{k}}^2}}}{\xi_{\boldsymbol{k}}/E_{\boldsymbol{k}}} = \sqrt{E_{\boldsymbol{k}}^2 - \xi_{\boldsymbol{k}}^2}, \tag{D.17}$$

which gives an excitation energy with gap $\Delta_{\boldsymbol{k}}$ at zero energy (the Fermi energy)

$$E_{\boldsymbol{k}} = \sqrt{\xi_{\boldsymbol{k}}^2 + \Delta_{\boldsymbol{k}}^2}. \tag{D.18}$$

The gap $\Delta_{\boldsymbol{k}}$ represents the mimimum energy required to break up a pair, or consequently, the energy that the superconductor gains by pairing. Combining Eqs. (D.4), (D.16) and (D.18), the BCS gap equation can be written

$$\Delta_{\boldsymbol{k}} = -\sum_{\boldsymbol{l}} u_{\boldsymbol{l}} v_{\boldsymbol{l}} V_{\boldsymbol{k}\boldsymbol{l}} = -\sum_{\boldsymbol{l}} V_{\boldsymbol{k}\boldsymbol{l}} \frac{\Delta_{\boldsymbol{l}}}{2\sqrt{\xi_{\boldsymbol{l}}^2 + \Delta_{\boldsymbol{l}}^2}}. \tag{D.19}$$

The gap equation in Eq. (D.19) is valid at zero temperature. As the temperature rises above 0 K, more unpaired (quasi)electrons are excited. The following term needs to be considered to account for the occupation of the unpaired states

$$1 - n_{\boldsymbol{k}\uparrow} - n_{-\boldsymbol{k}\downarrow} = 1 - c_{\boldsymbol{k}\uparrow}^\dagger c_{\boldsymbol{k}\uparrow} - c_{-\boldsymbol{k}\downarrow}^\dagger c_{-\boldsymbol{k}\downarrow}. \tag{D.20}$$

The thermal average of this expression is

$$\langle 1 - n_{\boldsymbol{k}\uparrow} - n_{-\boldsymbol{k}\downarrow} \rangle = 1 - 2f(E) = \tanh(\beta E/2) \tag{D.21}$$

where $\beta \equiv k_B T$, and $f(E) \equiv (\exp(\beta E) + 1)^{-1}$ is the Fermi-Dirac distribution. The term $\tanh(\beta E/2)$ accounts for the probability that the pair state $(\boldsymbol{k}\uparrow, -\boldsymbol{k}\downarrow)$ is available for the supercondensate formation at temperature T

$$\lim_{T\to 0} \tanh(\beta E/2) = \lim_{\beta\to\infty} \tanh(\beta E/2) = 1, \tag{D.22}$$

i.e. at $T = 0$ K, the "vacuum" is perfect and all quasiparticles are paired. The expression in Eq. (D.21) is added to Eq. (D.21), yielding the temperature-dependent gap equation

$$\begin{aligned} \Delta_{\boldsymbol{k}} &= -\sum_{\boldsymbol{l}} V_{\boldsymbol{kl}} \frac{\Delta_{\boldsymbol{l}}}{2\sqrt{\xi_{\boldsymbol{l}}^2 + \Delta_{\boldsymbol{l}}^2}} (1 - 2f(E_k)) \\ &= -\sum_{\boldsymbol{l}} V_{\boldsymbol{kl}} \frac{\Delta_{\boldsymbol{l}}}{2\sqrt{\xi_{\boldsymbol{l}}^2 + \Delta_{\boldsymbol{l}}^2}} \tanh\left(\frac{\beta}{2}\sqrt{\xi_{\boldsymbol{l}}^2 + \Delta_{\boldsymbol{l}}^2}\right). \end{aligned} \tag{D.23}$$

For a weak electron-phonon coupling, which is valid for all elemental superconductors except Pb and Hg,

$$V_{\boldsymbol{kl}} = -V_0, \tag{D.24}$$

$$\Delta_{\boldsymbol{k}} = \Delta, \tag{D.25}$$

for $\boldsymbol{k}, \boldsymbol{l} < \boldsymbol{k}_D$, where $\boldsymbol{k}_D$ is the Debye momentum, yielding the weak-coupling gap equation (s-wave)

$$1 = V_0 \sum_{\boldsymbol{l}} \frac{\tanh\left(\frac{\beta}{2}\sqrt{\xi_{\boldsymbol{l}}^2 + \Delta^2}\right)}{2\sqrt{\xi_{\boldsymbol{l}}^2 + \Delta^2}}. \tag{D.26}$$

D.2 Integral expression of the gap equation

Turning the sum into an integral following App. C, the BCS gap equation becomes

$$\Delta(\theta_{p_F}) = -\int_0^{2\pi} \frac{d\theta_{p'_F}}{2\pi} \int_{-\infty}^{\infty} d\xi N(\xi) V(\theta_{p_F}, \theta_{p'_F}) \frac{\Delta(\theta_{p'_F}) \tanh\left(\frac{\beta}{2}\sqrt{\xi^2 + \Delta^2(\theta_{p'_F})}\right)}{2\sqrt{\xi^2 + \Delta^2(\theta_{p'_F})}}, \tag{D.27}$$

where the volume $\mathcal{V}$ is absorbed into the DOS N. Here, both Δ and V is allowed to have an angular dependence, through the basis function $\eta(\theta_{p_F})$

$$\Delta(\boldsymbol{p}_F) = \Delta\eta(\theta_{p_F}), \tag{D.28}$$

$$V(\xi, \boldsymbol{p}_F, \boldsymbol{p}'_F) = \begin{cases} -V_0 \eta(\theta_{p_F}) \eta^*(\theta_{p'_F}), & -\hbar\omega_D \le \xi \le \hbar\omega_D \\ 0, & \text{otherwise,} \end{cases} \tag{D.29}$$

where ω_D is the Debye frequency, and θ_{p_F} is the angle between a scattering direction and the Fermi momentum. The basis functions forms an orthogonal basis

$$\eta_a \eta_b^* = |\eta_a|^2 \delta_{ab}. \tag{D.30}$$

Examples of typical s-wave and d-wave basis functions are

$$\eta_s(\theta_{p_F}) = 1, \tag{D.31}$$
$$\eta_{d_{x^2-y^2}}(\theta_{p_F}) = a\cos(2\theta_{p_F}), \tag{D.32}$$

respectively, where a is a normalization constant. Choosing $a = \sqrt{2}$ yields

$$\int_0^{2\pi} \frac{d\theta_{p_F}}{2\pi} |\eta(\theta_{p_F})|^2 = 1. \tag{D.33}$$

Note! Many authors choose to absorb the factor $\sqrt{2}$ into Δ such that the magnitude corresponds to the maximal gap in the DOS, but this gives the basis function a different normalization. Later on, a will be reintroduced to show how the term propagates. Inserting the basis functions and multiplying by $\eta^*(\theta_{p_F})$ yields, due to Eq. (D.30),

$$\Delta = V_0 \int_0^{2\pi} \frac{d\theta_{p'_F} |\eta(\theta_{p'_F})|^2}{2\pi} \int_{-\hbar\omega_D}^{\hbar\omega_D} d\xi N(\xi) \frac{\Delta \tanh\left(\frac{\beta}{2}\sqrt{\xi^2 + \Delta^2 |\eta(\theta_{p'_F})|^2}\right)}{2\sqrt{\xi^2 + \Delta^2 |\eta(\theta_{p'_F})|^2}}. \tag{D.34}$$

Recall that ξ is the single-particle energy measured relative to the Fermi energy in the normal state, and that in this formalism, μ is the energy shift of the chemical potential between the normal and superconducting states. If there is a particle-hole symmetry close to the Fermi surface, then the shift fulfills $\mu = 0$. As stated earlier, this is quite generally a good approximation [71]. Furthermore, the density of states $N(\xi)$ typically varies on the energy scale of the Fermi energy $\epsilon_F \gg \hbar\omega_D \gg \Delta$, which means that $N(\xi) \simeq N(0) \equiv N_F$ is a good approximation in the integral in Eq. (D.34). The integral is symmetric around $\xi = 0$, and for a bulk superconductor, Eq. (D.34) can be divided by Δ, yielding

$$1 = V_0 N_F \int_0^{2\pi} \frac{d\theta_{p'_F} |\eta(\theta_{p'_F})|^2}{2\pi} \int_0^{\hbar\omega_D} d\xi \frac{\tanh\left(\frac{\beta}{2}\sqrt{\xi^2 + \Delta^2 |\eta(\theta_{p'_F})|^2}\right)}{\sqrt{\xi^2 + \Delta^2 |\eta(\theta_{p'_F})|^2}}. \tag{D.35}$$

D.3 Derivation of T_c

Deriving an expression for the transition temperature T_c has been a fundamental problem since the discovery of superconductivity. For the unconventional superconductors, it is still an ongoing quest in some sense. Rather than trying to find the exact numerical value of T_c, however, having an expression for T_c is useful for

other purposes. For example, while T_c is a value that is typically measured in experiment, the superconducting coupling-constant ($\lambda = NV$) is not, and having an expression for T_c then makes it possible to "eliminate" the coupling constant (and also cutoff frequency as it turns out) in favor of T_c. This procedure will now be shown for the BCS theory, but this practice is carried out in quasiclassical theory as well.

Starting from Eq. (D.35) under the assumption of weak electron-phonon coupling, noting that the equation is even in ξ, and taking the limit $T \to T_c \Rightarrow \Delta \to 0$,

$$\frac{1}{VN_F} = A\int_0^{\hbar\omega_c} d\xi \frac{\tanh\left(\frac{\xi}{2k_BT_c}\right)}{\xi}, \tag{D.36}$$

$$A \equiv \int_0^{2\pi} \frac{d\theta_{p_F}}{2\pi} \left|\eta(\theta_{p_F})\right|^2. \tag{D.37}$$

Here, $A = 1$ for orthonormal basis functions, but many authors do not use normalized basis functions for d-wave (the term is kept to show how the end result differs). Typically, the Debye frequency (ω_D) is much less than the Fermi frequency (ω_F), such that $\hbar\omega_D \ll \epsilon_F$, where ϵ_F is the Fermi energy. The cutoff frequency is chosen to be the Debye frequency. It is assumed that the density of states is constant close to the Fermi surface, such that in the integrand $N(\xi) \approx N(0) =: N_F$, where $N(0)$ is the normal-state density of states at the Fermi surface. Making the substitution $x = \xi/2k_BT_c$ where $x_c \equiv \hbar\omega_D/2k_BT_c$, Eq. (D.36) can be integrated by parts

$$\begin{aligned}
\frac{1}{VN_FA} &= \int_0^{x_c} dx \frac{\tanh(x)}{x} \\
&= \Big[\tanh(x)\ln(x)\Big]_{x=0}^{x=x_c} - \int_0^{x_c} \frac{\ln(x)}{\cosh^2(x)} dx \\
&= \tanh(x_c)\ln(x_c) - \left(\ln\frac{\pi}{4} - \gamma_E\right) \\
&= \tanh\left(\frac{\hbar\omega_D}{2k_BT_c}\right)\ln\left(\frac{\hbar\omega_D}{2k_BT_c}\right) - \left(\ln\frac{\pi}{4} - \gamma_E\right),
\end{aligned} \tag{D.38}$$

where

$$\gamma_E \equiv \lim_{n\to\infty}\left(\sum_{k=1}^{n}\frac{1}{k} - \ln n\right) \approx 0.577, \tag{D.39}$$

is the Euler-Mascheroni constant (or simply the Euler constant). Assuming that $k_BT_c \ll \hbar\omega_D$, the term $\tanh\left(\hbar\omega_D/2k_BT_c\right) \approx 1$. The transition temperature is

$$T_c = \frac{2e^{\gamma_E}}{\pi}\frac{\hbar\omega_D}{k_B}e^{-1/VN_FA} \tag{D.40}$$

$$\approx 1.13\Theta_D e^{-1/VN_FA}, \tag{D.41}$$

as expected [21], where $\Theta_D = \hbar\omega_D/k_B$ is the Debye temperature.

D.4 The BCS gap at zero temperature

Using the same assumptions as in the previous section (weak electron-phonon coupling and $N(\xi) \approx N_F$), and taking the limit $T \to 0$, the gap equation becomes

$$\begin{aligned}\frac{1}{VN_F} &= \int_0^{2\pi} \frac{d\theta_{p_F}}{2\pi} \int_0^{\hbar\omega_D} d\xi \frac{|\eta|^2}{\sqrt{\xi^2 + \Delta^2|\eta|^2}} \\ &= \int_0^{2\pi} \frac{d\theta_{p_F}}{2\pi} |\eta|^2 \left[\ln\left(\xi + \sqrt{\xi^2 + \Delta^2|\eta|^2}\right)\right]_{\xi=0}^{\xi=\hbar\omega_D} \\ &= \int_0^{2\pi} \frac{d\theta_{p_F}}{2\pi} |\eta|^2 \left(\ln\left(\frac{\hbar\omega_D}{\Delta|\eta|}\right) + \ln\left(1 + \sqrt{1 + \left(\frac{\Delta|\eta|}{\hbar\omega_D}\right)^2}\right)\right), \end{aligned} \tag{D.42}$$

where $\eta = \eta(\theta_{p_F})$ are the basis functions

$$\eta_s(\theta_{p_F}) = 1 \qquad (s\text{-wave}), \tag{D.43}$$

$$\eta_{d_{x^2-y^2}}(\theta_{p_F}) = a\cos(2\theta_{p_F}) \qquad (d\text{-wave}), \tag{D.44}$$

where a is a normalization constant, such that

$$A_s \equiv \int_0^{2\pi} \frac{d\theta_{p_F}}{2\pi} |\eta_s|^2 = 1, \tag{D.45}$$

$$A_d \equiv \int_0^{2\pi} \frac{d\theta_{p_F}}{2\pi} \left|\eta_{d_{x^2-y^2}}\right|^2 = \frac{a^2}{2}. \tag{D.46}$$

Due to a separation of scales ($\Delta \ll \hbar\omega_D \ll \epsilon_F$),

$$\frac{1}{VN_F} \approx \int_0^{2\pi} \frac{d\theta_{p_F}}{2\pi} |\eta|^2 \ln\left(\frac{2\hbar\omega_D}{\Delta|\eta|}\right). \tag{D.47}$$

Inserting the basis functions, Eq. (D.47) becomes

$$(s\text{-wave}): \qquad \frac{1}{VN_F A_s} = \ln\left(\frac{2\hbar\omega_D}{\Delta_s}\right), \tag{D.48}$$

$$(d\text{-wave}): \qquad \frac{1}{VN_F A_d} = \ln\left(\frac{4\hbar\omega_D}{a\Delta_{d_{x^2-y^2}}}\right) - \frac{1}{2}. \tag{D.49}$$

Solving for Δ

$$\Delta_s(T=0) = 2\hbar\omega_D e^{-1/VN_F A_s}, \tag{D.50}$$

$$\Delta_{d_{x^2-y^2}}(T=0) = \frac{4\hbar\omega_D}{a} e^{-\frac{1}{2}} e^{-1/VN_F A_d} \tag{D.51}$$

Using Eq. (D.40) to eliminate the coupling constant and the cutoff frequency,

$$\Delta_s(T=0) = \pi e^{-\gamma_E} k_B T_c \qquad \approx 1.76 k_B T_c, \tag{D.52}$$

$$\Delta_{d_{x^2-y^2}}(T=0) = \frac{2\pi}{a} e^{-\gamma_E - \frac{1}{2}} k_B T_c \approx \begin{cases} 1.51 k_B T_c, & a = 1, \\ 2.14 k_B T_c, & a = \sqrt{2}. \end{cases} \tag{D.53}$$

Note that the maximal d-wave gap is $\sim 2.14 k_B T_c$ [37].

D.5 The functional form of the BCS gap close to T_c

Close to T_c, the small parameters Δ_0, δ and ΔT are introduced

$$\Delta \xrightarrow[T\to T_c^-]{} \Delta_0, \tag{D.54}$$
$$\delta \equiv \Delta_0|\eta(\theta_{p'_F})|, \tag{D.55}$$
$$T \xrightarrow[T\to T_c^-]{} T_c - \Delta T, \tag{D.56}$$
$$\beta \xrightarrow[T\to T_c^-]{} \frac{1}{k_B(T_c-\Delta T)}, \tag{D.57}$$

such that Eq. (D.35) becomes

$$1 = V_0 N_F \int_0^{2\pi} \frac{d\theta_{p'_F}|\eta(\theta_{p'_F})|^2}{2\pi} \int_0^{\hbar\omega_D} d\xi \frac{\tanh\left(\frac{\sqrt{\xi^2+\delta^2}}{2k_B(T_c-\Delta T)}\right)}{\sqrt{\xi^2+\delta^2}}. \tag{D.58}$$

Expansion in the small parameters yields

$$\frac{1}{\sqrt{\xi^2+\delta^2}} = \frac{1}{\xi}\left(1-\frac{\delta^2}{\xi^2}+\mathcal{O}\left(\delta^4\right)\right), \tag{D.59}$$
$$\sqrt{\xi^2+\delta^2} = \xi\left(1+\frac{\delta^2}{\xi^2}+\mathcal{O}\left(\delta^4\right)\right), \tag{D.60}$$
$$\frac{1}{2k_B(T_c-\Delta T)} = \frac{1}{2k_BT_c}\left(1+\frac{\Delta T}{T_c}+\mathcal{O}\left(\Delta T^2\right)\right), \tag{D.61}$$
$$\frac{\sqrt{\xi^2+\delta^2}}{2k_B(T_c-\Delta T)} = \frac{\xi}{2k_BT_c}\left(1+\frac{\Delta T}{T_c}+\frac{\delta^2}{\xi^2}+\mathcal{O}\left(\Delta T^2,\Delta T\delta^2,\delta^4\right)\right), \tag{D.62}$$
$$\tanh\left(a+\delta\right) = \tanh(a)+\frac{\delta}{\cosh^2(a)}+\mathcal{O}\left(\delta^2\right). \tag{D.63}$$

Combining Eqs. (D.59), (D.62) and (D.63), it is found that

$$\begin{aligned}
\frac{\tanh\left(\frac{\sqrt{\xi^2+\delta^2}}{2k_B(T_c-\Delta T)}\right)}{\sqrt{\xi^2+\delta^2}} &\approx \frac{1}{\xi}\left(1-\frac{1}{2}\frac{\delta^2}{\xi^2}\right)\tanh\left[\frac{\xi}{2k_BT_c}\left(1+\frac{\Delta T}{T_c}+\frac{\delta^2}{\xi^2}\right)\right] \\
&\approx \frac{1}{\xi}\left(1-\frac{1}{2}\frac{\delta^2}{\xi^2}\right)\left(\tanh\left(\frac{\xi}{2k_BT_c}\right)+\frac{\frac{\xi}{2k_BT_c}\left(\frac{\Delta T}{T_c}+\frac{1}{2}\frac{\delta^2}{\xi^2}\right)}{\cosh^2\left(\frac{\xi}{2k_BT_c}\right)}\right) \\
&\approx \frac{\tanh\left(\frac{\xi}{2k_BT_c}\right)}{\xi}+\frac{\Delta T}{2k_BT_c^2\cosh^2\left(\frac{\xi}{2k_BT_c}\right)} \\
&\quad +\frac{\delta^2}{\xi^2 4k_BT_c}\left(\frac{1}{\cosh^2\left(\frac{\xi}{2k_BT_c}\right)}-\frac{\tanh\left(\frac{\xi}{2k_BT_c}\right)}{\frac{\xi}{2k_BT_c}}\right).
\end{aligned} \tag{D.64}$$

Inserting this result back into Eq. (D.58) yields the gap equation

$$1 = I_1 + I_2 + I_3, \tag{D.65}$$

where

$$I_1 = V_0 N_F \int_0^{2\pi} \frac{d\theta_{p'_F} |\eta(\theta_{p'_F})|^2}{2\pi} \int_0^{\hbar\omega_D} d\xi \frac{\tanh\left(\frac{\xi}{2k_B T_c}\right)}{\xi}, \tag{D.66}$$

$$I_2 = V_0 N_F \frac{\Delta T}{2k_B T_c^2} \int_0^{2\pi} \frac{d\theta_{p'_F} |\eta(\theta_{p'_F})|^2}{2\pi} \int_0^{\hbar\omega_D} d\xi \frac{1}{\cosh^2\left(\frac{\xi}{2k_B T_c}\right)}, \tag{D.67}$$

$$I_3 = \frac{V_0 N_F}{4k_B T_c} \int_0^{2\pi} \frac{d\theta_{p'_F} |\eta(\theta_{p'_F})|^2 \delta^2}{2\pi} \int_0^{\hbar\omega_D} \frac{d\xi}{\xi^2} \left(\frac{1}{\cosh^2\left(\frac{\xi}{2k_B T_c}\right)} - \frac{\tanh\left(\frac{\xi}{2k_B T_c}\right)}{\frac{\xi}{2k_B T_c}} \right). \tag{D.68}$$

The first integral I_1 is itself the gap equation, such that

$$I_1 = 1, \tag{D.69}$$

by definition. For the remaining two integrals, the following substitution is introduced

$$x = \frac{\xi}{2k_B T_c}, \tag{D.70}$$

$$dx = \frac{d\xi}{2k_B T_c}, \tag{D.71}$$

$$x \xrightarrow[\xi \to \hbar\omega_D]{} \frac{\hbar\omega_D}{2k_B T_c}. \tag{D.72}$$

In the weak-coupling limit

$$k_B T_c \ll \hbar\omega_D \ll E_F, \tag{D.73}$$

and the integrals I_2 and I_3 can be taken to infinity. Defining

$$a \equiv \int_0^{2\pi} \frac{d\theta_{p'_F} |\eta(\theta_{p'_F})|^2}{2\pi}, \tag{D.74}$$

where $a = 1$ for normalized base functions (like η_s and $\eta_{d_{x^2-y^2}}$, but $a = 1/2$ for $\eta_{d'_{x^2-y^2}}$ defined below). Carrying out the substitution, the integral I_2 becomes

$$\begin{aligned} I_2 &= a V_0 N_F \frac{\Delta T}{2k_B T_c^2} 2k_B T_c \int_0^{\infty} dx \frac{1}{\cosh^2(x)} \\ &= a V_0 N_F \frac{\Delta T}{T_c}. \end{aligned} \tag{D.75}$$

Inserting the definition $\delta \equiv \Delta_0|\eta(\theta_{p'_F})|$, the integral I_3 becomes

$$\begin{aligned} I_3 &= \frac{V_0 N_F \Delta_0^2}{4k_B T_c} \frac{1}{2k_B T_c} \int_0^{2\pi} \frac{d\theta_{p'_F} |\eta(\theta_{p'_F})|^4}{2\pi} \int_0^\infty \frac{dx}{x^2} \left(\frac{1}{\cosh^2(x)} - \frac{\tanh(x)}{x} \right) \\ &= \frac{V_0 N_F \Delta_0^2}{8(k_B T_c)^2} \tilde{\eta} \int_0^\infty \frac{dx}{x^2} \left(\frac{1}{\cosh^2(x)} - \frac{\tanh(x)}{x} \right), \end{aligned} \tag{D.76}$$

where

$$\tilde{\eta} \equiv \int_0^{2\pi} \frac{d\theta_{p'_F} |\eta(\theta_{p'_F})|^4}{2\pi} = \begin{cases} 1, & \text{if} \quad \eta_s(\theta_{p_F}) = 1, \\ \frac{3}{2}, & \text{if} \quad \eta_{d_{x^2-y^2}}(\theta_{p_F}) = \sqrt{2}\cos(\theta_{p_F}), \\ \frac{3}{8}, & \text{if} \quad \eta_{d'_{x^2-y^2}}(\theta_{p_F}) = \cos(\theta_{p_F}), \end{cases} \tag{D.77}$$

and

$$\int_0^\infty \frac{dx}{x^2} \left(\frac{1}{\cosh^2(x)} - \frac{\tanh(x)}{x} \right) = -\frac{7\zeta(3)}{8\pi^2}. \tag{D.78}$$

Here, ζ is the Riemann zeta function. Combining the results for I_1, I_2 and I_3, the gap equation finally becomes

$$1 = 1 + aV_0 N_F \frac{\Delta T}{T_c} - V_0 N_F \frac{\Delta_0^2}{8(k_B T_c)^2} \tilde{\eta} \frac{7\zeta(3)}{8\pi^2}. \tag{D.79}$$

At an infinitesimal temperature ΔT below the transition temperature, the bulk order parameter is finally found to be

$$\Delta_0^2 = \frac{8\pi^2}{7\zeta(3)} a\tilde{\eta}^{-1} k_B^2 T_c \Delta T. \tag{D.80}$$

D.6 Slope of the BCS gap at T_c

The slope of the order parameter can also be evaluated as $\Delta T \to 0$, by first noting that

$$\left. \frac{d\Delta_0^2}{d\beta} \right|_{T_c} = \left. \frac{d\Delta T}{d\beta} \right|_{T_c} \left. \frac{d\Delta_0^2}{d\Delta T} \right|_{\Delta T \to 0}, \tag{D.81}$$

where

$$\Delta T = T_c - T = T_c - \frac{1}{k_B \beta}, \tag{D.82}$$

$$\frac{d\Delta T}{d\beta} = \frac{1}{k_B \beta^2} = k_B T^2. \tag{D.83}$$

Applying this to Eq. (D.80), the slope becomes

$$\left. \frac{d\Delta_0^2}{d\beta} \right|_{T_c} = \frac{8\pi^2}{7\zeta(3)} a\tilde{\eta}^{-1} (k_B T_c)^3. \tag{D.84}$$

Appendix E

The Riccati formalism

In this appendix, the quasiclassical Green function will be rewritten in terms of electron-hole coherence functions, through the use of the so-called Shelankov projectors [70, 80, 97]. The purpose of this is to automatically encode the normalization condition of the quasiclassical Green function into the equations, thus removing spurious solutions and ensuring numerical stability.

In the first section, the Shelankov projectors and the coherence functions are introduced, and it is proven that these projectors fulfill certain properties due to the normalization condition. In the second section, expressions for the spin-space Green functions are obtained. The projectors are substituted into the Eilenberger equation in the third section, recasting the latter into a set of coupled Riccati ordinary differential equations. The Riccati amplitudes to be solved for in these equations are the coherence functions γ and $\tilde{\gamma}$, to be defined in this appendix. In the fourth section, the Riccati equations are solved analytically under certain assumptions. Some of the derivations in this appendix follow Ref. [150] and discussions with its author.

E.1 Projectors and coherence functions

A projector P is a linear transformation from a vector space V onto itself that fulfills idempotency, which means that having projected onto a state x, nothing changes upon applying the same projection operator again,

$$P^2 x = Px, \quad \forall x \in V. \tag{E.1}$$

Following the formalism of Ref. [97], the projection operators for retarded particle-like (+) and hole-like (−) excitations in Nambu space are introduced as

$$\hat{P}_+ = \frac{1}{2}\left(\hat{1} + \frac{\hat{g}}{-i\pi}\right) \tag{E.2}$$

$$\hat{P}_- = \frac{1}{2}\left(\hat{1} - \frac{\hat{g}}{-i\pi}\right), \tag{E.3}$$

respectively. It is straightforward to prove that $\hat{P}_\pm$ in Eqs. (E.2) and (E.3) are projection operators fulfilling idempotency

$$\begin{aligned}\hat{P}_\pm^2 &= \frac{1}{4}\left(\hat{1} \pm \frac{\hat{g}}{-i\pi}\right)^2 \\ &= \frac{1}{4}\left(\hat{1} + \frac{\hat{g}^2}{-\pi^2} \pm 2\frac{\hat{g}}{-i\pi}\right) \\ &= \frac{1}{2}\left(\hat{1} \pm \frac{\hat{g}}{-i\pi}\right) = \hat{P}_\pm, \end{aligned} \tag{E.4}$$

where the normalization condition $\hat{g}^2 = -\pi^2\hat{1}$ was used in the last step. In addition, the projectors are complementary, since

$$\hat{P}_\pm + \hat{P}_\mp = \frac{1}{2}\left(\hat{1} \pm \frac{\hat{g}}{-i\pi}\right) + \frac{1}{2}\left(\hat{1} \mp \frac{\hat{g}}{-i\pi}\right) = \hat{1}. \tag{E.5}$$

A set of operators which are both idempotent and complementary are also orthogonal

$$\begin{aligned}\hat{P}_\pm\hat{P}_\mp &= \frac{1}{2}\left(\hat{1} \pm \frac{\hat{g}}{-i\pi}\right)\frac{1}{2}\left(\hat{1} \mp \frac{\hat{g}}{-i\pi}\right) \\ &= \frac{1}{4}\left(\hat{1} - \frac{\hat{g}^2}{-\pi^2}\right) \\ &= \frac{1}{4}\left(\hat{1} - \hat{1}\right) = \hat{0}, \end{aligned} \tag{E.6}$$

where the normalization condition was used again. An orthogonal projection operator P can be cast on a general form

$$P = A(A^TA)^{-1}A^T, \tag{E.7}$$

where the middle term $(A^TA)^{-1}$ is a normalizing factor. The analogy of the transpose in Nambu space is particle-hole conjugation, denoted by the "tilde operator" $\tilde{A}(\boldsymbol{p}_F, \boldsymbol{R}; z, t) = A^*(-\boldsymbol{p}_F, \boldsymbol{R}; -z^*, t)$. The projection operators can then be decomposed into the retarded, complex, spin-matrices $\gamma(\mathbf{p}_F, \mathbf{R}; z)$ and $\tilde{\gamma}(\mathbf{p}_F, \mathbf{R}; z)$ as

$$\hat{P}_+ = \begin{pmatrix} 1 \\ -\tilde{\gamma} \end{pmatrix}(1 - \gamma\tilde{\gamma})^{-1}(1, \gamma) \tag{E.8}$$

$$\hat{P}_- = \begin{pmatrix} -\gamma \\ 1 \end{pmatrix}(1 - \tilde{\gamma}\gamma)^{-1}(\tilde{\gamma}, 1). \tag{E.9}$$

Here, the matrix inversion is defined through $(1 + ab)^{-1}(1 + ab) = 1$. It will now be shown that this new form of $\hat{P}_\pm$ also satisfies idempotency, complementarity

and orthogonality. Using the matrix inversion relation, idempotency is shown

$$\begin{aligned}
\hat{P}_+^2 &= \begin{pmatrix} 1 \\ -\tilde{\gamma} \end{pmatrix} (1-\gamma\tilde{\gamma})^{-1}(1,\gamma) \begin{pmatrix} 1 \\ -\tilde{\gamma} \end{pmatrix} (1-\gamma\tilde{\gamma})^{-1}(1,\gamma) \\
&= \begin{pmatrix} 1 \\ -\tilde{\gamma} \end{pmatrix} (1-\gamma\tilde{\gamma})^{-1}(1-\gamma\tilde{\gamma})(1-\gamma\tilde{\gamma})^{-1}(1,\gamma) \\
&= \begin{pmatrix} 1 \\ -\tilde{\gamma} \end{pmatrix} (1-\gamma\tilde{\gamma})^{-1}(1,\gamma) = \hat{P}_+ \qquad \text{(E.10)} \\
\hat{P}_-^2 &= \begin{pmatrix} -\gamma \\ 1 \end{pmatrix} (1-\tilde{\gamma}\gamma)^{-1}(\tilde{\gamma},1) \begin{pmatrix} -\gamma \\ 1 \end{pmatrix} (1-\tilde{\gamma}\gamma)^{-1}(\tilde{\gamma},1) \\
&= \begin{pmatrix} -\gamma \\ 1 \end{pmatrix} (1-\tilde{\gamma}\gamma)^{-1}(1-\tilde{\gamma}\gamma)(1-\tilde{\gamma}\gamma)^{-1}(\tilde{\gamma},1) \\
&= \begin{pmatrix} -\gamma \\ 1 \end{pmatrix} (1-\tilde{\gamma}\gamma)^{-1}(\tilde{\gamma},1) = \hat{P}_-. \qquad \text{(E.11)}
\end{aligned}$$

Using the relation $(1+ab)^{-1}a = a(1+ba)^{-1}$, complementarity is proven

$$\begin{aligned}
\hat{P}_+ + \hat{P}_- &= \begin{pmatrix} 1 \\ -\tilde{\gamma} \end{pmatrix} (1-\gamma\tilde{\gamma})^{-1}(1,\gamma) + \begin{pmatrix} -\gamma \\ 1 \end{pmatrix} (1-\tilde{\gamma}\gamma)^{-1}(\tilde{\gamma},1) \\
&= \begin{pmatrix} (1-\gamma\tilde{\gamma})^{-1} & (1-\gamma\tilde{\gamma})^{-1}\gamma \\ -\tilde{\gamma}(1-\gamma\tilde{\gamma})^{-1} & -\tilde{\gamma}(1-\gamma\tilde{\gamma})^{-1}\gamma \end{pmatrix} \\
&\quad + \begin{pmatrix} -\gamma(1-\tilde{\gamma}\gamma)^{-1}\tilde{\gamma} & -\gamma(1-\tilde{\gamma}\gamma)^{-1} \\ (1-\tilde{\gamma}\gamma)^{-1}\tilde{\gamma} & (1-\tilde{\gamma}\gamma)^{-1} \end{pmatrix} \\
&= \begin{pmatrix} (1-\gamma\tilde{\gamma})^{-1} - \gamma\tilde{\gamma}(1-\gamma\tilde{\gamma})^{-1} & (1-\gamma\tilde{\gamma})^{-1}\gamma - (1-\gamma\tilde{\gamma})^{-1}\gamma \\ -\tilde{\gamma}(1-\gamma\tilde{\gamma})^{-1} + \tilde{\gamma}(1-\gamma\tilde{\gamma})^{-1} & -(1-\gamma\tilde{\gamma})^{-1}\tilde{\gamma}\gamma + (1-\gamma\tilde{\gamma})^{-1} \end{pmatrix} \\
&= \begin{pmatrix} 1 & 0 \\ 0 & 1 \end{pmatrix} = \hat{1}. \qquad \text{(E.12)}
\end{aligned}$$

Orthogonality still holds

$$\begin{aligned}
\hat{P}_+\hat{P}_- &= \begin{pmatrix} 1 \\ -\tilde{\gamma} \end{pmatrix} (1-\gamma\tilde{\gamma})^{-1}(1,\gamma) \begin{pmatrix} -\gamma \\ 1 \end{pmatrix} (1-\tilde{\gamma}\gamma)^{-1}(\tilde{\gamma},1) \\
&= \begin{pmatrix} 1 \\ -\tilde{\gamma} \end{pmatrix} (1-\gamma\tilde{\gamma})^{-1}(-\gamma+\gamma)(1-\tilde{\gamma}\gamma)^{-1}(\tilde{\gamma},1) \\
&= \hat{0} \qquad \text{(E.13)} \\
\hat{P}_-\hat{P}_+ &= \begin{pmatrix} -\gamma \\ 1 \end{pmatrix} (1-\tilde{\gamma}\gamma)^{-1}(\tilde{\gamma},1) \begin{pmatrix} 1 \\ -\tilde{\gamma} \end{pmatrix} (1-\gamma\tilde{\gamma})^{-1}(1,\gamma) \\
&= \begin{pmatrix} -\gamma \\ 1 \end{pmatrix} (1-\tilde{\gamma}\gamma)^{-1}(\tilde{\gamma}-\tilde{\gamma})(1-\gamma\tilde{\gamma})^{-1}(1,\gamma) \\
&= \hat{0}, \qquad \text{(E.14)}
\end{aligned}$$

since a factors of $(-\gamma+\gamma)=(\tilde{\gamma}-\tilde{\gamma})=0$ appear in both expressions. Rewriting Eqs. (E.2)–(E.3), it is noted that

$$\hat{g} = -i\pi(\hat{P}_+ - \hat{P}_-) \tag{E.15}$$
$$= \mp i\pi(2\hat{P}_\pm - \hat{1}). \tag{E.16}$$

It is now possible to derive Eqs. (2.64)–(2.65), which expresses the quasiclassical Green function in terms of the coherence functions. This is done by inserting the projectors in Eqs. (E.8)–(E.9) into Eq. (E.15) to obtain

$$\hat{g} = -i\pi\hat{N}\otimes\begin{pmatrix}(\sigma_0+\gamma\otimes\tilde{\gamma}) & 2\gamma\\ -2\tilde{\gamma} & -(\sigma_0+\tilde{\gamma}\otimes\gamma)\end{pmatrix}, \tag{E.17}$$

$$\hat{N} = \begin{pmatrix}(\sigma_0-\gamma\otimes\tilde{\gamma})^{-1} & 0\\ 0 & (\sigma_0-\tilde{\gamma}\otimes\gamma)^{-1}\end{pmatrix}, \tag{E.18}$$

where the spin-dependence of the coherence functions is written explicitly as

$$\gamma = (\gamma_s+\boldsymbol{\gamma}_t\cdot\boldsymbol{\sigma})\,i\sigma_2, \tag{E.19}$$
$$\tilde{\gamma} = i\sigma_2\,(\tilde{\gamma}_s-\tilde{\boldsymbol{\gamma}}_t\cdot\boldsymbol{\sigma})\,. \tag{E.20}$$

Comparing Eq. (E.17) with Eq. (2.43), it is seen that the coherence functions can be expressed in terms of the quasiparticle and pair propagators as $\gamma=-(i\pi-g)^{-1}f$ and $\tilde{\gamma}=(i\pi+\tilde{g})^{-1}\tilde{f}$. Noting that the inverse is nothing but a projector in spin-space, one can see that it is possible to interpret the coherence functions as the particle- and hole-like projections of the pair propagator in spin-space.

E.2 Scalar spin-singlet Green functions

For a unitary singlet system with $\gamma=\gamma_s i\sigma_2$ and $\tilde{\gamma}=i\sigma_2\tilde{\gamma}_s$, the Green function $\hat{g}$ in Nambu $\otimes$ spin-space is

$$\hat{g} = \begin{pmatrix}g_0\sigma_0+\boldsymbol{g}\cdot\boldsymbol{\sigma} & (f_s+\boldsymbol{f}_t\cdot\boldsymbol{\sigma})\,i\sigma_2\\ i\sigma_2\left(\tilde{f}_s-\tilde{\boldsymbol{f}}_t\cdot\boldsymbol{\sigma}\right) & \sigma_2\,(\tilde{g}_0-\tilde{\boldsymbol{g}}\cdot\boldsymbol{\sigma})\,\sigma_2\end{pmatrix} \overset{\text{singlet}}{=} \begin{pmatrix}g_0\sigma_0 & f_s i\sigma_2\\ i\sigma_2\tilde{f}_s & \tilde{g}_0\sigma_0\end{pmatrix} \tag{E.21}$$

Substituting the coherence functions into the Green function in Eq. (E.17) and comparing to Eq. (E.21), the scalar Green functions are found to be

$$g_0 = -i\pi\frac{1-\gamma_s\tilde{\gamma}_s}{1+\gamma_s\tilde{\gamma}_s}, \tag{E.22}$$
$$\tilde{g}_0 = i\pi\frac{1-\gamma_s\tilde{\gamma}_s}{1+\gamma_s\tilde{\gamma}_s}, \tag{E.23}$$
$$f_s = -2i\pi\frac{\gamma_s}{1+\gamma_s\tilde{\gamma}_s}, \tag{E.24}$$
$$\tilde{f}_s = 2i\pi\frac{\tilde{\gamma}_s}{1+\gamma_s\tilde{\gamma}_s}. \tag{E.25}$$

E.3 Deriving the Riccati equations

The quasiclassical Green function $\hat{g} = \mp i\pi(2\hat{P}_\pm - \hat{1})$ in Eq. (E.16) will now be substituted into the Eilenberger equation in Eq. (2.41). It is noted that $\hat{1}$ commutes with every operator in Eq. (2.41), and that $\nabla_R\hat{1} = 0$. Substituting $\hat{g} = \mp i\pi(2\hat{P}_\pm - \hat{1})$ and re-scaling then yields equations of motion for the Shelankov projectors

$$i\hbar\boldsymbol{v}_F \cdot \boldsymbol{\nabla}_R\hat{P}_\pm + \left[z\hat{\tau}_3 - \hat{h}, \hat{P}_\pm\right] = \hat{0}, \tag{E.26}$$

where $z\hat{\tau}_3$ and $\hat{h}$ are the diagonal and off-diagonal self-energies, respectively. Choosing the + branch and acting with $\hat{P}_-$ from the left or right yields

$$\begin{aligned} i\hbar\boldsymbol{v}_F \cdot \hat{P}_-\boldsymbol{\nabla}_R\hat{P}_+ + \hat{P}_-(z\hat{\tau}_3 - \hat{h})\hat{P}_+ &= \hat{0} && \text{(E.27)} \\ i\hbar\boldsymbol{v}_F \cdot (\boldsymbol{\nabla}_R\hat{P}_+)\hat{P}_- - \hat{P}_+(z\hat{\tau}_3 - \hat{h})\hat{P}_- &= \hat{0}, && \text{(E.28)} \end{aligned}$$

respectively, where orthogonality of the projectors have been used. The gradient term in Eq. (E.27) can be rewritten as

$$\begin{aligned} \hat{P}_-\boldsymbol{\nabla}_R\hat{P}_+ &= \hat{P}_-\begin{pmatrix} 0 \\ -\boldsymbol{\nabla}_R\tilde{\gamma} \end{pmatrix}(1-\gamma\tilde{\gamma})^{-1}(1,\gamma) \\ &\quad + \hat{P}_-\begin{pmatrix} 1 \\ -\tilde{\gamma} \end{pmatrix}\boldsymbol{\nabla}_R(1-\gamma\tilde{\gamma})^{-1}(1,\gamma) \\ &\quad + \hat{P}_-\begin{pmatrix} 1 \\ -\tilde{\gamma} \end{pmatrix}(1-\gamma\tilde{\gamma})^{-1}(0,\boldsymbol{\nabla}_R\gamma) \\ &= \hat{P}_-\begin{pmatrix} 0 \\ -\boldsymbol{\nabla}_R\tilde{\gamma} \end{pmatrix}(1-\gamma\tilde{\gamma})^{-1}(1,\gamma), \end{aligned} \tag{E.29}$$

due to orthogonality between the last factor in $\hat{P}_-$ and $\left(\begin{smallmatrix} 1 \\ -\tilde{\gamma} \end{smallmatrix}\right)$. Similarly,

$$(\boldsymbol{\nabla}_R\hat{P}_+)\hat{P}_- = \begin{pmatrix} 1 \\ -\tilde{\gamma} \end{pmatrix}(1-\gamma\tilde{\gamma})^{-1}(0,\boldsymbol{\nabla}_R\gamma)\hat{P}_-. \tag{E.30}$$

Equations (E.27) and (E.28) are written explicitly as

$$\begin{aligned} \hat{0} &= i\hbar\boldsymbol{v}_F \cdot \begin{pmatrix} -\gamma \\ 1 \end{pmatrix}(1-\tilde{\gamma}\gamma)^{-1}(\tilde{\gamma},1)\begin{pmatrix} 0 \\ -\boldsymbol{\nabla}_R\tilde{\gamma} \end{pmatrix}(1-\gamma\tilde{\gamma})^{-1}(1,\gamma) \\ &\quad + \begin{pmatrix} -\gamma \\ 1 \end{pmatrix}(1-\tilde{\gamma}\gamma)^{-1}(\tilde{\gamma},1)(z\hat{\tau}_3 - \hat{h})\begin{pmatrix} 1 \\ -\tilde{\gamma} \end{pmatrix}(1-\gamma\tilde{\gamma})^{-1}(1,\gamma) && \text{(E.31)} \\ \hat{0} &= i\hbar\boldsymbol{v}_F \cdot \begin{pmatrix} 1 \\ -\tilde{\gamma} \end{pmatrix}(1-\gamma\tilde{\gamma})^{-1}(0,\boldsymbol{\nabla}_R\gamma)\begin{pmatrix} -\gamma \\ 1 \end{pmatrix}(1-\tilde{\gamma}\gamma)^{-1}(\tilde{\gamma},1) \\ &\quad + \begin{pmatrix} 1 \\ -\tilde{\gamma} \end{pmatrix}(1-\gamma\tilde{\gamma})^{-1}(1,\gamma)(z\hat{\tau}_3 - \hat{h})\begin{pmatrix} -\gamma \\ 1 \end{pmatrix}(1-\tilde{\gamma}\gamma)^{-1}(\tilde{\gamma},1), && \text{(E.32)} \end{aligned}$$

respectivley. Equation (E.31) is simiplified by multiplying from the left with the inverse of $\begin{pmatrix} -\gamma \\ 1 \end{pmatrix}(1-\tilde{\gamma}\gamma)^{-1}$, and from the right with the inverse of $(1-\gamma\tilde{\gamma})^{-1}(1,\gamma)$. Equation (E.32) is simiplified by multiplying from the left with the inverse of $\begin{pmatrix} 1 \\ -\tilde{\gamma} \end{pmatrix}(1-\gamma\tilde{\gamma})^{-1}$, and from the right with the inverse of $(1-\tilde{\gamma}\gamma)^{-1}(\tilde{\gamma},1)$. This yields

$$i\hbar \boldsymbol{v}_F \cdot (\tilde{\gamma},1) \begin{pmatrix} 0 \\ -\boldsymbol{\nabla}_R\tilde{\gamma} \end{pmatrix} + (\tilde{\gamma},1)(z\hat{\tau}_3 - \hat{h}) \begin{pmatrix} 1 \\ -\tilde{\gamma} \end{pmatrix} = \hat{0} \tag{E.33}$$

$$i\hbar \boldsymbol{v}_F \cdot (0,\boldsymbol{\nabla}_R\gamma) \begin{pmatrix} -\gamma \\ 1 \end{pmatrix} - (1,\gamma)(z\hat{\tau}_3 - \hat{h}) \begin{pmatrix} -\gamma \\ 1 \end{pmatrix} = \hat{0}. \tag{E.34}$$

For the problems studied in this thesis, the self-energies are

$$z\hat{\tau}_3 - \hat{h} = \begin{pmatrix} z & \Delta \\ -\tilde{\Delta} & -z \end{pmatrix}. \tag{E.35}$$

The Riccati equations (in spin-space) are

$$(i\hbar \boldsymbol{v}_F \cdot \boldsymbol{\nabla}_R + 2z)\,\gamma = \gamma\tilde{\Delta}\gamma - \Delta, \tag{E.36}$$

$$(i\hbar \boldsymbol{v}_F \cdot \boldsymbol{\nabla}_R - 2z)\,\tilde{\gamma} = \tilde{\gamma}\Delta\tilde{\gamma} - \tilde{\Delta}. \tag{E.37}$$

E.4 Analytic solutions

Assuming a spin-singlet system with

$$\gamma = \gamma_s i\sigma_2, \tag{E.38}$$

$$\tilde{\gamma} = i\sigma_2\tilde{\gamma}_s, \tag{E.39}$$

$$\Delta = \Delta_s i\sigma_2, \tag{E.40}$$

$$\tilde{\Delta} = i\sigma_2\tilde{\Delta}_s, \tag{E.41}$$

the Riccati equations in Eqs. (E.36) and (E.37) can due to redundancy be written as the scalar equations

$$(i\hbar \boldsymbol{v}_F \cdot \boldsymbol{\nabla} + 2z)\,\gamma_s = -\Delta_s - \tilde{\Delta}_s\gamma_s^2, \tag{E.42}$$

$$(i\hbar \boldsymbol{v}_F \cdot \boldsymbol{\nabla} - 2z)\,\tilde{\gamma}_s = -\tilde{\Delta}_s - \Delta_s\tilde{\gamma}_s^2. \tag{E.43}$$

Note the sign-change due to a factor $(i\sigma_2)^2 = -\sigma_0$. Choosing a coordinate system such that the x-axis coincides with $\hat{\boldsymbol{v}}_F$, it is possible to write

$$\boldsymbol{v}_F \cdot \boldsymbol{\nabla} \to \mathrm{sign}(v_F)\partial_x. \tag{E.44}$$

Recall that γ and $\tilde{\gamma}$ have stable solutions in opposite integration directions. The Riccati equations are rewritten

$$\partial_x\gamma_s = i\Delta_s + 2iz\gamma_s + i\tilde{\Delta}_s\gamma_s^2, \tag{E.45}$$

$$\partial_x\tilde{\gamma}_s = i\tilde{\Delta}_s - 2iz\tilde{\gamma}_s + i\Delta_s\tilde{\gamma}_s^2. \tag{E.46}$$

A Riccati equation of the form

$$y'(x) = q_0(x) + q_1(x)y(x) + q_2(x)y^2(x) \tag{E.47}$$

has a solution

$$y(x) = y_h + \frac{1}{w(x)}, \tag{E.48}$$

where y_h is the homogeneous solution and $w(x)$ satisfies the linear ODE

$$w'(x) + [q_1(x) + 2q_2(x)y_h]\, w(x) = -q_2(x). \tag{E.49}$$

The homogeneous solutions to the coherence functions are found through simple algebra

$$\gamma_{s,h} = \frac{-z \pm i\Omega}{\tilde{\Delta}_s} = \frac{-\Delta_s}{z \pm i\Omega}, \tag{E.50}$$

$$\tilde{\gamma}_{s,h} = \frac{z \pm i\Omega}{\Delta_s} = \frac{\tilde{\Delta}_s}{z \mp i\Omega}, \tag{E.51}$$

$$\Omega \equiv \sqrt{|\Delta_s|^2 - z^2}. \tag{E.52}$$

The choice of sign depends on which quantities are studied, i.e. retarded or advanced. The retarded (advanced) quantities have poles in the upper (lower) half-plane with energies $z = \epsilon + i0^{\pm}$. Here ϵ is a real energy and $0^{\pm}$ an infinitesimal shift. To obtain the correct bounded solutions, the upper sign is chosen for retarded quantities, and the lower sign for advanced.

Matching the coefficients in Eqs. (E.45)–(E.46) with Eq. (E.49), it is found that

$$w' + \left(2iz + 2i\tilde{\Delta}_s\gamma_{s,h}\right) w = -i\tilde{\Delta}_s, \tag{E.53}$$

$$\tilde{w}' + \left(-2iz + 2i\Delta_s\tilde{\gamma}_{s,h}\right) \tilde{w} = -i\Delta_s, \tag{E.54}$$

with the solutions

$$w(x) = \frac{\exp(\pm 2\Omega x)}{\pm 2i\Omega C} - \frac{\tilde{\Delta}_s}{\pm 2i\Omega}, \tag{E.55}$$

$$\tilde{w}(x) = \frac{\exp(\pm 2\Omega x)}{\pm 2i\Omega \tilde{C}} - \frac{\Delta_s}{\pm 2i\Omega}, \tag{E.56}$$

where C and $\tilde{C}$ are integration constants to be determined. Substituting these expressions into Eqs. (E.45)–(E.48) and rearranging yields

$$\gamma_s = \gamma_{s,h} + \frac{\pm 2i\Omega C \exp(\mp 2\Omega x)}{1 - \tilde{\Delta}_s C \exp(\mp 2\Omega x)}, \tag{E.57}$$

$$\tilde{\gamma}_s = \tilde{\gamma}_{s,h} + \frac{\pm 2i\Omega \tilde{C} \exp(\mp 2\Omega x)}{1 - \Delta_s \tilde{C} \exp(\mp 2\Omega x)}. \tag{E.58}$$

$$\tag{E.59}$$

The correct bounded solutions for retarded quantities are given by the upper signs for γ and the lower signs for $\tilde{\gamma}$. Let $\gamma_{s,0}$ and $\tilde{\gamma}_{s,0}$ denote given initial values of the respective trajectories, such that

$$\gamma_{s,0} \equiv \gamma_s(x=0) = \gamma_{s,h} + \frac{2i\Omega C}{1-\tilde{\Delta}_s C}, \tag{E.60}$$

$$\tilde{\gamma}_{s,0} \equiv \tilde{\gamma}_s(x'=0) = \tilde{\gamma}_{s,h} + \frac{2i\Omega \tilde{C}}{1+\Delta_s \tilde{C}}. \tag{E.61}$$

Solving for C and $\tilde{C}$,

$$C = \frac{\gamma_{s,0}-\gamma_{s,h}}{2i\Omega + \tilde{\Delta}_s\left(\gamma_{s,0}-\gamma_{s,h}\right)}, \tag{E.62}$$

$$\tilde{C} = \frac{\tilde{\gamma}_{s,0}-\tilde{\gamma}_{s,h}}{2i\Omega - \Delta_s\left(\tilde{\gamma}_{s,0}-\tilde{\gamma}_{s,h}\right)}. \tag{E.63}$$

Summarizing for retarded quantities,

$$\gamma_s = \gamma_{s,h} + \frac{2i\Omega C \exp\left(-2\Omega x\right)}{1-\tilde{\Delta}_s C \exp\left(-2\Omega x\right)}, \tag{E.64}$$

$$\tilde{\gamma}_s = \tilde{\gamma}_{s,h} + \frac{2i\Omega \tilde{C} \exp\left(2\Omega x\right)}{1+\Delta_s \tilde{C} \exp\left(2\Omega x\right)} \tag{E.65}$$

$$\gamma_{s,h} = \frac{-\Delta_s}{z+i\Omega}, \tag{E.66}$$

$$\tilde{\gamma}_{s,h} = \frac{\tilde{\Delta}_s}{z+i\Omega}, \tag{E.67}$$

$$\Omega \equiv \sqrt{|\Delta_s|^2 - z^2}. \tag{E.68}$$

In a discrete lattice, a piecewise order parameter is assumed. This is a reasonable assumption if the discrete grid size is much smaller than the coherence length, which is the length-scale that the order parameter is inherently assumed to vary over in quasiclassics. The trajectories are then solved in discrete steps, where the solution in the previous step is the initial value for the new step.

Appendix F

Spin-triplet superconductivity

This PhD project was initially spent studying spin-triplet superconductivity. The pairing symmetry of interest was a p-wave superconductor, e.g. Sr_2RuO_4 [151], and in particular, the p_x+ip_y pairing symmetry [129, 130], with spin fixed perpendicular to the superconducting plane $\boldsymbol{d_k} = \hat{\boldsymbol{z}}$ (unitary). This is outside the scope of paper I and paper II. This appendix derives the Green functions in terms of Riccati amplitudes for both unitary and non-unitary superconductors. The Riccati equations for a superconductor with a mixed singlet-triplet pairing symmetry is derived. The analytic solutions to the Riccati equations are introduced for a unitary triplet pairing. The appendix also includes a table that compares various expressions between singlet and triplet superconductors.

F.1 Scalar spin-triplet Green functions

Using the Shelankov projectors in App. E.1, the Green functions in Nambu$\otimes$spin-space where found to be

$$\hat{g} = \begin{pmatrix} g_0\sigma_0 + \boldsymbol{g}\cdot\boldsymbol{\sigma} & (f_s + \boldsymbol{f}_t\cdot\boldsymbol{\sigma})\, i\sigma_2 \\ i\sigma_2\left(\tilde{f}_s - \tilde{\boldsymbol{f}}_t\cdot\boldsymbol{\sigma}\right) & \sigma_2\left(\tilde{g}_0 - \tilde{\boldsymbol{g}}\cdot\boldsymbol{\sigma}\right)\sigma_2 \end{pmatrix}, \tag{F.1}$$

$$\hat{g} = -i\pi\hat{N}\otimes\begin{pmatrix} (1+\gamma\otimes\tilde{\gamma}) & 2\gamma \\ -2\tilde{\gamma} & -(1+\tilde{\gamma}\otimes\gamma) \end{pmatrix} \tag{F.2}$$

$$\hat{N} = \begin{pmatrix} (1-\gamma\otimes\tilde{\gamma})^{-1} & 0 \\ 0 & (1-\tilde{\gamma}\otimes\gamma)^{-1} \end{pmatrix}. \tag{F.3}$$

Consider a spin-triplet system with the following coherence functions in spin-space

$$\gamma = \boldsymbol{\gamma}_t\cdot\boldsymbol{\sigma}i\sigma_2 = \gamma_t\boldsymbol{d}\cdot\boldsymbol{\sigma}i\sigma_2, \tag{F.4}$$

$$\tilde{\gamma} = -i\sigma_2\tilde{\boldsymbol{\gamma}}_t\cdot\boldsymbol{\sigma} = -i\sigma_2\tilde{\gamma}_t\boldsymbol{d}\cdot\boldsymbol{\sigma}. \tag{F.5}$$

The goal is to express the spin-space Green functions in Eq. (F.1) in terms of the coherence functions $\boldsymbol{\gamma}_t$ and $\tilde{\gamma}_t$ by equating Eqs. (F.1) and (F.2). To do so,

Eqs. (F.4) and (F.5) are substituted into Eq. (F.2) and reworked a bit, starting with the terms in $\hat{N}$. By using the following expressions,

$$(\boldsymbol{a}\cdot\boldsymbol{\sigma})(\boldsymbol{b}\cdot\boldsymbol{\sigma}) = \boldsymbol{a}\cdot\boldsymbol{b} + i\boldsymbol{\sigma}\cdot(\boldsymbol{a}\times\boldsymbol{b}), \tag{F.6}$$

$$\boldsymbol{a}\cdot\boldsymbol{\sigma} = \begin{pmatrix} a_z & a_x - ia_y \\ a_x + ia_y & -a_z \end{pmatrix}, \tag{F.7}$$

it is possible to rewrite the upper left term in $\hat{N}$ as

$$\begin{aligned}
(1-\gamma\otimes\tilde{\gamma})^{-1} &= (1-(\boldsymbol{\gamma}_t\cdot\boldsymbol{\sigma})(\tilde{\boldsymbol{\gamma}}_t\cdot\boldsymbol{\sigma}))^{-1} \\
&= (\underbrace{1-\boldsymbol{\gamma}_t\cdot\tilde{\boldsymbol{\gamma}}_t}_{\equiv a} - \boldsymbol{\sigma}\cdot\underbrace{i\boldsymbol{\gamma}_t\times\tilde{\boldsymbol{\gamma}}_t}_{\equiv b})^{-1} \\
&= (a\sigma_0 - \boldsymbol{\sigma}\cdot\boldsymbol{b})^{-1} \\
&= \begin{pmatrix} a+b_z & b_x - ib_y \\ b_x+ib_y & a-b_z \end{pmatrix} \frac{1}{(a+b_z)(a-b_z)-(b_x-b_y)(b_x+ib_y)} \\
&= \frac{a\sigma_0+\boldsymbol{\sigma}\cdot\boldsymbol{b}}{a^2-\boldsymbol{b}\cdot\boldsymbol{b}} \\
&= \frac{1-\boldsymbol{\gamma}_t\cdot\tilde{\boldsymbol{\gamma}}_t + i\boldsymbol{\sigma}\cdot(\boldsymbol{\gamma}_t\times\tilde{\boldsymbol{\gamma}}_t)}{1-2(\boldsymbol{\gamma}_t\cdot\tilde{\boldsymbol{\gamma}}_t)+(\boldsymbol{\gamma}_t\cdot\boldsymbol{\gamma}_t)(\tilde{\boldsymbol{\gamma}}_t\cdot\tilde{\boldsymbol{\gamma}}_t)}.
\end{aligned} \tag{F.8}$$

Similarly, it is possible to rewrite the lower right term in $\hat{N}$ as

$$(1-\tilde{\gamma}\otimes\gamma)^{-1} = \frac{1-\tilde{\boldsymbol{\gamma}}_t\cdot\boldsymbol{\gamma}_t + i\sigma_2\boldsymbol{\sigma}\cdot(\tilde{\boldsymbol{\gamma}}_t\times\boldsymbol{\gamma}_t)\sigma_2}{1-2(\tilde{\boldsymbol{\gamma}}_t\cdot\boldsymbol{\gamma}_t)+(\boldsymbol{\gamma}_t\cdot\boldsymbol{\gamma}_t)(\tilde{\boldsymbol{\gamma}}_t\cdot\tilde{\boldsymbol{\gamma}}_t)}. \tag{F.9}$$

The common denominators in $\hat{N}$ can be taken out of the matrix. Next, it is noted that the diagonal elements of $\hat{g}$ in Eq. (F.2) can be written as

$$1+\gamma\otimes\tilde{\gamma} = 1+\boldsymbol{\gamma}_t\cdot\tilde{\boldsymbol{\gamma}}_t + i\boldsymbol{\sigma}\cdot(\boldsymbol{\gamma}_t\times\tilde{\boldsymbol{\gamma}}_t), \tag{F.10}$$

$$1+\tilde{\gamma}\otimes\gamma = 1+\boldsymbol{\gamma}_t\cdot\tilde{\boldsymbol{\gamma}}_t + i\sigma_2\boldsymbol{\sigma}\cdot(\tilde{\boldsymbol{\gamma}}_t\times\boldsymbol{\gamma}_t)\sigma_2. \tag{F.11}$$

Next, Eqs. (F.8)–(F.11) are inserted into $\hat{g}$ and $\hat{N}$ in Eq. (F.2). After quite some algebra in the matrix multiplication between $\hat{g}$ and $\hat{N}$, it is found that

$$\hat{g} = -i\pi\frac{\begin{pmatrix} g_{11} & g_{12} \\ g_{21} & g_{22}\end{pmatrix}}{1-2(\boldsymbol{\gamma}_t\cdot\tilde{\boldsymbol{\gamma}}_t)+(\boldsymbol{\gamma}_t\cdot\boldsymbol{\gamma}_t)(\tilde{\boldsymbol{\gamma}}_t\cdot\tilde{\boldsymbol{\gamma}}_t)}, \tag{F.12}$$

$$g_{11} = 1-(\boldsymbol{\gamma}_t\cdot\boldsymbol{\gamma}_t)(\tilde{\boldsymbol{\gamma}}_t\cdot\tilde{\boldsymbol{\gamma}}_t)+2i(\boldsymbol{\gamma}_t\times\tilde{\boldsymbol{\gamma}}_t)\cdot\boldsymbol{\sigma}, \tag{F.13}$$

$$g_{12} = (\boldsymbol{\gamma}_t\cdot\boldsymbol{\sigma}-(\boldsymbol{\gamma}_t\cdot\boldsymbol{\gamma}_t)\tilde{\boldsymbol{\gamma}}_t\cdot\boldsymbol{\sigma})2i\sigma_2, \tag{F.14}$$

$$g_{21} = 2i\sigma_2(\tilde{\boldsymbol{\gamma}}_t\cdot\boldsymbol{\sigma}-(\tilde{\boldsymbol{\gamma}}_t\cdot\tilde{\boldsymbol{\gamma}}_t)\boldsymbol{\gamma}_t\cdot\boldsymbol{\sigma}), \tag{F.15}$$

$$g_{22} = -i\sigma_2(1-(\boldsymbol{\gamma}_t\cdot\boldsymbol{\gamma}_t)(\tilde{\boldsymbol{\gamma}}_t\cdot\tilde{\boldsymbol{\gamma}}_t)+2i\boldsymbol{\sigma}\cdot(\tilde{\boldsymbol{\gamma}}_t\times\boldsymbol{\gamma}_t))\sigma_2. \tag{F.16}$$

In comparing Eqs. (F.12)–(F.16) with Eq. (F.1), it is found that

$$g_0 = -i\pi \frac{1-(\boldsymbol{\gamma}_t\cdot\boldsymbol{\gamma}_t)(\tilde{\boldsymbol{\gamma}}_t\cdot\tilde{\boldsymbol{\gamma}}_t)}{1-2(\boldsymbol{\gamma}_t\cdot\tilde{\boldsymbol{\gamma}}_t)+(\boldsymbol{\gamma}_t\cdot\boldsymbol{\gamma}_t)(\tilde{\boldsymbol{\gamma}}_t\cdot\tilde{\boldsymbol{\gamma}}_t)}, \tag{F.17}$$

$$\tilde{g}_0 = i\pi \frac{1-(\boldsymbol{\gamma}_t\cdot\boldsymbol{\gamma}_t)(\tilde{\boldsymbol{\gamma}}_t\cdot\tilde{\boldsymbol{\gamma}}_t)}{1-2(\boldsymbol{\gamma}_t\cdot\tilde{\boldsymbol{\gamma}}_t)+(\boldsymbol{\gamma}_t\cdot\boldsymbol{\gamma}_t)(\tilde{\boldsymbol{\gamma}}_t\cdot\tilde{\boldsymbol{\gamma}}_t)}, \tag{F.18}$$

$$\boldsymbol{g} = 2\pi \frac{\boldsymbol{\gamma}_t\times\tilde{\boldsymbol{\gamma}}_t}{1-2(\boldsymbol{\gamma}_t\cdot\tilde{\boldsymbol{\gamma}}_t)+(\boldsymbol{\gamma}_t\cdot\boldsymbol{\gamma}_t)(\tilde{\boldsymbol{\gamma}}_t\cdot\tilde{\boldsymbol{\gamma}}_t)}, \tag{F.19}$$

$$\tilde{\boldsymbol{g}} = -2\pi \frac{\boldsymbol{\gamma}_t\times\tilde{\boldsymbol{\gamma}}_t}{1-2(\boldsymbol{\gamma}_t\cdot\tilde{\boldsymbol{\gamma}}_t)+(\boldsymbol{\gamma}_t\cdot\boldsymbol{\gamma}_t)(\tilde{\boldsymbol{\gamma}}_t\cdot\tilde{\boldsymbol{\gamma}}_t)}, \tag{F.20}$$

$$\boldsymbol{f} = -2i\pi \frac{\boldsymbol{\gamma}_t-(\boldsymbol{\gamma}_t\cdot\boldsymbol{\gamma}_t)\tilde{\boldsymbol{\gamma}}_t}{1-2(\boldsymbol{\gamma}_t\cdot\tilde{\boldsymbol{\gamma}}_t)+(\boldsymbol{\gamma}_t\cdot\boldsymbol{\gamma}_t)(\tilde{\boldsymbol{\gamma}}_t\cdot\tilde{\boldsymbol{\gamma}}_t)}, \tag{F.21}$$

$$\tilde{\boldsymbol{f}} = 2i\pi \frac{\tilde{\boldsymbol{\gamma}}_t-(\tilde{\boldsymbol{\gamma}}_t\cdot\tilde{\boldsymbol{\gamma}}_t)\boldsymbol{\gamma}_t}{1-2(\boldsymbol{\gamma}_t\cdot\tilde{\boldsymbol{\gamma}}_t)+(\boldsymbol{\gamma}_t\cdot\boldsymbol{\gamma}_t)(\tilde{\boldsymbol{\gamma}}_t\cdot\tilde{\boldsymbol{\gamma}}_t)}. \tag{F.22}$$

$$\tag{F.23}$$

The expressions for a unitary system, i.e. where all the cross products vanish due to $\boldsymbol{d}\times\boldsymbol{d}^*=0$, are summarized in Tab. F.1 on p. 194.

F.2 Pure triplet and mixed singlet-triplet pairing

Allowing for a mixed singlet (s) and triplet (t) pairing symmetry, the spinful coherence functions and the order parameter can be written as

$$\gamma = (\gamma_s+\boldsymbol{\gamma}_t\cdot\boldsymbol{\sigma})\,i\sigma_2, \tag{F.24}$$

$$\Delta = (\Delta_s+\boldsymbol{\Delta}_t\cdot\boldsymbol{\sigma})\,i\sigma_2, \tag{F.25}$$

where bold symbols denote vectors, i.e. $\boldsymbol{\gamma}_t=\gamma_t\boldsymbol{d}_k$, $\boldsymbol{\Delta}_t=\Delta_t\boldsymbol{d}_k$, and σ are the Pauli spin matrices, with

$$\boldsymbol{\sigma}^* = -\sigma_2\boldsymbol{\sigma}\sigma_2. \tag{F.26}$$

Recall that the tilde operation for particle-hole conjugation is defined as

$$\tilde{\alpha}(\boldsymbol{p}_F,\boldsymbol{R};z,t) = \alpha^*(-\boldsymbol{p}_F,\boldsymbol{R};-z^*,t), \tag{F.27}$$

and that

$$\Delta_s(-\boldsymbol{p}_F,\boldsymbol{R}) = \Delta_s(\boldsymbol{p}_F,\boldsymbol{R}), \tag{F.28}$$

$$\Delta_t(-\boldsymbol{p}_F,\boldsymbol{R}) = -\Delta_t(\boldsymbol{p}_F,\boldsymbol{R}). \tag{F.29}$$

Applying the tilde operation to γ and using Eqs. (F.26) and (F.27)

$$\begin{aligned}\tilde{\gamma}(\boldsymbol{p}_F,\boldsymbol{R};z) &= \gamma^*(-\boldsymbol{p}_F,\boldsymbol{R};-z^*)\\ &= (\gamma_s^*(-\boldsymbol{p}_F,\boldsymbol{R};-z^*)-\sigma_2\boldsymbol{\gamma}_t^*(-\boldsymbol{p}_F,\boldsymbol{R};-z^*)\cdot\boldsymbol{\sigma}\sigma_2)\,i\sigma_2\\ &= i\sigma_2\left(\tilde{\gamma}_s(\boldsymbol{p}_F,\boldsymbol{R};z)-\tilde{\boldsymbol{\gamma}}_t(\boldsymbol{p}_F,\boldsymbol{R};z)\cdot\boldsymbol{\sigma}\right).\end{aligned} \tag{F.30}$$

Similarly for Δ, it is found that

$$\begin{aligned}\tilde{\Delta}(\boldsymbol{p}_F,\boldsymbol{R}) &= \Delta^*(-\boldsymbol{p}_F,\boldsymbol{R})\\ &= i\sigma_2\left(\tilde{\Delta}_s(\boldsymbol{p}_F,\boldsymbol{R})-\tilde{\boldsymbol{\Delta}}_t(\boldsymbol{p}_F,\boldsymbol{R})\cdot\boldsymbol{\sigma}\right)\end{aligned} \tag{F.31}$$

Thus,

$$\tilde{\gamma} = i\sigma_2\left(\tilde{\gamma}_s-\tilde{\boldsymbol{\gamma}}_t\cdot\boldsymbol{\sigma}\right), \tag{F.32}$$

$$\tilde{\Delta} = i\sigma_2\left(\tilde{\Delta}_s-\tilde{\boldsymbol{\Delta}}_t\cdot\boldsymbol{\sigma}\right). \tag{F.33}$$

Substitution of γ, Δ and $\tilde{\Delta}$ into the Riccati Eq. (E.36) yields

$$\begin{aligned}0 &= \left(i\hbar\boldsymbol{v}_F\cdot\boldsymbol{\nabla}+2\epsilon\right)\left(\gamma_s+\boldsymbol{\gamma}_t\cdot\boldsymbol{\sigma}\right)i\sigma_2+\left(\Delta_s+\boldsymbol{\Delta}_t\cdot\boldsymbol{\sigma}\right)i\sigma_2\\ &\quad-\left(\gamma_s+\boldsymbol{\gamma}_t\cdot\boldsymbol{\sigma}\right)i\sigma_2 i\sigma_2\left(\tilde{\Delta}_s-\tilde{\boldsymbol{\Delta}}_t\cdot\boldsymbol{\sigma}\right)\left(\gamma_s+\boldsymbol{\gamma}_t\cdot\boldsymbol{\sigma}\right)i\sigma_2.\end{aligned} \tag{F.34}$$

Multiplying from the right with $-i\sigma_2$ and noting that $\sigma_i^2=\sigma_0$ is the unit matrix, it is found that

$$\begin{aligned}0 &= \left[\left(i\hbar\boldsymbol{v}_F\cdot\boldsymbol{\nabla}+2\epsilon\right)\gamma_s+\Delta_s\right]+\left(\gamma_s\gamma_s+\boldsymbol{\gamma}_t\cdot\boldsymbol{\gamma}_t\right)\tilde{\Delta}_s-2\left(\boldsymbol{\gamma}_t\cdot\tilde{\boldsymbol{\Delta}}_t\right)\gamma_s\\ &+ \left[\left(i\hbar\boldsymbol{v}_F\cdot\boldsymbol{\nabla}+2\epsilon\right)\boldsymbol{\gamma}_t+\boldsymbol{\Delta}_t\right]\cdot\boldsymbol{\sigma}+\left(-\gamma_s\gamma_s+\boldsymbol{\gamma}_t\cdot\boldsymbol{\gamma}_t\right)\tilde{\boldsymbol{\Delta}}_t\cdot\boldsymbol{\sigma}-2\left(\boldsymbol{\gamma}_t\cdot\tilde{\boldsymbol{\Delta}}_t\right)\boldsymbol{\gamma_t}\cdot\boldsymbol{\sigma}\\ &+ 2\left(\gamma_s\tilde{\Delta}_s\right)\boldsymbol{\gamma}_t\cdot\boldsymbol{\sigma}.\end{aligned} \tag{F.35}$$

Here, the identity $(\boldsymbol{a}\cdot\boldsymbol{\sigma})(\boldsymbol{b}\cdot\boldsymbol{\sigma})=\boldsymbol{a}\cdot\boldsymbol{b}+i\boldsymbol{\sigma}\cdot(\boldsymbol{a}\times\boldsymbol{b})$ was used, with any cross products neglected since a unitary triplet system is considered, i.e. $\boldsymbol{\gamma}_t\times\tilde{\boldsymbol{\gamma}}_t=\gamma_t\tilde{\gamma}_t\boldsymbol{d}\times\boldsymbol{d}^*=\hat{\boldsymbol{z}}\times\hat{\boldsymbol{z}}^*=0$. Using the fact that $\sigma_{1,2,3}$ are traceless, it is possible to take the trace of Eq. (F.35) to obtain a Riccati equation for γ_s, as well as a Riccati equation for γ_t by multiplying Eq. (F.35) with $\boldsymbol{\sigma}$ before taking the trace. Similarly, substituting $\tilde{\gamma}$, Δ and $\tilde{\Delta}$ into Eq. (E.37) and following the same steps, Riccati equations for $\tilde{\gamma}_s$ and $\tilde{\gamma}_t$ are obtained. These are

$$\left(i\hbar\boldsymbol{v}_F\cdot\boldsymbol{\nabla}+2\epsilon\right)\gamma_s = -\left(\gamma_s\gamma_s+\boldsymbol{\gamma}_t\cdot\boldsymbol{\gamma}_t\right)\tilde{\Delta}_s+2\left(\boldsymbol{\gamma}_t\cdot\tilde{\boldsymbol{\Delta}}_t\right)\gamma_s-\Delta_s, \tag{F.36}$$

$$\left(i\hbar\boldsymbol{v}_F\cdot\boldsymbol{\nabla}-2\epsilon\right)\tilde{\gamma}_s = -\left(\tilde{\gamma}_s\tilde{\gamma}_s+\tilde{\boldsymbol{\gamma}}_t\cdot\tilde{\boldsymbol{\gamma}}_t\right)\Delta_s+2\left(\tilde{\boldsymbol{\gamma}}_t\cdot\boldsymbol{\Delta}_t\right)\tilde{\gamma}_s-\tilde{\Delta}_s, \tag{F.37}$$

$$\begin{aligned}\left(i\hbar\boldsymbol{v}_F\cdot\boldsymbol{\nabla}+2\epsilon\right)\boldsymbol{\gamma}_t &= \left(\gamma_s\gamma_s-\boldsymbol{\gamma}_t\cdot\boldsymbol{\gamma}_t\right)\tilde{\boldsymbol{\Delta}}_t+2\left(\boldsymbol{\gamma}_t\cdot\tilde{\boldsymbol{\Delta}}_t\right)\boldsymbol{\gamma}_t-\boldsymbol{\Delta}_t\\ &\quad-2\left(\gamma_s\tilde{\Delta}_s\right)\boldsymbol{\gamma}_t,\end{aligned} \tag{F.38}$$

$$\begin{aligned}\left(i\hbar\boldsymbol{v}_F\cdot\boldsymbol{\nabla}-2\epsilon\right)\tilde{\boldsymbol{\gamma}}_t &= \left(\tilde{\gamma}_s\tilde{\gamma}_s-\tilde{\boldsymbol{\gamma}}_t\cdot\tilde{\boldsymbol{\gamma}}_t\right)\boldsymbol{\Delta}_t+2\left(\tilde{\boldsymbol{\gamma}}_t\cdot\boldsymbol{\Delta}_t\right)\tilde{\boldsymbol{\gamma}}_t-\tilde{\boldsymbol{\Delta}}_t\\ &\quad-2\left(\tilde{\gamma}_s\Delta_s\right)\tilde{\boldsymbol{\gamma}}_t.\end{aligned} \tag{F.39}$$

Note that these equations are not in spin space, and that the equations couple the singlet and triplet parts. It is possible to decouple these equations with the following substitution

$$\gamma_\pm \equiv \pm(\gamma_s\pm\gamma_t), \tag{F.40}$$

$$\tilde{\gamma}_\pm \equiv \pm(\tilde{\gamma}_s\pm\tilde{\gamma}_t), \tag{F.41}$$

$$\Delta\pm \equiv \pm(\Delta_s\pm\Delta_t), \tag{F.42}$$

$$\tilde{\Delta}_\pm \equiv \pm(\Delta^*\pm\Delta_t^*), \tag{F.43}$$

yielding the decoupled Riccati equations for mixed singlet-triplet pairing [152]

$$(i\hbar \boldsymbol{v}_F \cdot \boldsymbol{\nabla} + 2\epsilon)\,\gamma_\pm = -\tilde{\Delta}_\pm \gamma_\pm^2 - \Delta_\pm, \tag{F.44}$$
$$(i\hbar \boldsymbol{v}_F \cdot \boldsymbol{\nabla} - 2\epsilon)\,\tilde{\gamma}_\pm = -\Delta_\pm \tilde{\gamma}_\pm^2 - \tilde{\Delta}_\pm. \tag{F.45}$$

These equations are solved analogously to the spin-singlet case in App. E.4. The singlet and triplet amplitudes are then obtained from the solutions using Eqs. (F.40) and (F.41). For a pure triplet pairing, Eqs. (F.38) and (F.39) simplify to

$$(i\hbar \boldsymbol{v}_F \cdot \boldsymbol{\nabla} + 2\epsilon)\,\gamma_t = -\Delta_t + \tilde{\Delta}_t \gamma_t^2, \tag{F.46}$$
$$(i\hbar \boldsymbol{v}_F \cdot \boldsymbol{\nabla} - 2\epsilon)\,\tilde{\gamma}_t = -\tilde{\Delta}_t + \Delta_t \tilde{\gamma}_t^2. \tag{F.47}$$

Again, these equations are are solved analogously to the spin-singlet case in App. E.4, and have the analytic solutions presented in the Tab. F.1 in the following section.

F.3 Comparison of singlet and triplet expressions

Table F.1 compares different expressions between pure spin-singlet and pure spin-triplet superconductors that are unitary, i.e. the spin-triplet superconductor is assumed to have a spin projection perpendicular to the superconducting plane $\boldsymbol{d_k} = \hat{\boldsymbol{z}}$. Here, s denotes singlet and t triplet, while I and II are the first and second integration domains along the trajectory $x\hat{\boldsymbol{v_F}}$, respectively. None of the expressions are in spin-space (i.e. scalars), and $\Omega \equiv \sqrt{-\Delta\tilde{\Delta} - \epsilon^2}$. The singlet and triplet expressions for the Green functions are derived in Apps. E.2 and F.1, respectively. The solutions to the Riccati equations are derived in App. E.4.

Table F.1: *Comparison of pure spin-singlet and pure spin-triplet expressions in scalar form*

Expression	**Singlet**	**Triplet**
g_0	$-i\pi\dfrac{1-\gamma_s\tilde{\gamma}_s}{1+\gamma_s\tilde{\gamma}_s}$	$-i\pi\dfrac{1+\gamma_t\tilde{\gamma}_t}{1-\gamma_t\tilde{\gamma}_t}$
$\tilde{g}_0$	$i\pi\dfrac{1-\gamma_s\tilde{\gamma}_s}{1+\gamma_s\tilde{\gamma}_s}$	$i\pi\dfrac{1+\gamma_t\tilde{\gamma}_t}{1-\gamma_t\tilde{\gamma}_t}$
f	$-2i\pi\dfrac{\gamma_s}{1+\gamma_s\tilde{\gamma}_s}$	$-2i\pi\dfrac{\gamma_t}{1-\gamma_t\tilde{\gamma}_t}$
$\tilde{f}$	$2i\pi\dfrac{\tilde{\gamma}_s}{1+\gamma_s\tilde{\gamma}_s}$	$2i\pi\dfrac{\tilde{\gamma}_t}{1-\gamma_t\tilde{\gamma}_t}$
Matsubara symmetry	$f_s(-\epsilon_n)=\tilde{f}_s^*(\epsilon_n)$	$f_t(-\epsilon_n)=-\tilde{f}_t^*(\epsilon_n)$
$\gamma_{\text{homogeneous}}$	$\gamma_{s,0}=\dfrac{-\Delta_s}{\epsilon+i\Omega}$	$\gamma_{t,0}=\dfrac{-\Delta_t}{\epsilon+i\Omega}$
$\tilde{\gamma}_{\text{homogeneous}}$	$\tilde{\gamma}_{s,0}=\dfrac{\Delta_s^*}{\epsilon+i\Omega}$	$\tilde{\gamma}_{t,0}=\dfrac{-\Delta_t^*}{\epsilon+i\Omega}$
γ	$\gamma_{s,0}+\dfrac{2i\Omega C\exp(-2\Omega x)}{1-\Delta_s^* C\exp(-2\Omega x)}$	$\gamma_{t,0}+\dfrac{2i\Omega C\exp(-2\Omega x)}{1-\Delta_t^* C\exp(-2\Omega x)}$
$\tilde{\gamma}$	$\tilde{\gamma}_{s,0}+\dfrac{2i\Omega\tilde{C}\exp(2\Omega x)}{1+\Delta_s\tilde{C}\exp(2\Omega x)}$	$\tilde{\gamma}_{t,0}+\dfrac{2i\Omega\tilde{C}\exp(2\Omega x)}{1-\Delta_t\tilde{C}\exp(2\Omega x)}$
C	$\dfrac{\gamma_{s,0}^{\mathrm{I}}-\gamma_{s,0}^{\mathrm{II}}}{2i\Omega+\Delta_s^*\left(\gamma_{s,0}^{\mathrm{I}}-\gamma_{s,0}^{\mathrm{II}}\right)}$	$\dfrac{\gamma_{t,0}^{\mathrm{I}}-\gamma_{t,0}^{\mathrm{II}}}{2i\Omega+\Delta_t^*\left(\gamma_{t,0}^{\mathrm{I}}-\gamma_{t,0}^{\mathrm{II}}\right)}$
$\tilde{C}$	$\dfrac{\tilde{\gamma}_{s,0}^{\mathrm{II}}-\tilde{\gamma}_{s,0}^{\mathrm{I}}}{2i\Omega-\Delta_s\left(\tilde{\gamma}_{s,0}^{\mathrm{II}}-\tilde{\gamma}_{s,0}^{\mathrm{I}}\right)}$	$\dfrac{\tilde{\gamma}_{t,0}^{\mathrm{II}}-\tilde{\gamma}_{t,0}^{\mathrm{I}}}{2i\Omega+\Delta_t\left(\tilde{\gamma}_{t,0}^{\mathrm{II}}-\tilde{\gamma}_{t,0}^{\mathrm{I}}\right)}$

Appendix G

A useful Matsubara symmetry

In this appendix, it will be shown how to reduce the sum over Matsubara frequencies from $\sum_{\epsilon_n=-\epsilon_c}^{\epsilon_c} \longrightarrow \sum_{\epsilon_n=0}^{\epsilon_c}$. This greatly improves the numerical calculation time of the gap equation, and also applies to Ozaki summation. For more details, please refer to App. C in Ref. [69]. The Matsubara Green function is defined as

$$\hat{g}^M = \begin{pmatrix} g^M & f^M \\ \tilde{f}^M & \tilde{g}^M \end{pmatrix}, \tag{G.1}$$

which obeys the symmetry

$$\left(\hat{g}^M(\hat{p}_F, \vec{R}; \epsilon_n)\right)^\dagger = \hat{\tau}_3 \hat{g}^M(\hat{p}_F, \vec{R}; -\epsilon_n)\hat{\tau}_3. \tag{G.2}$$

Dropping the M superscript and inserting the left and right-hand sides of Eq. (G.2),

$$\begin{pmatrix} g^\dagger & \tilde{f}^\dagger \\ f^\dagger & \tilde{g}^\dagger \end{pmatrix} = \begin{pmatrix} g(\hat{p}_F, \vec{R}; -\epsilon_n) & -f(\hat{p}_F, \vec{R}; -\epsilon_n) \\ -\tilde{f}(\hat{p}_F, \vec{R}; -\epsilon_n) & \tilde{g}(\hat{p}_F, \vec{R}; -\epsilon_n) \end{pmatrix}, \tag{G.3}$$

yielding

$$\hat{f}(-\epsilon_n) = -\left(\hat{\tilde{f}}(\epsilon_n)\right)^\dagger, \tag{G.4}$$

$$\hat{g}(-\epsilon_n) = (\hat{g}(\epsilon_n))^\dagger = \hat{g}^*(\epsilon_n). \tag{G.5}$$

Thus, for a singlet and triplet pair-propagator, the scalar components satisfies

$$f_s(-\epsilon_n) = \tilde{f}_s^*(\epsilon_n), \tag{G.6}$$

$$f_t(-\epsilon_n) = -\tilde{f}_t^*(\epsilon_n), \tag{G.7}$$

respectively. The sum in the gap equation then simplifies to only positive energies

$$\sum_{|\epsilon_n|\leq\Omega_c} f_s = \sum_{0<\epsilon_n\leq\Omega_c} \left(f_s + \tilde{f}_s^*\right), \tag{G.8}$$

$$\sum_{|\epsilon_n|\leq\Omega_c} f_t = \sum_{0<\epsilon_n\leq\Omega_c} \left(f_t - \tilde{f}_t^*\right). \tag{G.9}$$

References

[1] L. D. Landau, Sov. Phys. JEPT **3**, 920 (1957) (cit. on p. 4).

[2] L. D. Landau, Sov. Phys. JEPT **5**, 101 (1957) (cit. on p. 4).

[3] L. D. Landau, Sov. Phys. JEPT **8**, 70 (1959) (cit. on p. 4).

[4] N. Ashcroft and N. Mermin, *Solid State Physics* (Brooks/Cole, 1976) (cit. on pp. 4, 6, 72, 167).

[5] G. Burns, *Solid state physics* (Academic Press, 1985) (cit. on p. 4).

[6] L. Landau and E. Lifshitz, *Statistical Physics*, v. 5 (Elsevier Science, 2013) (cit. on p. 4).

[7] M. P. Marder, *Condensed Matter Physics*, 2nd (John Wiley & Sons, Inc., 2010) (cit. on p. 4).

[8] M. Cohen and S. Louie, *Fundamentals of Condensed Matter Physics* (Cambridge University Press, 2016) (cit. on p. 4).

[9] P. Phillips, *Advanced Solid State Physics* (Cambridge University Press, 2012) (cit. on pp. 4, 5, 78).

[10] G. Mahan, *Many-Particle Physics*, Physics of Solids and Liquids (Springer US, 2013) (cit. on p. 4).

[11] P. Coleman, *Introduction to Many-Body Physics* (Cambridge University Press, 2015) (cit. on p. 4).

[12] M. Born and V. Fock, "Beweis des Adiabatensatzes", Z. Phys. **51**, 165–180 (1928) (cit. on p. 4).

[13] P. F. Dahl, *Superconductivity : its historical roots and development from mercury to the ceramic oxides*, English (American Institute of Physics New York, 1992) (cit. on p. 5).

[14] H. Kamerlingh Onnes, "Further experiments with Liquid Helium. D. On the change of Electrical Resistance of Pure Metals at very low Temperatures, etc. V. The Disappearance of the resistance of mercury", Koninklijke Nederlandse Akademie van Wetenschappen Proceedings Series B Physical Sciences **14**, 113–115 (1911) (cit. on p. 5).

[15] W. Meissner and R. Ochsenfeld, "Ein neuer Effekt bei Eintritt der Supraleitfähigkeit", Naturwissenschaften **21**, 787–788 (1933) (cit. on p. 6).

[16] C. Timm, "Theory of Superconductivity", 2012 (cit. on pp. 6, 72, 171).

[17] H. Fröhlich, "Theory of the Superconducting State. I. The Ground State at the Absolute Zero of Temperature", Phys. Rev. **79**, 845–856 (1950) (cit. on p. 6).

[18] E. Maxwell, "Isotope Effect in the Superconductivity of Mercury", Phys. Rev. **78**, 477–477 (1950) (cit. on p. 6).

[19] C. A. Reynolds, B. Serin, W. H. Wright, and L. B. Nesbitt, "Superconductivity of Isotopes of Mercury", Phys. Rev. **78**, 487–487 (1950) (cit. on p. 6).

[20] J. Bardeen, L. N. Cooper, and J. R. Schrieffer, "Microscopic Theory of Superconductivity", Phys. Rev. **106**, 162–164 (1957) (cit. on pp. 7, 17).

[21] J. Bardeen, L. N. Cooper, and J. R. Schrieffer, "Theory of Superconductivity", Phys. Rev. **108**, 1175–1204 (1957) (cit. on pp. 7, 17, 176).

[22] L. N. Cooper, "Bound Electron Pairs in a Degenerate Fermi Gas", Phys. Rev. **104**, 1189–1190 (1956) (cit. on p. 7).

[23] P. Ehrenfest and J. R. Oppenheimer, "Note on the Statistics of Nuclei", Phys. Rev. **37**, 333–338 (1931) (cit. on p. 7).

[24] H. A. Bethe and R. F. Bacher, "Nuclear Physics A. Stationary States of Nuclei", Rev. Mod. Phys. **8**, 82–229 (1936) (cit. on p. 7).

[25] A. F. Andreev, "The Thermal Conductivity of the Intermediate State in Superconductors", Sov. Phys. JETP **19**, 1228 (1964), [Zh. Eksp. Teor. Fiz.46,1823(1964)] (cit. on p. 9).

[26] C. W. J. Beenakker, "Why Does a Metal—Superconductor Junction Have a Resistance?", in *Quantum Mesoscopic Phenomena and Mesoscopic Devices in Microelectronics*, edited by I. O. Kulik and R. Ellialtioğlu (Springer Netherlands, Dordrecht, 2000), pp. 51–60 (cit. on p. 9).

[27] P. D. Gennes and E. Guyon, "Superconductivity in "normal" metals", Physics Letters **3**, 168 –169 (1963) (cit. on p. 9).

[28] N. R. Werthamer, "Theory of the Superconducting Transition Temperature and Energy Gap Function of Superposed Metal Films", Phys. Rev. **132**, 2440–2445 (1963) (cit. on p. 9).

[29] L. D. Landau, "Theory of phase transformations. I", Sov. Phys. JETP **11**, 26 (1937), [Zh. Eksp. Teor. Fiz.7,19(1937)] (cit. on p. 9).

[30] Y. Nambu, "Quasi-Particles and Gauge Invariance in the Theory of Superconductivity", Phys. Rev. **117**, 648–663 (1960) (cit. on pp. 9, 20).

[31] J. Goldstone, "Field theories with « Superconductor » solutions", Il Nuovo Cimento **19**, 154–164 (1961) (cit. on p. 9).

[32] F. Steglich, J. Aarts, C. D. Bredl, W. Lieke, D. Meschede, W. Franz, and H. Schäfer, "Superconductivity in the Presence of Strong Pauli Paramagnetism: $CeCu_2Si_2$", Phys. Rev. Lett. **43**, 1892–1896 (1979) (cit. on p. 10).

[33] Jérome, D., Mazaud, A., Ribault, M., and Bechgaard, K., "Superconductivity in a synthetic organic conductor (TMTSF)2PF6", J. Physique Lett. **41**, 95–98 (1980) (cit. on p. 10).

[34] J. G. Bednorz and K. A. Müller, "Possible highTc superconductivity in the Ba-La-Cu-O system", Z. Phys. B **64**, 189–193 (1986) (cit. on p. 10).

[35] J. Nagamatsu, N. Nakagawa, T. Muranaka, Y. Zenitani, and J. Akimitsu, "Superconductivity at 39K in magnesium diboride", Nature **410**, 63–64 (2001) (cit. on p. 10).

[36] D. J. Van Harlingen, "Phase-sensitive tests of the symmetry of the pairing state in the high-temperature superconductors—Evidence for $d_{x^2-y^2}$ symmetry", Rev. Mod. Phys. **67**, 515–535 (1995) (cit. on p. 11).

[37] C. C. Tsuei and J. R. Kirtley, "Pairing symmetry in cuprate superconductors", Rev. Mod. Phys. **72**, 969 (2000) (cit. on pp. 11, 79, 177).

[38] C. Poole, H. Farach, R. Creswick, and R. Prozorov, *Superconductivity* (Elsevier Science, 2010) (cit. on p. 11).

[39] Z. Diao, D. Campanini, L. Fang, W.-K. Kwok, U. Welp, and A. Rydh, "Microscopic parameters from high-resolution specific heat measurements on superoptimally substituted $BaFe_2(As_{1-x}P_x)_2$ single crystals", Phys. Rev. B **93**, 014509 (2016) (cit. on pp. 11, 72, 152).

[40] L. J. Buchholtz and G. Zwicknagl, "Identification of p-wave superconductors", Phys. Rev. B **23**, 5788–5796 (1981) (cit. on pp. 11, 120).

[41] C.-R. Hu, "Midgap surface states as a novel signature for d^2_{xa}-x^2_b-wave superconductivity", Phys. Rev. Lett. **72**, 1526 (1994) (cit. on pp. 11, 12, 101).

[42] S. Kashiwaya and Y. Tanaka, "Tunnelling effects on surface bound states in unconventional superconductors", Rep. Prog. Phys. **63**, 1641 (2000) (cit. on pp. 12, 101).

[43] T Löfwander, V. S. Shumeiko, and G Wendin, "Andreev bound states in high- T c superconducting junctions", Supercond. Sci. Technol. **14**, R53 (2001) (cit. on pp. 12, 101).

[44] G. Volovik and L. Gor'kov, "Superconducting classes in heavy-fermion systems", Sov. Phys. JETP **61**, 843 (1985) (cit. on pp. 12, 101).

[45] M. Sigrist and K. Ueda, "Phenomenological theory of unconventional superconductivity", Rev. Mod. Phys. **63**, 239 (1991) (cit. on pp. 12, 101).

[46] M. Håkansson, T. Löfwander, and M. Fogelström, "Spontaneously broken time-reversal symmetry in high-temperature superconductors", Nat. Phys. **11**, 755–760 (2015) (cit. on pp. 12, 14, 101, 119, 127, 154).

[47] P. Holmvall, A. B. Vorontsov, M. Fogelstrom, and T. Lofwander, "Spontaneously broken translational symmetry at edges of high-temperature superconductors: thermodynamics in magnetic field", ArXiv e-prints (2017), arXiv:1711.07946 [cond-mat.supr-con] (cit. on pp. 12, 14, 101).

[48] P. Holmvall, T. Löfwander, and M. Fogelström, "Spontaneous generation of fractional vortex-antivortex pairs at single edges of high-Tc superconductors", ArXiv e-prints (2017), arXiv:1706.06165 [cond-mat.supr-con], accepted for publication in J. of Physics: Conf. Ser., the proceedings of the 28th International Conference on Low Temperature Physics (cit. on pp. 12, 14, 101).

[49] H. Bruus and K. Flensberg, *Many-Body Quantum Theory in Condensed Matter Physics: An Introduction*, Oxford Graduate Texts (OUP Oxford, 2004) (cit. on p. 12).

[50] S. Higashitani, "Mechanism of Paramagnetic Meissner Effect in High-Temperature Superconductors", J. Soc. Phys. Jpn. **66**, 2556 (1997) (cit. on pp. 14, 101).

[51] Y. S. Barash, M. S. Kalenkov, and J. Kurkijärvi, "Low-temperature magnetic penetration depth in *d*-wave superconductors: Zero-energy bound state and impurity effects", Phys. Rev. B **62**, 6665 (2000) (cit. on pp. 14, 101).

[52] T. Löfwander, V. S. Shumeiko, and G. Wendin, "Time-reversal symmetry breaking at Josephson tunnel junctions of purely $\boldsymbol{d}$ -wave superconductors", Phys. Rev. B **62**, R14653 (2000) (cit. on pp. 14, 101).

[53] A. B. Vorontsov, "Broken Translational and Time-Reversal Symmetry in Unconventional Superconducting Films", Phys. Rev. Lett. **102**, 177001 (2009) (cit. on pp. 14, 101, 120, 127, 154).

[54] Y. Nagai, Y. Ota, and K. Tanaka, "Time-reversal symmetry breaking and gapped surface states due to spontaneous emergence of new order in *d*-wave nanoislands", Phys. Rev. B **96**, 060503 (2017) (cit. on pp. 14, 101).

[55] M. Covington, M. Aprili, E. Paraoanu, L. H. Greene, F. Xu, J. Zhu, and C. A. Mirkin, "Observation of Surface-Induced Broken Time-Reversal Symmetry in $YBa_2Cu_3O_7$ Tunnel Junctions", Phys. Rev. Lett. **79**, 277 (1997) (cit. on pp. 14, 101).

[56] K. Krishana, N. P. Ong, Q. Li, G. D. Gu, and N. Koshizuka, "Plateaus Observed in the Field Profile of Thermal Conductivity in the Superconductor Bi2Sr2CaCu2O8", Science **277**, 83 (1997) (cit. on pp. 14, 101).

[57] Y. Dagan and G. Deutscher, "Doping and Magnetic Field Dependence of In-Plane Tunneling into $YBa_2Cu_3O_{7-x}$: Possible Evidence for the Existence of a Quantum Critical Point", Phys. Rev. Lett. **87**, 177004 (2001) (cit. on pp. 14, 101).

[58] R. Gonnelli, A. Calzolari, D. Daghero, L. Natale, G. Ummarino, V. Stepanov, and M. Ferretti, "Evidence for pseudogap and phase-coherence gap separation by Andreev reflection experiments in $Au/La_{2-x}Sr_xCuO_4$ point-contact junctions", Eur. Phys. J. B **22**, 411 (2001) (cit. on pp. 14, 101).

[59] G. Elhalel, R. Beck, G. Leibovitch, and G. Deutscher, "Transition from a Mixed to a Pure *d*-Wave Symmetry in Superconducting Optimally Doped $YBa_2Cu_3O_{7-x}$ Thin Films Under Applied Fields", Phys. Rev. Lett. **98**, 137002 (2007) (cit. on pp. 14, 101).

[60] D. Gustafsson, D. Golubev, M. Fogelström, T. Claeson, S. Kubatkin, T. Bauch, and F. Lombardi, "Fully gapped superconductivity in a nanometre-size $YBa_2Cu_3O_{7-\delta}$ island enhanced by a magnetic field", Nat. Nanotechnol. **8**, 25 (2013) (cit. on pp. 14, 101).

[61] T. Watashige, Y. Tsutsumi, T. Hanaguri, Y. Kohsaka, S. Kasahara, A. Furusaki, M. Sigrist, C. Meingast, T. Wolf, H. v. Löhneysen, T. Shibauchi, and Y. Matsuda, "Evidence for Time-Reversal Symmetry Breaking of the Superconducting State near Twin-Boundary Interfaces in FeSe Revealed by Scanning Tunneling Spectroscopy", Phys. Rev. X **5**, 031022 (2015) (cit. on pp. 14, 101).

[62] W. K. Neils and D. J. Van Harlingen, "Experimental Test for Subdominant Superconducting Phases with Complex Order Parameters in Cuprate Grain Boundary Junctions", Phys. Rev. Lett. **88**, 047001 (2002) (cit. on pp. 14, 101).

[63] J. Kirtley, C. Tsuei, A. Ariando, C. Verwijs, S. Harkema, and H. Hilgenkamp, "Angle-resolved phase-sensitive determination of the in-plane gap symmetry in $YBa_2Cu_3O_{7-\delta}$", Nat. Phys. **2**, 190–194 (2006) (cit. on pp. 14, 101).

[64] M. Hachiya, K. Aoyama, and R. Ikeda, "Field-induced reentrant superconductivity in thin films of nodal superconductors", Phys. Rev. B **88**, 064519 (2013) (cit. on pp. 14, 154).

[65] S. Higashitani and N. Miyawaki, "Phase Transition to a Time-Reversal Symmetry-Breaking State in d-Wave Superconducting Films with Rough Surfaces", J. Soc. Phys. Jpn. **84**, 033708 (2015) (cit. on pp. 14, 120, 154).

[66] N. Miyawaki and S. Higashitani, "Temperature Dependence of the Critical Thickness of d-Wave Superconducting Films", Phys. Proc. **65**, 25 (2015) (cit. on pp. 14, 154).

[67] N. Miyawaki and S. Higashitani, "Fermi surface effect on spontaneous breaking of time-reversal symmetry in unconventional superconducting films", Phys. Rev. B **91**, 094511 (2015) (cit. on pp. 14, 154).

[68] N. Kopnin, *Theory of Nonequilibrium Superconductivity*, International Series of Monographs on Physics (OUP Oxford, 2009) (cit. on pp. 17, 25, 51).

[69] J. Serene and D Rainer, "The quasiclassical approach to superfluid 3He", Physics Reports **101**, 221 –311 (1983) (cit. on pp. 17, 25, 64, 195).

[70] A. Shelankov, "On the derivation of quasiclassical equations for superconductors", English, J. Low Temp. Phys. **60**, 29–44 (1985) (cit. on pp. 17, 25, 26, 55, 181).

[71] J. Schrieffer, *Theory Of Superconductivity*, Advanced Book Program Series (Avalon Publishing, 1983) (cit. on pp. 17, 77, 171, 175).

[72] P.-G. de Gennes, *Superconductivity of Metals and Alloys*, Advanced book classics (Advanced Book Program, Perseus Books, 1999) (cit. on pp. 17, 171).

[73] M. Tinkham, *Introduction to Superconductivity: Second Edition*, Dover Books on Physics (Dover Publications, 2004) (cit. on pp. 17, 18, 72, 79, 87, 159, 171).

[74] N. N. Bogoljubov, "On a new method in the theory of superconductivity", Il Nuovo Cimento (1955-1965) **7**, 794–805 (1958) (cit. on p. 19).

[75] J. G. Valatin, "Comments on the theory of superconductivity", Il Nuovo Cimento (1955-1965) **7**, 843–857 (1958) (cit. on p. 19).

[76] D. J. Scalapino, Y. Wada, and J. C. Swihart, "Strong-Coupling Superconductor at Nonzero Temperature", Phys. Rev. Lett. **14**, 102–105 (1965) (cit. on p. 19).

[77] J. C. Swihart, D. J. Scalapino, and Y. Wada, "Solution of the Gap Equation for Pb, Hg, and Al", Phys. Rev. Lett. **14**, 106–108 (1965) (cit. on p. 19).

[78] P. Delsing, "Lecture notes: Superconductivity and Low temperature physics", 2017 (cit. on pp. 19, 72, 171).

[79] L. Gor'kov, " On the Energy Spectrum of Superconductors ", Sov. Phys. JETP **7**, 505 (1958), [Zh. Eksp. Teor. Fiz.34,735(1958)] (cit. on p. 22).

[80] M. Eschrig, "Scattering problem in nonequilibrium quasiclassical theory of metals and superconductors: General boundary conditions and applications", Phys. Rev. B **80**, 134511 (2009) (cit. on pp. 23, 25, 26, 29, 181).

[81] T. Matsubara, "A New Approach to Quantum-Statistical Mechanics", Prog. Theor. Phys. **14**, 351–378 (1955) (cit. on pp. 24, 40).

[82] G. Eilenberger, "Transformation of Gorkov's equation for type II superconductors into transport-like equations", Z. Phys. A **214**, 195–213 (1968) (cit. on pp. 25, 26, 65, 67).

[83] A. I. Larkin and Y. N. Ovchinnikov, "Quasiclassical Method in the Theory of Superconductivity", Sov. Phys. JETP **28**, 1200 (1969), [Zh. Eksp. Teor. Fiz. 55, 2262(1969)] (cit. on pp. 25, 26).

[84] M. Eschrig, J. Heym, and D. Rainer, "Corrections to Fermi-liquid theory of correlated metals", J. Low Temp. Phys. **95**, 323–327 (1994) (cit. on p. 25).

[85] M. Eschrig, D. Rainer, and J. A. Sauls, "Effects of strong magnetic fields on pairing fluctuations in high-temperature superconductors", Phys. Rev. B **59**, 12095–12113 (1999) (cit. on p. 25).

[86] J. A. Sauls and M Eschrig, "Vortices in chiral, spin-triplet superconductors and superfluids", New J. Phys. **11**, 075008 (2009) (cit. on pp. 25, 27, 29, 33).

[87] M. Ozana, "Mesoscopic Superconductivity: Quasiclassical Approach", PhD thesis (Umeå University, 2001) (cit. on p. 25).

[88] A. Shelankov and M. Ozana, "Quasiclassical theory of superconductivity: A multiple-interface geometry", Phys. Rev. B **61**, 7077–7100 (2000) (cit. on p. 25).

[89] M. Ozana and A. Shelankov, "Superconductivity in Multiple Interface Geometry: Applicability of Quasiclassical Theory", J. Low Temp. Phys. **124**, 223–243 (2001) (cit. on p. 25).

[90] M. Ozana and A. Shelankov, "Quasiclassical theory of superconductivity: Interfering paths", Phys. Rev. B **65**, 014510 (2001) (cit. on p. 25).

[91] M. Ozana, A. Shelankov, and J. Tobiska, "Bogoliubov–de Gennes versus quasiclassical description of Josephson layered structures", Phys. Rev. B **66**, 054508 (2002) (cit. on p. 25).

[92] R. Grein, T. Löfwander, and M. Eschrig, "Inverse proximity effect and influence of disorder on triplet supercurrents in strongly spin-polarized ferromagnets", Phys. Rev. B **88**, 054502 (2013) (cit. on p. 28).

[93] Y. Nagato, K. Nagai, and J. Hara, "Theory of the Andreev reflection and the density of states in proximity contact normal-superconducting infinite double-layer", J. Low Temp. Phys. **93**, 33–56 (1993) (cit. on p. 29).

[94] N. Schopohl and K. Maki, "Quasiparticle spectrum around a vortex line in a d -wave superconductor", Phys. Rev. B **52**, 490 (1995) (cit. on p. 29).

[95] N. Schopohl, "Transformation of the Eilenberger Equations of Superconductivity to a Scalar Riccati Equation", eprint arXiv:cond-mat/9804064 (1998), eprint: `cond-mat/9804064` (cit. on p. 29).

[96] M. Eschrig, J. A. Sauls, and D. Rainer, "Electromagnetic response of a vortex in layered superconductors", Phys. Rev. B **60**, 10447–10454 (1999) (cit. on p. 29).

[97] M. Eschrig, "Distribution functions in nonequilibrium theory of superconductivity and Andreev spectroscopy in unconventional superconductors", Phys. Rev. B **61**, 9061–9076 (2000) (cit. on pp. 29, 181).

[98] A. B. Vorontsov and J. A. Sauls, "Thermodynamic properties of thin films of superfluid $^3\mathrm{He}-A$", Phys. Rev. B **68**, 064508 (2003) (cit. on pp. 29, 64).

[99] M. Håkansson, *Mesoscopic thin film superconductors - A computational framework* (Institutionen för mikroteknologi och nanovetenskap, Tillämpad kvantfysik, Chalmers tekniska högskola, 2015) (cit. on pp. 31, 33).

[100] Y. Nagai, K. Tanaka, and N. Hayashi, "Quasiclassical numerical method for mesoscopic superconductors: Bound states in a circular d-wave island with a single vortex", Phys. Rev. B **86**, 094526 (2012) (cit. on p. 35).

[101] D. G. Anderson, "Iterative Procedures for Nonlinear Integral Equations", J. ACM **12**, 547–560 (1965) (cit. on p. 38).

[102] H. F. Walker and P. Ni, "Anderson acceleration for fixed-point iterations", SIAM J. Numer. Anal. **49**, 1715–1735 (2011) (cit. on p. 38).

[103] A. Ask, "Modelling the superconducting state in mesoscopic unconventional d-wave superconductors", MA thesis (Gothenburg University, 2015) (cit. on p. 38).

[104] D. Persson, "Charge transport through superconducting nanodevices", PhD thesis (Chalmers University of Technology, 2016) (cit. on p. 38).

[105] O. Ahlén, G. Bohlin, K. Carlsson, M. Gren, P. Holmvall, and P. Säterskog, "GPU Implementation of the Feynman Path-Integral Method in Quantum Mechanics", BA thesis (Chalmers University of Technology, 2011) (cit. on p. 39).

[106] T. Ozaki, "Continued fraction representation of the Fermi-Dirac function for large-scale electronic structure calculations", Phys. Rev. B **75**, 035123 (2007) (cit. on p. 40).

[107] J. Sakurai and J. Napolitano, *Modern Quantum Mechanics* (Addison-Wesley, 2011) (cit. on pp. 46, 57).

[108] A. A. Abrikosov, "On the Magnetic properties of superconductors of the second group", Sov. Phys. JETP **5**, 1174–1182 (1957), [Zh. Eksp. Teor. Fiz.32,1442(1957)] (cit. on p. 53).

[109] R. Feynman, R. Leighton, and M. Sands, *The Feynman Lectures on Physics, Vol. II: The New Millennium Edition: Mainly Electromagnetism and Matter*, Feynman Lectures on Physics (Basic Books, 2011) (cit. on p. 56).

[110] D. Griffiths, *Introduction to Electrodynamics* (Prentice Hall, 1999) (cit. on p. 57).

[111] A. B. Vorontsov, "Lecture notes: Quasiclassics and free energy", 2017 (cit. on p. 64).

[112] J. M. Luttinger and J. C. Ward, "Ground-State Energy of a Many-Fermion System. II", Phys. Rev. **118**, 1417–1427 (1960) (cit. on p. 64).

[113] C. D. Dominicis and P. C. Martin, "Stationary Entropy Principle and Renormalization in Normal and Superfluid Systems. I. Algebraic Formulation", J. Math. Phys. **5**, 14–30 (1964), eprint: https://doi.org/10.1063/1.1704062 (cit. on p. 64).

[114] C. D. Dominicis and P. C. Martin, "Stationary Entropy Principle and Renormalization in Normal and Superfluid Systems. II. Diagrammatic Formulation", J. Math. Phys. **5**, 31–59 (1964), eprint: https://doi.org/10.1063/1.1704064 (cit. on p. 64).

[115] J. D. Jackson, *Classical electrodynamics*, 3rd ed. (Wiley, New York, NY, 1999) (cit. on pp. 68, 159).

[116] V. Schmidt, P. Müller, and A. Ustinov, *The Physics of Superconductors: Introduction to Fundamentals and Applications* (Springer, 1997) (cit. on pp. 71, 72).

[117] D. Schroeder, *An Introduction to Thermal Physics* (Addison Wesley Longman, 2000) (cit. on p. 72).

[118] H. Won and K. Maki, "d", Phys. Rev. B **49**, 1397–1402 (1994) (cit. on p. 79).

[119] J. Srivastava and S. Rao, *Models and Methods of High-Tc Superconductivity: Some Frontal Aspects*, Horizons in world physics v. 2 (Nova Science, 2003) (cit. on p. 82).

[120] A. B. Vorontsov and I. Vekhter, "Unconventional superconductors under a rotating magnetic field. I. Density of states and specific heat", Phys. Rev. B **75**, 224501 (2007) (cit. on pp. 82, 83).

[121] L. F. Chibotaru, A. Ceulemans, V. Bruyndoncx, and V. V. Moshchalkov, "Symmetry-induced formation of antivortices in mesoscopic superconductors", Nature **408**, 833–835 (2000) (cit. on pp. 85, 89).

[122] M. Iavarone, A. Scarfato, F. Bobba, M. Longobardi, G. Karapetrov, V. Novosad, V. Yefremenko, F. Giubileo, and A. M. Cucolo, "Imaging the spontaneous formation of vortex-antivortex pairs in planar superconductor/ferromagnet hybrid structures", Phys. Rev. B **84**, 024506 (2011) (cit. on pp. 85, 89).

[123] C. D. Giorgio, D. D'Agostino, A. M. Cucolo, M. Iavarone, A. Scarfato, G. Karapetrov, S. A. Moore, M. Polichetti, D. Mancusi, S. Pace, V. Novosad, V. Yefremenko, and F. Bobba, "Superconducting Vortex-Antivortex Pairs: Nucleation and Confinement in Magnetically Coupled Superconductor Ferromagnet Hybrids", in *Vortex Dynamics and Optical Vortices*, edited by H. Perez-de Tejada (InTech, Rijeka, 2017) Chap. 03 (cit. on pp. 85, 89).

[124] I. V. Grigorieva, W. Escoffier, J. Richardson, L. Y. Vinnikov, S. Dubonos, and V. Oboznov, "Direct Observation of Vortex Shells and Magic Numbers in Mesoscopic Superconducting Disks", Phys. Rev. Lett. **96**, 077005 (2006) (cit. on pp. 85, 89).

[125] H. J. Zhao, V. R. Misko, F. M. Peeters, V. Oboznov, S. V. Dubonos, and I. V. Grigorieva, "Vortex states in mesoscopic superconducting squares: Formation of vortex shells", Phys. Rev. B **78**, 104517 (2008) (cit. on pp. 85, 89).

[126] H. J. Zhao, V. R. Misko, F. M. Peeters, S. Dubonos, V. Oboznov, and I. V. Grigorieva, "Vortex configurations in mesoscopic superconducting triangles: Finite-size and shape effects", Europhys. Lett. **83**, 17008 (2008) (cit. on pp. 85, 89).

[127] W. Wu, H. J. Zhao, B Li, and Z. X. Shi, "Finite-size and shape effects on vortex configurations in superconducting isosceles right triangles", Supercond. Sci. Technol. **30**, 125004 (2017) (cit. on pp. 85, 89).

[128] C. Caroli, P. D. Gennes, and J. Matricon, "Bound Fermion states on a vortex line in a type II superconductor", Physics Letters **9**, 307 –309 (1964) (cit. on p. 85).

[129] C Kallin and A. J. Berlinsky, "Is Sr_2RuO_4 a chiral p-wave superconductor?", J. Phys. Condens. Matter **21**, 164210 (2009) (cit. on pp. 85, 98, 100, 189).

[130] C. Kallin, "Chiral p-wave order in Sr_2RuO_4", Rep. Prog. Phys. **75**, 042501 (2012) (cit. on pp. 85, 98, 100, 189).

[131] Y. Maeno, S. Kittaka, T. Nomura, S. Yonezawa, and K. Ishida, "Evaluation of Spin-Triplet Superconductivity in Sr2RuO4", J. Soc. Phys. Jpn. **81**, 011009 (2012) (cit. on pp. 85, 100).

[132] D. Rainer, J. A. Sauls, and D. Waxman, "Current carried by bound states of a superconducting vortex", Phys. Rev. B **54**, 10094–10106 (1996) (cit. on p. 89).

[133] P. Fulde and R. A. Ferrell, "Superconductivity in a Strong Spin-Exchange Field", Phys. Rev. **135**, A550–A563 (1964) (cit. on p. 108).

[134] A. I. Larkin and I. U. N. Ovchinnikov, "Inhomogeneous state of superconductors", Sov. Phys. JETP **20**, 762–769 (1965) (cit. on p. 108).

[135] K. Maki, "Effect of Pauli Paramagnetism on Magnetic Properties of High-Field Superconductors", Phys. Rev. **148**, 362–369 (1966) (cit. on p. 108).

[136] W. Zhang, J. Kurkijärvi, and E. V. Thuneberg, "Order parameter of superfluid ^3B near surfaces", Phys. Rev. B **36**, 1987–1995 (1987) (cit. on p. 120).

[137] A. B. Vorontsov and J. A. Sauls, "Crystalline Order in Superfluid ^{3}He Films", Phys. Rev. Lett. **98**, 045301 (2007) (cit. on p. 120).

[138] K. Nagai, Y. Nagato, M. Yamamoto, and S. Higashitani, "Surface Bound States in Superfluid 3He", J. Soc. Phys. Jpn. **77**, 111003 (2008) (cit. on p. 120).

[139] E. V. Thuneberg and T. H. Virtanen, "Fermi-liquid theory of Fermi–Bose mixtures", Phys. Rev. B **83**, 245137 (2011) (cit. on p. 120).

[140] T. Mizushima, Y. Tsutsumi, T. Kawakami, M. Sato, M. Ichioka, and K. Machida, "Symmetry-Protected Topological Superfluids and Superconductors - From the Basics to 3He", J. Soc. Phys. Jpn. **85**, 022001 (2016) (cit. on p. 120).

[141] A. M. Mounce, S. Oh, and W. P. Halperin, "Nuclear magnetic resonance studies of vortices in high temperature superconductors", Front. Phys. **6**, 450–462 (2011) (cit. on p. 145).

[142] J. A. Lee, Y. Xin, I. Stolt, W. P. Halperin, A. P. Reyes, P. L. Kuhns, and M. K. Chan, "Magnetic-field-induced vortex-lattice transition in $HgBa_2CuO_{4+\delta}$", Phys. Rev. B **95**, 024512 (2017) (cit. on p. 145).

[143] H. Saadaoui, G. D. Morris, Z. Salman, Q. Song, K. H. Chow, M. D. Hossain, C. D. P. Levy, T. J. Parolin, M. R. Pearson, M. Smadella, D. Wang, L. H. Greene, P. J. Hentges, R. F. Kiefl, and W. A. MacFarlane, "Search for broken time-reversal symmetry near the surface of superconducting $YBa_2Cu_3O_{7-\delta}$ films using β-detected nuclear magnetic resonance", Phys. Rev. B **83**, 054504 (2011) (cit. on p. 145).

[144] D. Vasyukov, Y. Anahory, L. Embon, D. Halbertal, J. Cuppens, L. Neeman, A. Finkler, Y. Segev, Y. Myasoedov, M. L. Rappaport, M. E. Huber, and E. Zeldov, "A scanning superconducting quantum interference device with single electron spin sensitivity", Nat. Nanotechnol. **8**, 639–644 (2013) (cit. on p. 152).

[145] M. Pelliccione, A. Jenkins, P. Ovartchaiyapong, C. Reetz, E. Emmanouilidou, N. Ni, and A. C. Bleszynski Jayich, "Scanned probe imaging of nanoscale magnetism at cryogenic temperatures with a single-spin quantum sensor", Nat. Nanotechnol. **11**, 700–705 (2016) (cit. on p. 152).

[146] G. J. C. van Baarle, A. M. Troianovski, T. Nishizaki, P. H. Kes, and J. Aarts, "Imaging of vortex configurations in thin films by scanning-tunneling microscopy", Appl. Phys. Lett. **82**, 1081–1083 (2003) (cit. on p. 152).

[147] Y. Noat, V. Cherkez, C. Brun, T. Cren, C. Carbillet, F. Debontridder, K. Ilin, M. Siegel, A. Semenov, H.-W. Hübers, and D. Roditchev, "Unconventional superconductivity in ultrathin superconducting NbN films studied by scanning tunneling spectroscopy", Phys. Rev. B **88**, 014503, 014503 (2013) (cit. on p. 152).

[148] C. Carbillet, S. Caprara, M. Grilli, C. Brun, T. Cren, F. Debontridder, B. Vignolle, W. Tabis, D. Demaille, L. Largeau, K. Ilin, M. Siegel, D. Roditchev, and B. Leridon, "Confinement of superconducting fluctuations due to emergent electronic inhomogeneities", Phys. Rev. B **93**, 144509 (2016) (cit. on p. 152).

[149] D. Rugar, R. Budakian, H. Mamin, and B. Chui, "Single spin detection by magnetic resonance force microscopy", Nature **430**, 329–332 (2004) (cit. on p. 152).

[150] N. Wennerdal, "Theory of Surface Spectroscopy for Noncentrosymmetric Superconductors", PhD thesis (Royal Holloway, University of London, 2016) (cit. on p. 181).

[151] K. Ishida, H. Mukuda, Y. Kitaoka, K. Asayama, Z. Q. Mao, Y. Mori, and Y. Maeno, "Spin-triplet superconductivity in Sr_2RuO_4 identified by ^{17}O Knight shift", Nature **396**, 658–660 (1998) (cit. on p. 189).

[152] M. Fogelström, "Structure of the core of magnetic vortices in *d*-wave superconductors with a subdominant triplet pairing mechanism", Phys. Rev. B **84**, 064530 (2011) (cit. on p. 193).

Appended Papers

Paper I

Spontaneously broken translational symmetry at edges of high-temperature superconductors: thermodynamics in magnetic field

P. Holmvall,[1,*] A. B. Vorontsov,[2,†] M. Fogelström,[1,‡] and T. Löfwander[1,§]

[1] *Department of Microtechnology and Nanoscience - MC2, Chalmers University of Technology, SE-41296 Göteborg, Sweden*

[2] *Department of Physics, Montana State University, Montana 59717, USA*

(Dated: November 22, 2017)

We investigate equilibrium properties, including structure of the order parameter, superflow patterns, and thermodynamics of low-temperature surface phases of layered $d_{x^2-y^2}$-wave superconductors in magnetic field. At zero external magnetic field, time-reversal symmetry and continuous translational symmetry along the edge are broken spontaneously in a second order phase transition at a temperature $T^* \approx 0.18T_c$, where T_c is the superconducting transition temperature. At the phase transition there is a jump in the specific heat that scales with the ratio between the edge length D and layer area $\mathcal{A}$ as $(D\xi_0/\mathcal{A})\Delta C_d$, where ΔC_d is the jump in the specific heat at the d-wave superconducting transition and ξ_0 is the superconducting coherence length. The phase with broken symmetry is characterized by a gauge invariant superfluid momentum $\boldsymbol{p}_s$ that forms a non-trivial planar vector field with a chain of sources and sinks along the edges with a period of approximately $12\xi_0$, and saddle point disclinations in the interior. To find out the relative importance of time-reversal and translational symmetry breaking we apply an external field that breaks time-reversal symmetry explicitly. We find that the phase transition into the state with the non-trivial $\boldsymbol{p}_s$ vector field keeps its main signatures, and is still of second order. In the external field, the saddle point disclinations are pushed towards the edges, and thereby a chain of edge motifs are formed, where each motif contains a source, a sink, and a saddle point. Due to a competing paramagnetic response at the edges, the phase transition temperature T^* is slowly suppressed with increasing magnetic field strength, but the phase with broken symmetry survives into the mixed state.

I. INTRODUCTION

Superconducting devices are often experimentally realized as thin-film circuits or hybrid structures operating in the mesoscopic regime.[1–4] At this length-scale, where the size of circuit elements become comparable with the superconducting coherence length, the nature of the superconducting state may be dictated by various finite-size or surface/interface effects[5]. This holds true in particular for unconventional superconductors, such as the high-temperature superconductors with an order parameter of $d_{x^2-y^2}$ symmetry that changes sign around the Fermi surface. Scattering at surfaces, or any defect, then leads to substantial pair breaking and formation of Andreev states with energies within the superconducting gap[6,7]. Today, the material control of high-temperature superconducting films is sufficiently good that many advanced superconducting devices can work at elevated temperatures[8,9]. This raises the question how the specific surface physics of d-wave superconductors influence devices.

From a theory point of view, the physics at specular pair-breaking surfaces of d-wave superconductors is rich and interesting. The reason is the formation of zero-energy (midgap) Andreev states due to the sign change of the d-wave order parameter for quasiparticles scattered at the surface[6,7,10]. In modern terms, there is a flat band of spin-degenerate zero-energy surface states as function of the parallel component of the momentum, $p_{||}$, which is a good quantum number for a specular surface. The large spectral weight of these states exactly at zero energy (i.e. at the Fermi energy), is energetically unfavorable. Different scenarios have been proposed, within which there is a low-temperature instability and a phase transition into a time-reversal symmetry broken phase where the flat band is split to finite energies, thus lowering the free energy of the system. One scenario is presence of a subdominant pairing interaction and appearance of another order parameter component $\pi/2$ out of phase with the dominant one[11–14], for instance a subdominant s-wave resulting in an order parameter combination $\Delta_d + i\Delta_s$. The phase transition is driven by a split of the flat band of Andreev states to $\pm\Delta_s$. The split Andreev states carry current along the surface, which results in a magnetic field that is screened from the bulk. In a second scenario, exchange interactions drive a ferromagnetic transition at the edge where the flat Andreev band is instead spin split[15,16]. A third scenario involves spontaneous appearance of supercurrents[17–19] that Doppler shifts the Andreev states and thereby lowers the free energy. This scenario involves coupling of the electrons to the electromagnetic gauge field $\boldsymbol{A}(\boldsymbol{R})$, and was first considered theoretically for a translationally invariant edge. In this case the transition is a result of the interplay of weakly Doppler shifted surface bound states, decaying away from the surface on the scale of the superconducting coherence length ξ_0, and weak diamagnetic screening currents, decaying on the scale of the penetration depth λ. The resulting transition temperature is very low, of order $T^* \sim (\xi_0/\lambda)T_c$, where T_c is the d-wave superconducting transition temperature. Later, the transition temperature was shown to be enhanced in a film geometry[20–24] where two par-

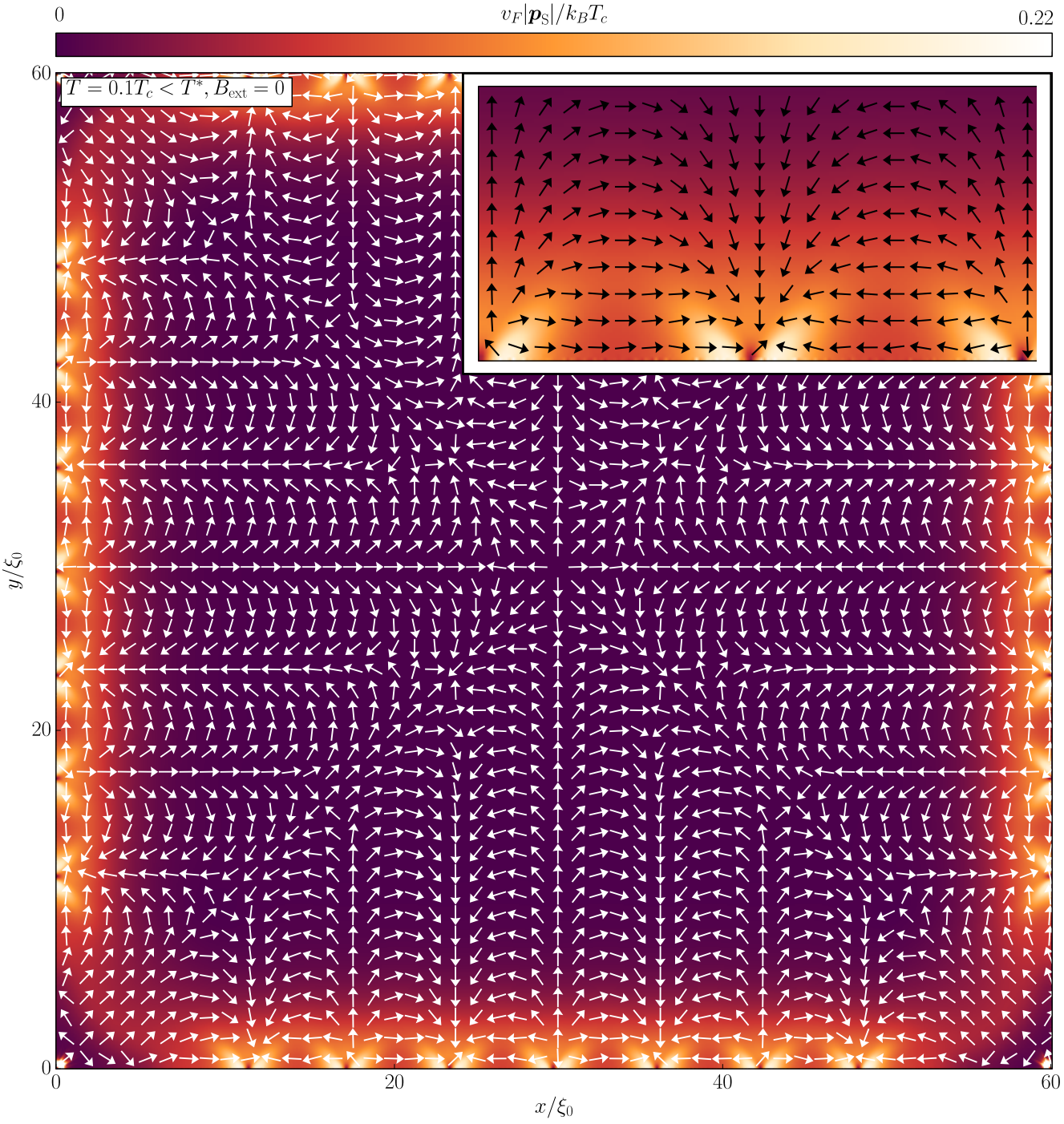

FIG. 1. For $B_{ext} = 0$, the superfluid momentum $\boldsymbol{p}_s$ forms a non-trivial planar vector field with a regular chain of sources and sinks along the edge (each with winding number $n = 1/2$), thereby breaking continuous translational symmetry along the edge. Matching saddle point disclinations with winding number $n = -1$ are formed in the interior, along the grain diagonals. Because of the particular grain geometry, four edge sources at the middle of the sides and four corner sources plus an $n = 1$ source in the center are matched by four saddle points near the grain center. The temperature is $T = 0.1T_c$, which is well below T^*. As a consequence, the splay patterns are rather stiff, leading to triangular shapes near the edges. The stiffness is clear from the magnitude variation shown in colorscale and in the inset.

allel pair breaking edges are separated by a distance of the order of a few coherence lengths. The suppression of the order parameter between the pairbreaking edges can be viewed as an effective Zeeman field that splits the Andreev states and enhances the transition temperature. The mechanism does not involve subdominant channels or coupling to magnetic field, but depends on film thickness D, and the transition temperature decays rapidly with increasing thickness as $T^* \sim (\xi_0/D)T_c$. In this paper we consider a modified scenario[25,26] where spontaneous supercurrents also break translational symmetry along the edge. This scenario too does not rely on any additional interaction term in the Hamiltonian. Instead, as we will discuss below, it relies on the development of a texture in the gradient of the d-wave order parameter phase χ, or more precisely in the gauge invariant superfluid momentum

$$\boldsymbol{p}_s(\boldsymbol{R}) = \frac{\hbar}{2}\nabla\chi(\boldsymbol{R}) - \frac{e}{c}\boldsymbol{A}(\boldsymbol{R}), \tag{1}$$

where $\hbar$ is Planck's constant, e the charge of the electron, c the speed of light, and $\boldsymbol{A}$ the vector potential. This superfluid momentum spontaneously takes the form of a planar vector field with a chain of sources and sinks along the edge and saddle point disclinations in the grain interior, see Fig. 1. The free energy is lowered by a large split of the flat band of Andreev states by a Doppler shift $\boldsymbol{v}_F \cdot \boldsymbol{p}_s$, where $\boldsymbol{v}_F$ is the Fermi velocity. This free energy gain is maximized by maximizing the magnitude of $\boldsymbol{p}_s$, which is achieved by the peculiar vector field in Fig. 1. The balance of the Doppler shift gain and the energy cost in the disclinations with $\nabla \times \boldsymbol{p}_s \neq 0$ and the splay patterns between them leads to a high $T^* \approx 0.18T_c$. The inhomogeneous vector field induces a chain of loop-currents at the edge circulating clockwise and anti-clockwise. The induced magnetic fluxes of each loop are a fraction of the flux quantum and forms a chain of fluxes with alternating signs along the edge. In this paper we study the thermodynamics of this phase in more depth and investigate the influence of an external magnetic field, explicitly breaking time-reversal symmetry. As we shall see, in the external magnetic field, the phase transition is still of second order and is still characterized by the non-trivial vector field $\boldsymbol{p}_s(\boldsymbol{R})$ breaking continuous translational symmetry along the edge.

Which of these outlined scenarios wins will ultimately depend on material properties of a specific high-temperature superconducting sample, or material properties of other candidate d-wave superconductors, e.g. FeSe. In the third scenario, studied in Ref. 25 and 26 and in this paper, the resulting transition temperature is large, $T^* \sim 0.18T_c$. It means that the interaction terms in the Hamiltonian for the other scenarios would have to be sufficiently large in order to compete. It is even possible that one or another scenario wins in different parts of the material's phase diagram[15].

From an experimental point of view, the surface physics of d-wave superconductors is complicated by for instance surface roughness, inhomogeneous stoichiometry, and presence of impurities. The formation of a band of Andreev states centered at zero energy is well established by numerous tunnelling experiments, in agreement with the expectation for d-wave symmetry of the order parameter, as reviewed in Refs. 6 and 7. One consistent experimental result is that the band is typically quite broad, with a width that saturates at low temperature. On the other hand, the establishment of a time-reversal symmetry breaking phase remains under discussion, see for instance Refs. 27 and 28. Several tunneling experiments on YBCO[29–31] show a split of the zero-bias conductance peak, while others do not[32,33]. Other probes indicating time-reversal symmetry breaking include thermal conductivity[34], Coulomb blockade in nanoscale islands[5], and STM tunneling at grain boundaries in FeSe[35].

As we argued in Refs. 25 and 26 within the scenario with spontaneous loop currents, the split of the Andreev band might be difficult to resolve in a tunneling experiment because of the broken translational symmetry along the edge and associated variations in the superflow field. This leads to a smearing effect for tunnel contacts with an area larger than the coherence length and an expected wide, largely temperature-independent, peak centered at zero energy. In fact, this would be consistent with most tunneling experiments. With an eye to inspire a new generation of experiments, we present results for the interplay between an external magnetic field, that induces screening supercurrents, and the phase transition at T^* into a state with the spontaneous loop currents at the edges. After a brief overview in Section II of the quasiclassical formalism that we use, we will in Section III present results that show this interplay from different points of view. First, we will show the spontaneous currents and induced magnetic fields and relate them to the disclinations in the superfluid momentum; second, we study the magnetic field dependent thermodynamics of the phase transition. Finally in Section IV, we summarize our results and provide an outlook.

II. THEORETICAL MODEL

Our aim is to investigate the ground state of clean mesoscopic d-wave superconducting grains in an external magnetic field applied perpendicular to the crystal ab-plane, as shown in Fig. 2. As a typical geometry we consider a square grain with sidelengths $D = 60\xi_0$, where $\xi_0 = \hbar v_F/(2\pi k_B T_c)$ is the zero-temperature superconducting coherence length. Here, v_F is the normal state Fermi velocity, and k_B the Boltzmann constant. The sides of the system are assumed to be misaligned by a 45° rotation with respect to the crystal ab-axes, inducing maximal pair-breaking at the edges.

The external field is directed perpendicular to the xy-plane,

$$\boldsymbol{B}_{\rm ext} = -B_{\rm ext}\hat{\boldsymbol{z}} \parallel \hat{\boldsymbol{c}}. \tag{2}$$

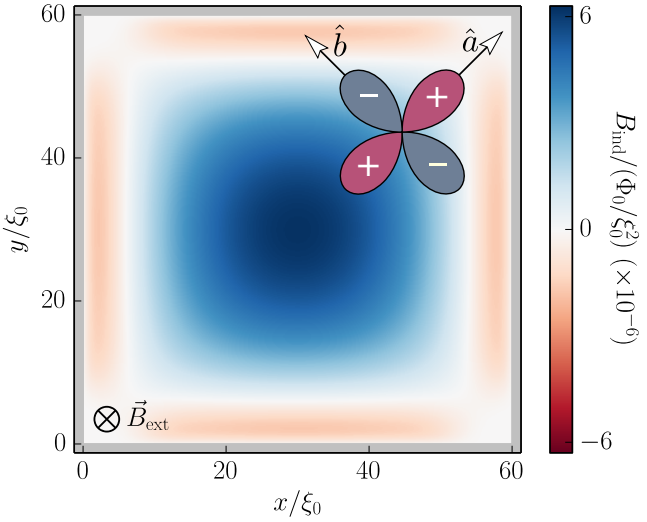

FIG. 2. (Color online) The system consists of a d-wave superconducting grain exposed to an external magnetic field $\boldsymbol{B}_{\rm ext} = -B_{\rm ext}\hat{\boldsymbol{z}}$. The crystal ab-axes are rotated 45° relative to the grain edges, inducing pair-breaking at the edges of the system. The color scale shows the magnetic field $B_{\rm ind}$ induced in response to an external field of size $B_{\rm ext} = \Phi_0/2\mathcal{A}$ at a temperature $T = 0.2T_c$. There is a diamagnetic response carried by the condensate in the interior, and a paramagnetic response carried by mid-gap surface Andreev states at the edges.

We shall consider rather small external fields, and will use a field scale $B_{g1} = \Phi_0/\mathcal{A}$, corresponding to one flux quantum threading the grain of area $\mathcal{A} = D^2 = 60\xi_0 \times 60\xi_0$. The flux quantum $\Phi_0 = hc/(2|e|)$ is given in Gaussian CGS units. The field B_{g1} is larger than the lower critical field $B_{c1} \propto \Phi_0/\lambda_0^2$, where vortices can enter a macroscopically large superconductor, since the grain side length is smaller than the penetration depth. We assume that $\lambda_0 = 100\xi_0$, relevant for YBCO). The upper critical field $B_{c2} \propto \Phi/\xi_0^2$ is much larger than any field we include in this study. To be precise, we parameterize the field strength as

$$B_{\rm ext} = bB_{g1}, \;\; B_{g1} \equiv \frac{\Phi_0}{\mathcal{A}}, \tag{3}$$

and will consider $b \in [0, 1.5]$.

A. Quasiclassical theory

We utilize the quasiclassical theory of superconductivity[36–38], which is a theory based on a separation of scales[39–42]. For instance the atomic scale is assumed small compared with the superconducting coherence length, $\hbar/p_F \ll \xi_0$. This separation of scales makes it possible to systematically expand all quantities in small parameters such as $\hbar/p_F\xi_0$, Δ/ϵ_F, and k_BT_c/ϵ_F, where Δ is the superconducting order parameter, p_F is the Fermi momentum, and ϵ_F is the Fermi energy. In equilibrium, the central object of the theory is the quasiclassical Green's function $\hat{g}(\boldsymbol{p}_F, \boldsymbol{R}; z)$, which is a function of quasiparticle momentum on the Fermi surface $\boldsymbol{p}_F$, the quasiparticle center-of-mass coordinate $\boldsymbol{R}$, and the quasiparticle energy z. The latter is real $z = \epsilon + i0^+$ with an infinitesimal imaginary part $i0^+$ for the retarded Green's function, or an imaginary Matsubara energy $z = i\epsilon_n = i\pi k_BT(2n+1)$ in the Matsubara technique (n is an integer). To keep the notation compact, the dependence on the parameters $\boldsymbol{p}_F$, $\boldsymbol{R}$, and z will often not be written out. The *hat* on $\hat{g}$ denotes Nambu (electron-hole) space

$$\hat{g} = \begin{pmatrix} g & f \\ -\tilde{f} & \tilde{g} \end{pmatrix}, \tag{4}$$

where g and f are the quasiparticle and pair propagators, respectively. The tilde operation denotes particle-hole conjugation

$$\tilde{\alpha}(\boldsymbol{p}_F, \boldsymbol{R}; z) = \alpha^*(-\boldsymbol{p}_F, \boldsymbol{R}; -z^*). \tag{5}$$

The quasiclassical Green's function is parameterized in terms of two scalar coherence functions, $\gamma(\boldsymbol{p}_F, \boldsymbol{R}; z)$ and $\tilde{\gamma}(\boldsymbol{p}_F, \boldsymbol{R}; z)$, as[43–49]

$$\hat{g} = -\frac{i\pi}{1+\gamma\tilde{\gamma}} \begin{pmatrix} 1-\gamma\tilde{\gamma} & 2\gamma \\ 2\tilde{\gamma} & -1+\gamma\tilde{\gamma} \end{pmatrix}. \tag{6}$$

Note that with this parameterization, the Green's function is automatically normalized to $\hat{g}^2 = -\pi^2$. The coherence functions obey two Riccati equations

$$(i\hbar\boldsymbol{v}_F \cdot \boldsymbol{\nabla} + 2z + 2\frac{e}{c}\boldsymbol{v}_F \cdot \boldsymbol{A})\gamma = -\tilde{\Delta}\gamma^2 - \Delta, \tag{7}$$

$$(i\hbar\boldsymbol{v}_F \cdot \boldsymbol{\nabla} - 2z - 2\frac{e}{c}\boldsymbol{v}_F \cdot \boldsymbol{A})\tilde{\gamma} = -\Delta\tilde{\gamma}^2 - \tilde{\Delta}, \tag{8}$$

where $\boldsymbol{A}$ is the vector potential. These first order nonlinear differential equations are solved by integration along straight (ballistic) quasiparticle trajectories. Quantum coherence is retained along these trajectories, but not between neighboring trajectories. A clean superconducting grain in vacuum is assumed by imposing the boundary condition of perfect specular reflection of quasiparticles along the edges of the system.

The superconducting order parameter is assumed to have pure d-wave symmetry

$$\Delta(\boldsymbol{p}_F, \boldsymbol{R}) = \Delta_d(\boldsymbol{R})\eta_d(\theta), \tag{9}$$

where θ is the angle between the Fermi momentum $\boldsymbol{p}_F$ and the crystal $\hat{\mathbf{a}}$-axis, and $\eta_d(\theta)$ is the d-wave basis function

$$\eta_d(\theta) = \sqrt{2}\cos(2\theta), \tag{10}$$

fulfilling the normalization condition

$$\int \frac{d\theta}{2\pi} |\eta_d(\theta)|^2 = 1. \tag{11}$$

The order parameter amplitude satisfies the gap equation

$$\Delta_d(\boldsymbol{R}) = \lambda_d N_F k_B T \sum_{|\epsilon_n|\leq\Omega_c} \int \frac{d\theta}{2\pi} \eta_d^*(\theta) f(\boldsymbol{p}_F, \boldsymbol{R}; \epsilon_n), \tag{12}$$

where λ_d is the pairing interaction, N_F is the density of states at the Fermi level in the normal state, and Ω_c is a cutoff energy. The pairing interaction and the cutoff energy are eliminated in favor of the superconducting transition temperature T_c (see for example Ref. 50) as

$$\frac{1}{\lambda_d N_F} = \ln \frac{T}{T_c} + \sum_{n\geq 0} \frac{1}{n+\frac{1}{2}}. \tag{13}$$

The above equations are solved self-consistently with respect to γ, $\tilde{\gamma}$, and Δ_d. As an initial condition, a homogeneous superconductor is assumed at the start of the trajectories. Along the trajectory and after a few self-consistent iterations, the information of the initial condition is lost[51].

We choose an electromagnetic gauge where the vector potential has the form

$$\boldsymbol{A}_{\rm ext}(\boldsymbol{R}) = \frac{1}{2}\boldsymbol{B}_{\rm ext} \times \boldsymbol{R}. \tag{14}$$

The total vector potential $\boldsymbol{A}(\boldsymbol{R})$, that enters Eqs. (7)-(8), is given by $\boldsymbol{A}_{\rm ext}(\boldsymbol{R})$ and the field $\boldsymbol{A}_{\rm ind}(\boldsymbol{R})$ induced by the currents $\boldsymbol{j}(\boldsymbol{R})$ in the superconductor [Eq.(21) below]:

$$\boldsymbol{A}(\boldsymbol{R}) = \boldsymbol{A}_{\rm ext}(\boldsymbol{R}) + \boldsymbol{A}_{\rm ind}(\boldsymbol{R}). \tag{15}$$

The vector potential $\boldsymbol{A}_{\rm ind}(\boldsymbol{R})$ should be solved from Ampère's circuit law

$$\boldsymbol{\nabla} \times \boldsymbol{\nabla} \times \boldsymbol{A}_{\rm ind}(\boldsymbol{R}) = \frac{4\pi}{c}\boldsymbol{j}(\boldsymbol{R}). \tag{16}$$

To take the full electrodynamics into account, $A_{\rm ind}(\boldsymbol{R})$ also needs to be computed self-consistently in each iteration. However, the strength of the electrodynamic back-coupling scales as κ^{-2}, where $\kappa \equiv \lambda_0/\xi_0$ is the dimensionless Ginzburg-Landau parameter. The electrodynamic back-coupling can therefore safely be neglected for type II superconductors (typically $\kappa^{-1} \approx 10^{-2}$ for the cuprates).

The induced magnetic flux density is computed as

$$\boldsymbol{B}_{\rm ind} = \boldsymbol{\nabla} \times \boldsymbol{A}_{\rm ind}. \tag{17}$$

We shall neglect the problem of the field distribution around the superconductor and focus on the field induced at the ab-plane where we have simply $\boldsymbol{B}_{\rm ind} = B_{\rm ind}\hat{\boldsymbol{z}}$.

B. Gauge transformation

Once the Green's function and the order parameter have been determined self-consistently, we can perform a gauge transformation in order to make the order parameter a real quantity and in the process extract the superfluid momentum $\boldsymbol{p}_s$. This can be illustrated by transforming the Riccati equation in Eq. (7). To begin with, the self-consistently obtained order parameter is complex, i.e.

$$\Delta(\boldsymbol{p}_F, \boldsymbol{R}) = |\Delta_d(\boldsymbol{R})|\eta_d(\theta)\, e^{i\chi(\boldsymbol{R})}. \tag{18}$$

We make the ansatz

$$\gamma(\boldsymbol{p}_F, \boldsymbol{R}; z) = \gamma_0(\boldsymbol{p}_F, \boldsymbol{R}; z)\, e^{i\chi(\boldsymbol{R})}, \tag{19}$$

and put that into the Riccati equation. We obtain

$$\left[i\hbar\boldsymbol{v}_F \cdot \boldsymbol{\nabla} + 2(z - \boldsymbol{v}_F \cdot \boldsymbol{p}_s)\right]\gamma_0 = -|\Delta_d|\eta_d(\gamma_0^2 + 1), \tag{20}$$

where $\boldsymbol{p}_s$ is defined in Eq. (1).

C. Observables

The current density is computed within the Matsubara technique through the formula

$$\boldsymbol{j}(\boldsymbol{R}) = 2\pi e N_F k_B T \sum_{\epsilon_n} \int \frac{d\theta}{2\pi} \boldsymbol{v}_F g(\boldsymbol{p}_F, \boldsymbol{R}; \epsilon_n). \tag{21}$$

In the results section we shall show this current density in units of the depairing current

$$j_d \equiv 4\pi|e|k_B T_c N_F v_F. \tag{22}$$

The free-energy difference between the superconducting and the normal states is calculated with the Eilenberger free-energy functional[36]

$$\Omega_S(B,T) - \Omega_N(B,T) = \int d\boldsymbol{R} \left\{ \frac{\boldsymbol{B}_{\rm ind}(\boldsymbol{R})^2}{8\pi} + |\Delta(\boldsymbol{R})|^2 N_F \ln\frac{T}{T_c} + 2\pi N_F k_B T \sum_{\epsilon_n>0} \left[\frac{|\Delta(\boldsymbol{R})|^2}{\epsilon_n} + i\mathcal{I}(\boldsymbol{R};\epsilon_n) \right] \right\}, \tag{23}$$

$$\mathcal{I}(\boldsymbol{R},\epsilon_n) = \int \frac{d\theta}{2\pi} \left[\tilde{\Delta}(\boldsymbol{p}_F,\boldsymbol{R})\gamma(\boldsymbol{p}_F,\boldsymbol{R};\epsilon_n) - \Delta\tilde{\gamma}(\boldsymbol{p}_F,\boldsymbol{R};\epsilon_n) \right]. \tag{24}$$

We have verified that this form of the free energy give the same results as the Luttinger-Ward functional[25,39,48].

The entropy and specific heat capacity are obtained from the thermodynamic definitions

$$S = -\frac{\partial \Omega}{\partial T}, \tag{25}$$

$$C = T\frac{\partial S}{\partial T} = -T\frac{\partial^2 \Omega}{\partial T^2}. \tag{26}$$

III. RESULTS

In Fig. 3 we show the influence of a rather weak external magnetic field, $B = 0.5B_{g1}$, applied to the d-wave superconducting grain with pair breaking edges for varying temperature near the phase transition temperature T^*. The left and right columns show the currents and the magnetic field densities, respectively, induced in response to the applied field. To be concrete we discuss a few selected sets of model parameters, as listed in Table I. First, for $T > T^*$ (parameter set I), the expected diamagnetic response of the condensate in the inner part of the grain is present, see Fig. 3(a) and Fig. 3(e). On the other hand, midgap quasiparticle Andreev surface states respond paramagnetically. This situation is well established theoretically and experimentally through measurements of the competition between the diamagnetic and paramagnetic responses seen as a low-temperature upturn in the penetration depth[52]. Upon lowering the temperature to $T \gtrsim T^*$ (parameter set II), see Fig. 3(b) and Fig. 3(f), the paramagnetic response at the edge becomes locally suppressed and enhanced, forming a sequence of local minima and maxima in the induced currents and fields. The bulk response is on the other hand relatively unaffected. Finally, as $T < T^*$ (parameter set III), see Fig. 3(c) and Fig. 3(g), the regions of minum current turns into regions with reversed currents. The resulting loop currents with clock-wise and anti-clockwise circulations induces magnetic fluxes along the surface with opposite signs between neighboring fluxes. The situation for $T < T^*$ in an external magnetic field can be compared with the one in zero magnetic field displayed in Fig. 3(d) and Fig. 3(h), and also discussed before in Ref. 25. In the presence of the magnetic field, there is an imbalance between positive and negative fluxes, while in zero external magnetic field, the total induced flux integrated over the grain area is zero.

Let us quantify the symmetry broken phase in a magnetic field by plotting the superfluid momentum defined in Eq. (1), see Fig. 4. For $T \gtrsim T^*$ (parameter set II), the amplitude of $\mathbf{p}_s$ varies along the edge (coordinate x), see Fig. 4(a), reflecting the varying paramagnetic response in Fig. 3(b) and Fig. 3(f). For $T < T^*$ (parameter set III), sources and sinks have appeared pairwise together with a saddle point disclination, see Fig. 4(b). The left disclinations in the figure are not well developed because of the proximity to the corner. Finally, in Fig. 4(c), we show the vector field at a lower temperature when the chain of sources, sinks, and saddle points are well established and the magnitude of $\mathbf{p}_s$ is large, much larger than in the interior part of the grain still experiencing diamagnetism. In a magnetic field, the vector field far from the surface has a preferred direction reflecting the diamagnetic response of the interior grain. This shifts the sources and sinks along the surface, as compared with the regular chain for zero field in Fig. 1, and moves the saddle points to the surface region.

From a vector field perspective,[53,54] the edge sources and sinks each have a Poincaré index (winding number) of $n = 1/2$. It is not $n = 1$ because they lie exactly on the edge. On the other hand, the saddle point has index $n = -1$. Thus, a motif with one edge source, one edge sink, and one saddle point sum up to zero and annihilate at T^*. In the same fashion, increasing the magnetic field strength, the motif gets smaller as the disclinations are forced towards each other to match the superflow in the bulk. However, the magnitude of $\boldsymbol{p}_s$ near the surface due to Meissner screening of the bulk is not large enough to force an annihilation of the motifs. The broken symmetry phase therefore survives the application of an external magnetic field within the whole Meissner state, $b \in [0, 1]$.

In Fig. 5 we show the superfluid momentum for a higher field $B_{\rm ext} = 1.5B_{g1}$, in the mixed state where an Abrikosov vortex resides in the grain center. We find that also in this case the phase with edge loop currents survives. For higher fields, more vortices enter the grain (not shown), still keeping the edge phase intact. However, the exact configuration of Abrikosov vortices becomes geometry dependent and the free energy landscape is very flat. Therefore, the full investigation of the geometry dependent phase diagram for very large fields is beyond the scope of this paper.

Let us investigate further how the currents and magnetic fields are induced at T^*. As we have seen, the paramagnetic response and the spontaneously appearing edge loop currents compete, as they both lead to shifts of midgap Andreev states. As the temperature is lowered, the strength of the paramagnetic response increases slowly and linearly, while the strength of the loop currents increases highly non-linearly. This is illustrated in Fig. 6, by plotting the area-averaged current magnitude

$$\bar{j} = \frac{1}{\mathcal{A}} \int d^2R\, |\boldsymbol{j}(\boldsymbol{R})|, \tag{27}$$

as a function of temperature for the cases when $B_{\rm ext} = 0$ (solid line), $B_{\rm ext} = 0.5B_{g1}$ (dashed line), and for comparison also for a system without pair-breaking edges

Set	Temperature	External magnetic field
(I)	$T = 0.182T_c > T^*$	$B_{\rm ext} = 0.5B_{g1}$
(II)	$T = 0.176T_c \gtrsim T^*$	$B_{\rm ext} = 0.5B_{g1}$
(III)	$T = 0.17T_c < T^*$	$B_{\rm ext} = 0.5B_{g1}$
(IV)	$T = 0.17T_c < T^*$	$B_{\rm ext} = 0$

TABLE I. Sets of parameters used for presenting results. The field scale $B_{g1} = \Phi_0/\mathcal{A}$ corresponds to an external magnetic flux through the grain area exactly equal to one flux quantum.

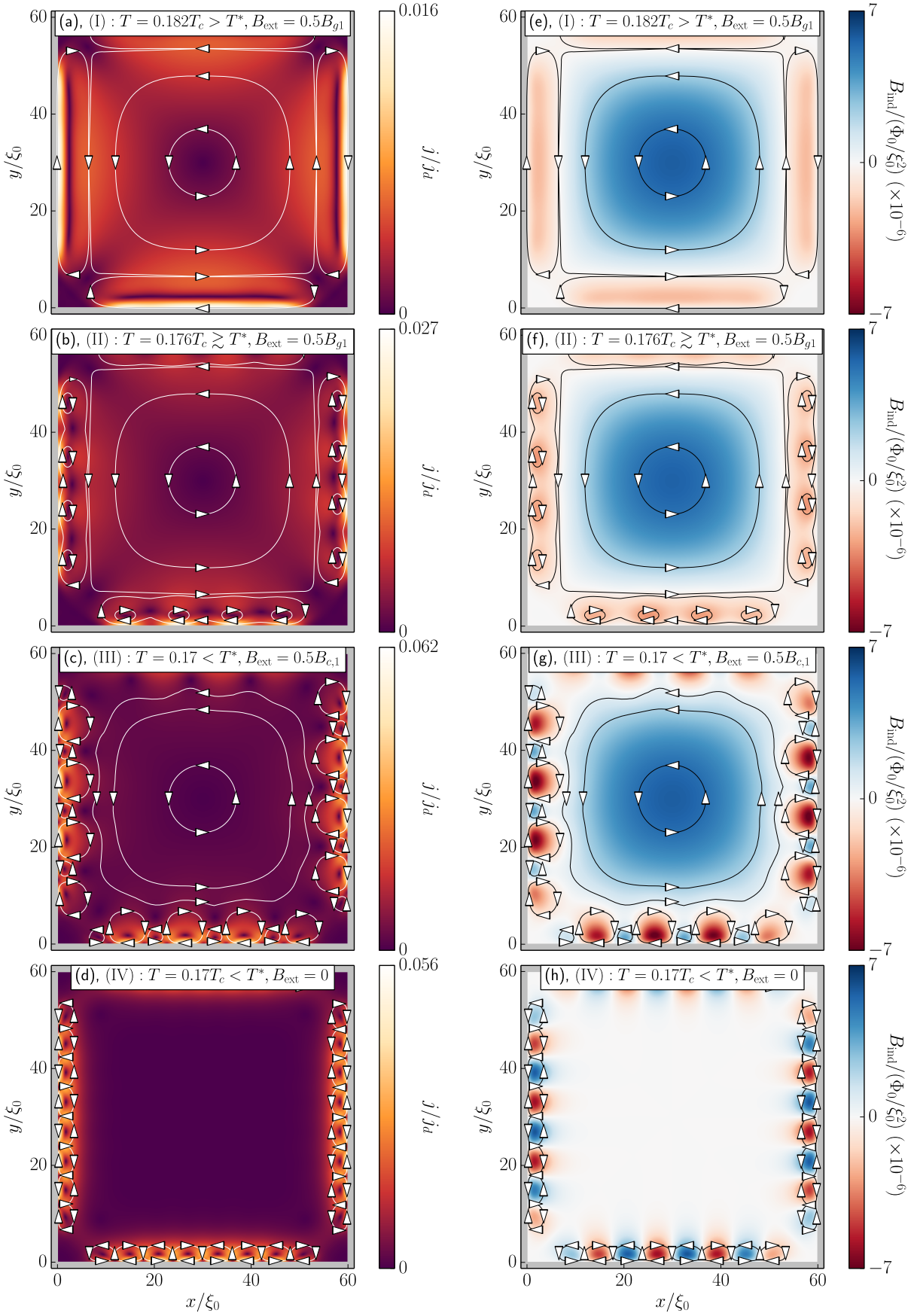

FIG. 3. (Color online) (a)–(d) Total current magnitude and (e)–(h) induced magnetic flux density for different temperatures and external fields (see annotations). Lines and arrows have been added to illustrate the flow of the currents.

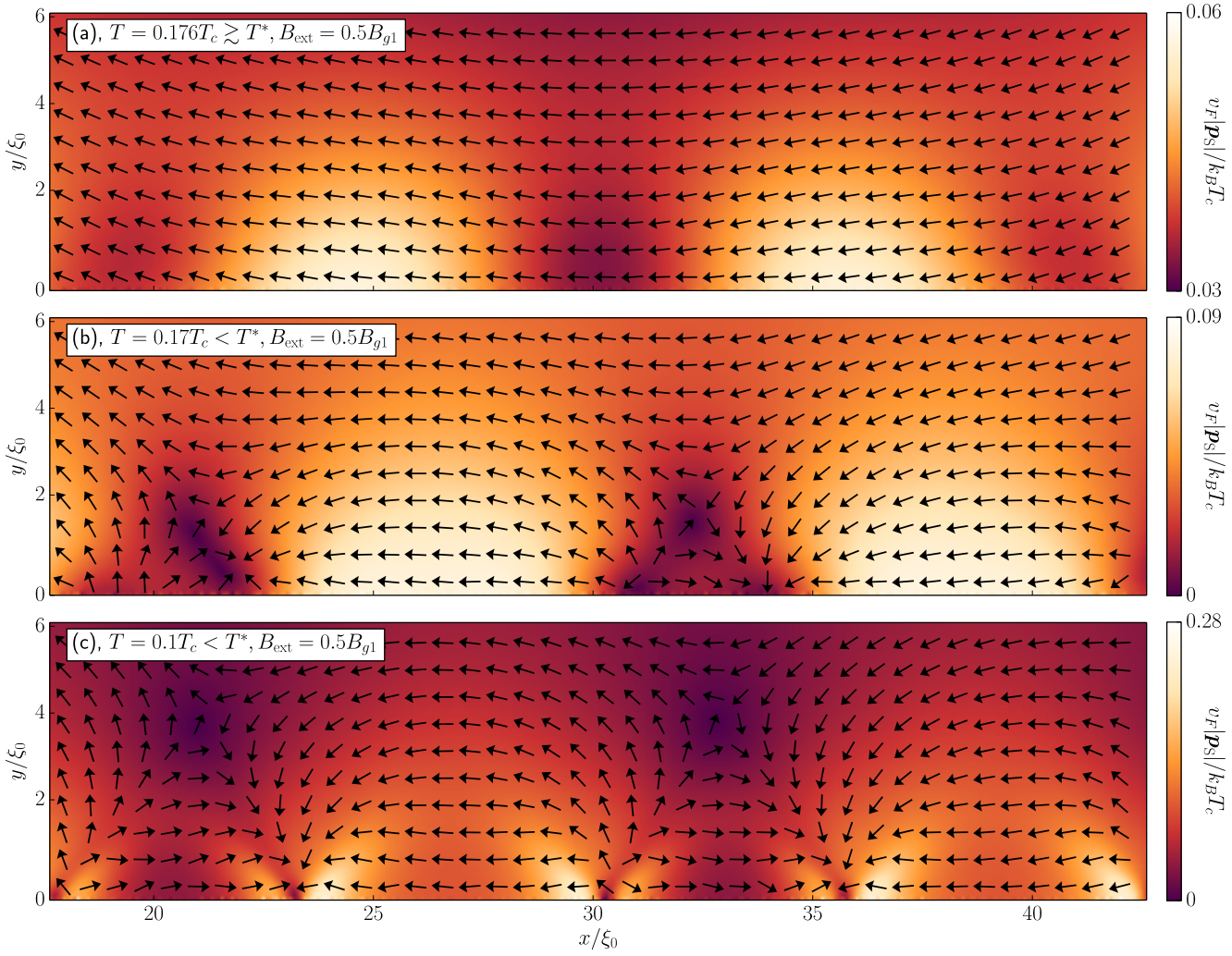

FIG. 4. The superfluid momentum induced in an external magnetic field of $B_{\rm ext} = 0.5B_{g1}$ for lowering temperatures from top to bottom. At the phase transition, source-sink-saddle-point motifs appear and separate along the edge breaking translational invariance along the edge coordinate x. At the same time the magnitude $|\boldsymbol{p}_s|$ grows large. Note the different color scales are used in the subfigures in order to enhance visibility.

having only a diamagnetic response at $B_{\rm ext} = 0.5B_{g1}$ (dash-dotted line). The paramagnetic response is fully suppressed at low temperatures $T < T^*$. Such a sudden disappearance of the paramagnetic response at a temperature T^* should be experimentally measurable, for example in the penetration depth or by using nano-squids[55,56].

We show in Fig. 7(a) the total induced magnetic flux through the grain

$$\Phi_{\rm ind} = \int d^2R\, B_{\rm ind}(\boldsymbol{R}), \tag{28}$$

and in Fig. 7(b) the area-averaged order parameter magnitude

$$\overline{\Delta}_d = \frac{1}{\mathcal{A}} \int d^2R\, |\Delta_d(\boldsymbol{R})|, \tag{29}$$

both as functions of temperature for different values of $B_{\rm ext}$. The figures also show results for a d-wave grain without pair-breaking edges at $B_{\rm ext} = 0.5B_{g1}$ (dash-dotted line). For better visibility, the latter results have been scaled by a factor 0.4 and 0.9 in (a) and (b), respectively. Two different trends are distinguishable in the observables for $T < T^*$ and $T > T^*$, separated by a "kink". The induced magnetic flux through the grain area decreases as T decreases down to T^* due to the increasing paramagnetic response that competes with the diamagnetic one. At T^*, the inhomogeneous edge state appear and starts competing with the paramagnetic response. Thus, the total magnetic flux increases again. At the same time the order parameter is partially healed.

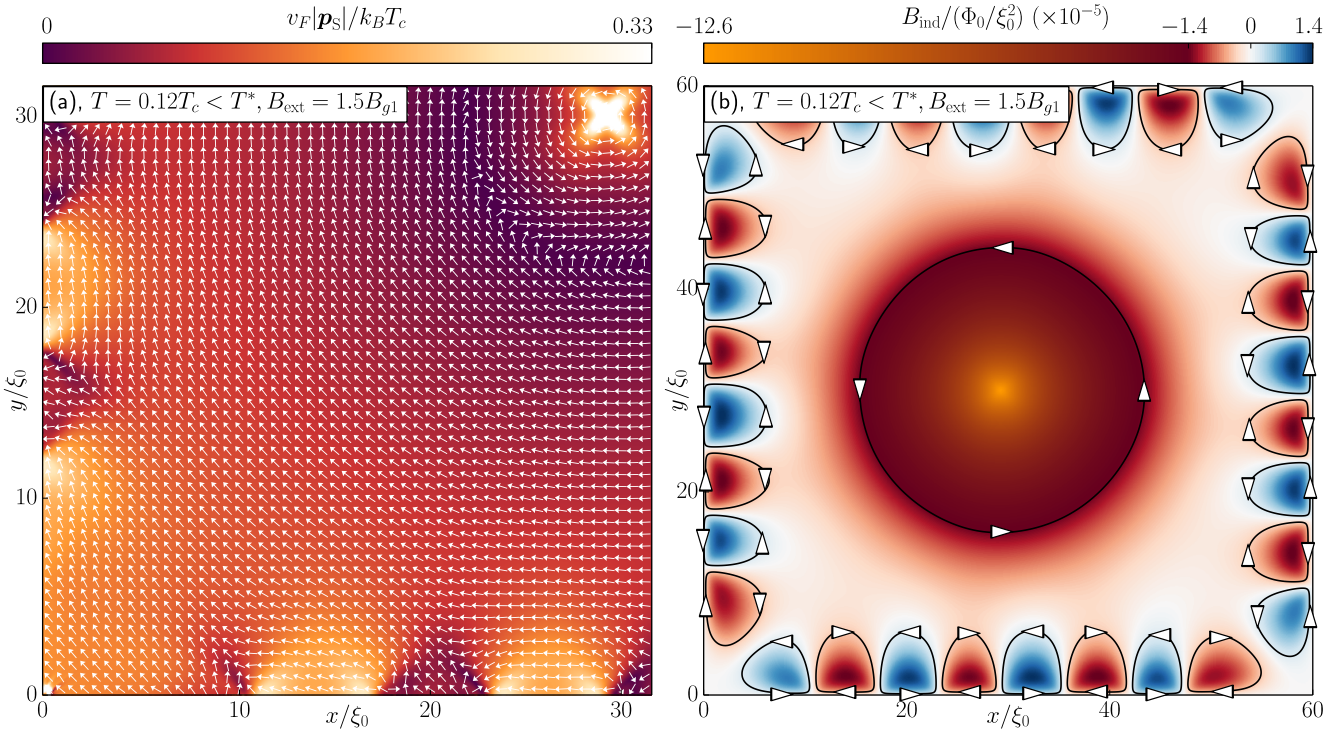

FIG. 5. (Color online) (a) Superfluid momentum $\boldsymbol{p}_s(\boldsymbol{R})$ and (b) the induced field $B_{\rm ind}(\boldsymbol{R})$ at $T = 0.1T_c < T^*$ and $B_{\rm ext} = 1.5B_{g1}$, with an Abrikosov vortex stabilized in the center of the grain. The penetration depth is larger than the size of the grain, which means that the Abrikosov vortex is overlapping with the induced fluxes at the pair-breaking edges. The colormap for the flux density has been chosen to show that the edge fluxes (red to blue colors) are similar to those in Fig. 3.

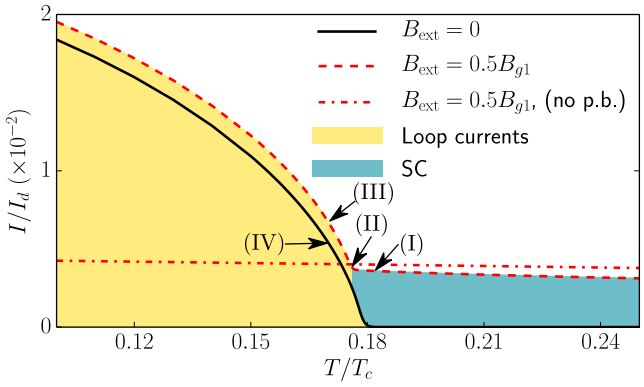

FIG. 6. (Color online) Area-averaged current magnitude defined in Eq. (27), versus temperature, without any external magnetic field (solid line), with an external magnetic field of magnitude $B_{\rm ext} = 0.5B_{g1}$ (dashed line), and for a system without pair-breaking edges at $B_{\rm ext} = 0.5B_{g1}$ (dash-dotted line). The latter has only a diamagnetic response. Letters (I)–(IV) indicate the parameter values corresponding to the fields in Fig. 3, see Table I.

A. Phase transition and thermodynamics

The sudden changes with a discontinuity in the derivative as function of temperature of the total induced current, the magnetic flux, as well as the order parameter (Fig. 6-Fig. 7) indicate that there is a phase transition occurring at the temperature T^*. In zero external magnetic field, we showed in Ref. 25 that there is a second order phase transition at T^*, where both time-reversal symmetry and continuous translational symmetry along the edge are spontaneously broken. Let us now investigate the thermodynamics in an external magnetic field already explicitly breaking time-reversal symmetry.

In Fig. 8(a) we plot the free energy difference between the superconducting and normal states $\Omega_S - \Omega_N$, defined in Eq. (23), for external field $B = 0.5B_{g1}$ (red dashed line) and for zero field (solid black line). For comparison, we show the free energy difference for a purely real order parameter in zero field (black fine line), i.e. without the symmetry breaking edge loop currents. For $T < T^*$, this solution is not the global minimum of the free energy, and we therefore refer to it as a *meta-stable* state. To enhance the visibility of the differences in free energy between the possible solutions, we show in Fig. 8(b) the free energy difference with respect to the metastable state, i.e. $\Omega_S - \Omega_{ms}$. The small slope in the red dashed line at $T > T^*$ in Fig. 8 (b) is caused by the shift of mid-gap Andreev states due to the paramagnetic response, which increases as T decreases. The phase transition temperature T^* for the second order phase transition can be identified with the "knee" in the entropy difference defined in

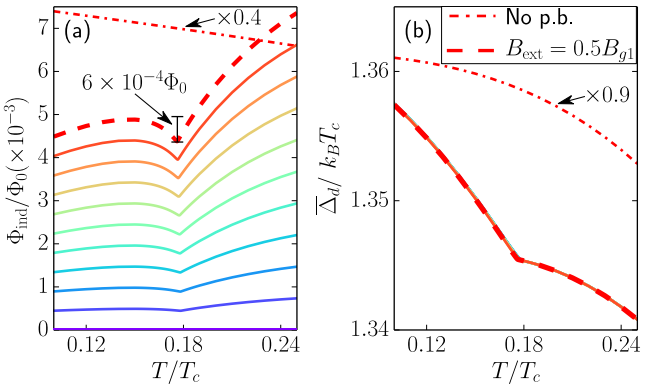

FIG. 7. (Color online) (a) Temperature dependence of the induced magnetic flux defined in Eq. (28). The solid lines indicate, from bottom to top (colors purple to red), the external field magnitude from $B_{\rm ext}=0$ to $B_{\rm ext}=0.5B_{g1}$ in steps of $0.05B_{g1}$. The line corresponding to zero field lies exactly at zero since there is an equal amount of positive and negative fluxes induced in this case, see Fig. 3. Panel (b) shows the area-averaged order parameter magnitude defined in Eq. (29) versus temperature. Results are also shown for a system without pair-breaking edges (dash-dotted line) at $B_{\rm ext}=0.5B_{g1}$, but scaled with a factor 0.4 and 0.9 in (a) and (b), respectively.

Eq. (25), see Fig. 8(c) and Fig. 8(d). Since time-reversal symmetry is already explicitly broken by the external magnetic field, the phase transition signals breaking of continuous translational symmetry and establishment of the vector field $\boldsymbol{p}_s$ with the chain of disclinations along the edge, as shown in Fig. 4.

The knee in the entropy leads to a jump in the specific heat, as shown in Fig. 8(e) and Fig. 8(f). The heat capacity is expressed in units of the heat capacity jump at the normal-superconducting phase transition at T_c for a bulk d-wave system

$$\Delta C_d=\frac{2\alpha}{3}\mathcal{A}k_B^2T_cN_F, \tag{30}$$

where

$$\alpha=\frac{8\pi^2}{7\zeta(3)}, \tag{31}$$

with ζ being the Riemann-zeta function. The jump in heat capacity at the phase transition is an edge-to-area effect, and grows linearly as the sample becomes smaller. The jump is roughly 4.5% of ΔC_d for the mesoscopic $\mathcal{A}=60\times60\xi_0^2$ grain considered here, and grows as the size of the grain is reduced. The phase transition temperature T^* is extracted as a function of $B_{\rm ext}$ as the midpoint temperature of the jump in the specific heat. Fig. 9 shows a phase diagram where the T^*, extracted in this way from the specific heat, is plotted versus external field strength (crosses). We compare this with T^* extracted as the minimum [the "kink", see Fig. 7(a)] in the induced flux. The small lowering of T^* with increased $B_{\rm ext}$ is caused by the competing paramagnetic response.

From the above it is clear that the phase with edge loop-currents shows extreme robustness against an external magnetic field in the whole Meissner region ($B_{\rm ext}\leq B_{g1}$). The magnitude of the spontaneously formed superfluid momentum $\boldsymbol{p}_s$ at the edge grows nonlinearly to be very large for $T<T^*$, fueled by the lowering of the free energy by Doppler shifts of the flat band of Andreev surface states. The corresponding correction to $\boldsymbol{p}_s$ due to the process of screening of the external magnetic field, is in comparison small. Thereby, T^* is not dramatically shifted in a magnetic field and the symmetry broken phase below T^* is robust.

IV. SUMMARY AND CONCLUSIONS

We have used the quasiclassical theory of superconductivity to study mesoscopic superconducting grains with pair-breaking edges. Using this method, a phase which spontaneously breaks translational symmetry and $\mathcal{T}$-symmetry was found in our previous study[25] and we have in this paper discussed the magnetic field dependent thermodynamics in detail. We have shown that the phase should be quantified in terms of its order parameter, the vector field $\boldsymbol{p}_s(\boldsymbol{R})$, which contains edge sources and sinks, as well as saddle point disclinations. At these points $\nabla\times\boldsymbol{p}_s\neq0$. We have studied how an external magnetic field in both the Meissner state ($B_{\rm ext}<B_{c1}$) and the mixed state ($B_{c1}<B_{\rm ext}<B_{c2}$) affects this phase, and in particular, how the transition temperature T^* into this phase varies with the intensity of the external field. Above T^*, the external field gives rise to the usual diamagnetic Meissner current in the bulk sample, and a paramagnetic response along pair-breaking edges. The paramagnetic current is carried by quasiparticles (midgap states), typically survives a coherence length into the sample, and gives rise to a tiny Doppler shift of mid-gap states that competes with the loop-current phase. As the temperature approaches T^*, two types of nodes form where the paramagnetic response is locally suppressed and enhanced. As the temperature is lowered below T^*, current loops appears at the nodes with opposite circulations in neighboring loops. The loop current strength increases highly non-linearly, suppressing the paramagnetic response. As the strength of the external magnetic field increases, the size of the Doppler shift due to the paramagnetic response grows linearly. Therefore, T^* decreases slightly as the magnitude of the external field increases. The influence of the external field, and in particular the sudden disappearance of the paramagnetic response, leads to observables which we argue should be visible in experiment. For example the "kink" in the total induced flux at the T^*. The vortices should be directly observable with recently developed scanning probes[55,56], and the sudden disappearance of the paramagnetic response should to be observable with nano-SQUIDS and possibly in penetration-depth experiments. Furthermore, the large jump in heat capacity at the phase

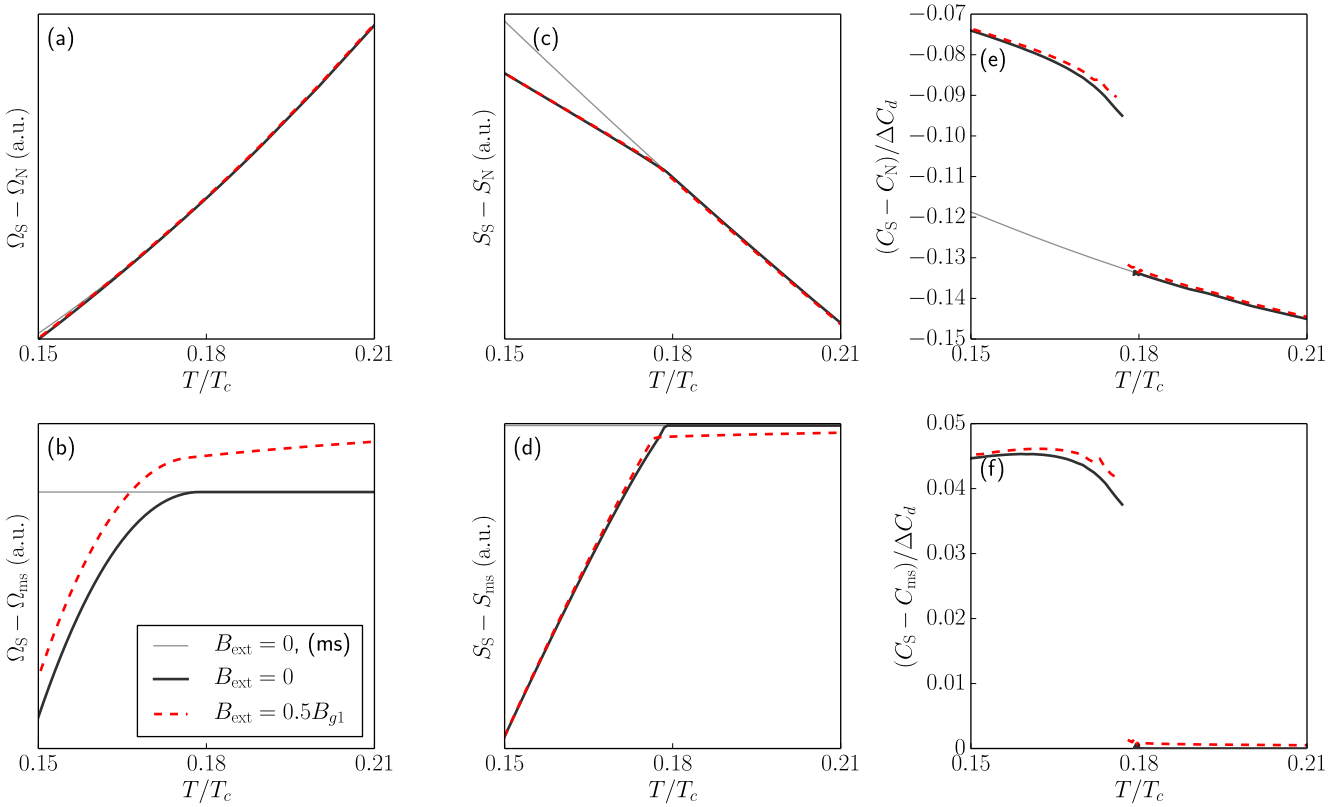

FIG. 8. (Color online) (a)–(b) free energy, (c)–(d) entropy, and (e)–(f) specific heat capacity, versus temperature. The lines correspond to a system with purely real order parameter without edge currents (black fine line), a system with spontaneous edge currents in zero magnetic field (black solid line), and in a finite external field $B = 0.5B_{g1}$ (red dashed line). In the lower panels (b), (d), and (f), the quantities have been subtracted by the corresponding values of the system with a purely real order parameter, the meta-stable (ms) state. The heat capacity is normalized by the heat capacity jump in the normal-superconducting phase transition for a bulk d-wave system, denoted ΔC_d.

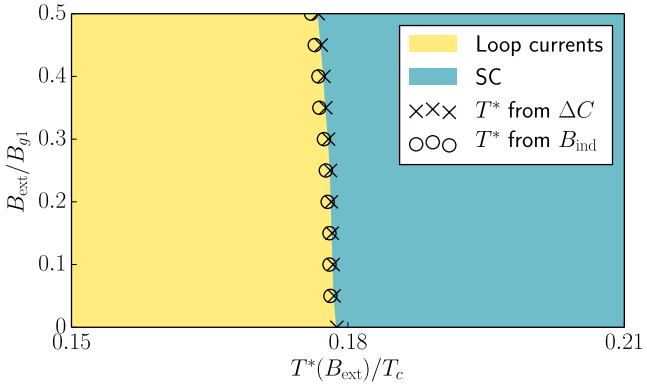

FIG. 9. (Color online) Phase diagram of the d-wave superconductor with pair breaking edges, showing the transition temperature T^* to a state with spontaneously broken continuous translational symmetry versus the external magnetic flux density. The crosses show T^* extraced from the jump in the specific heat in Fig. 8(e), while the open circles show T^* extracted from the minimum of the total induced magnetic flux in Fig. 7(a).

transition should be observable with nanocalorimetry[57].

ACKNOWLEDGMENTS

We thank the Swedish Research Council for financial support. It is a pleasure to thank Mikael Håkansson, Niclas Wennerdal, and Per Rudquist for valuable discussions.

* holmvall@chalmers.se
† anton.vorontsov@montana.edu
‡ mikael.fogelstrom@chalmers.se
§ tomas.lofwander@chalmers.se

[1] G. N. Gol'tsman, O. Okunev, G. Chulkova, A. Lipatov, A. Semenov, K. Smirnov, B. Voronov, A. Dzardanov, C. Williams, and R. Sobolewski, Appl. Phys. Lett. **79**, 705 (2001).
[2] S. De Franceschi, L. Kouwenhoven, C. Schönenberger, and W. Wernsdorfer, Nat. Nanotechnol. **5**, 703 (2010).
[3] U. Welp, K. Kadowaki, and R. Kleiner, Nat. Photon. **7**, 702 (2013).
[4] A. Fornieri and F. Giazotto, Nat. Nanotechnol. **12**, 944 (2017).
[5] D. Gustafsson, D. Golubev, M. Fogelström, T. Claeson, S. Kubatkin, T. Bauch, and F. Lombardi, Nat. Nanotechnol. **8**, 25 (2013).
[6] S. Kashiwaya and Y. Tanaka, Rep. Prog. Phys. **63**, 1641 (2000).
[7] T. Löfwander, V. S. Shumeiko, and G. Wendin, Supercond. Sci. Technol. **14**, R53 (2001).
[8] R. Baghdadi, R. Arpaia, S. Charpentier, D. Golubev, T. Bauch, and F. Lombardi, Phys. Rev. Appl. **4**, 014022 (2015).
[9] M. Xie, M. L. Chukharkin, S. Ruffieux, J. F. Schneiderman, A. Kalabukhov, M. Arzeo, T. Bauch, F. Lombardi, and D. Winkler, Supercond. Sci. Technol. **30**, 0 (2017).
[10] C.-R. Hu, Phys. Rev. Lett. **72**, 1526 (1994).
[11] M. Matsumoto and H. Shiba, J. Soc. Phys. Jpn. **64**, 3384 (1995).
[12] M. Matsumoto and H. Shiba, J. Soc. Phys. Jpn. **64**, 4867 (1995).
[13] M. Fogelström, D. Rainer, and J. A. Sauls, Phys. Rev. Lett. **79**, 281 (1997).
[14] M. Sigrist, Prog. Theor. Phys. **99**, 899 (1998).
[15] C. Honerkamp, K. Wakabayashi, and M. Sigrist, Europhys. Lett. **50**, 368 (2000).
[16] A. C. Potter and P. A. Lee, Phys. Rev. Lett. **112**, 117002 (2014).
[17] S. Higashitani, J. Soc. Phys. Jpn. **66**, 2556 (1997).
[18] Y. S. Barash, M. S. Kalenkov, and J. Kurkijärvi, Phys. Rev. B **62**, 6665 (2000).
[19] T. Löfwander, V. S. Shumeiko, and G. Wendin, Phys. Rev. B **62**, R14653 (2000).
[20] A. B. Vorontsov, Phys. Rev. Lett. **102**, 177001 (2009).
[21] M. Hachiya, K. Aoyama, and R. Ikeda, Phys. Rev. B **88**, 064519 (2013).
[22] S. Higashitani and N. Miyawaki, J. Soc. Phys. Jpn. **84**, 033708 (2015).
[23] N. Miyawaki and S. Higashitani, Phys. Proc. **65**, 25 (2015).
[24] N. Miyawaki and S. Higashitani, Phys. Rev. B **91**, 094511 (2015).
[25] M. Håkansson, T. Löfwander, and M. Fogelström, Nat. Phys. **11**, 755 (2015).
[26] P. Holmvall, T. Löfwander, and M. Fogelström, accepted in the proceedings of the 28th International Conference on Low Temperature Physics, to be published in Journal of Physics: Conference Series (2017), arXiv:1706.06165.
[27] J. Kirtley, C. Tsuei, A. Ariando, C. Verwijs, S. Harkema, and H. Hilgenkamp, Nat. Phys. **2**, 190 (2006).
[28] H. Saadaoui, G. D. Morris, Z. Salman, Q. Song, K. H. Chow, M. D. Hossain, C. D. P. Levy, T. J. Parolin, M. R. Pearson, M. Smadella, D. Wang, L. H. Greene, P. J. Hentges, R. F. Kiefl, and W. A. MacFarlane, Phys. Rev. B **83**, 054504 (2011).
[29] M. Covington, M. Aprili, E. Paraoanu, L. H. Greene, F. Xu, J. Zhu, and C. A. Mirkin, Phys. Rev. Lett. **79**, 277 (1997).
[30] Y. Dagan and G. Deutscher, Phys. Rev. Lett. **87**, 177004 (2001).
[31] G. Elhalel, R. Beck, G. Leibovitch, and G. Deutscher, Phys. Rev. Lett. **98**, 137002 (2007).
[32] W. K. Neils and D. J. Van Harlingen, Phys. Rev. Lett. **88**, 047001 (2002).
[33] G. Deutscher, Rev. Mod. Phys. **77**, 109 (2005).
[34] K. Krishana, N. P. Ong, Q. Li, G. D. Gu, and N. Koshizuka, Science **277**, 83 (1997).
[35] T. Watashige, Y. Tsutsumi, T. Hanaguri, Y. Kohsaka, S. Kasahara, A. Furusaki, M. Sigrist, C. Meingast, T. Wolf, H. v. Löhneysen, T. Shibauchi, and Y. Matsuda, Phys. Rev. X **5**, 031022 (2015).
[36] G. Eilenberger, Z. Phys. **214**, 195 (1968).
[37] A. I. Larkin and Y. N. Ovchinnikov, Sov. Phys. JETP **28**, 1200 (1969).
[38] A. Shelankov, J. Low Temp. Phys. **60**, 29 (1985).
[39] J. Serene and D. Rainer, Phys. Rep. **101**, 221 (1983).
[40] M. Eschrig, J. Heym, and D. Rainer, J. Low Temp. Phys. **95**, 323 (1994).
[41] M. Eschrig, D. Rainer, and J. A. Sauls, Phys. Rev. B **59**, 12095 (1999).
[42] J. A. Sauls and M. Eschrig, New J. Phys. **11**, 075008 (2009).
[43] Y. Nagato, K. Nagai, and J. Hara, J. Low Temp. Phys. **93**, 33 (1993).
[44] N. Schopohl and K. Maki, Phys. Rev. B **52**, 490 (1995).
[45] N. Schopohl, cond-mat/9804064.
[46] M. Eschrig, J. A. Sauls, and D. Rainer, Phys. Rev. B **60**, 10447 (1999).
[47] M. Eschrig, Phys. Rev. B **61**, 9061 (2000).
[48] A. B. Vorontsov and J. A. Sauls, Phys. Rev. B **68**, 064508 (2003).
[49] M. Eschrig, Phys. Rev. B **80**, 134511 (2009).
[50] R. Grein, T. Löfwander, and M. Eschrig, Phys. Rev. B **88**, 054502 (2013).
[51] Y. Nagai, K. Tanaka, and N. Hayashi, Phys. Rev. B **86**, 094526 (2012).
[52] H. Walter, W. Prusseit, R. Semerad, H. Kinder, W. Assmann, H. Huber, H. Burkhardt, D. Rainer, and J. A. Sauls, Phys. Rev. Lett. **80**, 3598 (1998).
[53] N. D. Mermin, Rev. Mod. Phys. **51**, 591 (1979).
[54] F. Effenberger and D. Weiskopf, Comput. Visual Sci. **13**, 377 (2011).
[55] D. Vasyukov, Y. Anahory, L. Embon, D. Halbertal, J. Cuppens, L. Neeman, A. Finkler, Y. Segev, Y. Myasoedov, M. L. Rappaport, M. E. Huber, and E. Zeldov, Nat. Nanotechnol. **8**, 639 (2013).
[56] M. Pelliccione, A. Jenkins, P. Ovartchaiyapong, C. Reetz, E. Emmanouilidou, N. Ni, and A. C. Bleszynski Jayich, Nat. Nanotechnol. **11**, 700 (2016).
[57] Z. Diao, D. Campanini, L. Fang, W. K. Kwok, U. Welp, and A. Rydh, Phys. Rev. B **93**, 014509 (2016).

Paper II

Spontaneous generation of fractional vortex-antivortex pairs at single edges of high-Tc superconductors

P Holmvall, T Löfwander and M Fogelström

Department of Microtechnology and Nanoscience – MC2, Chalmers University of Technology, SE-41296 Göteborg, Sweden

E-mail: holmvall@chalmers.se, tomas.lofwander@chalmers.se, mikael.fogelstrom@chalmers.se

Abstract. Unconventional d-wave superconductors with pair-breaking edges are predicted to have ground states with spontaneously broken time-reversal and translational symmetries. We use the quasiclassical theory of superconductivity to demonstrate that such phases can exist at any single pair-breaking facet. This implies that a greater variety of systems, not necessarily mesoscopic in size, should be unstable to such symmetry breaking. The density of states averaged over the facet displays a broad peak centered at zero energy, which is consistent with experimental findings of a broad zero-bias conductance peak with a temperature-independent width at low temperatures.

1. Introduction

It was established already in the 1990s that a number of high-temperature superconductors have an order parameter with $d_{x^2-y^2}$ symmetry [1]. In such materials, quasiparticle scattering at surfaces or off defects, where the sign of the d-wave order parameter changes for incoming and outgoing scattering trajectories, leads to the formation of Andreev bound states at zero energy [2–4]. For an ideal specular surface with [110]-orientation, all scattering trajectories include the sign change, and the spectral weight of these zero-energy Andreev bound states is very large: they form a flat band at zero energy as function of momentum parallel to the interface, $k_\parallel$. Shifting these mid-gap states to finite energies can lead to lowering of the free energy. Any mechanism providing such a shift can then lead to a phase transition into a new ground state with an associated broken symmetry [5, 6]. Several mechanisms have been proposed, all leading to spontaneous time-reversal symmetry breaking: development of a subdominant superconducting component of the order parameter in a time-reversal symmetry breaking combination with the dominant, e.g. $d_{x^2-y^2} + is$, [7–9]; magnetic ordering [10]; and, finally, spontaneous supercurrents [11–16]. The first two scenarios require an additional coupling constant leading to an associated mean-field order parameter, while the last does not. Which scenario that would be realized experimentally depends on material parameters, for instance the strength of the coupling constants. It was shown in Ref. [15] that the transition temperature within the third scenario is very large, of the order of 20% of the superconducting transition temperature T_c. As a consequence, the other scenarios can compete only if their corresponding

coupling constants are very large, or if the phase with spontaneous supercurrents is suppressed for one reason or another.

So far, there are several transport experiments supporting spontaneous time-reversal symmetry breaking [17–23]. But direct measurements of the associated supercurrents and magnetic fields remain controversial [24, 25]. In our previous studies [15], we showed that this controversy could be related to the manner in which these currents and magnetic fields appear. We found a translational and time-reversal symmetry-breaking phase, in which a staggered pattern of fractional vortex-antivortex pairs forms like a necklace along the pair-breaking surface. The symmetric proportion of vortices to antivortices effectively eliminates any net current and magnetic flux, and the small size of the vortices of a few coherence lengths makes direct observation challenging.

Vorontsov found that a phase gradient can be generated through spontaneous time-reversal symmetry breaking in thin films [14, 26–29], caused by finite-size effects in the form of a proximity of two pair-breaking interfaces. In our previous work [15] we studied mesoscopic grains with only pair-breaking edges and found that the vortex-antivortex phase is more energetically favorable than the thin-film phase predicted by Vorontsov. In this study, we show that the vortex-antivortex phase can occur without finite-size effects. This is done by considering a system with a single pair-breaking edge.

2. Model and methods

We study a mesoscopic superconducting grain in vacuum and equilibrium, with a d-wave pairing symmetry. The sides of the system are perfectly aligned with the crystal ab-axes, except one facet which is misaligned by a 45° rotation (see Fig. 1). The facet gives rise to mid-gap states associated with surface pair-breaking, and has a side-length given in units of the superconducting coherence length $\xi_0 \equiv \hbar v_F/2\pi k_B T_c$. Furthermore, a clean superconductor and a cylindrical Fermi surface is assumed.

To study this system, the quasiclassical theory of superconductivity [30, 31] is used. In this formulation, the superconducting d-wave order parameter $\Delta_d(\boldsymbol{R})$ depends on the anomalous Green's function (pair propagator) $f(\boldsymbol{p}_F, \boldsymbol{R}; \epsilon_n)$ through the gap equation

$$\Delta_d(\boldsymbol{R}) = V_d k_B T \int \frac{d\theta_{p_F}}{2\pi} \eta_d^*(\theta_{p_F}) \sum_{|\epsilon_n| \leq \Omega_c} f(\boldsymbol{p}_F, \boldsymbol{R}; \epsilon_n), \tag{1}$$

at spatial coordinate $\boldsymbol{R}$, quasiparticle momentum $\boldsymbol{p}_F$ and Matsubara energy ϵ_n (these parameters will from now on be dropped for a compact notation). Here, θ_{p_F} is the angle between the Fermi momentum and the crystal ab-axes, $\eta_d(\theta_{p_F}) = \sqrt{2}\cos(2\theta_{p_F})$ the d-wave order parameter basis function, $V_d = -N_F\lambda_d$ the pair-potential, N_F the normal-state density of states at the Fermi surface, λ_d the pairing interaction, and Ω_c the cutoff energy. The anomalous Green's function is the off-diagonal component of the Matsubara Green's function

$$\hat{g} = \begin{pmatrix} g & f \\ -\tilde{f} & \tilde{g} \end{pmatrix}, \tag{2}$$

where *hat* denotes Nambu (electron-hole) space. The tilde operation denotes particle-hole conjugation, $\tilde{g}(\boldsymbol{p}_F, \boldsymbol{R}; \epsilon_n) = g^*(-\boldsymbol{p}_F, \boldsymbol{R}, \epsilon_n)$ [and the same for $\tilde{f}$]. The Green's function is obtained by solving the Eilenberger equation with the associated normalization condition

$$i\hbar \boldsymbol{v}_F \cdot \boldsymbol{\nabla}_R \hat{g} + \left[\hat{\tau}_3 z - \hat{\Delta}, \hat{g}\right] = \hat{0}, \tag{3}$$

$$\hat{g}^2 = -\pi^2 \hat{1}, \tag{4}$$

where $\hat{\Delta} = i(\hat{\tau}_2 \Re\Delta_d + \hat{\tau}_1 \Im\Delta_d)\eta_d(\theta_{p_F})$, and $\hat{\tau}_i$ $(i = 1, 2, 3)$ are the three Pauli matrices in Nambu space. The Eilenberger equation and the gap equation are solved self-consistently by the so-called Riccati technique (see for instance Ref. [32]). After self-consistency has been achieved, we compute observables such as the current density

$$\boldsymbol{j}(\boldsymbol{R}) = 4\pi e N_F k_B T \int \frac{d\theta_{p_F}}{2\pi} \boldsymbol{v}_F(\boldsymbol{p}_F) \sum_{\epsilon_n} g(\boldsymbol{p}_F, \boldsymbol{R}; \epsilon_n). \tag{5}$$

The magnetic flux density induced by the current density is calculated through Maxwells equations and Ampère's circuit law.

3. Results and discussion

Figure 1 shows the induced magnetic flux density for two different superconducting grains that both have a single pair-breaking facet. The flux is generated by the fractional vortex-antivortex phase, and the pair-breaking facet is formed by cutting away either a triangular corner or a triangular section in the middle of a square grain, as shown in Figs. 1 (a) and (b), respectively. Thus, in the latter case, the pair-breaking facet is completely surrounded by bulk superconductivity. The fact that the phase persists in these two systems clearly illustrates a contrast to the Vorontsov phase [14], which relies on the proximity of two pair-breaking edges. Figure 1 (c) shows a magnification of the pair-breaking facet in Figure 1 (a). As shown, there

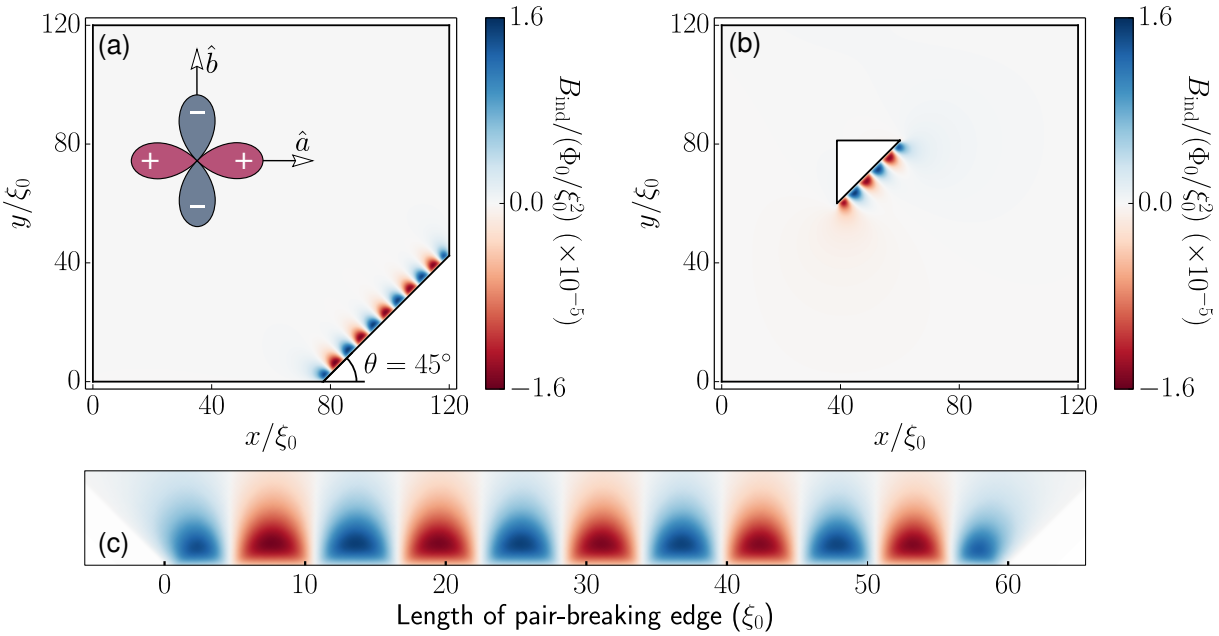

Figure 1. (Color online) (a) A d-wave superconducting grain at temperature $T = 0.1T_c$ with a spontaneously induced magnetic flux density, due to spontaneous generation of fractional vortices and antivortices. The latter breaks time-reversal and translational (along the facet) symmetries, and is linked to an energetically favorable Doppler shift of mid-gap states to finite energies. These mid-gap states are formed through pair-breaking along the diagonal grain facet, which is rotated 45° relative to the crystal ab-axes. All other grain edges are perfectly aligned with the crystal axes, as indicated by the graphics. In panel (b), a triangular portion of a square superconductor has been cut away, such that the pair-breaking facet is surrounded by bulk superconductivity. Panel (c) is a magnification of the pair-breaking facet in panel (a).

might be an unequal number of vortices and antivortices for certain sizes, although the flux density sums to zero. This is illustrated further in Fig. 2, where we vary the length of the pair-breaking facet in corner-cut systems. Each panel shows the induced flux along the pair-breaking facet in a square grain of side-length $120\xi_0$. The length of the facet varies from $2.5\xi_0$ in panel (a), to $66\xi_0$ in panel (f). There are two relevant regimes; one when the length of the facet is comparable to the fractional vortex size ($\sim 5\xi_0$), and another when it is much larger. In the latter case, the fractional vortices have a fairly constant diameter of $5\xi_0$, except the corner, or (outermost, vortices which are generally smaller. Lengthening the facet increases the size of the corner vortices, until they reach the same size as the central vortices, and new corner vortices are formed. Therefore, there might be an unequal number of vortices and antivortices for certain sizes. The flux density sums to zero, however, thanks to the corner vortices being much smaller. This again illustrates the fractionality of the vortices. The most striking feature, however, is that the phase survives even as the facet becomes smaller than $5\xi_0$, yielding a system with a single fractional vortex and a clear net flux. The system obviously finds it more favorable to shift the mid-gap states at the expense of having a net flux. Thus, the system with a single pair-breaking facet seems to lack a critical minimum size, in contrast to both the thin-film geometry [14], and the mesoscopic grain where all sides are pair-breaking [15].

Finally, Figs. 3 (a)–(b) show the density of states (DOS) along the facet for the systems in Figs. 2 (a)–(b), respectively. All other systems have an identical DOS as in panel (b). The solid

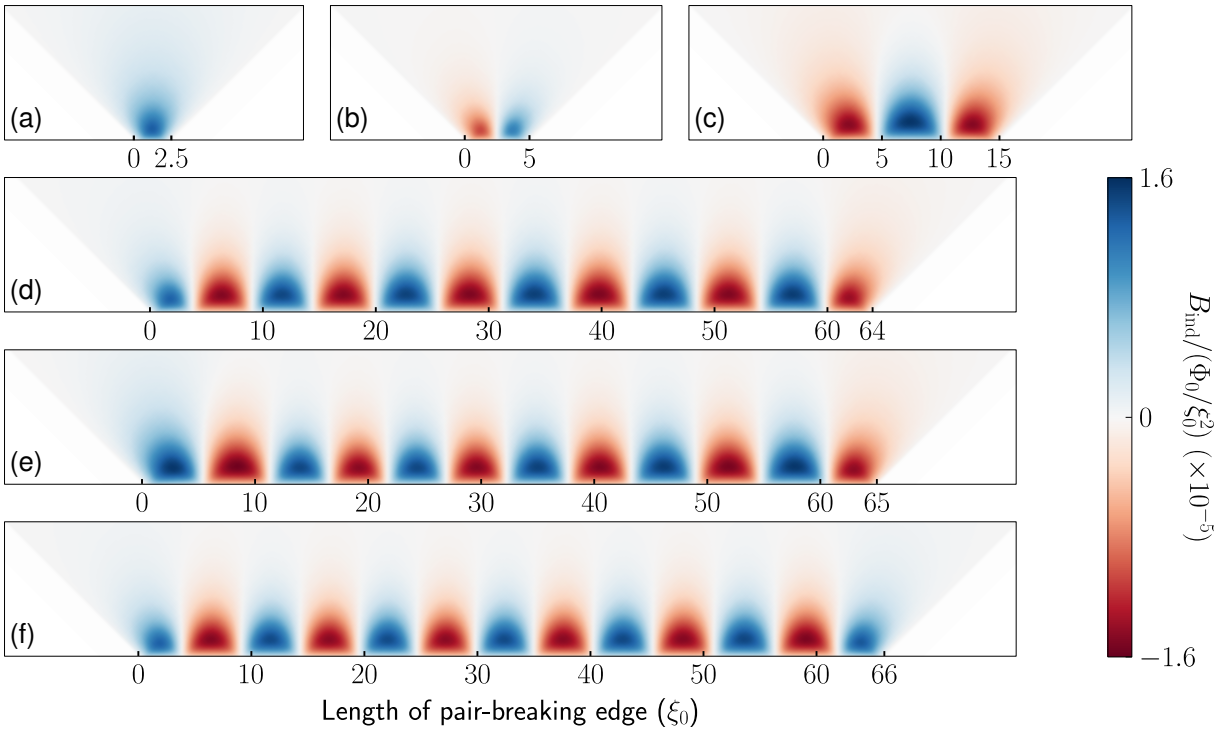

Figure 2. (Color online) Magnetic flux density due to spontaneous fractional vortices along a pair-breaking facet, where the length of the facet varies from panel (a) to (f). In each panel, the system is a square grain with a side-length of $120\xi_0$, with one of the corners cut off at a 45° angle to generate the pair-breaking facet, as illustrated in Fig. 1 (a). Due to finite-size effects, there might be an unequal amount of vortices and antivortices, although the total flux still adds to zero. The only exception is when the facet is smaller than the typical vortex size ($\sim 5\xi_0$) as in panel (a), at which point there is a single vortex and a net flux. The temperature is $T = 0.1T_c$.

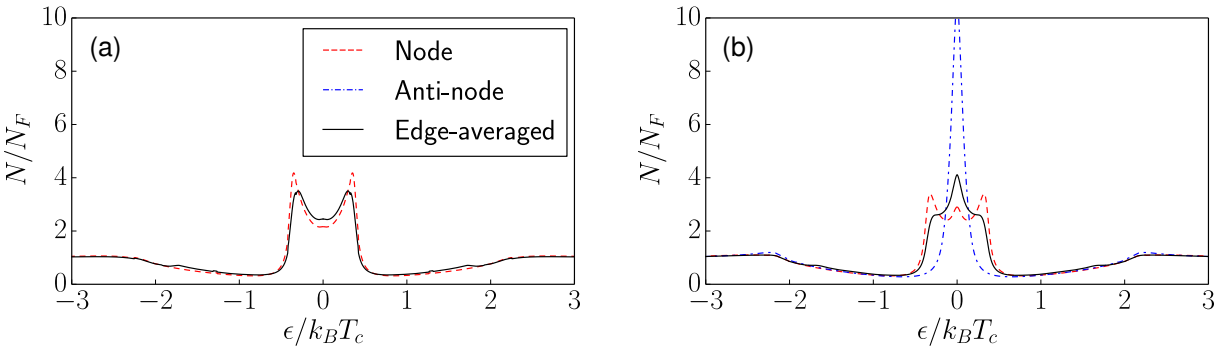

Figure 3. (Color online) Density of states as a function of energy at the pair-breaking facet, evaluated in the middle of a vortex current (dashed line) and between vortices (dot-dashed line). The solid line is the facet-averaged density of states. Panels (a)–(b) correspond to the systems in Figs. 2 (a)–(b), respectively. The rest of the systems have an identical DOS as in panel (b).

lines represent the facet-averaged DOS, the dashed lines the local DOS at a node (vortex) and the dot-dashed lines the local DOS at an anti-node (between vortices). System (a) has a single vortex, resulting in a fully split peak. All other systems show a wide peak in the facet-averaged DOS. This result would be observable in a tunneling experiment as a conductance peak centered at zero energy with a rather large width, that at low temperatures is temperature independent. Only for system (a), or with a very local probe (point contact with a diameter smaller than the superconducting coherence length) would a split conductance peak be observable.

4. Conclusions

We have used the quasiclassical theory of superconductivity to study a phase that spontaneously breaks translational and time-reversal symmetries at pair-breaking edges, in unconventional d-wave superconductors. Similar phases have been suggested by theory for quite some time, but up until now, have relied on finite-size effects and the proximity of two such pair-breaking edges. We have shown that such finite-size effects are not necessary for such a phase to exist, and that there is no clear critical size below which the phase disappears. This implies that any system with pair-breaking edges should be unstable to the formation of fractional vortices. Therefore, the phase should be present at a greater variety of systems than previously proposed, and lead to a broadening of zero-bias conductance peaks.

Acknowledgments

We thank the Swedish Research Council (VR) for financial support. It is a pleasure to thank Mikael Håkansson, Niclas Wennerdal and Anton Vorontsov for valuable discussions.

References

[1] Tsuei C C and Kirtley J R 2000 *Rev. Mod. Phys.* **72** 969
[2] Hu C R 1994 *Phys. Rev. Lett.* **72** 1526
[3] Kashiwaya S and Tanaka Y 2000 *Rep. Prog. Phys.* **63** 1641
[4] Löfwander T, Shumeiko V S and Wendin G 2001 *Supercond. Sci. Technol.* **14** R53
[5] Volovik G and Gor'kov L 1985 *Sov. Phys. JETP* **61** 843
[6] Sigrist M and Ueda K 1991 *Rev. Mod. Phys.* **63** 239
[7] Matsumoto M and Shiba H 1995 *J. Phys. Soc. Jpn.* **64** 3384
[8] Matsumoto M and Shiba H 1995 *J. Phys. Soc. Jpn.* **64** 4867

[9] Fogelström M, Rainer D and Sauls J A 1997 *Phys. Rev. Lett.* **79** 281
[10] Potter A C and Lee P A 2014 *Phys. Rev. Lett.* **112** 117002
[11] Higashitani S 1997 *J. Soc. Phys. Jpn.* **66** 2556
[12] Barash Y S, Kalenkov M S and Kurkijärvi J 2000 *Phys. Rev. B* **62** 6665
[13] Löfwander T, Shumeiko V S and Wendin G 2000 *Phys. Rev. B* **62** R14653
[14] Vorontsov A B 2009 *Phys. Rev. Lett.* **102** 177001
[15] Håkansson M, Löfwander T and Fogelström M 2015 *Nat. Phys.* **11** 755
[16] Nagai Y, Ota Y and Tanaka K 2017 *Phys. Rev. B* **96** 060503
[17] Covington M, Aprili M, Paraoanu E, Greene L H, Xu F, Zhu J and Mirkin C A 1997 *Phys. Rev. Lett.* **79** 277
[18] Krishana K, Ong N P, Li Q, Gu G D and Koshizuka N 1997 *Science* **277** 83
[19] Dagan Y and Deutscher G 2001 *Phys. Rev. Lett.* **87** 177004
[20] Gonnelli R, Calzolari A, Daghero D, Natale L, Ummarino G, Stepanov V and Ferretti M 2001 *Eur. Phys. J. B* **22** 411
[21] Elhalel G, Beck R, Leibovitch G and Deutscher G 2007 *Phys. Rev. Lett.* **98** 137002
[22] Gustafsson D, Golubev D, Fogelström M, Claeson T, Kubatkin S, Bauch T and Lombardi F 2013 *Nat. Nanotechnol.* **8** 25
[23] Watashige T, Tsutsumi Y, Hanaguri T, Kohsaka Y, Kasahara S, Furusaki A, Sigrist M, Meingast C, Wolf T, Löhneysen H v, Shibauchi T and Matsuda Y 2015 *Phys. Rev. X* **5** 031022
[24] Neils W K and Van Harlingen D J 2002 *Phys. Rev. Lett.* **88** 047001
[25] Kirtley J, Tsuei C, Ariando A, Verwijs C, Harkema S and Hilgenkamp H 2006 *Nat Phys* **2** 190
[26] Hachiya M, Aoyama K and Ikeda R 2013 *Phys. Rev. B* **88** 064519
[27] Higashitani S and Miyawaki N 2015 *J. Soc. Phys. Jpn.* **84** 033708
[28] Miyawaki N and Higashitani S 2015 *Phys. Proc.* **65** 25
[29] Miyawaki N and Higashitani S 2015 *Phys. Rev. B* **91** 094511
[30] Eilenberger G 1968 *Z. Phys.* **214** 195
[31] Larkin A I and Ovchinnikov Y N 1969 *Sov. Phys. JETP* **28** 1200
[32] Eschrig M 2009 *Phys. Rev. B* **80** 134511